Longitudinal and Transverse Magnetization in Low-Dimensional Molecule-Based Quantum Magnets

Von der Fakultät für Physik und Geowissenschaften
der Technischen Universität Carolo-Wilhelmina
zu Braunschweig
zur Erlangung des Grades einer
Doktorin der Naturwissenschaften
(Dr.rer.nat.)
genehmigte

Dissertation

von

Anja U. B. Wolter

aus Braunschweig

1. Referent: Jun.-Prof. Dr. S. Süllow

2. Referent: Prof. Dr. M. Lang

eingereicht am: 29.09.2005

mündliche Prüfung (Disputation) am: 09.02.2006

Druckjahr (elektronische Veröffentlichung): 2006

Vorabveröffentlichungen der Dissertation

Teilergebnisse aus dieser Arbeit wurden mit Genehmigung der Fakultät für Physik und Geowissenschaften, vertreten durch den Mentor der Arbeit, in folgenden Beiträgen vorab veröffentlicht:

Publikationen

- A. U. B. Wolter, Hans-Henning Klauss, F. Jochen Litterst, T. Burghardt, Andreas Eichler, Ralf Feyerherm, S. Süllow, *A pressure study of the antiferromagnetic phase of* $FePM_2Cl_2$ *(PM = pyrimidine)*, Polyhedron **22** (2003) 2139.

- A. U. B. Wolter, P. Wzietek, F. J. Litterst, S. Süllow, D. Jérome, R. Feyerherm, H.-H. Klauss, ^{13}C *NMR on the S = 1/2 antiferromagnetically coupled spin chain compound* $[PM\cdot Cu(NO_3)_2\cdot(H_2O)_2]_n$ *(PM = pyrimidine)*, Polyhedron **22** (2003) 2273.

- A. U. B. Wolter, H. Rakoto, M. Costes, A. Honecker, W. Brenig, A. Klümper, H.-H. Klauss, F. J. Litterst, R. Feyerherm, D. Jérome, S. Süllow, *High-field magnetization study of the S =1 /2 antiferromagnetic Heisenberg chain* $[PM\ Cu(NO_3)_2(H_2O)_2]_n$ *with a field-induced gap*, Phys. Rev. B **68** (2003) 220406(R).

- A. U. B. Wolter, P. Wzietek, S. Süllow, F. J. Litterst, P. Auban-Senzier, D. Jérome, R. Feyerherm, H.-H. Klauss, ^{13}C*-NMR under pressure on* $[PM\cdot Cu(NO_3)_2\cdot(H_2O)_2]_n$, J. Magn. Magn. Mater. **272-276** (2004) 1056.

- A. U. B. Wolter, P. Wzietek, S. Süllow, F. J. Litterst, P. Auban-Senzier, D. Jérome, R. Feyerherm, H.-H. Klauss, ^{13}C*-NMR study of the S = 1/2 antiferromagnetically coupled spin chain compound* $[PM\cdot Cu(NO_3)_2\cdot(H_2O)_2]_n$ *under pressure*, J. Phys. IV (France) **114** (2004) 147.

- A. U. B. Wolter, P. Wzietek, D. Jérome, S. Süllow, F. J. Litterst, R. Feyerherm, H.-H. Klauss, *Observation of solitons in the S = 1/2 antiferromagnetic chain* $[CuPM(NO_3)_2(H_2O)_2]_n$ *by* ^{13}C*-NMR*, J. Magn. Magn. Mater. **290-291** (2005) 302.

- A. U. B. Wolter, P. Wzietek, S. Süllow, F. J. Litterst, A. Honecker, W. Brenig, R. Feyerherm, H.-H. Klauss, *Giant Spin Canting in the S = 1/2 Antiferromagnetic Chain* $[CuPM(NO_3)_2(H_2O)_2]_n$ *Observed by* ^{13}C*-NMR*, Phys. Rev. Lett. **94** (2005) 057204.

- J. Kreitlow, D. Menzel, A. U. B. Wolter, J. Schoenes, S. Süllow, R. Feyerherm, K. Doll, *Pressure dependence of* $C_4N_2H_4$*-mediated superexchange in* $XCl_2(C_4N_2H_4)_2$*, (X = Fe, Co, Ni)*, Phys. Rev. B **72** (2005) 134418.

- A. U. B. Wolter, H. Rakoto, J.-M. Broto, A. Honecker, W. Brenig, A. Klümper, H.-H. Klauss, F. J. Litterst, S. Süllow, *High-field Magnetization Study of the* $S = 1/2$ *antiferromagnetic Heisenberg chain* $Cu(C_6H_5COO)_2\cdot 3H_2O$, Physica B, in print (2005).

Tagungsbeiträge

- A. U. B. Wolter, H. H. Klauß, S. Süllow, F. J. Litterst, R. Feyerherm, P. Wzietek, D. Jérome, *NMR Untersuchungen an der antiferromagnetischen 1D Heisenberg Spinkette* $(PM\ Cu(NO_3)_2(H_2O)_2)_n$ (talk), DPG Frühjahrstagung 2002, Regensburg, Germany, 11.-15.03.2002.

- Anja Wolter, Hans-Henning Klauß, Stefan Süllow, Jochen Litterst, Pawel Wzietek, Denis Jérome, Ralf Feyerherm, *A Microscopic Study of* $[PM\ Cu(NO_3)_2(H_2O)_2]_n$*: a* $S = 1/2$ *Heisenberg Chain with a Field Induced Excitation Gap* (poster), VIII$^{\mathrm{th}}$ International Conference on Molecule-based Magnets, ICMM´2002, Valencia, Spain, 05.10.-10.10.2002.

- A. U. B. Wolter, S. Süllow, H.-H. Klauss, F. J. Litterst, P. Wzietek, D. Jérome, R. Feyerherm, ^{13}*C-NMR on the* $S = 1/2$ *afm coupled spin chain compound* $[PM\cdot Cu(NO_3)_2\cdot (H_2O)_2]_n$ *(PM = pyrimidine)* (poster), DPG Frühjahrstagung 2003, Dresden, Germany, 24.-28.03.2003.

- A. U. B. Wolter, S. Süllow, H.-H. Klauss, F. J. Litterst, P. Wzietek, D. Jérome, R. Feyerherm, ^{13}*C-NMR on the* $S = 1/2$ *afm coupled spin chain compound* $[PM\cdot Cu(NO_3)_2\cdot (H_2O)_2]_n$ *(PM = pyrimidine)* (poster), International Conference on Magnetism 2003, Rome, Italy, 27.7.-01.8.2003.

- A. U. B. Wolter, P. Wzietek, D. Jérome, S. Süllow, F. J. Litterst, A. Honecker, W. Brenig, R. Feyerherm, H.-H. Klauss, *Observation of a transverse magnetization in the* $S = 1/2$ *afm chain* $[PM\ Cu(NO_3)_2(H_2O)_2]_n$ *by* ^{13}*C-NMR* (poster), Joint European Magnetic Symposia, Dresden, Germany, 05.09.-10.09.2004.

- A. U. B. Wolter, H. Rakoto, J.-M. Broto, A. Honecker, W. Brenig, A. Klümper, H.-H. Klauss, F. J. Litterst, S. Süllow, *High-field Magnetization Study of the* $S = 1/2$ *antiferromagnetic Heisenberg chain* $Cu(C_6H_5COO)_2\cdot 3H_2O$ (poster), The International Conference on Strongly Correlated Electron Systems, Vienna, Austria, 26.07.-30.07.2005.

Contents

1 Introduction

Starting with the discovery of magnetized iron ore in ancient times, magnetism has been fascinating mankind ever since. With the first application of lodestone in compasses, innumerable magnetic devices with increasing sophistication have been developed, many of which have had an enormous impact on todays society. Applications of magnetism and magnetic materials range from everyday electronic devices used for information storage in computers to transformers and motors involved in the generation and utilization of electric power. Due to the importance of such devices for modern technology there is a constant need for new magnetic materials. A prominent example of this close link between basic science and industry is the observation of a giant magnetoresistance in thin magnetic multilayers [1], which has already been utilized in read heads of computer hard drives after the extraordinarily short period of ten years.

One of the reasons for the profound interest in magnetism during the last two decades has been the relevance of magnetism for high-temperature superconductivity in new transition metal oxides such as $La_{2-x}(Ba,Sr)_xCuO_4$ [2] and $YBa_2Cu_3O_7$ [3] as two well-known examples of the cuprates. In these materials the electronic motion predominantly occurs in two-dimensional CuO_2 layers. As result, the compounds show effects of strong electronic quantum correlations and magnetism in low dimensions, *viz.*, exchange interactions leading to a dominant magnetic coupling much stronger in the 2D planes than along the third axis. This way, a collective behavior of microscopic properties of electrons such as quantum effects is scaled up to a macroscopic strongly interacting ensemble.

In order to understand the quantum correlations of such 2D systems, it is common to first refer to systems with a lower dimensionality. Here, the quasi one-dimensional, ladder-type "telephone number compound" $Sr_{14-x}Ca_xCu_{24}O_{41}$ [4, 5] is a prominent example, in which a superconducting state is realized by applying pressure. The combination of enhanced quantum fluctuations for $S = 1/2$ and $S = 1$ with the low-dimensional magnetic exchange pathway accounts for the suppression of long-range magnetic order in low-dimensional magnets (Mermin-Wagner theorem), which sets the stage for an enormous variety of novel ground state properties, exotic quasiparticles and many-body states. Understanding these effects is the most intriguing challenge in solid state physics at present.

There are different approaches how one-dimensional electron systems can be realized, and the resulting systems can be divided into *natural* and *artificial* ones. A classic group of systems, which display signatures of one-dimensional physics, are strongly anisotropic organic and inorganic conductors consisting of atomic chains or ladders. For instance, among the most prominent ones are the Bechgaard salts tetramethyltetraselenafulvalene $(TMTSF)_2X$ and tetramethyltetrathiafulvalene $(TMTTF)_2X$ [6, 7, 8] ($X = PF_6$, AsF_6, Br, ClO_4, and other inorganic radicals). One avenue for the search for artificial magnetic materials is the possibility via reducing the dimension of the systems. Low-dimensional systems like nanoclusters and thin films are an attractive class of objects for the search of new magnetic materials that apart from being of fundamental interest are the basis of the rapidly developing field of nanophysics and nanotechnology.

A new electronic ground state, the *Luttinger liquid*, is the central concept to describe these low-dimensional quantum spin systems. This model was developed by Tomonaga [9] and Luttinger [10] in the early sixties and advanced by many theoreticians since. In contrast to interacting electrons in higher dimensions, which are usually discussed in terms of Fermi liquid theory, strong electronic correlations in this new state of matter lead to pronounced many-body effects and thus to radically different properties, such as to important low-energy collective excitations, a spin-charge separation, a power-law behavior of the single-particle density of states and quantum critical points as well as to the Peierls and Spin-Peierls transitions [11, 12, 13, 14]. In this context, due to the complexity of the many-body effects, the interplay between experiment and theory promises to be mutually beneficial.

Even after more than sixty years of intense experimental and theoretical studies, in the field of low-dimensional quantum magnetism there is a rich variety of unsolved issues and topics, posing a great challenge to condensed matter physicists. In this situation, the design of new quantum magnetic systems is necessary. Here, the synthesis of molecule-based magnetic systems seems to be very promising due to the possibility of chemical tailoring, *viz.*, the design of magnetic compounds with a choice of model systems where one can tune not only the number of spins but also the local spin value S, going for instance from a quasi-classical $S = 5/2$ limit (for Fe^{3+} clusters) to the quantum $S = 1/2$ limit (for Cu^{2+} clusters). Molecule-based magnets consist of magnetic centers (intermetallic ions or radicals) which are magnetically coupled via organic ligands representing the magnetic exchange pathway. It is a field that is essentially multidisciplinary [15], since it involves synthetic and theoretical chemistry as well as experimental and theoretical physics, and one of its challenges is to design molecular systems that exhibit predictable magnetic properties through chemical tailoring. Since years the field of molecule-based magnetism has been the focus of intense research efforts [16, 17, 18], playing an important role in the emerging field of multi-functional compounds, which combine technologically relevant magnetic properties with other physical properties such as conductivity [19] or optical activity [20]. It leads to the use of molecular systems in optical and optoelectronical applications, sensors, pharmaceutic usage etc. For instance, research on spin crossover compounds has recently received considerable attention with the recognition that such materials, which can be switched between two spin states (high and low spin), represent the most spectacular example of molecular bistability [15, 21, 22, 23, 24]. At the current stage in spin crossover research three types of applications may be envisaged, *i.e.*, thermal displays, optical switches and pressure sensors, the latter exploiting the molecular and crystal volume changes, which accompany the spin transition [25, 26, 27].

To understand the intrinsic properties of low-dimensional quantum magnets, such as quantum phase transitions, quantum critical points and frustration, it is important to explore simple and well-controlled model systems. Much insight can be gained by studying low-dimensional magnetic systems like the $S = 1/2$ antiferromagnetically coupled Heisenberg chain ($S = 1/2$ AFHC). It is of great interest, since it is one of few interacting quantum many body systems, which analytically are exactly solvable. Over the past thirty years a number of anisotropic materials have been found that constitute very good realizations of the one-dimensional antiferromagnetic Heisenberg model, *e.g.*, $SrCuO_2$ [28, 29], Sr_2CuO_3 [28, 30], $KCuF_3$ [31, 32, 33], $CsCuCl_4$ [34] or $Cu(C_4H_4N_2)(NO_3)_2$ [35]. Their ordering temperatures are very small compared to the exchange coupling constant along the chain direction, indicating highly one-dimensional character, where interchain interactions can safely be neglected.

Isotropic $S = 1/2$ AFHCs with uniform nearest-neighbor exchange interactions have a singlet ground state with triplet excitations. Even at $T = 0$ their ground state is gapless and is not magnetically ordered. Their spin dynamics are not described by magnons (bosons) as for 3-dimensional ordered magnets, but as massless domain-wall like $S = 1/2$ spinons (fermions), which are always created in pairs. The excitation spectrum is governed by a gapless two-particle continuum restricted by a lower and an upper dispersing boundary and has experimentally been verified in several one-dimensional quantum spin chains [32, 36, 37]. While some of the physical properties of the $S = 1/2$ antiferromagnetic Heisenberg chain may be computed exactly using the Bethe ansatz, it is also very illuminating to map the spin chain onto a one-dimensional system of interacting fermions. This gives important insight into the spinon continuum, which may be viewed as the particle-hole continuum of the fermion model, and has consequences for the thermodynamic properties of the system such as the magnetization and the specific heat.

Moreover, the $S = 1/2$ AFHC is unique due to its criticality to even small perturbations, *viz.*, small changes in an external parameter can lead to dramatic qualitative changes in the fundamental properties of the correlated electron system. It is therefore often denoted as a critical spin liquid, which is associated by a rich phase diagram and a modification of the low energy excitations of isotropic spin chains. Here, external parameters to study the phase diagram are pressure, frustration or the application of a magnetic field, the latter causing a substantial rearrangement of the excitation spectrum, making the soft modes incommensurate [37, 38], although the spinon continuum remains gapless.

The model systems which are studied in this thesis represent $S = 1/2$ AFHCs perturbed by an alternating g tensor and/or the Dzyaloshinskii-Moriya (DM) interaction, leading to a doubling of the unit cell in a magnetic field and induced transverse "long-range" antiferromagnetic order. Whereas the Heisenberg exchange $J\mathbf{S}_i \cdot \mathbf{S}_{i+1}$ prefers collinear spin arrangements, the DM interaction $\mathbf{D} \cdot (\mathbf{S}_i \times \mathbf{S}_{i+1})$ prefers canted ones. These peculiarities are often realized in spin chains with an alternating local environment of the magnetic ion as consequence of the residual spin-orbit coupling in these systems [39, 40]. Then, an interesting situation can develop since the application of a uniform field induces an additional staggered field, which has been predicted to be perpendicular and proportional to the external magnetic field. In field theoretical language, a staggered field is a relevant perturbation for the spinon Luttinger liquid, yielding an energetic distinction between reversed domains, which confines spinons in massive multi-particle bound states. Resulting from this extension of the uniform $S = 1/2$ antiferromagnetic Heisenberg chain are additional uniform and staggered magnetization components parallel and perpendicular to the external field and the opening of a spin excitation gap $\Delta \propto H^{2/3}$. Whereas these effects are most pronounced for one magnetically main axis, they vanish for the perpendicular direction. Hence, these materials open the unique possibility to directly study and compare the critical behavior of an ideal $S = 1/2$ AFHC chain with the one of a spin chain that has been exposed to small perturbations.

The gapped phase can be effectively described by the quantum sine-Gordon field theory [39, 40], with the excitation spectrum changing to solitons, antisolitons and their bound states called breathers [41, 42, 43]. Solitons are fundamentally different from spinons of ideal $S = 1/2$ AFHCs, being localized wave entities that propagate with little change of form. They occur under certain circumstances from wave propagation in nonlinear dispersive media. First identified as unusual persistent waves in shallow water (solitons) by J. Scott Russell in 1834 while riding along the Edinburgh-Glasgow Canal [44], cooperative non-linear waves have since been found for instance in Bose-Einstein condensates [45, 46] and strongly correlated electron systems [47, 48, 49]. Important technical applications of solitons are for instance a fast transmission of information by optical fibres over large distances [50]. The underlying sine-Gordon model is one of the few nonlinear equations that can be solved exactly. It has been used to analyze condensed matter systems ranging from quasi 1D easy-plane ferromagnets to 1D Josephson Junctions [51].

The $S = 1/2$ chain with a staggered field may prove to be the best system yet in which to explore the thermodynamic properties and the rich excitation spectrum of the sine-Gordon model through experiment [41, 43, 52, 53]. The dramatic effect of a staggered field was first discovered on the staggered $S = 1/2$ AFHC cooper benzoate by means of neutron scattering experiments [48], and has since been used to describe several one-dimensional spin chain systems, that is, copper pyrimidine dinitrate (CuPM) [52, 54], $CuCl_2 \cdot 2$(dimethylsulfoxide) [53] and Yb_4As_3 [55, 56, 57]. A quantitative theoretical model for staggered $S = 1/2$ AFHCs including the staggered g-tensor and the DM interaction has been developed by Oshikawa and Affleck [39, 40]. It is based on the quantum sine-Gordon model and describes both the thermodynamic properties as well as the dynamic excitations in these materials. However, generic features of this model, *i.e.*, the magnitude and direction of the staggered magnetization, its temperature dependence and direct evidence for the massive particle excitations have never (fully) been verified, motivating the present work.

The experimental techniques to study these open issues are in particular magnetization measurements, nuclear magnetic resonance, muon spin relaxation and neutron diffraction. Usually, the first information about the magnetic properties of a new system is obtained from magnetization data as thermodynamic probe. Since the field range of interest is of the order of the magnetic exchange coupling J/k_B, that is about 18 K and 36 K for the samples studied here, copper benzoate and copper pyrimidine dinitrate, respectively, properties of interest need to be studied up to very high magnetic fields. Therefore, magnetization experiments in pulsed magnetic fields up to 53 T have been used in this work to explore the magnetization curve up to saturation. On the other hand, NMR experiments provide microscopic local information at the position of the chosen atomic nucleus. The microscopic spin orientation as well as q-integrated information of spin excitations at essentially zero energy (μeV range) can be obtained. This way, spin canting, as expected to result from the interaction of the staggered g-tensor and the DM interaction in staggered $S = 1/2$ AFHCs, can be observed.

To conclude, the outline of this thesis is as follows: Prior to an accurate treatment of the issues associated to the staggered $S = 1/2$ antiferromagnetically coupled Heisenberg spin chains, the basics of the theoretical concepts of uniform and staggered one-dimensional magnets will be introduced in Chapter 2. It includes both the presentation of the general magnetic interactions present in one-dimensional magnets (the collinear Heisenberg and the antisymmetric Dzyaloshinskii- Moriya interaction) and the comparison of the thermodynamic properties and spin excitations of uniform with those of staggered $S = 1/2$ AFHCs.

Chapter 3 provides a survey of the experimental techniques used in this work, *i.e.*, high-field magnetization and NMR. Here, the physical entities measured in high-field magnetization and NMR as well as the experimental realization will be discussed.

Subsequently, Chapter 4 will provide a short characterization of the investigated samples, copper pyrimidine dinitrate and copper benzoate, including their crystallographic structure and their basic magnetic properties reported so far.

Chapter 5 and Chapter 6 contain the main results of this thesis for the longitudinal and staggered magnetization of the anisotropic $S = 1/2$ AFHCs copper benzoate and copper pyrimidine dinitrate. Via high-field magnetization investigations in the directions of maximum and zero spin excitation gap the qualitatively different behavior of the longitudinal magnetization components will be established in Chapter 5. The data are analyzed via exact diagonalization of a linear spin chain with up to 20 sites, on basis of the thermodynamic Bethe ansatz equations or via the TMRG method. For both directions a very good agreement between experimental data and theoretical calculations is found. The magnetic coupling strength J/k_B along the chain direction is extracted for copper pyrimidine dinitrate and copper benzoate and the field dependence of the staggered magnetization component is successfully determined. In addition, the anisotropy parameter c, which relates the staggered field to the external uniform field, is obtained for both compounds.

Finally, in Chapter 6, from the local susceptibility of copper pyrimidine dinitrate, measured by NMR at the three inequivalent carbon sites in the pyrimidine molecule, a giant spin canting is deduced. The averaged magnitude of the transverse staggered magnetization for the three inequivalent carbon sites, the extracted spin canting of $(52\pm4)^\circ$ at 10 K and 9.3 T and its temperature dependence are in excellent agreement with exact diagonalization calculations on basis of the staggered $S = 1/2$ AFHC model. This way, for the first time the existence of the transverse staggered field for CuPM is directly proven by means of NMR. Moreover, temperature dependent spin-lattice relaxation investigations on copper pyrimidine dinitrate are performed to study the proposed particle-like spin excitations. From these studies the magnetic excitation spectrum of CuPM is deduced at a constant applied magnetic field of 9.3 T. The experimental data are discussed in context with recent ESR investigations on the same compound.

With the main objective of this work being the determination of the local magnetization and the exotic spin excitation spectrum, the final part in Chapter 6 mainly deals with the pressure dependence of the characteristic physical properties of CuPM, *i.e.*, the staggered magnetization and the spin excitations. From the NMR studies on CuPM the magnetic exchange parameter J/k_B and the size of the spin gap Δ are determined as function of pressure. The observed response is discussed in comparison to related molecular materials.

The results of this work are summarized in Chapter 7. Open issues and future projects regarding for instance alternative ways to tune the magnetic properties of a staggered $S = 1/2$ AFHC will be outlined.

2 One-Dimensional Quantum Magnetism

"Magnetic order" has been known to exist since ancient times. Yet, only in the 20^{th} century physicists began to understand the principles and mechanisms behind what is now called the field of "Magnetism". First theoretical approaches to describe magnetism started with Ising in 1925 [58, 59]. He investigated the one-dimensional version of a model which is now well known under his name, in order to provide a microscopic justification for the Weiss molecular field approach. Subsequently, the study of magnetic systems realized in three-dimensional bulk materials, but whose magnetic interactions are restricted to dimensions D<3, has been quite rewarding for theoretical physicists, since here one could obtain exact solutions without having to deal with the complications inherent to models in 3D [60]. Although the original aim was to get a better understanding of experimental observations in 3D magnetically coupled crystals via simpler low-dimensional models, by now, the field of low-dimensional magnetism has become a very active research topic in its own right. Since more than 40 years, particular attention has been paid to verify the theoretical predictions for low-dimensional magnetic model systems by studying real materials, *viz.*, how the models can be realized or to be expected to exist in nature [61], making low-dimensional magnetism an ideal playground for the interplay between experiment and theory.

Low-dimensional materials provide a unique possibility to study ground and excited states of quantum models, with their strongly interacting excitations leading to unusual instabilities and new quasiparticles [62, 63]. Here, a major impulse to the field came from the discovery of high temperature superconductivity, which turned out to be intimately connected to the strong magnetic fluctuations possible in low-dimensional (low-D) materials. The chance to find interesting new quantum phases of matter and to study the interplay of quantum and thermal fluctuations makes this field attractive for theorists as well as experimentalists, yielding a lively number of publications since years. Emphasis in today's research is laid upon effects like quantum spin fluctuations, best exemplified in low-spin systems like compounds with either Cu^{2+} ions (spin $S = 1/2$), or Ni^{2+} ions ($S = 1$) [12, 64].

The following section 2.1 will provide a short description of those terms in the Hamiltonian used to describe the low-dimensional magnetic materials relevant to this work. Sections 2.2 and 2.3 will present the basic properties of the model for the uniform $S = 1/2$ antiferromagnetically (afm) coupled Heisenberg chain and of the Oshikawa-Affleck model for the staggered $S = 1/2$ afm Heisenberg chain, respectively.

2.1 The Heisenberg Model and Magnetic Interactions in One-Dimensional Systems

The macroscopic magnetic properties of a material are mostly determined by the relevant interactions between existing magnetic moments, which according to the Bohr-van-Leeuwen-theorem cannot exist in a classical world. Hence, magnetism is a pure quantum phenomenon and results out of a combination of the electrostatic Coulomb interaction, the electronic spin, and the Pauli exclusion principle for fermions. The Pauli exclusion principle forbids two electrons with equal spin number to occupy the same region in space, which they may for opposite spins. Accordingly, the Coulomb energy is different for both cases, yielding the magnetic interaction.

Heisenberg [65] demonstrated that the magnetic interaction of two localized valence electron spins $\mathbf{S}_i$ and $\mathbf{S}_j$ can be described by the *Heisenberg* Hamiltonian

$$\mathrm{H} = -\sum_{i,j} J_{ij}\mathbf{S}_i\mathbf{S}_j, \tag{1}$$

with J_{ij} as the exchange coupling constant, which measures the energetic difference between different spin configurations. Whereas for $J_{ij} > 0$ a parallel arrangement of two spins is favored, $J_{ij} < 0$ yields an antiparallel arrangement of $\mathbf{S}_i$ and $\mathbf{S}_j$. As the electrons are localized in this model, and with possible orbital moments quenched due to their crystallographic environment, the Heisenberg model exclusively describes magnetism in insulators. In the case of conductors other models, such as the Hubbard model, are invoked to explain magnetism.

For one-dimensional magnets, whose localized electronic spins form a spin chain, the Hamiltonian in Eq. 1 is often decomposed into longitudinal and transverse terms. Assuming an interaction only between nearest neighbor magnetic moments and an anisotropic exchange coupling $J := J_x = J_y \neq J_z$, the Hamiltonian is written as

$$\mathrm{H} = -J\sum_{i}(\frac{1}{2}(S_i^+S_{i+1}^- + S_i^-S_{i+1}^+) + \Delta S_i^zS_{i+1}^z), \tag{2}$$

with $S^{\pm} = S^x \pm iS^y$ and the anisotropy parameter Δ (here, $\Delta = \frac{J_z}{J_x} = \frac{J_z}{J_y}$). Eq. 2 represents the XXZ model in 1D and is one of the important models of many-body solid state physics, in particular in the case of an antiferromagnetic coupling. For a spin chain consisting of $S = 1/2$-ions, it can be solved exactly by the *Bethe ansatz* equations [66]. Its ground state is a spin singlet without any long-range order, in agreement with the *Mermin-Wagner theorem* for low-dimensional magnetic systems. Mermin and Wagner [67] discovered that the competition between the ordering effect of a high-coordination number in high dimensional lattices and the disordering effect of thermal and quantum fluctuations is favored by disorder in low-dimensional systems. This leads to thermal fluctuations alone being sufficient to suppress magnetic order at finite temperatures in one- and two-dimensional magnets with continuous symmetry. At zero temperature only quantum fluctuations survive, which are strong enough to prevent magnetic ordering for 1D magnets, in contrast to two-dimensional magnets, which (possibly) may order at $T = 0$.

In case of low-dimensional magnetic systems with significant single-ion anisotropy, such as Ni-systems, the spin dimension can be reduced, yielding a simplified Hamiltonian: the Hamiltonian of the XX model for $\Delta = 0$, and the one of the Ising model for $|\Delta| \rightarrow \infty$. Whereas in the Ising model all spins are aligned in either the z or -z direction, the Heisenberg model allows all three spin components. Since for Cu^{2+} ions the single ion anisotropy is usually small and can be treated in terms of an anisotropic g-factor, one starts with the isotropic Heisenberg model for Cu^{2+}-systems, *i.e.* the XXX model with isotropic exchange interactions $J_x = J_y = J_z$ ($\Rightarrow \Delta = 1$). In the presence of an external magnetic field $\mathbf{H}$, the Hamiltonian of the isotropic Heisenberg chain is written as

$$\mathrm{H} = -\sum_i (J\mathbf{S}_i \cdot \mathbf{S}_{i+1} + g\mu_B \mathbf{H} \cdot \mathbf{S}_i). \tag{3}$$

The second term $-\sum_i g\mu_B \mathbf{H} \cdot \mathbf{S}_i$ represents the Zeeman term, were g is the Landé g-factor and μ_B the Bohr magneton.

The Heisenberg model is applicable for a *direct exchange* between two neighboring atoms with overlapping electronic densities. However, many magnetic ions are unable to interact by direct exchange, since their magnetic orbitals often lie well inside the ion (within a radius of about 0.3 Å) and thus do not overlap with the corresponding orbitals of neighboring ions. This is the case for partially filled f-shells in the rare earth metals, where the f-electrons are magnetically coupled to each other through their interactions with the conduction electrons. This mechanism is known as *indirect exchange* or *RKKY interaction.* In contrast, in insulating materials with magnetic ions well separated via nonmagnetic ions another source for magnetic interaction needs to be taken into account. It is then possible for the magnetic ions to have a magnetic interaction mediated through the electrons of their nonmagnetic neighbors (the ligands). This type of interaction is called *superexchange* and will be described in more detail in the following section due to its relevance for this work.

Indirect exchange interactions: Superexchange

In 1934 Kramers [68] first gave an explanation for the *superexchange*, proposing that a magnetic exchange pathway is provided by mixing small amounts of excited states into the ground state. Whereas in the ground state the orbitals of the intermediate ions are completely filled, the excited states are represented by intermediate ions with unpaired electronic spins, stemming from an electron transfer to the metal ions. Anderson [69] gave a detailed formulation of Kramers´ mechanism and showed that it has the correct order of magnitude. The strength and sign of this interaction depends on both the electronic overlap between cations and anions and the bond angle between contributing orbitals. It can roughly be estimated by the semi-empirical *Goodenough-Kanamori-Anderson* (GKA) rules [70, 71, 72], which take into account the occupation of the various d-levels as dictated by ligand field theory.

A typical superexchange coupled system contains pairs of paramagnetic transition metal ions separated by one or more closed shell ions. According to Anderson´s theory [72], superexchange occurs because the metal atom d-orbitals, in which the unpaired spins originate, overlap with filled s- and p-orbitals of the intermediate atoms. As a consequence of this overlap the orbitals containing the unpaired spins are no longer localized metal d-orbitals, but

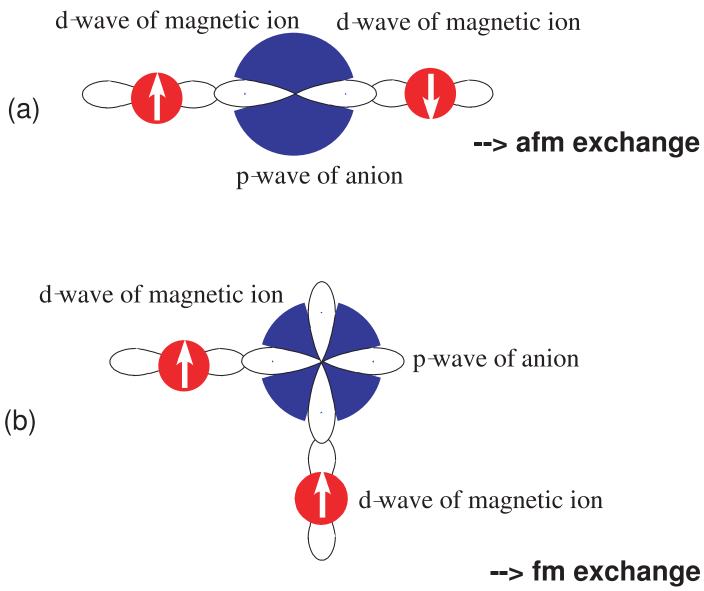

Figure 1: *Examples for the superexchange of magnetic ions with a partially filled d-shell interacting with each other via p-electrons of the diamagnetic ion. (a) Whereas a bond angle of 180° yields a strong antiferromagnetic exchange, (b) an angle of 90° yields a ferromagnetic exchange interaction.*

are antibonding orbitals that encompass both the metal atom, on which the spin originated, and the intermediate atoms. The spins in two such delocalized magnetic orbitals, originating from two different metal atoms, can interact in two ways: *(i)* overlap of the magnetic orbitals, which couples the spins antiparallel in the low energy state, whereas *(b)* orthogonality of the magnetic orbitals couples the spins parallel in the low energy state.

The total isotropic exchange coupling of two metal ions is the sum of the contributions of the above type for all of the unpaired spins. Whereas for a bond angle of 180° the GKA rules usually yield a strong antiferromagnetic exchange between the magnetic ions with a partially filled *d*-level, a weak ferromagnetic exchange is predicted for a bond angle of 90° (Fig. 1). For intermediate values between 90° and 180°, further theoretical calculations indicated that usually as soon as the bond angle exceeds its critical value (close to 90°), the magnetic interaction between neighboring spins becomes antiferromagnetic again. The reason for the superexchange coupling depending on orbital symmetry properties can be understood as follows: When two magnetic orbitals have the same symmetry in the region of contact, they have non-zero overlap and therefore antiparallel coupling occurs, whereas they are orthogonal and ferromagnetic coupling dominates when they have different symmetry. The Hamiltonian which describes the superexchange coupling is of the same form as the Heisenberg Hamiltonian for direct exchange (Eqs. 1-3). Here, J is determined by the different possible superexchange pathways/contributions, which in comparison to a direct exchange yield additional terms in the kinetic and potential energy of the interacting electrons, respectively.

Origin of anisotropic contributions to the superexchange

For low-dimensional magnetic materials anisotropic contributions to the superexchange may arise from an interplay between spin-orbit coupling and superexchange. Then, the g-factor in the Zeeman term of Eq. 3 has to be substituted by an anisotropic $\overleftrightarrow{g}$-tensor. Further, additional anisotropic contributions have to be added to the Hamiltonian:

$$\mathrm{H} = -\sum_i (J\mathbf{S}_i \cdot \mathbf{S}_{i+1} + \mu_B(\overleftrightarrow{g} \cdot \mathbf{H}) \cdot \mathbf{S}_i + \mathrm{H}_{AS}), \qquad (4)$$

with

$$\mathrm{H}_{AS} = \mathbf{D} \cdot \mathbf{S}_i \times \mathbf{S}_{i+1} + \mathbf{S}_i \cdot \overleftrightarrow{A} \cdot \mathbf{S}_{i+1}. \qquad (5)$$

The first term of H_{AS}, *i.e.*, $\mathrm{H}_{DM} = \mathbf{D} \cdot \mathbf{S}_i \times \mathbf{S}_{i+1}$, describes the antisymmetric Dzyaloshinskii-Moriya (DM) interaction, with $\mathbf{D}$ as the Dzyaloshinskii-Moriya vector. Its magnitude and direction strongly depends on the underlying crystallographic structure and the local environment of the magnetic ions. This type of exchange interaction favors a canting of the spins, since the coupling energy is minimized for perpendicular spins $\mathbf{S}_i$ and $\mathbf{S}_{i+1}$. The second term in Eq. 5 represents symmetric anisotropic contributions, where $\overleftrightarrow{A}$ has second order tensorial character. For instance, dipolar interactions between two neighboring electronic spins represent an additional source for anisotropic contributions and should be considered in the Hamiltonian. Due to their small magnitude in the one-dimensional magnets considered in this work, they can be neglected and will not be considered any further.

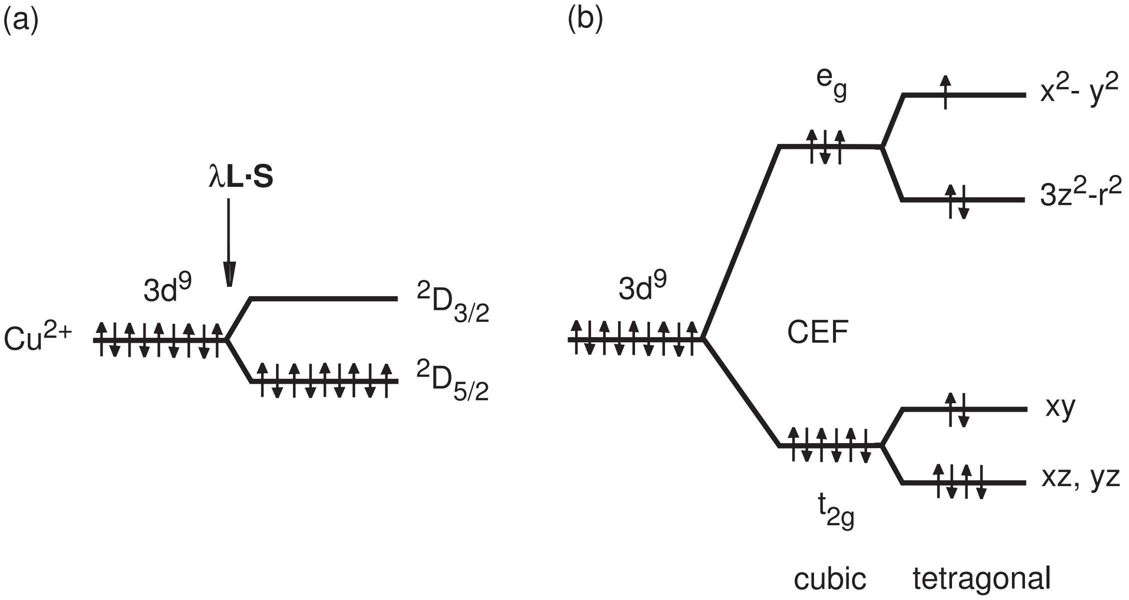

Figure 2: *(a) Ground state of the free Cu*$^{2+}$ *ion due to spin-orbit coupling* $\lambda\mathbf{L}\cdot\mathbf{S}$*. (b) Energy levels of Cu*$^{2+}$ *ions in octahedral (viz. cubic) and tetragonal crystalline environment induced by a crystal electric field. The hole with* S = *1/2 occupies the highest energy level* $x^2 - y^2$*, representing the "ground state" of the system.*

The electronic configuration of free Cu ions is [Ar] $3d^9$, which with Hund´s rule results in an orbital momentum $L = 2$ and total spin $S = 1/2$, its ground state being a $^2D_{5/2}$ configuration (Fig. 2(a)). In a crystal electric field (CEF), however, Hund´s third rule, the LS-coupling, which stems from the spin-orbit coupling alone, must be modified. In an octahedral or tetragonal crystalline environment, the CEF partially lifts the fivefold degeneracy of the Cu orbitals. Its effects can be predicted qualitatively by considering the spatial charge-density distribution. The five $3d$-orbitals split into the *magnetic* triplet t_{2g} (xz, yz, xy) and the *nonmagnetic*[1] doublet e_g ($x^2 - y^2$, $3z^2 - r^2$), the doublet lying higher in energy due to a larger Coulomb interaction with the local environment (Fig. 2(b)). Therefore, for Cu^{2+} ions the hole in the $3d$-shell occupies the e_g states. In octahedral coordination the local symmetry of Cu^{2+} is cubic, and the t_{2g} and e_g states maintain a three- and twofold orbital degeneracy, respectively. Conversely, a tetragonal displacement lifts this degeneracy (Fig. 2b). Then, the t_{2g} orbitals split into the xz, yz and xy states, the latter lying higher in energy as the first two. Furthermore, a tetragonal symmetry causes a raise in energy of the single occupied e_g orbital by minimizing the total energy of the system. For a tetragonal displacement in z-direction, the single occupied e_g orbital is the $x^2 - y^2$ state representing the "*nonmagnetic* ground state" of the system.

Whereas the undisturbed e_g states in a crystal electric field are pure spin states with g=2, a remaining small spin-orbit coupling $\lambda \mathbf{L} \cdot \mathbf{S}$, which might arise from an anisotropic crystallographic structure, causes an admixture of the magnetic t_{2g} states into the "*nonmagnetic* ground state" via their orbital momentum. This leads to an anisotropic g-factor and anisotropic contributions to the superexchange, especially via the antisymmetric DM interaction. The mechanism underlying the DM interaction will be explained for the case of the Cu-O-Cu superexchange bond pathway of the high-T_c superconductor La_2CuO_4 [73, 74, 75, 76, 77].

For Cu^{2+} ions in a low-symmetry crystallographic environment, which, for example, is fulfilled in the case of a tilted CuO_6 octahedron, the oxygen site of the Cu-O-Cu bond does not have inversion symmetry. This situation is schematically illustrated in Fig. 3 for the $3d_{xz}$- and $2p_\sigma$-orbitals of the Cu-O-Cu bond. Due to the tilting of the CuO_6 octahedron by the angle ϕ with respect to the CuO_2 plane, the $2p_\sigma$-orbital is raised above the plane, while the $3d_{xz}$-orbitals rest in the plane but rotate by ϕ. Electrons hopping from the $3d_{x^2-y^2}$ ground state orbital to a neighboring Cu ion via the intermediate oxygen couple to the orbital moment of the admixed $3d_{xz}$-orbitals by the remaining small spin-orbit coupling and start to precess due to their orbital momentum. The strength of this effect depends on the LS-coupling λ, the orbital overlap $\propto \phi$ and the resulting hopping amplitudes t_{dp} between the participating $3d$- and $2p$-orbitals. It leads to a rotation of the spin, whose magnitude and orientation is defined by the DM vector $\mathbf{D}$. In the case of $\mathrm{H}_{LS} << \mathrm{H}_{CEF}$ the magnitude of

---

[1] Here, the term *nonmagnetic* means that the expectation value of the l_z component of the e_g states is zero, *i.e.*, the orbital moment is quenched.

the DM interaction is approximated as

$$|\mathbf{D}| \propto \frac{\Delta g}{g} J, \tag{6}$$

with $\Delta g = |g - 2|$ typically of the order 0.1, while the symmetric anisotropy ($\overleftrightarrow{A}$) scales with $(\Delta g/g)^2 J$. Hence, the antisymmetric DM interaction is the dominant part of Eq. 5 and the symmetric part of H_{AS} is usually neglected.

For two magnetic ions, located at the points A and B, respectively, and the point bisecting the straight line AB denoted as C, Moriya [78] obtained rules for the determination of the orientation of $\mathbf{D}$:

- When a center of inversion is located at C, $\mathbf{D} = 0$.
- When a mirror plane perpendicular to AB passes through C, $\mathbf{D}$ || to the mirror plane or $\mathbf{D} \perp$ to AB.
- When there is a mirror plane including A and B, $\mathbf{D} \perp$ to the mirror plane.
- When a twofold rotation axis perpendicular to AB passes through C, $\mathbf{D} \perp$ to the twofold axis.
- When there is a n-fold axis ($n \geq 2$) along AB, $\mathbf{D}$ || to AB.

2.2 The Uniform $S = 1/2$ Antiferromagnetic Heisenberg Chain Model

The magnetic properties of the uniform $S = 1/2$ antiferromagnetic Heisenberg chain (uniform $S = 1/2$ AFHC) in zero and non-zero external magnetic field are described by Eq. 3, with the exchange coupling J being restricted to one dimension, *i.e.*, the direction along the chain. They have been extensively studied by many theoretical groups since 1931 [38, 66, 79, 80, 81, 82, 83, 84, 85, 86, 87]. In particular, in 1964 Bonner and Fisher [80] formulated the problem in a way which even nowadays induces theoretical work on the uniform $S = 1/2$ AFHC model. Their numerical studies are based upon exact diagonalization calculations for linear chains (and rings) of up to $N = 11$ spins and yield the thermodynamic properties of the $S = 1/2$ AFHC, *i.e.*, the specific heat, the magnetic susceptibility and the magnetization. More recently, highly accurate results by various authors [82, 85, 86, 87], which are based upon analytical Bethe ansatz [88] and field theory calculations, are in perfect agreement with the early numerical results by Bonner and Fisher for not too low temperatures. A summary of their results for the specific heat, magnetic spin susceptibility and magnetization of the uniform $S = 1/2$ AFHC will be presented in section 2.2.1.

The elementary excitations of the uniform $S = 1/2$ antiferromagnetic Heisenberg chain have been obtained by des Cloizeaux and Pearson in 1962 [79]. In 1981 Müller et al. [38]

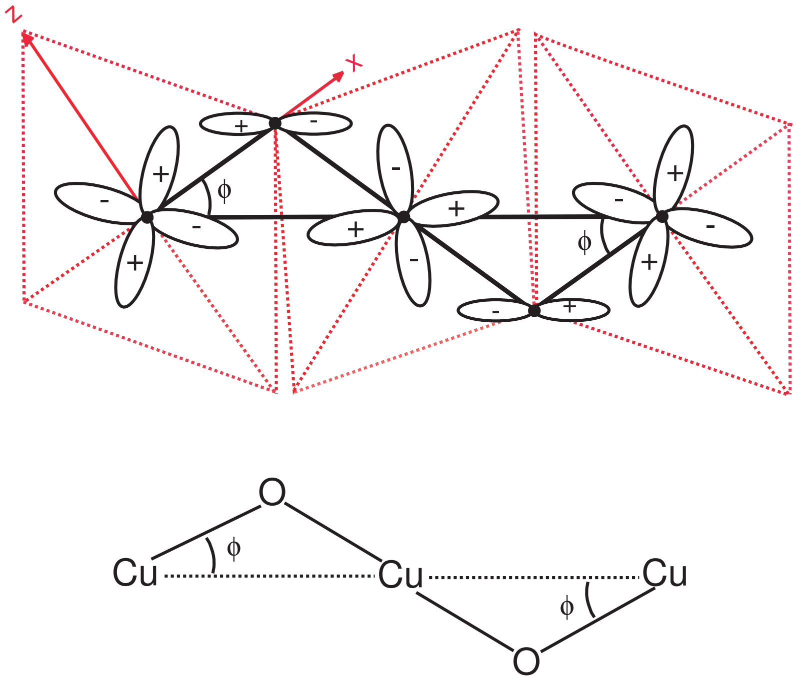

Figure 3: *Cu $3d_{xz}$-orbitals and O $2p_\sigma$-orbitals of a Cu-O-Cu bond parallel to the x-axis in a low-symmetry phase (for instance an orthorhombic phase). ϕ is the tilting angle of the CuO_6 octahedra.*

presented a new approach, based upon analytical Bethe ansatz calculations of excitation energies and densities of states combined with finite-chain calculations of matrix elements. Their extensive studies yield a good quantitative agreement with former results and with neutron scattering data of the uniform $S = 1/2$ AFHC $CuCl_2{\cdot}2N(C_5D_5)$ in both zero and non-zero external magnetic fields [38, 64]. The central results of the so-called Müller ansatz will be summarized in section 2.2.2.

2.2.1 Thermodynamic Properties of the Uniform S =1/2 AFHC

The thermodynamic bulk properties specific heat C, magnetic spin susceptibility χ and magnetization M are obtained by calculating the entropy S and the free energy F as function of temperature T and magnetic field H, respectively. For this, usage is made from the relations in statistical mechanics, $C = \mathrm{T}(\partial^2 F/\partial T^2)|_H = T(\partial S/\partial T)|_H$, $M = -1/N(\partial F/\partial H)|_T$ and $\chi = (\partial M/\partial H)|_T = -1/N(\partial^2 F/\partial H^2)|_T$.

Magnetic specific heat of the uniform $S = 1/2$ AFHC

The zero-field magnetic specific heat of the uniform $S = 1/2$ antiferromagnetic Heisenberg chain is given exactly in the $T \to 0$ limit by a linear temperature dependence $C(T \to 0) = (2/3)Nk_B^2T/J$, with $J > 0$ as the exchange coupling constant. This can be understood from the linear dispersion relation of the fermionic spinons at low energy, which implies that the low-temperature specific heat of the $S = 1/2$ AFHC should be linear in T. For higher temperatures, the zero-field magnetic specific heat passes through a maximum C^{max} at a temperature T_C^{max}, with

$$\frac{C^{max}}{Nk_B} \simeq 0.34971, \tag{7}$$

$$\frac{k_B T_C^{max}}{J} \simeq 0.48028. \tag{8}$$

The analytic function for $C(T)$ in the temperature interval $T \geq 0.001J/k_B$ is given by the high-temperature series expansion of the form [87]

$$\frac{C(T)}{Nk_B} = \frac{3}{16}\frac{J^2}{k_B^2 T^2}\Big(1 + \sum_{n=1}^{\infty} \frac{c_n}{(k_B T/J)^n}\Big), \tag{9}$$

$$\text{with } \mathrm{c}_1 = \frac{1}{2},\ \ \mathrm{c}_2 = \mathrm{c}_3 = -\frac{5}{16},\ \ \mathrm{c}_4 = \frac{7}{256},\ \ \mathrm{c}_5 = \frac{917}{7680}. \tag{10}$$

As stated above, the electronic specific heat coefficient $C(T)/T$ of the uniform S =1/2 AFHC approaches the value $(2/3)Nk_B^2/J$ as $T \rightarrow 0$. The initial deviation from this constant is positive and approximately quadratic in T. In zero field, $C(T)/T$ exhibits a smooth maximum at a temperature $T_{C/T}^{max}$, which Johnston et al. [87] determined as

$$\frac{(C/T)^{max} J}{Nk_B^2} \simeq 0.89737 \tag{11}$$

$$\text{at } \frac{\mathrm{k_B T_{C/T}^{max}}}{\mathrm{J}} \simeq 0.30717. \tag{12}$$

The T dependence of the magnetic specific heat C as well as the electronic specific heat coefficient $C(T)/T$ are shown in Fig. 4 in the interval $0 \leq k_B T/J \leq 2$. The zero-field data exhibit the behavior described above, with the broad maxima and the zero-temperature values of $C(T)$ and $C(T)/T$, respectively. With the application of an external field H, the maximum of $C(T)$ is reduced and shifts to lower temperatures. However, at the saturation field $H_{sat} = 2J/(g\mu_B)$, which represents a critical field above which the antiferromagnet becomes fully magnetized at zero temperature, there remains a broad maximum at a higher temperature. For $H = H_{sat}$ this behavior is qualitatively different for the electronic specific heat coefficient. Here, $C(T)/T$ diverges as $T \rightarrow 0$, while $C(T)$ is equal to zero at $T = 0$.

In the low temperature region $T < 0.001J/k_B$, the difference between the electronic specific heat coefficient $C(T)/T$ and its zero temperature value, (2/3) Nk_B^2/J, is divergent. This is the signature of the existence of logarithmic corrections to the specific heat in this temperature region [85, 86, 89]. However, as they are small, a detailed discussion is omitted here. An intuitive explanation to justify these corrections will be given later in the section about the magnetic susceptibility of the uniform $S = 1/2$ afm Heisenberg chain, for which the logarithmic corrections are much more important.

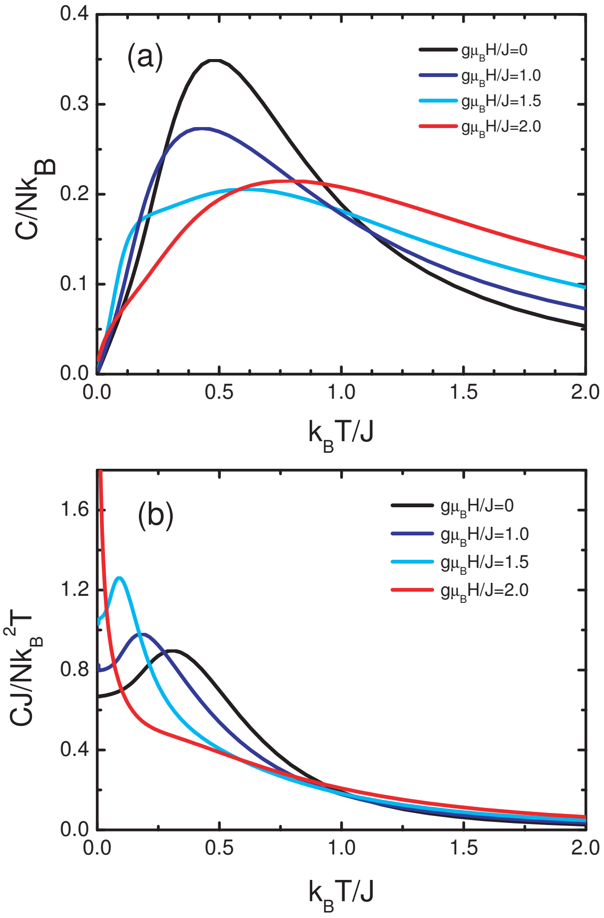

Figure 4: *(a) The temperature dependence of the magnetic specific heat* $C(T)$ *of the uniform* $S = 1/2$ *antiferromagnetic Heisenberg chain for various external fields, as calculated by Klümper [85]. (b) Plot of the data from (a) as the electronic specific heat coefficient* $C(T)/T$.

The integration of the electronic specific heat coefficient data versus T yields the magnetic entropy, $S(T)= \int C(T)/TdT$. $S(T)$ allows an estimate of the maximum magnetic entropy that could be associated with possible transitions into the long-range magnetically ordered state below a critical temperature T_c involving $S = 1/2$ Heisenberg chains. This results from the conservation of magnetic entropy, implying that the magnetic fluctuations will shift some entropy to above T_c. Conversely, the entropy associated to the magnetic transition will be reduced.

Magnetization of the uniform $S = 1/2$ AFHC

The magnetization M of the uniform $S = 1/2$ antiferromagnetic Heisenberg chain is given by $M = \text{-}N^{-1}\ (\partial F/\partial H)|_T$. F denotes the free energy, which is equal to the lowest eigenvalue of the Hamiltonian of the uniform $S = 1/2$ AFHC in an external magnetic field H (Eq. 3). The magnetization as function of the external field, as obtained by the thermodynamic Bethe

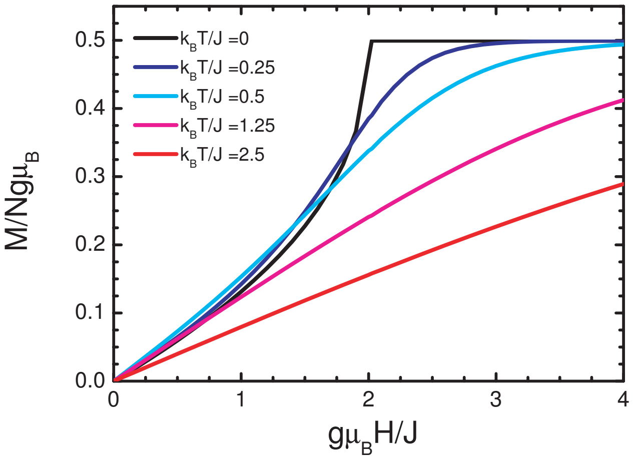

Figure 5: *The magnetization curves $M(H)$ for the uniform $S = 1/2$ antiferromagnetic Heisenberg chain at temperatures $0 \leq k_BT/J \leq 2.5$, as calculated by Klümper [85].*

ansatz by Klümper [85], is shown in Fig. 5.

Starting from zero field, $M(H = 0) = 0$ at $T = 0$, M increases monotonically with increasing external field, as

$$M(H) = \frac{1}{\pi} \arcsin \frac{1}{1 - \frac{\pi}{2} + \frac{\pi J}{g\mu_B H}} \tag{13}$$

for $0 \leq H \leq H_{sat} = 2J/(g\mu_B)$. The slope of the limiting magnetization curve at $H = 0$ is the zero point susceptibility $\chi(0)$ (see below). Whereas $M(H)$ has a sharp cusp at H_{sat} for $T = 0$, the cusp is constantly rounded for temperatures $T > 0$, and the saturation of the magnetization is delayed to fields $H > H_{sat}$.

Considering the derivative of the magnetization, $(\partial M/\partial H)|_T = \chi(H)$, one can distinguish three different intervals: *(i)* a monotonically increasing curve for $T = 0$, which diverges towards the saturation field and abruptly jumps to zero at $H \geq H_{sat}$, *(ii)* an intermediate regime for $0 < T < T_c$, where $(\partial M/\partial H)|_T$ passes through a maximum and subsequently approaches zero at a field $H > H_{sat}$, and *(iii)* a regime for $T > T_c$, where $(\partial M/\partial H)|_T$ monotonically decreases towards zero. For the uniform $S = 1/2$ AFHC the inflection point T_c is given by $T_c = 1.2J/k_B$.

Magnetic susceptibility of the uniform $S = 1/2$ AFHC

The magnetic spin susceptibility χ of the uniform $S = 1/2$ antiferromagnetic Heisenberg chain was calculated by Bonner and Fisher [80] in 1964. Later, the calculations were refined by Eggert et al. [82], Klümper [85] and Klümper and Johnston [86]. At zero temperature the spin susceptibility of the uniform $S = 1/2$ AFHC is $\chi(0) = Ng^2\mu_B^2/(\pi^2 J)$. For higher

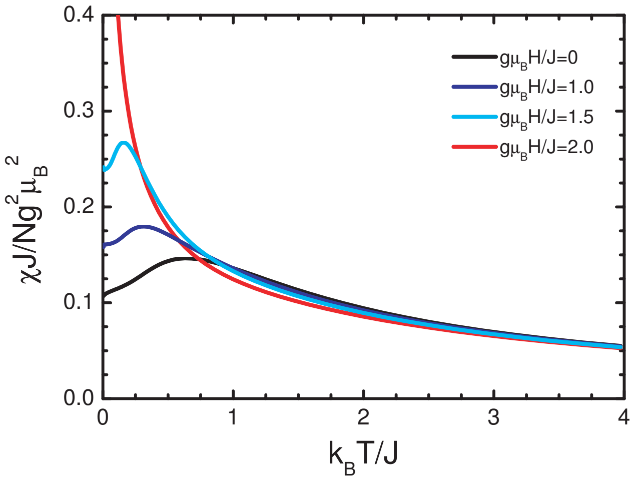

Figure 6: *The temperature dependent spin susceptibility $\chi(T)$ of the uniform S = 1/2 antiferromagnetic Heisenberg chain for various external fields in the interval 0 $\leq g\mu_B H/J \leq$ 2 as calculated by Klümper [85].*

temperatures, $\chi(T)$ exhibits a broad maximum χ^{max} at a temperature T^{max}, given by

$$\frac{\chi^{max}J}{Ng^2\mu_B^2} \simeq 0.146926, \tag{14}$$

$$\frac{k_BT^{max}}{J} \simeq 0.640851, \tag{15}$$

implying that

$$\chi^{max}T^{max} \simeq 0.094158\frac{Ng^2\mu_B^2}{k_B}. \tag{16}$$

Since the product $\chi^{max}T^{max}$ is independent of J, it is a good initial test of whether the $S = 1/2$ afm Heisenberg chain model might be applicable to a particular compound or not.

The temperature dependence of the spin susceptibility is shown in Fig. 6 for different values of the external field H. In the limit $H \to 0$ the data follow the behavior denoted above, with the values χ^{max}, T^{max} according to Eqs. 14 and 15, respectively. With the application of an external field H, the maximum of $\chi(T)$ shifts to lower temperatures and raises in height, until at H_{sat}=$2J/(g\mu_B)$, the spin susceptibility diverges as $T \to 0$.

Eggert et al. [82] derived an expression for the temperature dependence of χ by using the Bethe ansatz. These data are in very good agreement with the results by Klümper [85] shown in Fig. 6, but differ significantly from the Bonner-Fisher results for $T < 0.25\ J/k_B$. The result of Eggert et al. [82] is written as

$$\chi(T) = g^2(\frac{N_A\mu_B^2}{4k_B})F(\frac{J}{k_BT})\frac{1}{T} = \frac{C_u}{T}F(\frac{J}{k_BT}), \tag{17}$$

where $F(x = J/k_BT)$ is an empirical rational function. Feyerherm et al. [54] found

$$F(x) = \frac{1 + 0.08516x + 0.23351x^2}{1 + 0.73382x + 0.13696x^2 + 0.53568x^3} \tag{18}$$

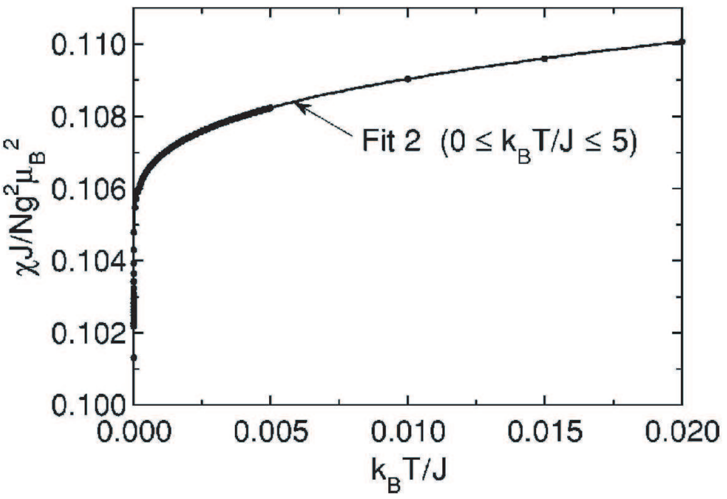

Figure 7: *The spin susceptibility* $\chi(T)$ *of the uniform* $S = 1/2$ *AFHC in the temperature interval* $0 \leq k_BT/J \leq 0.02$*, as calculated by Klümper and Johnston [86], together with a fit obtained by Johnston et al. [87]. The figure is taken from Ref. [87].*

for $T > 0.05J/k_B$. Note that $F(x) \to 1$ for $T \to \infty$.

As $T \to 0$, a simple expansion of the spin susceptibility in the variable $x{=}J/k_BT$ fails. Such a nonanalytic behavior in x can be viewed as arising from the strong correlations between the quasiparticles, *i.e.*, the elementary excitations of the system are not free, but show nontrivial scattering processes. Spinons with low energies ϵ_1 and ϵ_2 have a scattering phase $\phi(\epsilon_1,\epsilon_2) \approx \phi_0$ + const$/|\log(\epsilon_1\epsilon_2)|$. Hence, in an expansion in the single variable x, it has to be supplemented by a term $1/\log(x)$. Eggert et al. [82] obtained analytically exact results for the magnetic susceptibility down to much lower temperatures than before ($T \geq 0.003\ J/k_B$) by the thermodynamic Bethe ansatz and field theory methods. They found that with decreasing temperature, after passing through the maximum, the slope of χ starts to increase below the inflection point at $T \approx 0.087J/k_B$, approaching infinity as $T \to 0$. For low temperatures $T < 0.1\ J/k_B$ the leading order T dependence of the logarithmic correction is written as

$$\chi(T \to 0) \approx \chi(0) \cdot (1 + \frac{1}{2\ln(\frac{T_0}{T})}), \tag{19}$$

with $\chi(0) = Ng^2\mu_B^2/(\pi^2 J)$ and $T_0 \approx 7.7J/k_B$. Their calculations are in good agreement with more recent results with higher accuracy by Klümper and Johnston [86], the latter being depicted in Fig. 7 for the low temperature interval $0 \leq k_BT/J \leq 0.02$. Here, the infinite slope of $\chi(T)$ is discernable as $T \to 0$.

The Wilson-Sommerfeld ratio for metals, the normalized ratio of the spin susceptibility $\chi(T)$ and the electronic specific heat coefficient $C(T)/T$, reads

$$R_W(T) = \frac{4\pi^2 k_B^2 \chi(T) T}{3g^2\mu_B^2 C(T)} \tag{20}$$

for $S = 1/2$ quasiparticles. Whereas $R_W = 1$ for the degenerate electron gas of a metal, the Wilson-Sommerfeld ratio yields values between $1<R_W\leq 10$ for exchange-enhanced metals. For the $S = 1/2$ Heisenberg chain, $R_W = 2$ as $T \rightarrow 0$. With increasing T and up to $T \approx 0.4J/k_B$, R_W is nearly independent of T to within ± 10%. At higher temperatures, the system crosses over to the expected local moment Heisenberg behavior, where $R_W \propto T^2$. Thus, according to the Wilson-Sommerfeld ratio the uniform $S = 1/2$ Heisenberg chain behaves like a Fermi liquid at low temperatures (small logarithmic corrections being neglected). This can be understood from its elementary excitations, which are $S = 1/2$ spinons with a Fermi surface, *i.e.*, Fermi points in one dimension. Since the spinons carry no charge, the chain is an insulator. The deviation of R_W from unity and the existence of logarithmic corrections are due to spinon interactions.

2.2.2 Spin Correlations of the Uniform $S = 1/2$ AFHC

First explicit results for the ground state of the uniform $S = 1/2$ antiferromagnetic Heisenberg chain were obtained by Hulthén [90] in 1938. He found that the zero field ground state E_0 is a spin singlet, given by

$$E_0 = -NJ \ln 2, \tag{21}$$

with $J > 0$ as the exchange coupling constant for the antiferromagnetic case.

In the absence of an external magnetic field, the lowest lying excitations are the des Cloizeaux-Pearson triplets [79], with a total spin $S^T = 1$ and a double-sine limiting dispersion in (q, ω) space

$$\epsilon_1(q) = E_1(q) - E_0 = \frac{\pi J}{2}|sinq|. \tag{22}$$

Finite-chain calculations [91] as well as exact equations by Yamada et al. [92] and Müller et al. [93], using the Bethe ansatz approach, revealed the existence of an extended continuum of excited triplet states (Fig. 8) above the des Cloizeaux-Pearson states, whose upper boundary is given by

$$\epsilon_2(q) = \pi J|sin\frac{q}{2}|. \tag{23}$$

These gapless excitations were later named *two-spinon* states. Their interpretation as dispersion for the basic constituents of a particle-hole continuum was first given by Faddeev and Takhtajan [62].

Significant progress in the understanding of the $T = 0$ dynamics was achieved by Müller et al. [38] through a highly accurate result for the dynamic spin structure factor

$$S_{\alpha\alpha}(q,\omega) = \frac{1}{N}\sum_{l,r} e^{-iqr} \int_{-\infty}^{+\infty} e^{-i\omega t} < S_l^\alpha(t) S_{l+r}^\alpha > dt \tag{24}$$

of the uniform $S = 1/2$ antiferromagnetic Heisenberg chain[2], which is governed by the gapless

---

[2] Due to the rotational symmetry in spin space, the off diagonal components of $S(q,\omega)$ vanish and the two transverse components $S_{xx}(q,\omega)$ and $S_{yy}(q,\omega)$ are identical with the longitudinal component $S_{zz}(q,\omega)$ in the absence of an external field.

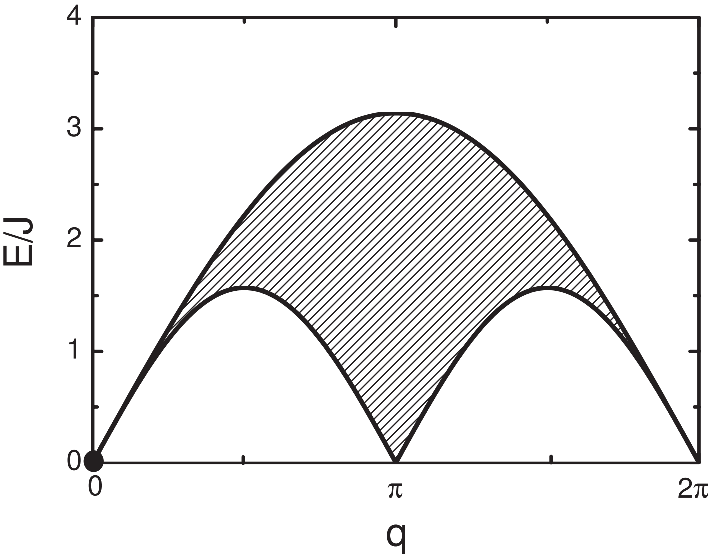

Figure 8: *The excitation spectrum of the uniform $S = 1/2$ AFHC for zero external field. The center of the Brillouin zone is at $q = 0$ and the zone boundary at $q = \pi$. The circle denotes the singlet ($S^T = 0$) ground state and the solid lines the lower (ϵ_1) and upper boundary (ϵ_2) of the two-spinon continuum, respectively.*

continuum of excitations. Since the dynamic structure factor is related to the dynamic spin susceptibility via the fluctuation-dissipation theorem, it represents an important physical property for a direct comparison between experimental and theoretical data. A detailed derivation of the dynamic spin structure factor $S_{\alpha\alpha}(q, \omega)$ and its connection with the dynamic spin susceptibility and $1/T_1$ in NMR is given in sec. 3.1.3. In this chapter, the presentation will be restricted to the specific results for $S_{\alpha\alpha}(q, \omega)$ in the case of uniform $S = 1/2$ AFHCs. Müller et al. [38] calculated the excitation energies and densities of states by an analytical Bethe ansatz and combined them with finite-chain calculations of matrix elements. This way, they obtained the $T = 0$ dynamic structure factor $S_{\alpha\alpha}(q, \omega)$ for a finite system with even N and periodic boundary conditions.

For temperatures $T > 0$, an appreciable amount of spectral weight develops at energies below the lower edge $\epsilon_1(q)$ of the spin wave continuum, which is called the *diffusive tail*. For $T > 0.5\ J/k_B$, in fact, the diffusive tail is already comparable in its spectral weight to the part at $\hbar\omega \geq \epsilon_1(q)$, which represents the *quantum tail* of the excitation spectrum. Further, whereas the value for the $q = \pi$ contribution is infinite in the thermodynamic limit at $T = 0$, indicating that the magnetic structure is clearly governed by the staggered, antiferromagnetic mode, this predominance is increasingly destroyed by thermal fluctuations for $T > 0$ and the spectral weight is redistributed over q-space.

The striking feature, however, is that the contribution from $\pi/2 < \mathrm{q} \lesssim \pi$, which are already large at $T = 0$, initially increase with T, having a maximum at some finite T, and then decrease again in the high temperature limit. Thus, the onset of thermal fluctuations, softening the antiferromagnetic structure, enhances the modes with wave numbers just below $q = \pi$. Remarkably, this is a similar effect as for the application of small magnetic fields parallel to the z-axis, which will be shown in the following.

With the application of an external magnetic field H the ground state of the uniform $S = 1/2$ Heisenberg chain is no longer a spin singlet. The Zeeman term of the Hamiltonian in Eq. 3 progressively depresses states of larger total spin, so that the ground state becomes successively a state belonging to a triplet, to a quintet etc. In comparison to the case of zero external field, where the ground state singlet is completely invariant under rotation in spin space, the external field reduces the rotational symmetry. As consequence, a separate treatment of the longitudinal $S_{zz}(q,\omega)$ and transverse fluctuations $S_{xx}(q,\omega)$=$S_{yy}(q,\omega)$ is necessary.

The boundaries of the gapless two-spinon continua of the uniform $S = 1/2$ AFHC are shown in Fig. 9 for spin fluctuations parallel and perpendicular to the external field. Obviously, for $H > 0$ incommensurate zero-frequency modes can be detected in both the longitudinal and the transverse excitations, with wave vectors that are related to the magnetization as

$$q_i = n\pi \pm 2\pi < S_z > . \tag{25}$$

As the incommensurate modes are gapless, they represent a gap density modulation that persists on an arbitrary long time scale. For the longitudinal excitations parallel to the external field these modes progressively move from the zone boundary ($q = \pi$) to the zone center ($q = 0$) as H increases from zero to H_{sat}. Hence, the spectral weight in $S_{zz}(q,\omega)$ is increasingly absorbed by the static part at $q = 0$, $\omega = 0$. Since the spectral weight of the lowest boundary of $S_{zz}(q,\omega)$ continuously diminishes as the field increases, the relative importance of the longitudinal fluctuations decreases as the saturation field is approached.

For the transverse fluctuations perpendicular to the external field, the incommensurate low energy modes move in the opposite direction, *i.e.*, from the zone center at $q = 0$ to the zone boundary at $q = \pi$, for increasing external magnetic fields. In contrast to the longitudinal excitations the spectral weight of $S_{xx}(q,\omega)$ increases towards $q = \pi$ and towards its lowest boundary, increasing the relative importance of the transverse dynamic structure factor in the case of an applied external field.

2.3 The Staggered $S = 1/2$ Antiferromagnetic Heisenberg Chain Model

The magnetic properties in zero and non-zero external magnetic field **H** of a one-dimensional $S = 1/2$ antiferromagnetic Heisenberg chain with alternating local symmetry are described by an extension of Eq. 3, with the Hamiltonian written as

$$\mathrm{H} = \sum_i (J\mathbf{S}_i \cdot \mathbf{S}_{i+1} - \mu_B(\overleftrightarrow{g} \cdot \mathbf{H}) \cdot \mathbf{S}_i - (-1)^i \mathbf{D} \cdot (\mathbf{S}_i \times \mathbf{S}_{i+1})), \tag{26}$$

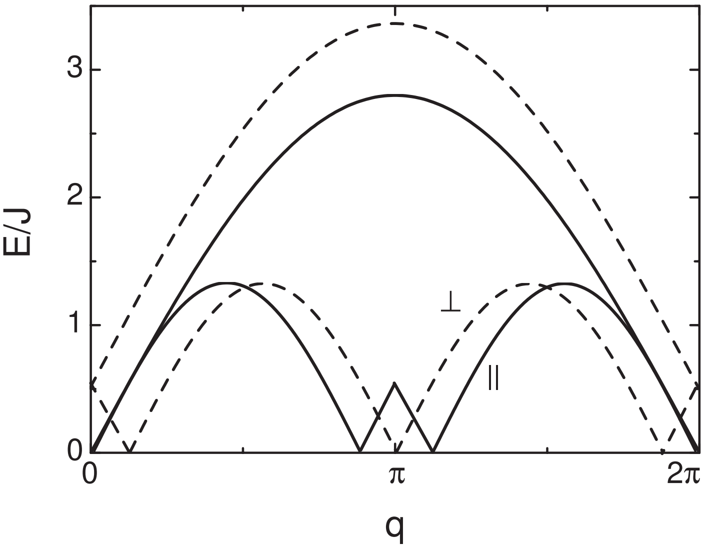

Figure 9: *The boundaries of the two-spinon continua of the uniform S = 1/2 AFHC for spin fluctuations parallel (solid lines) and perpendicular (dashes lines) to the external field. The center of the Brillouin zone is at q = 0 and the zone boundary at $q = \pi$. Note incommensurate soft modes near $q = \pi$ for fluctuations parallel to the external field.*

which has been studied by various theoretical groups [39, 40, 41, 42, 94, 95]. Note that due to the definition of the Hamiltonian in Eq. 26, in the following for a staggered antiferromagnetically coupled spin chain $J/k_B > 0$, according to the common description in literature (see *e.g.*, Refs. [39, 40]).

Oshikawa and Affleck [39, 40] were the first proposing this extended model to describe the thermodynamic properties and dynamic spin correlations of a $S = 1/2$ antiferromagnetic Heisenberg chain with alternating local symmetry, and which will be called the *staggered S* = 1/2 AFHC hereafter. Their model is based on an effective staggered field perpendicular to the external uniform field, resulting from a staggered gyromagnetic tensor $\overleftrightarrow{g} = \overleftrightarrow{g}_u \pm \overleftrightarrow{g}_s$, *i.e.*, a g-tensor with alternating off-diagonal elements, and the Dzyaloshinskii-Moriya interaction in the presence of an external field $\mathbf{H}$. The staggered field $\mathbf{h}_s$ follows from a transformation of the Hamiltonian in Eq. 26 through a rotation in spin space around $\mathbf{D}$ by an angle $\pm\arctan(D/J)/2$ on even/odd sites, this way adjusting the local coordinate frames of neighboring magnetic ions. Defining the external field direction as the z-axis and taking into account that $\mathbf{h}_s$ is approximately perpendicular to $\mathbf{H}$ and $h_s \ll H$, the Hamiltonian can finally be rewritten as [3]

$$\mathrm{H} = \sum_i (J\mathbf{S}_i \cdot \mathbf{S}_{i+1} - \mu_B g^z H S_i^z - \mu_B (-1)^i h_s S_i^x). \tag{27}$$

g^z is the effective g-value for the magnetic field orientation along z, with $g^z = |\overleftrightarrow{g} \cdot \mathbf{H}|/|\mathbf{H}|$,

---

[3] Note, that a small exchange anisotropy is neglected here.

and h_s is the absolute value of the staggered field $\mathbf{h}_s$, with

$$\mathbf{h}_s \approx \frac{1}{2J}\mathbf{D} \times \overleftrightarrow{g_u} \cdot \mathbf{H} + \overleftrightarrow{g}_s \cdot \mathbf{H}. \tag{28}$$

The first part of Eq. 28 represents the contribution from the DM interaction, and the second part the one from the staggered g-tensor. Notably, these contributions may cancel each other for a specific external magnetic field orientation, resulting in a zero staggered field and thus uniform $S = 1/2$ antiferromagnetic Heisenberg behavior (see sec. 2.2).

Oshikawa and Affleck analyzed the model within linear spin-wave theory as well as in the bosonization approach, where the only effect of the uniform field is a shift of the soft-mode momentum k_F and the renormalization of the compactification radius R [41, 96]. The coupling constant R specifies the scaling dimension of the perturbation in the bosonization approach and strongly depends on the value of the applied field. Here, the effective low-energy theory for Eq. 27 is given by the sine-Gordon (SG) model [39, 40, 41] with the Lagrangian density

$$L = \frac{1}{2}(\partial_\mu \phi)^2 + const \cdot h_s \cos(2\pi R\tilde{\phi}), \tag{29}$$

where the transverse staggered field has been mapped onto the operator $\cos(2\pi R\tilde{\phi})$. ϕ is the boson field and $\tilde{\phi}$ the dual field. First identified in the 19^{th} century as unusual persistent waves in shallow water (solitons) [44], the sine-Gordon model has since been used to analyze condensed matter systems ranging from quasi 1D easy-plane ferromagnets to 1D Josephson Junctions [51]. However, the $S = 1/2$ chain with a staggered field may prove to be the best system yet in which to explore the rich excitation spectrum of this model through experiment [41, 43, 52, 53].

The sine-Gordon model is one of the few nonlinear equations that can be solved exactly. In contrast to the uniform $S = 1/2$ chain its elementary excitations become massive relativistic particles with a nonlinear dispersion [41, 42, 96, 97]. These topological objects are either fermionic solitons and antisolitons obeying the Pauli principle, or their scalar repulsive bosonic bound states called breathers satisfying the Fermi statistics[4]. A schematic representation of a breather is given in Fig. 10. With the presence of a staggered field the domain-wall-like solitons of the SG model separate regular from irregular antiferromagnetic domains, leading to interactions and bound breather states. Note, that the sine-Gordon solitons and breathers are fundamentally different from the spinons of the uniform $S = 1/2$ chain first due to their massive particle character and secondly because they all exhibit a gap in the spin excitation spectrum. The soliton gap is usually referred to as soliton mass gap $\Delta_S \propto H^{2/3}$ and can in principle be calculated exactly [99].

The effect of the staggered field $\mathbf{h}_s$ on the thermodynamic properties of the staggered $S = 1/2$ AFHC has been calculated by Oshikawa and Affleck [39, 40] using the sine-Gordon quantum field theory. Further, Shibata and Ueda [94] and Lou et al. [95] calculated the

---

[4] In 1D the repulsion plays the same role as the Pauli principle: a state with one momentum cannot be occupied twice.

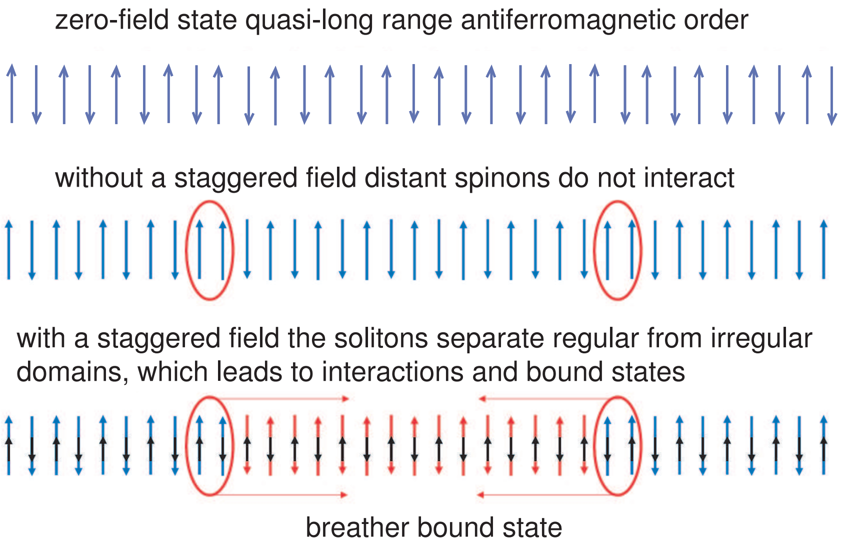

Figure 10: *Schematic representation of the effect of a staggered field on staggered $S = 1/2$ antiferromagnetic Heisenberg chains, leading to interactions and bound breather states; figure after C. Broholm [98].*

staggered magnetization and specific heat by means of the density matrix renormalization group method (DMRG). A summary of the results for the specific heat, total magnetic spin susceptibility and magnetization of the staggered $S = 1/2$ AFHC in both uniform and staggered magnetic fields will be presented in section 2.3.1.

The consequences for the dynamic spin correlations resulting from the staggered field have also been described by Oshikawa and Affleck [40] on basis of the quantum sine-Gordon model. Essler and Tsvelik [41] and Essler, Furusaki and Hikihara [100] calculated the dynamical magnetic susceptibilities close to the antiferromagnetic wave vector by the form factor method. Further, they determined the relative spectral weights of the excitations expected in neutron scattering experiments within the SG model, *i.e.*, the spectral weights of the soliton, antisoliton and breathers. Here, the essential results will be given in section 2.3.2.

2.3.1 Thermodynamic Properties of the Staggered $S = 1/2$ AFHC

The thermodynamic properties specific heat C, physical spin susceptibility χ_{phys} and magnetization m_{phys} of a staggered $S = 1/2$ antiferromagnetic Heisenberg chain are obtained from their thermodynamic definition (see section 2.2.1). Due to the coexistence of the external and the induced staggered magnetic fields for staggered $S = 1/2$ AFHCs, one has to calculate the derivative of the free energy with respect to both uniform field H and staggered field h_s, which are related to each other by

$$c = h_s/(gH). \tag{30}$$

The material constant c strongly depends on the direction of the external magnetic field.

Magnetic specific heat of the staggered $S = 1/2$ AFHC

The zero-field magnetic specific heat of the staggered $S = 1/2$ antiferromagnetic Heisenberg chain is identical with the one of the uniform $S = 1/2$ AFHC described in section 2.2.1. With the application of an external uniform magnetic field H, a staggered field h_s is induced, which changes the low temperature behavior of the magnetic specific heat of the staggered chain. In the low temperature regime, as $T \to 0$, the specific heat is calculated to [42]

$$C \sim \sum_{\alpha=1}^{1/\xi} \frac{k_B}{\sqrt{2\pi} v_s}(1 + \frac{k_B T}{\Delta_\alpha} + \frac{3}{4}(\frac{k_B T}{\Delta_\alpha})^2) \cdot (\frac{\Delta_\alpha}{k_B T})^{3/2} \exp(-\Delta_\alpha / k_B T). \tag{31}$$

v_S is the spin-wave velocity, which is slightly field dependent and is given for zero field by $v_S(0) = \pi J/2$. Δ_α are the breather mass gaps

$$\Delta_\alpha = 2\Delta_S \sin(\alpha \pi \xi / 2), \tag{32}$$

with Δ_S as the soliton mass gap [99]. The coupling parameter ξ, which is related to the compactification radius R in Eq. 29, varies smoothly with the applied field and can be determined numerically through the Bethe ansatz for $h_s \ll H$ [40, 41].

The specific heat $C(T)$ and the electronic specific heat coefficient $C(T)/T$ of the staggered $S = 1/2$ antiferromagnetic Heisenberg chain for various staggered fields h_s and zero uniform field H are shown in Fig. 11. In some sense, this is a purely theoretical exercise, since in the experimental case the staggered field is only induced by the external magnetic field H. But since $C(T)$ is characterized by the lowest gap Δ in the excitation spectrum, which is constant for a constant external field, the low temperature behavior for zero and small applied fields is almost the same. For a constant staggered field h_s, the only effect of a simultaneous applied uniform field is a small shift of the maximum of the specific heat to lower temperatures and a decrease of the absolute value of C and C/T for the fields of interest [94]. Hence, Fig. 11 represents an appropriate visualization of the experimental situation.

Whereas the specific heat $C(T)$ of the uniform $S = 1/2$ antiferromagnetic Heisenberg chain follows a T-linear dependence, the specific heat of the staggered $S = 1/2$ AFHC shows a completely different behavior at low temperatures due to the opening of the spin excitation gap Δ. The existence of Δ results in an activated behavior of $C(T)$, with an initial exponential increase and subsequently a broad peak of $C(T)$ below $k_B T = \Delta$ (Fig. 11(a)). By plotting the quotient $C(T)/T$, as shown in Fig. 11(b), the sharp exponential decrease due to the gap below $k_B T \approx 0.3\ \Delta$ and the broad peak at temperatures $k_B T \approx 0.4\ \Delta$ can be seen even more clearly. For $k_B T > \Delta$ the electronic specific heat coefficient $C(T)/T$ of the staggered $S = 1/2$ AFHC approaches the uniform chain behavior asymptotically, as expected due to the vanishing influence of the spin excitation gap for increasing temperatures.

Magnetization of the staggered $S = 1/2$ AFHC

The magnetization of the staggered S =1/2 AFHC differs significantly from the one of the isotropic chain. This reflects the fact that the application of an external field H induces a

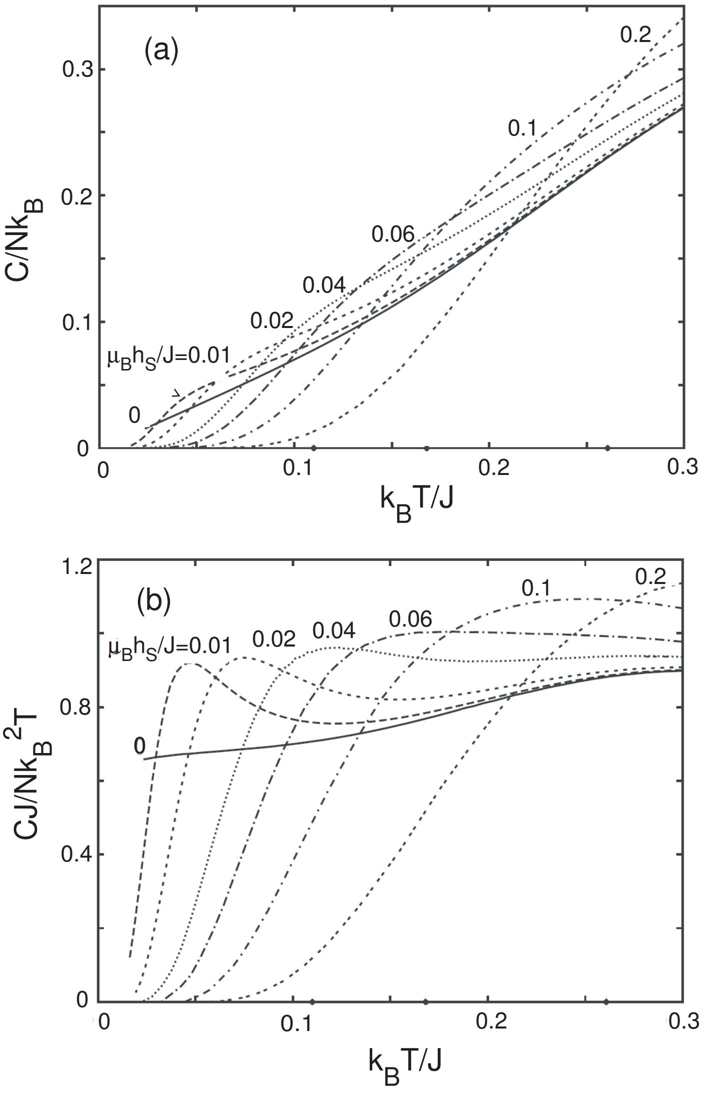

Figure 11: *The temperature dependence of (a) the magnetic specific heat C and (b) the electronic specific heat coefficient C/T of the staggered $S = 1/2$ AFHC for different values of the staggered field h_s; figure after Ref. [94], where the calculations have been done for $H = 0$.*

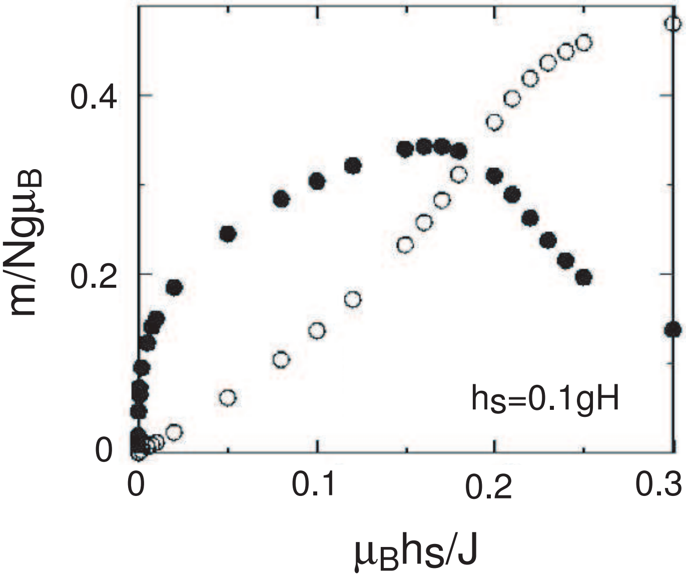

Figure 12: *The magnetization curve at $T = 0$ for the staggered $S = 1/2$ antiferromagnetic Heisenberg chain for a fixed ratio $c = h_s/(gH) = 0.1$, as calculated by Lou et al. [95]. The filled circles denote the staggered magnetization m_s, while the empty circles represent the uniform magnetization m_u; figure after Ref. [95].*

staggered field h_s, resulting in a uniform magnetization m_u induced by the uniform field and an additional staggered magnetization m_s induced by the staggered field. Following Eq. 30 the experimentally observable property, the physical magnetization m_{phys}, is the sum of the two contributions[5]

$$m_{phys} = -\frac{\partial F}{\partial H} - (cg)\frac{\partial F}{\partial h_s} \tag{33}$$

$$= m_u + (cg)\, m_s. \tag{34}$$

Lou et al. [95] performed numerical calculations of the ground state and the low energy excitations of the Hamiltonian (27) using the DMRG method. Their $T = 0$ results for simultaneously increasing uniform and staggered fields are shown in Fig. 12 for a fixed ratio $c = h_s/(gH) = 0.1$. While the staggered susceptibility diverges as $H \to 0$ due to a diverging staggered correlation length of the staggered Heisenberg model at $T = 0$, the zero field uniform susceptibility is zero. As can be clearly seen in the figure, the effect of the staggered field rises rapidly and is dominating at small fields. For $c = 0.1$ the staggered magnetization reaches a maximum at $\mu_B h_s/J \approx 0.17$, and then decreases with further increasing fields.

---

[5] From a phenomenological point of view it is obvious, that due to the approximately perpendicular character of the staggered magnetization m_s the experimentally observable property m_{phys} consists of the uniform magnetization and the projection of the staggered magnetization onto the direction of the external field. Hence, in Eq. 34 the staggered magnetization m_s is scaled with (cg), the ratio between the staggered and the uniform field, indicating the amount of the canting of m_s with respect to the external field H.

Since subsequently m_s decays fast to a small finite value after reaching its maximum, the uniform magnetization approaches a nearly saturated value 0.498 at high enough fields. Note, that m_u only qualitatively resembles the magnetization for the uniform $S = 1/2$ antiferromagnetic Heisenberg chain. The quantitative deviations stem from the staggered field h_s, reducing the absolute value of the uniform magnetization and hence delaying the saturation of the uniform magnetization component.

Magnetic susceptibility of the staggered $S = 1/2$ AFHC

The magnetic susceptibility of the staggered $S = 1/2$ AFHC has been calculated by Oshikawa and Affleck [39, 40] using the SG quantum field theory and by Shibata and Ueda [94] using the DMRG method. Whereas the SG quantum field theory by Oshikawa and Affleck yields very good results for small uniform fields, they should be substituted by the DMRG calculations of Shibata and Ueda in the presence of uniform fields $g\mu_B H \geq \Delta$.

The zero-field susceptibility of the staggered $S = 1/2$ antiferromagnetic Heisenberg chain differs from the zero-field susceptibility of the uniform $S = 1/2$ AFHC due to the staggered field h_s, which develops with the application of an (even very small) external uniform field H. In order to determine the experimentally observable susceptibility χ_{phys}, the free energy has to be written as a function of uniform and staggered fields. Noting that $\partial m_u/\partial h_s = \partial m_s/\partial H$, the physical susceptibility χ_{phys} is given by

$$\chi_{phys} = \frac{\partial m_u}{\partial H} + (cg)^2 \frac{\partial m_s}{\partial h_s} + 2(cg)\frac{\partial m_s}{\partial H}. \tag{35}$$

The second term in Eq. 35 is larger than the third, so one can approximate

$$\chi_{phys} \approx \chi_u + (cg)^2 \chi_s. \tag{36}$$

As mentioned in the previous subsection, the zero-field staggered susceptibility $\chi_s(H = 0)$ diverges as $T \to 0$, while the zero-field uniform susceptibility $\chi_u(H = 0) \to 0$. For fields sufficiently small compared to the saturation field $0 < g\mu_B H/J \ll g\mu_B H_{sat}/J$, the uniform susceptibility χ_u corresponds to the susceptibility of the uniform $S = 1/2$ AFHC as discussed in section 2.2.1, while $m_u(H)$, and thus χ_u, differ from the magnetization of the uniform $S = 1/2$ AFHC in the high-field region.

For small fields and temperatures $T > \Delta$ the staggered susceptibility χ_s is given by [40, 54]

$$\chi_s(T) = 0.2779(\frac{N_A \mu_B^2}{k_B})\frac{ln^{1/2}(J/(k_B T))}{T}. \tag{37}$$

Since the logarithmic term varies slowly with T, the staggered susceptibility varies as $1/T$ at low T. For temperatures $T < \Delta$, one has to carefully distinguish between low and high external field regimes for an appropriate expression for $\chi_s(T)$. Oshikawa and Affleck suggested a heuristic formula for the low-field region [40]

$$\chi_s(T, \Delta) = (\frac{N_A \mu_B^2}{k_B})\frac{ln^{1/2}(J/(k_B max(T, \Delta)))}{2(2\pi)^{3/2}}\chi_{SG}(T, \Delta), \tag{38}$$

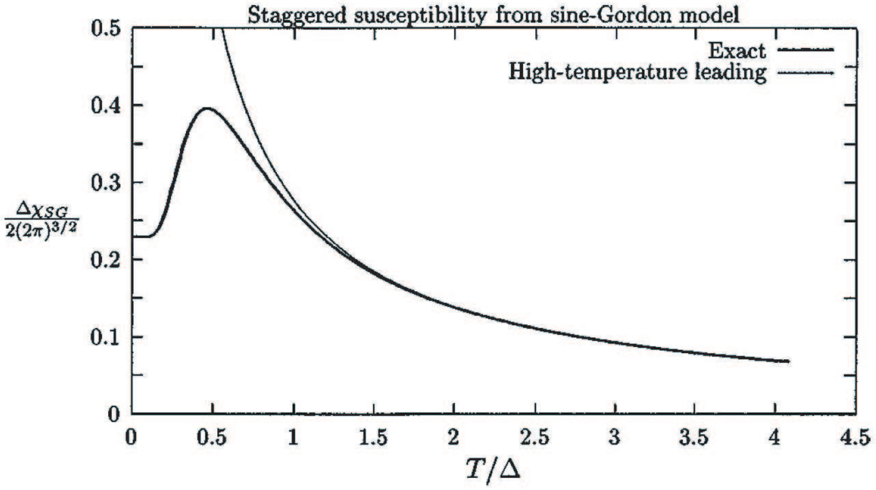

Figure 13: *The temperature dependent susceptibility of the sine-Gordon model χ_{SG}, scaled by a factor of $\Delta/(2(2\pi)^{3/2})$. The $T = 0$ value is given by 0.229 for zero external field. The figure is taken from Ref. [40].*

with the susceptibility of the sine-Gordon model χ_{SG}, which is depicted in Fig. 13.

Conversely, DMRG calculations by Shibata and Ueda [94] perfectly describe the staggered susceptibility $\chi_s(T)$ of the staggered $S = 1/2$ AFHC for $T < \Delta$ and larger external fields. Their results differ from the one by Oshikawa and Affleck only in the low temperature region. Whereas χ_{SG} goes through a maximum at $T \sim 0.5\ \Delta$, the calculations by Shibata and Ueda produce a monotonically increasing curve for $\chi_s(T)$ as $T \to 0$, which saturates at $T = 0$. The temperature dependent staggered magnetization $m_s(T)$ calculated by Shibata and Ueda [94] is illustrated in Fig. 14 for different external field values and ratios $c = h_s/(gH)$. The staggered susceptibility $\chi_s(T)$ for non-zero uniform fields H is obtained by dividing the staggered magnetization by the external field as $\chi_s(T) \simeq m_s(T)/H$.

2.3.2 Spin Correlations of the Staggered $S = 1/2$ AFHC

In the absence of an external uniform field H ($\Rightarrow h_s = 0$), the spin excitation spectrum of the staggered $S = 1/2$ AFHC is equal to the one of the isotropic chain as described in section 2.2.2. With the application of a uniform field, however, their ground states as well as their spin excitations significantly differ from each other. Oshikawa and Affleck [39, 40] analyzed the model Hamiltonian from Eq. 27 in the linear spin-wave theory in order to obtain results for the classical ground state of the staggered $S = 1/2$ antiferromagnetic Heisenberg chain in the presence of uniform and staggered fields. While their approach misses certain features caused by quantum fluctuations in one dimension, it is quite instructive. They found that the classical ground state is a canted antiferromagnetic structure with the canting angle

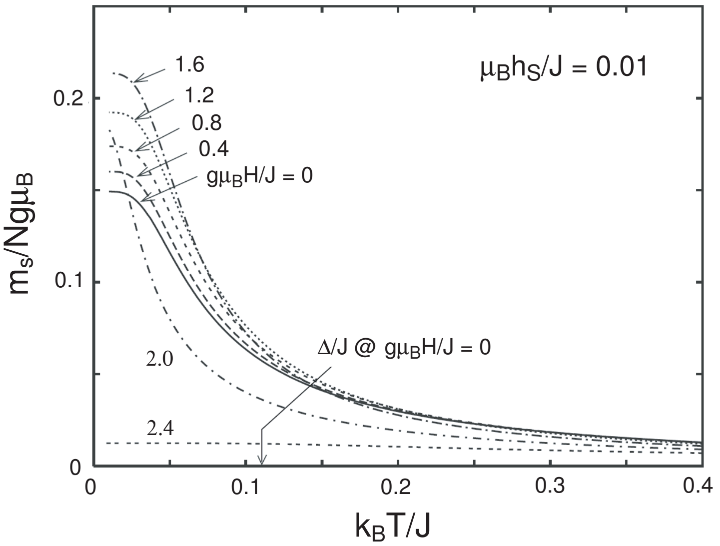

Figure 14: *The temperature dependence of the staggered magnetization m_s for a fixed value of the staggered field $\mu_B h_s/J$ = 0.01 and for several values of the uniform field 0 $\leq g\mu_B H/J$ $\leq$ 2.4; figure after Ref. [94].*

θ, measured from the z-axis,

$$\theta \approx sin^{-1}(g\mu_B H/4JS) - \frac{g\mu_B^2 H h_s}{16J^2S^2 - (g\mu_B H)^2}. \tag{39}$$

While the first term represents the solution for the uniform chain, the second term accounts for the perturbation of the staggered field. Fluctuations around this ground state to lowest order in $1/S$ yield two branches of spin waves in the antiferromagnetic Brillouin zone. For zero staggered field the minimum energies of the two modes are $E_+ = H$ and $E_- = 0$ at $q = 0$. The ”-” Goldstone mode corresponds to a coherent precession of the spins around the z-axis. Then, a non-zero staggered field h_s induces a finite gap into this mode. Taking into account 1D critical fluctuations, $E_-(q = 0)$ scales as $\sim h_s^{2/3}$. In the sine-Gordon model this behavior changes to $E_-(q = 0) \equiv \Delta_\alpha \propto h_s^{2/3}|ln(J/\mu_B h_s)|^{1/6}$.

The spectrum of the sine-Gordon model consists of the soliton-antisoliton doublet of mass Δ_S and their bound states called breathers. For fields $H \longrightarrow 0$, the excitation spectrum consists of a degenerate triplet composed of soliton, antisoliton, lowest breather B_1 and a second breather B_2, heavier by a factor $1/\sqrt{3}$. With increasing field the triplet splits up, with the lowest breather having a smaller mass than the degenerate soliton-antisoliton pair. Further, the number of breathers increases with increasing uniform and staggered fields. It is the field dependent compactification radius R of the SG model, which determines the number of breathers. As soon as the field increases and R decreases below $1/\sqrt{2\pi}$, a third breather drops below the soliton-antisoliton continuum at $2\Delta_S$, and again another one dropping below the continuum each time $2/(\pi R^2)$ passes through an integer. For instance for copper benzo-

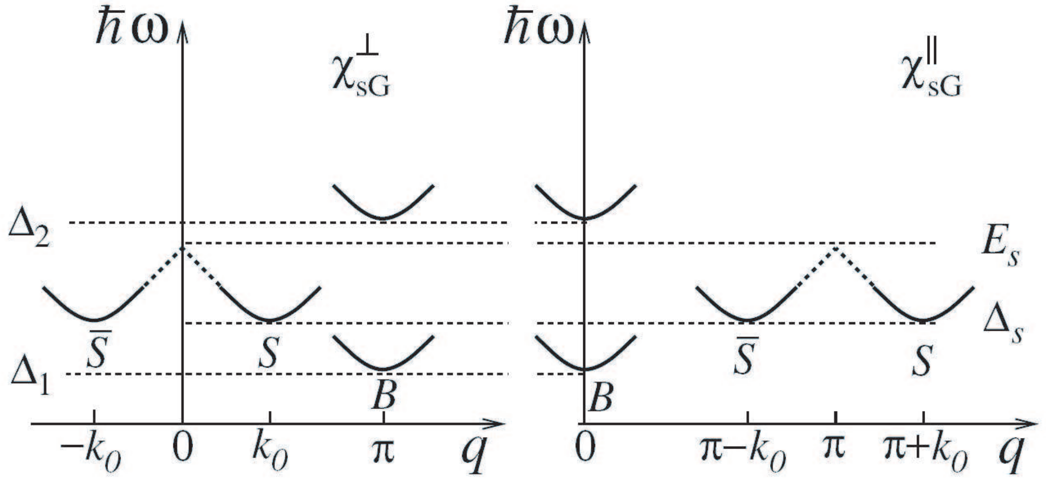

Figure 15: *A schematic view of the low-energy excitations perpendicular (left panel) and parallel (right panel) to the uniform field H of the staggered S = 1/2 AFHC. S and $\bar{S}$ denote the soliton and antisoliton, respectively, and B denotes breathers. Note incommensurate modes at $q = \pi \pm k_0$ for longitudinal fluctuations, which correspond to the (anti-)soliton modes in the spectrum. The figure is taken from Ref. [52].*

ate, with $J/k_B \approx 18.2$ K, a uniform field of 7 T corresponds to $\pi R^2 = 0.41$, with 3 breathers of masses 0.79 Δ_S, 1.45 Δ_S and 1.87 Δ_S, respectively [40].

Fig. 15 shows a schematic view of the low-energy excitation spectrum of the staggered S = 1/2 AFHC in the presence of uniform and staggered fields as predicted by the SG model, which is valid in the low-field regime. Gapless low-energy modes of the uniform S = 1/2 AFHC for fluctuations || and ⊥ to the external field at $q = 0$ and $q = \pi$, respectively, become gapped breather modes. Incommensurate spinon excitations || and ⊥ to the external field at $q = \pi \pm 2\pi < S_z >$ and $q = \pm 2\pi < S_z >$, however, become gapped (anti-)soliton excitations here. Just as in the case of the uniform chain, these incommensurate peaks progressively shift away from $q = 0$ and π with increasing uniform and staggered fields. But for the staggered S = 1/2 Heisenberg chain the modes eventually return to $q = 0$ and π around a critical field H^c. This is in contrast to the uniform chain behavior. The absolute value of H^c is material dependent, *i.e.*, it is a measure for the ratio between staggered and uniform field $c = h_s/(gH)$. For $c = 0.1$, for instance, Lou et al. [95] demonstrated that $g\mu_B H^c/J \approx 1.25$.

All these excitations govern the dynamic spin structure factor $S_{\alpha\alpha}(q,\omega)$ of the staggered S = 1/2 antiferromagnetic Heisenberg chain, whose explicit calculation has been performed by Essler and Tsvelik [41] and Essler, Furusaki and Hikihara [100]. The breathers, classified into even and odd, are created by the $q = \pi$ component of $S_{yy}(q,\omega)$ (odd breathers), the $q = \pi$ component of $S_{xx}(q,\omega)$ (even breathers) and by the $q = 0$ component of $S_{zz}(q,\omega)$. On the contrary, the soliton and antisoliton are created by the $q = \pi \pm 2\pi < S_z >$ Fourier modes of

$S_{zz}(q,\omega)$ and by the $q = \pm 2\pi < S_z >$ Fourier modes of $S_{xx}(q,\omega)$ and $S_{yy}(q,\omega)$. Note that even and odd breathers alternate in the spectrum of the SG model, with the spectral weight of heavier breathers always being significantly smaller than the one of the lightest breather mode.

3 Experimental Techniques

3.1 Nuclear Magnetic Resonance (NMR)

The detection of the magnetic resonance of protons placed in a magnetic field by applying a radio frequency by E. M. Purcell, R. V. Pound, and H. C. Torrey in 1945 can be considered as the birth of the NMR technique. Since then a large number of experimental refinements have been developed, *e.g.*, the pulsed Fourier-transform nuclear magnetic resonance in physics, the high-resolution NMR in chemistry and biology, or even the 2- or 3-dimensional imaging methods in medical diagnostics. These methods probe the local magnetic and electrostatic environment of the specified nucleus via the interaction with the surrounding electrons and nuclei. Therefore, NMR is closely related to other nuclear techniques like muon spin rotation, Mössbauer effect spectroscopy, perturbed angular correlation, and nuclear orientation. The time window of 10^{-6} to 10^{-8} s of NMR lies between those of electron spin resonance (10^{-8} to 10^{-10} s) and muon spin rotation (10^{-4} to 10^{-11} s). The relatively high sensitivity to small magnetic moments (down to 10^{-2} μ_{B}) and the excellent resolution of frequency variations of up to 10^{-8} makes NMR an excellent tool to investigate magnetic (relaxation) phenomena in solid state physics on a microscopic level.

The following sections 3.1.1, 3.1.2 and 3.1.3 provide a short description of the basic principles and interactions in a NMR experiment. Only those aspects which are relevant to the present work will be discussed in detail. Sections 3.1.4 and 3.1.5 will give a short overview of the NMR equipment used in this work. For an elaborate description of the technique, the reader is referred to the books of C. P. Slichter [101], A. Abragam [102], A. P. Guimarães [103] and E. Fukushima [104].

3.1.1 Basic Theory

The NMR signal stems from the interaction between an alternating magnetic field and polarized nuclear spins in a static magnetic field. Each nucleus carries a total angular momentum **I** due to the combination of orbital and spin moments of the nucleus, *i.e.*, the protons and neutrons. If $\mathbf{I} \neq 0$, the nucleus has a resulting magnetic moment $\boldsymbol{\mu_n} = \gamma_n \hbar \mathbf{I}$. In the following the different contributions to the total angular momentum will not be further distinguished and **I** will be called the *nuclear spin*. In a static magnetic field $\mathbf{B_0}$ directed along the z-direction the nuclear energy levels split into $2I{+}1$ states (nuclear Zeeman splitting). The corresponding Hamiltonian is written as

$$\mathrm{H}_Z = -\boldsymbol{\mu}_n \cdot \mathbf{B_0} = -\hbar \gamma_n B_0 I_z, \tag{40}$$

with the quantized energy levels

$$E = -m \hbar \gamma_n B_0, \tag{41}$$

where γ_n is the nuclear gyromagnetic ratio, I_z the nuclear spin operator in z-direction and m = -I,I+1,...,I-1,I. The product $\omega_L = \gamma_n B_0$ is called the Larmor frequency. It is the frequency of the precession of **I** around $\mathbf{B_0}$.

In the thermodynamic equilibrium the distribution over different levels is given by the Boltzmann distribution. Due to an unequal population of the m-levels a polarization, and hence magnetization, of the nuclear spin ensemble appears. However, the size of the magnetization from the nuclear spins is about 10^6 times smaller than the one of electronic moments. Therefore, instead of directly detecting the small resulting net magnetization **M** along $\mathbf{B_0}$, one better stimulates resonant transitions between the different energy levels by the application of electromagnetic radiation with a frequency $\omega_{rf} \approx \omega_L$, and studies the return of the spins towards the thermodynamic equilibrium after excitation. A radio frequency pulse can be treated as an additional alternating magnetic field $\mathbf{B_1}$ along the x-direction with frequency ω_L, which couples to the transverse components of **I**:

$$\mathrm{H} = -\hbar\gamma_n \mathbf{I}\cdot\mathbf{B_1} = -\hbar\gamma_n B_{1x} cos(\omega_L t) I_x. \tag{42}$$

Since relaxation of the nuclear spin ensemble cannot occur without the effect of perturbation, the nuclear spin system needs to strongly interact with its environment, *i.e.*, the lattice and the electronic moments around the nuclei. The characteristic relaxation times of the nuclear spin ensemble, which are the spin-lattice relaxation time T_1 and the spin-spin relaxation time T_2, describe the time evolution of the magnetization component parallel to the z-direction and perpendicular to it. Whereas mostly nuclear spin-spin interactions contribute to T_2, the spin-lattice relaxation time T_1 defines the characteristic time constant needed for the energy transfer between the excited nuclear spin ensemble and the lattice after a radio frequency pulse. Here, the absolute value of T_1 depends on the probability of magnetic or electrostatic fluctuations in the reservoir at the Larmor frequency.

In a classical approach the oscillating field $\mathbf{B_1}$ can be regarded as a superposition of two magnetic fields rotating in opposite directions. Only the field rotating into the direction of the precessing spins around $\mathbf{B_0}$ gives a contribution to the resonance, while the second field can be neglected. Thus, the time evolution of the nuclear magnetization **M** under the effect of a static magnetic field $\mathbf{B_0}$ and an oscillating magnetic field $\mathbf{B_1}$ is given by the classical Bloch equation

$$\frac{d\mathbf{M}}{dt} = \mathbf{M}\times\gamma_n(\mathbf{B_0}+\mathbf{B_1}), \tag{43}$$

which describes the Larmor precession of **M** around the magnetic field direction. In a quantum-mechanical approach, one has to turn to the Schrödinger equation in order to obtain the time evolution of the wavefunction Ψ:

$$-\frac{\hbar}{i}\frac{\partial\Psi}{\partial t} = -\boldsymbol{\mu}\cdot(\mathbf{B_0}+\mathbf{B_1})\Psi. \tag{44}$$

For a single spin both approaches lead to the same result and show that by generating a short radio frequency pulse with the nuclear Larmor frequency ω_L, the nuclear magnetization is rotated out of the direction of the static field by an angle $\theta = \gamma_n\ B_1\ t$. Whereas $\theta = \pi/2$

turns the magnetization completely into the xy-plane ($\pi/2$-pulse), a π-pulse inverts the magnetization. Right after the pulse $\mathbf{M}$ returns to its equilibrium state parallel to the z-direction by coherently rotating around $\mathbf{B_0}$, with $\overrightarrow{\omega_L}$ in a plane perpendicular to $\mathbf{B_0}$. This relaxation towards equilibrium in the xy-plane is detected in a NMR experiment.

To investigate the static properties of a material, one has to measure the resonance frequency. Phenomena like magnetism or superconductivity create internal fields inside the sample, causing a difference between the measured resonance frequency and the calculated one due to the static field $\mathbf{B_0}$. The internal fields originate from dipolar fields of the surrounding electrons and nuclei, from Fermi contact interaction with the electrons of the specimen itself and from internal (orbital) currents. The information about dynamic properties of the investigated system can be obtained either by determining the width of the resonance line, which is closely related to relaxation processes in the system, or by measuring the relaxation rate directly by the application of a special pulse sequence for $\mathbf{B_1}$, consisting of a series of $\pi/2$- and π-pulses.

3.1.2 Hyperfine Interactions

As result of local internal fields, the experimentally determined value of the Larmor frequency does not need to be equal to the calculated value $\omega_L = \gamma B_0$. The origin of this frequency shift is found in hyperfine interactions between the nuclear spin and its environment, changing the Zeeman splitting of the nuclear energy levels. The hyperfine interactions can be classified into two categories: interactions with the electronic environment and other nuclear spins, representing the magnetic hyperfine part, or with electric field gradients due to quadrupolar couplings.

The quantum-mechanical treatment of a system exposed to both external field and hyperfine fields can be performed by perturbation theory: In the limit of large external fields ($|\mathrm{H}_Z| \gg |\mathrm{H}_{HF}|$), the total Hamiltonian can be written as the sum of the Zeeman and a perturbing Hamiltonian, the latter representing the hyperfine interactions. Whereas second-order perturbation theory is necessary for the calculation of dynamic properties, first-order perturbation theory is sufficient to accurately describe the static properties (the shift of the resonance line), the latter being restricted to the secular terms of the Hamiltonian. Here, the secular parts strongly depend on whether the interacting spins are of same or different isotopic type.

A. Magnetic hyperfine interactions

The Hamiltonian for the coupling of the nucleus with neighboring electrons in an external field $\mathbf{B_0}$ is written as

$$\mathrm{H} = -\hbar\gamma_n \mathbf{I}(\overleftrightarrow{K} + \overleftrightarrow{\sigma})\mathbf{B_0}. \tag{45}$$

$\overleftrightarrow{K}$ is the Knight shift tensor and $\overleftrightarrow{\sigma}$ the chemical shift tensor, both representing the effects of the electrons. In contrast to the Knight shift tensor $\overleftrightarrow{K}$, which stems from the coupling of the nuclear spin **I** to the electronic spin **S**, the chemical shift tensor $\overleftrightarrow{\sigma}$ arises from the coupling of the nuclear spin **I** to the average orbital electronic moment from inner shells, which is nonzero in the presence of a magnetic field.

A.1 Chemical shift

The chemical shift represents the shift of the resonance frequency between a bare nucleus and a nucleus embedded in diamagnetic bulk matter with no spin or orbital electron paramagnetism. For magnetic materials, the contributions of the chemical shift stem only from orbital contributions from inner electronic shells. The origin of this frequency shift is twofold. First, in an applied magnetic field $\mathbf{B_0}$, the Larmor precession of the electronic charges is equivalent to an electric current producing a magnetic field $\mathbf{B_d}$ at the nucleus, adding to the applied field and being proportional to it. Secondly, the applied field $\mathbf{B_0}$ polarizes the electronic shells. The shells, deformed in this way, produce a magnetic field $\mathbf{B_p}$ proportional to $\mathbf{B_0}$ at the site of the nucleus.

The total field seen by the nucleus is $\mathbf{B}$=$\mathbf{B_0}$+$\mathbf{B_d}$+$\mathbf{B_p}$=$\mathbf{B_0}$(1-σ), with σ as the relative resonance frequency shift, which is independent of the magnitude of $\mathbf{B_0}$. The sign of the shift depends on the electronic distribution around the nucleus, *i.e.*, the form and specific arrangement of the considered orbitals. Its value varies for different chemical compounds, hence its name "chemical shift".

The Hamiltonian describing the interaction of the nucleus with electronic currents is given by the second part of Eq. 45,

$$\mathrm{H}_{CS} = -\hbar\gamma_n \mathbf{I} \cdot \overleftrightarrow{\sigma} \cdot \mathbf{B_0}, \tag{46}$$

with the chemical shift tensor $\overleftrightarrow{\sigma}$ depending on the orientation of the material in the external field. $\overleftrightarrow{\sigma}$ can be separated into an isotropic and an anisotropic part:

$$\overleftrightarrow{\sigma} = \sigma_{iso} \overleftrightarrow{1} + \overleftrightarrow{\sigma}_{aniso}, \tag{47}$$

$$\text{with } \sigma_{iso} = \frac{1}{3}(\sigma_{11} + \sigma_{22} + \sigma_{33}). \tag{48}$$

In first-order perturbation theory only the secular part of the Hamiltonian is considered in the high-field limit $|\mathrm{H}_Z| >> |\mathrm{H}_{CS}|$, *i.e.*,

$$\begin{aligned} \mathrm{H}_{CS} &= -\,\hbar\gamma_n B_0 \sigma_{zz} I_z, \\ \text{with } \sigma_{zz} &= (\sigma_{11} cos^2\theta_{1z} + \sigma_{22} cos^2\theta_{2z} + \sigma_{33} cos^2\theta_{3z}) \end{aligned} \tag{49}$$

as the experimentally determined component. σ_{11}, σ_{22} and σ_{33} can be obtained from orientation dependent measurements on single crystals. Here, the $cos^2\theta_{iz}$ (i = 1,2,3) are the angular cosines between the laboratory system (x, y, z) and the principle axes (1,2,3) of the chemical shift tensor.

In contrast to the chemical shift resulting from currents in inner orbitals, the orbital shift stems from currents due to electrons which are delocalized in the highest occupied orbitals and have a static orbital moment **L**. The orbital shift is given by

$$\mathrm{H}_{orb} = -\frac{\mu_0}{4\pi}\hbar^2\gamma_e\gamma_n\sum_j\frac{\mathbf{I}\cdot\mathbf{L_j}}{r_j^3}. \tag{50}$$

Under the assumption that the orbital moments of the electrons only act on the nucleus and that the feedback action of the nucleus is negligible[6], the interaction described in Eq. 50 can be treated in mean field theory. Here, $\mathbf{L_j}$ is replaced by its expectation value $< \mathbf{L_j} >$, leading to

$$\begin{aligned}\mathrm{H}_{orb} &= -\hbar\gamma_n\mathbf{I}\ (\frac{\mu_0}{4\pi}\hbar\gamma_e\sum_j\frac{< \mathbf{L_j} >}{r_j^3})\\ &=: -\hbar\gamma_n\mathbf{I}\cdot\mathbf{B_{orb}}.\end{aligned} \tag{51}$$

$\mathbf{B_{orb}}$ represents the local field at the nucleus, which stems from static orbital moments of the electronic environment.

A.2. Knight shift

In 1949, W. D. Knight was the first to discover a shift between the resonance frequencies of the same nucleus in a metal and in an insulator in a constant external magnetic field [105]. He found the difference arising from conduction electrons, which pass the nucleus. With the application of an external field $\mathbf{B_0}$ the conduction electrons are polarized, leading to an additional magnetic field at the nucleus. Since the conduction electrons are delocalized, each nuclear spin feels the magnetic field produced by all conduction electrons of the metal simultaneously. In the presence of $\mathbf{B_0}$ all orbits are occupied by two electrons with opposite spin except those near the top of the Fermi level. The excess number of electrons $n = V(N_+ - N_-)$ with spins parallel to the applied field is $\mu_B B_0 g(E_F)$, where $g(E_F)dE$ is the number of electronic states in the interval $[E,\, E + dE]$, and $E_F = k_B T_F$ is the Fermi energy. In the free electron model $g(E_F) = 3NV/(2E_F)$, and hence the paramagnetic susceptibility per unit volume is

$$\chi_{Pauli} = \frac{\mu_0 M}{B_0} = \frac{\mu_0\mu_B n}{VB_0} = \frac{3}{2}\mu_0\frac{N\mu_B^2}{k_B T_F}. \tag{52}$$

Even for bound, unpaired paramagnetic spins in an external magnetic field an additional shift, in comparison to a free ion, can be detected. This, in the following, will also be labelled *Knight shift*, although the historical meaning of the term only includes metals with conduction electrons. The value of the susceptibility $\chi_{para} = \mu_0 N\mu_B^2 p^2/(3k_B T)$ for bound electrons, with $p^2 = g^2 S(S+1)$, can be contrasted with χ_{Pauli}. Whereas χ_{para} is proportional to $1/T$, the susceptibility of the conduction electrons, χ_{Pauli}, is practically independent of

---

[6] The nuclear magnetic moment is about a factor 10^3 smaller than the electronic magnetic moment. Therefore, the field produced by the nuclear magnetic moment at the electron site is negligible.

temperature for $T << T_F$. Since T_F is of the order of 10^4 K, χ_{Pauli} is much smaller than the susceptibility of nonmetallic paramagnetic solids at all temperatures $< T_F$.

The general definition of the Knight shift K is given by

$$K = \frac{\Delta\omega_K}{\omega_L} = \frac{\Delta B_K}{B_0}, \tag{53}$$

with $\Delta\omega_K$ as the shift and ΔB_K as the additional field due to conduction electrons or bound, unpaired paramagnetic spins. Usually, K is proportional to the susceptibility of the paramagnetic spins, since the additional field ΔB_K originates from the polarization of the electronic spins. In the following, we will distinguish between the different contributions to the Knight shift, *i.e.*, the anisotropic dipolar and the isotropic Fermi contact contribution.

- *Dipolar contributions*

  These contributions stem from unpaired electronic spins in orbitals without spin density at the nucleus site, *i.e.*, the *p*-, *d*- or *f*-orbitals. In the general Knight shift tensor $\overleftrightarrow{K} = K_{iso}\overleftrightarrow{1} + \overleftrightarrow{K}_{dip}$ defined in Eq. 45, they represent the anisotropic part[7]. The Hamiltonian describing the coupling of the nuclear spin $\mathbf{I}$ with distant electron magnetic moments $\boldsymbol{\mu_e}$ = -$\hbar\gamma_e\mathbf{S}$ is of dipolar nature and can be written as

$$\begin{align*}
\mathrm{H}_{dip} &= -\frac{\mu_0}{4\pi}\gamma_e\gamma_n\hbar^2\sum_j\Big(\frac{\mathbf{I}\cdot\mathbf{S_j}}{r_j^3} - \frac{3(\mathbf{I}\cdot\mathbf{r_j})(\mathbf{S_j}\cdot\mathbf{r_j})}{r_j^5}\Big) \\
&= -\frac{\mu_0}{4\pi}\gamma_e\gamma_n\hbar^2\cdot\sum_j(I_x\ I_y\ I_z)\cdot\begin{pmatrix} \frac{r_j^2-3x_j^2}{r_j^5} & -\frac{3x_jy_j}{r_j^5} & -\frac{3x_jz_j}{r_j^5} \\ -\frac{3y_jx_j}{r_j^5} & \frac{r_j^2-3y_j^2}{r_j^5} & -\frac{3y_jz_j}{r_j^5} \\ -\frac{3z_jx_j}{r_j^5} & -\frac{3z_jy_j}{r_j^5} & \frac{r_j^2-3z_j^2}{r_j^5} \end{pmatrix}\cdot(S_{xj}\ S_{yj}\ S_{zj})^T \tag{54} \\
&= \sum_j \mathbf{I}\cdot\overleftrightarrow{A}_{j,dip}\cdot\mathbf{S_j}^T. \tag{55}
\end{align*}$$

  Here, $\mathbf{r}$ represents the vector from the site of the unpaired electron to the nucleus. Coordinates *x, y, z* of the electrons are taken with respect to a set of fixed sample axes (*e.g.*, the crystallographic axes). Note, that in this definition $\overleftrightarrow{A}_{dip}$ is given in units of energy.

  For the calculation of the anisotropic dipolar part of the Knight shift tensor $\overleftrightarrow{K}_{dip}$, one can treat the coupling between the nuclear and electronic spin in mean field approxi-

---

[7] The name *isotropic* part K_{iso} comes from the isotropic nature of the coupling between the electrons and nuclei. Since the Knight shift is related to the spin susceptibility χ_s, which may be very anisotropic, even the isotropic Knight shift may have tensorial character.

mation, where $\mathbf{S_j}$ is replaced by its expectation value $<\mathbf{S_j}>$:

$$\mathrm{H}_{dip} = -\gamma_n \hbar \mathbf{I}\ [\frac{\mu_0}{4\pi}\gamma_e\hbar \sum_j (\frac{<\mathbf{S_j}>}{r_j^3} - \frac{3<\mathbf{S_j}>\cdot \mathbf{r_j}}{r_j^5}\cdot \mathbf{r_j})] \tag{56}$$

$$=: -\gamma_n\hbar\mathbf{I}\cdot\mathbf{B_{dip}} \tag{57}$$

$$= -\gamma_n\hbar\mathbf{I}\cdot\overleftrightarrow{K}_{dip}\cdot\mathbf{B_0}. \tag{58}$$

$\overleftrightarrow{K}_{dip}$ follows from a comparison of Eq. 54/ 55 with Eq. 58, using $< S_{zj} > = -\mu_{zj}/(\hbar\gamma_e)$:

$$\overleftrightarrow{K}_{dip} = \frac{\overleftrightarrow{\chi_s}}{\mu_0 N\hbar^2\gamma_e\gamma_n}\overleftrightarrow{A}_{dip}. \tag{59}$$

Again, $\overleftrightarrow{A}_{dip}$ is given in units of energy. It is converted to magnetic field units (T) by multiplying with the factor $(\hbar\gamma_n)^{-1}$.

In first-order perturbation theory for systems with an isotropic susceptibility and a static magnetic field $\mathbf{B_0}$ along the z-axis, the tensors $\overleftrightarrow{K}_{dip}$ and $\overleftrightarrow{A}_{dip}$ can be reduced to their components K_{zz} and A_{zz}. A. Abragam [102] introduced the so-called dipolar alphabet for the dipolar Hamiltonian

$$\mathrm{H}_{dip} = -\frac{\mu_0\hbar^2}{4\pi}\frac{\gamma_e\gamma_n}{r^3}[\mathcal{A}+\mathcal{B}+\mathcal{C}+\mathcal{D}+\mathcal{E}+\mathcal{F}], \tag{60}$$

where the terms $\mathcal{A}$ till $\mathcal{F}$ describe the matrix elements which connect different energy levels of H_Z, caused by the presence of the hyperfine Hamiltonian H_{HF}.

For the static properties only the secular parts $\mathcal{A} = (1-3\cos^2\theta) < I_z >< S_z >$ and $\mathcal{B} = \frac{1}{2}(1-3\cos^2\theta)(< I_z >< S_z > - < \mathbf{I} >< \mathbf{S} >)$, which induce no change in the value of m, contribute to the splitting of the Zeeman energy levels. In the case of a transferred hyperfine coupling, *i.e.*, electronic spin **S** and nuclear spin **I** on different atoms, the only relevant term is $\mathcal{A}$, since the contributing energy states (*e.g.* $|+->$ and $|-+>$ for a $I = S = 1/2$ system) are not degenerate anymore. $\mathcal{B}$ merely produces a second-order energy shift. In the case of a transferred hyperfine coupling the first-order Hamiltonian becomes

$$\mathrm{H}_{dip} = -\hbar\gamma_n I_z\cdot\ [\frac{\mu_0}{4\pi}\gamma_e\hbar\sum_j(\frac{(1-3cos^2\theta) < S_{zj} >}{r_j^3})] = -\hbar\gamma_n I_z\cdot B_{dip}, \tag{61}$$

while

$$\mathrm{H}_{dip} = -\hbar\gamma_n\cdot\ [\frac{\mu_0}{8\pi}\gamma_e\hbar\sum_j(\frac{(1-3cos^2\theta)3 < I_z >< S_{zj} > - < \mathbf{I} >< \mathbf{S_j} >}{r_j^3})] \tag{62}$$

for an on-site hyperfine coupling, *i.e.*, **I** and **S** on the same atom. Here, θ is the angle between the vector connecting the two spins and the z-axis.

Eq. 61 yields the secular part of the Knight shift K_{zz}:

$$K_{zz} = \frac{B_{dip}}{B_0} = (\frac{\chi_s}{\mu_0 N \hbar^2 \gamma_e \gamma_n})A_{zz}, \tag{63}$$

with N as the number of conduction electrons or unpaired spins in insulators, χ_s as the general spin susceptibility and $A_{zz} = \frac{\mu_0}{4\pi}\hbar^2\gamma_e\gamma_n\sum_j \frac{(3cos^2\theta - 1)}{r_j^3}$ as the secular part of the hyperfine coupling (**I** and **S** on different atoms).

The orientation dependence of K_{zz} is given by

$$K_{zz} = K_{11}cos^2\alpha sin^2\beta + K_{22}sin^2\alpha sin^2\beta + K_{33}cos^2\beta, \tag{64}$$

α and β being the Euler angles between the laboratory system (x, y, z) and the principle axes $(1, 2, 3)$ of the Knight shift tensor, with K_{11}, K_{22} and K_{33} being its principle elements. The relation between the hyperfine tensor elements A_{aa} and K_{aa} $(a = x, y, z)$ is given by Eq. 63.

- *Fermi contact contribution and core polarization*

For orbitals with a negligible spin density at the nucleus, the dipolar approximation works well. However, this is not the case for s-electrons, which do have a finite probability at the nucleus and can couple directly to the nuclear moment. Here, the dipolar formular (Eq. 54) becomes divergent and in the calculations one has to consider the finite size of the nucleus, yielding a volume distribution of magnetic moments of nuclear particles.

Following the expression for the magnetic energy for isotropic interactions by Fermi [106], the Hamiltonian describing the direct, isotropic coupling between the nuclear spin **I** and unpaired electronic spins from s-orbitals is written as

$$\mathrm{H}_{FC} = \frac{2}{3}\mu_0\hbar^2\gamma_e\gamma_n\sum_j |\Psi_j(0)|^2\mathbf{I}\cdot\mathbf{S_j} \tag{65}$$

$$= \sum_j A_j\mathbf{I}\cdot\mathbf{S_j}. \tag{66}$$

Here, $|\Psi_j(0)|^2$ represents the electronic density of each s-electron at the nucleus site, and $\sum_j A_j = A_{iso}$ is the hyperfine coupling constant, which measures the magnetic interaction energy between the electron and the nucleus. If expressed in magnetic field units, it is referred to as the *hyperfine splitting* constant $a_{iso}=A_{iso}/(\hbar\gamma_n)$.

In mean field theory, the substitution of the spin operator with its expectation value $< \mathbf{S_j} >$ leads to an additional field at the nucleus, the Fermi contact field $\mathbf{B_{FC}}$, which is produced by the s-electron spins

$$\begin{aligned} \mathrm{H}_{FC} &= \hbar\gamma_n \mathbf{I} \cdot (\frac{2}{3}\mu_0 \hbar\gamma_e \sum_j |\Psi_j(0)|^2 < \mathbf{S_j} >) && (67) \\ &=: -\hbar\gamma_n \mathbf{I} \cdot \mathbf{B_{FC}} && (68) \\ &= -\hbar\gamma_n \mathbf{I} \cdot \overleftrightarrow{K}_{iso} \cdot \mathbf{B_0}. && (69) \end{aligned}$$

With Eq. 65/66 and 69, using the spin expectation value $< S_{zj} > = -\mu_{zj}/(\hbar\gamma_e)$ and $\sum_j \mu_j = \chi_s B_0/(\mu_0 N)$, the Knight shift $\overleftrightarrow{K}_{iso}$ due to the additional Fermi contact field $\mathbf{B_{FC}}$ follows as

$$\overleftrightarrow{K}_{iso} = A_{iso} \frac{\overleftrightarrow{\chi}_s}{\mu_0 N \hbar^2 \gamma_e \gamma_n}. \qquad (70)$$

In contrast to the dipolar hyperfine tensor $\overleftrightarrow{A}_{dip}$, the hyperfine splitting constant $A_{iso} = \frac{2}{3}\mu_0 \hbar^2 \gamma_e \gamma_n |\Psi(0)|^2$ is purely isotropic. It is a property of the spin system only, and it does not depend on the direction or magnitude of an external magnetic field. Anisotropy of $\overleftrightarrow{K}_{iso}$ solely stems from an anisotropic susceptibility tensor $\overleftrightarrow{\chi}_s$. In the case of isotropic systems, Eq. 70 can be simplified by a substitution of $\overleftrightarrow{K}_{iso}$ and $\overleftrightarrow{\chi}_s$ with $K_{zz,iso}$ and χ_s.

Even for closed s-shells, an isotropic contribution to the Knight shift can often be detected. This is due to the *core polarization* effect: Incomplete shells and conduction electrons may modify the radial distribution of closed s-shells, thus producing a non-compensated spin density at the origin. The resulting s-electron magnetization produces the *core polarization field* $\mathbf{B_{cp}}$ at the nucleus. It is, for example, dominant in the hyperfine field of the S-state rare-earth ions, such as Gd^{3+}, and in the ions of d-transition metals, such as Fe.

In normal metals the major part of the total Knight shift stems from isotropic Fermi contact interactions or the core polarization effect and is not due to anisotropic dipolar contributions. For the low-dimensional molecule-based materials considered in this work, both contributions are of about the same order of magnitude.

A.3 Coupling between nuclear spins

In addition to the electron-nucleus coupling, there exists another important interaction of nuclear spins with each other involving the electronic spin system, *i.e.*, the indirect nuclear coupling. The basic idea is that nuclear spins polarize electrons in bonding states, which then couple to a second nuclear spin. There is a tendency for electrons next to a nucleus to be polarized in the same direction as the nucleus, while distant electrons are polarized in the opposite direction. When a second nucleus is introduced, the energy of the system depends on whether the two nuclei have same or opposite polarizations. For an antiferromagnetic chain the state of opposite polarizations lies lower in energy, because then both nuclei couple to electrons with favorable spin orientations, while keeping the electron spin polarization opposite. The state of parallel polarization is higher in energy, since it is not possible to achieve consistently favorable electron spin orientations.

The full form of this indirect J-coupling between nuclear spins $\mathbf{I_1}$ and $\mathbf{I_2}$ is of tensorial character:

$$\mathrm{H}_{nn} = \mathbf{I_1} \cdot \overleftrightarrow{J} \cdot \mathbf{I_2}. \tag{71}$$

The J-coupling is either of dominant dipolar or isotropic nature, depending on the type of wave function of the bonding electrons. It results in a change of the line width and/or a resolved splitting of the resonance lines, both being independent of temperature and static magnetic field compared to the Knight shift.

In first-order perturbation theory, for large distances the Hamiltonian of the anisotropic dipolar J-coupling is written as [101, 107]

$$\mathrm{H}_{nn} = \hbar J_{zz}(2I_{1z}I_{2z} - \frac{1}{2}(I_1^+I_2^- + I_1^-I_2^+)) \text{ (homonuclear case)}, \tag{72}$$

$$\mathrm{H}_{nn} = \hbar J_{zz}(2I_{1z}I_{2z}) \text{ (heteronuclear case)}, \tag{73}$$

with $J_{zz} = \frac{1}{2}\omega_d(1 - 3cos^2\theta)$ as the coupling constant, $\hbar\omega_d = \frac{\mu_0}{4\pi}\frac{\hbar^2\gamma_{n1}\gamma_{n2}}{r^3}$ as the characteristic coupling energy and θ representing the angle between the external field $\mathbf{B_0}$ and the vector spanning from the one to the other nucleus. The orientation dependence of J_{zz} is described as in Eq. 64. Since $\hbar\omega_d$ is typically 10^3 times smaller than the nuclear Zeeman energy $\hbar\omega_L$, the indirect dipolar coupling causes a small, but notable perturbation of the nuclear energy levels.

For a purely isotropic J-coupling, the Hamiltonian is of the form

$$\mathrm{H}_{nn} = J_{iso}(I_{1x}I_{2x} + I_{1y}I_{2y} + I_{1z}I_{2z}), \tag{74}$$

$$J_{iso} = \frac{1}{3}(J_{11} + J_{22} + J_{33}). \tag{ 74$\prime$}$$

In the limit of high external fields ($|\mathrm{H}_Z| \gg |\mathrm{H}_{nn}|$) only the first-order secular part of the Hamiltonian has to be considered. As for the dipolar nuclear coupling discussed above, it strongly depends on whether the two spins are of the same (homonuclear case) or different isotopic type (heteronuclear case). For the latter case Eq. 74 becomes $\mathrm{H} = J_{iso}I_{1z}I_{2z}$.

B. Electric hyperfine interactions

For nuclei with I>1/2, which have an electric quadrupole moment Q due to their non-spherical charge distribution, the electric hyperfine interaction plays a crucial role. The electrostatic interaction between Q and an electric field gradient $V_{ij} = \frac{\partial^2 V}{\partial x_i \partial x_j}$ at the nucleus site, V being the electrostatic potential, causes a perturbation of the Zeeman splitting of the energy levels. A positively charged nucleus will align in an electric field gradient in order to minimize the Coulomb energy with the surrounding electronic charges. In its principal axes system the tensor of the electric field gradient V_{ij} can be described by the diagonal elements V_{xx}, V_{yy} and V_{zz}.

The Hamiltonian for the quadrupole interaction is written as [108]

$$\mathrm{H}_Q = \mathbf{I} \cdot \overleftrightarrow{P} \cdot \mathbf{I},$$
$$\text{with } \overleftrightarrow{P} = \frac{e^2 Q V_{zz}}{4I(2I-1)} \begin{pmatrix} \eta - 1 & 0 & 0 \\ 0 & -\eta - 1 & 0 \\ 0 & 0 & 2 \end{pmatrix}. \tag{75}$$

$\overleftrightarrow{P}$ is the quadrupolar coupling tensor, $\eta = \frac{V_{xx} - V_{yy}}{V_{zz}}$ the asymmetry parameter and $Q = \frac{1}{e}\int_V (3z^2 - r^2)\rho(\mathbf{r}) d^3r$ the quadrupole moment, with V as the volume and $\rho(\mathbf{r})$ as the charge density of the nucleus.

Assuming axial symmetry of the electric field gradient and $\mathrm{H}_Q > \mathrm{H}_Z$, the Hamiltonian of the electric field gradient in its principal axes system can be written as

$$\mathrm{H}_Q = \frac{eQV_{zz}}{4I(2I-1)}[(3I_z^2 - \mathbf{I}^2) + \eta(I_x^2 - I_y^2)] \tag{76}$$
$$= \hbar\omega_Q(3m^2 - I(I+1)), \tag{77}$$

where the characteristic quadrupolar coupling energy $\hbar\omega_Q$ is given by

$$\hbar\omega_Q = \frac{eQV_{zz}}{4I(2I-1)}. \tag{78}$$

In first order, it results in a splitting of the single value of the distance between different Zeeman levels into several different values, the magnitude of the shift of each level depending on $|m|$. Hence, the quadrupolar coupling leads to a shift of the center of gravity of the resonance and an increased number of resonance lines in a NMR experiment. For half-integral nuclear spins, however, the $m = \pm 1/2$ levels are shifted by the same amount of energy, and the transition frequency between the two is unaffected. Note, that in Eq. 76 the spin components I_x, I_y and I_z are related to the principal axes system of the electric field gradient. For more details about the quadrupolar coupling, the reader is referred to Refs. [101, 102]. In this work exclusively NMR investigations on ^{13}C with $I = 1/2$ will be presented, which are not sensitive to electric field gradients.

3.1.3 Relaxation Phenomena

In large external magnetic fields $\mathbf{B_0}$, fluctuating internal fields can be regarded as relaxation channels, which allow transitions between the eigenstates of the static nuclear spin system. Via these spin-flip processes the excited state, which is generated by a radio frequency pulse $\mathbf{B_1}$, returns to its thermodynamic equilibrium described by the Boltzmann statistics. Hence, the coupling between a nuclear spin system and a dynamic thermal reservoir (the lattice) leads to an exponential decay of the transverse components $< \mu_x(t) >$, $< \mu_y(t) >$, and to an increase of the longitudinal component $< \mu_z(t) >$ back to its equilibrium value $< \mu_z(0) >$.

This relaxation behavior is phenomenologically described by the Bloch equation (Eq. 43), including now T_1 and T_2 in order to take into account these relaxation processes:

$$\frac{d<\mu_x(t)>}{dt} = \gamma_n[<\boldsymbol{\mu}(t)> \times \mathbf{B}]_x - \frac{<\mu_x(t)>}{T_{2,x}}, \tag{79}$$

$$\frac{d<\mu_y(t)>}{dt} = \gamma_n[<\boldsymbol{\mu}(t)> \times \mathbf{B}]_y - \frac{<\mu_y(t)>}{T_{2,y}}, \tag{80}$$

$$\frac{d<\mu_z(t)>}{dt} = \gamma_n[<\boldsymbol{\mu}(t)> \times \mathbf{B}]_z - \frac{<\mu_z(t)> - <\mu_z(0)>}{T_1}, \tag{81}$$

with $\mathbf{B}$ as the total field $\mathbf{B} = \mathbf{B_0} + \mathbf{B_1}$. The longitudinal relaxation time T_1 represents the spin-lattice relaxation time and describes the characteristic time scale for an exchange of energy between the nuclear spin ensemble and the reservoir. The transverse relaxation time T_2 is called the spin-spin relaxation time and determines the decay of coherence between the different transverse components of the magnetization.

Calculation of the spin-lattice (T_1) and spin-spin relaxation time (T_2) in Redfield theory

The Hamiltonian acting on a nuclear spin can be divided into a static (time averaged) and a fluctuating part $\mathrm{H} = \mathrm{H}_{st} + \mathrm{H}_{fl}(t)$. H_{st} consists of the Zeeman and static hyperfine interaction terms, the latter mainly causing a shift of the calculated resonance frequency. The fluctuating part is written as

$$\mathrm{H}_{fl}(t) = \sum_j \mathbf{I} \cdot \overleftrightarrow{A_j} \cdot \delta\mathbf{S}_j + \sum_{\alpha\beta} \delta V_{\alpha\beta} Q_{\alpha\beta}. \tag{82}$$

The first term in Eq. 82 describes the magnetic coupling between a nucleus and fluctuating electronic spins, while the second term defines the electrostatic coupling between a nucleus and a fluctuating electric field gradient. $Q_{\alpha\beta} = eQ/[6I(2I-1)][3/2(I_\alpha I_\beta + I_\beta I_\alpha) - \delta_{\alpha\beta}\mathbf{I}^2]$ represent the nuclear quadrupole moments and $V_{\alpha\beta} = \partial^2 V/\partial x_\alpha x_\beta$ the electric field gradient. An additional term $\delta\mathbf{L}$ has been dropped in Eq. 82, since the ions considered in this work have no considerable static orbital moment. The magnetic relaxation mechanism defining the form of $\overleftrightarrow{A}_j$ is mediated through quadrupolar, dipolar or exchange coupling between the nucleus and the fluctuating part, their dominant mechanism depending on the origin of the fluctuations leading to the relaxation. Whereas phonon excitations are the most important source in the nuclear environment in nonmagnetic insulators, conduction electrons cause the dominant fluctuations at the nucleus site in nonmagnetic metals. In magnetic materials the magnetic spin excitations of unpaired spins are of great importance.

In the following, since exclusively ^{13}C-NMR will be presented in this work, only purely magnetic relaxation will be considered. In mean field approximation the Hamiltonian of the magnetic fluctuating part is written as

$$\mathrm{H}_{fl}(t) = -\hbar\gamma_n \mathbf{I} \cdot \mathbf{b}(t), \tag{83}$$

with $\mathbf{b}(t)$ as the fluctuating magnetic field. In order to study the time dependence of $\mathbf{b}(\mathrm{t})$, it is useful to define an autocorrelation function for the field at t and $t+\tau$. Assuming independent fluctuations of the three field components and an exponentially decaying autocorrelation with a single correlation time τ_c for each component of the fluctuating field, the autocorrelation function is defined as

$$G_{\alpha\alpha}(\tau) =< b_\alpha(t) b_\alpha(t+\tau) >_t =< b_\alpha^2 > exp(\frac{-|\tau|}{\tau_c}). \tag{84}$$

Here, $\alpha = x,y,z$, and τ_c is a function of temperature, *i.e.*, the fluctuations become faster and the correlation time decreases by warming the system. The Fourier transform of the autocorrelation function yields the *spectral density* $k_{\alpha\alpha}(\omega)$ of the fluctuating field components

$$k_{\alpha\alpha}(\omega) = \frac{1}{2}\int_{-\infty}^{\infty} < b_\alpha(t) b_\alpha(t+\tau) >_t e^{-i\omega\tau} d\tau. \tag{85}$$

The nuclear spin, which couples to the fluctuations, is described by time dependent coefficients $c_m(t)$ of the eigenstates in an external field: $|\Psi_t >= \sum_m c_m(t)|m>$. For the calculation of the time dependence of $c_m(t)$, the density matrix formalism is used [101], with the density matrix defined as

$$\rho_{mm\prime}(t) = c_m^*(t) c_{m\prime}(t). \tag{86}$$

Similarly, the density matrix can be expressed for a nuclear spin ensemble, using the thermodynamic average $\rho_{mm\prime}(t) = \overline{c_m^*(t) c_{m\prime}(t)}$. Its time dependence follows the von-Neumann equation

$$\frac{d\overleftrightarrow{\rho}}{dt} = \frac{i}{\hbar}[\overleftrightarrow{\rho}(t), \mathrm{H}_t], \tag{87}$$

with $\mathrm{H}_t = \mathrm{H}_{fl}(t) =$ - $\hbar\gamma_n \mathbf{I}\cdot\mathbf{b}(t)$ representing the magnetic coupling term to the lattice. Eq. 87 yields the relaxation rates T_1 and T_2. It describes the connection between the time dependent populated eigenstates of the nucleus in an external field, $\overleftrightarrow{\rho}(t)$, and the surrounding fluctuating local field. The fluctuating field induces transitions between nuclear energy levels and thus changes the population of the nuclear eigenstates. The calculation of the relaxation rates [101] results in

$$\frac{1}{T_1} = \gamma_n^2(k_{xx}(\omega_L) + k_{yy}(\omega_L)) = \gamma_n^2(< b_x^2 > + < b_y^2 >)\frac{\tau_c}{1+\omega_L^2\tau_c^2}, \tag{88}$$

$$\begin{aligned}\frac{1}{T_2} &= \frac{1}{2}(\frac{1}{T_{2x}} + \frac{1}{T_{2y}}) = \frac{\gamma_n^2}{2}(k_{xx}(\omega_L) + k_{yy}(\omega_L) + 2k_{zz}(0)) \\ &= \gamma_n^2(< b_z^2 > \tau_c + \frac{1}{2}(< b_x^2 > + < b_y^2 >)\frac{\tau_c}{1+\omega_L^2\tau_c^2}).\end{aligned} \tag{88\prime}$$

Often, the spin-spin relaxation rate $1/T_2$ is separated into a broadening due to the spread in the z-field, called *secular broadening* $1/T_{2\prime} = \gamma_n^2 < b_z^2 > \tau_c$, and a term due to the spread in the x- and y-field, called *lifetime broadening* $1/(2T_1)$. In Fig. 16 the dependence of $1/(2T_1)$ and $1/T_{2\prime}$ on the correlation time τ_c is illustrated, demonstrating that the longitudinal and

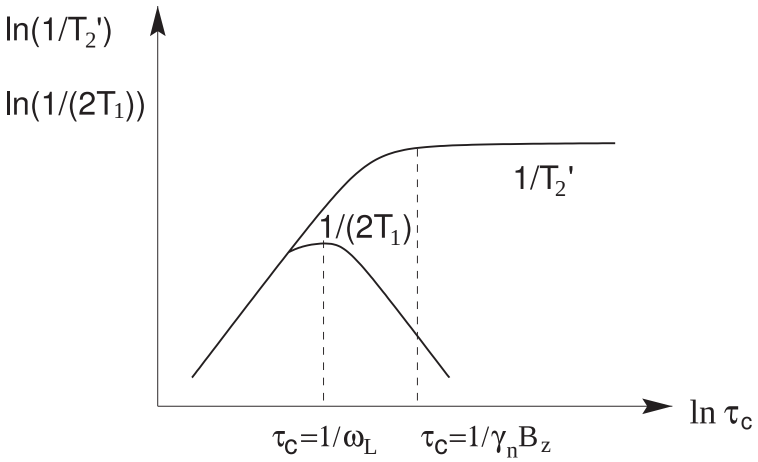

Figure 16: *The relaxation rates 1/(2T_1) and 1/$T_2{\prime}$ on a double-logarithmic scale as function of the correlation time τ_c.*

the transverse relaxation depend in a different way on τ_c. Whereas $1/(2T_1)$ passes through a maximum for $\omega_L \tau_c \approx 1$, $1/T_2{\prime}$ monotonously approaches saturation. The maximum of $1/(2T_1)$ occurs for correlation times comparable to the inverse of the Larmor frequency ω_L, namely, for fluctuations of the magnetic field with larger Fourier intensity at this frequency.

Dynamic susceptibility approach of calculating the spin-lattice (T_1) and spin-spin relaxation time (T_2)

One of the most important contributions that NMR makes to the understanding of a magnetic material is to provide a test of theoretical predictions for the dynamic susceptibility $\chi(\mathbf{q},\omega) = \chi{\prime}(\mathbf{q},\omega) + i\,\chi{\prime\prime}(\mathbf{q},\omega)$, $\omega \approx 0$. This function appears in the longitudinal relaxation rate ($\sum_{\mathbf{q}} \chi{\prime\prime}(\mathbf{q},\omega=0)$) and in the transverse relaxation rate ($\sum_{\mathbf{q}} \chi{\prime}(\mathbf{q},\omega=0)$) just as it has appeared in the Knight shift ($\chi{\prime}(\mathbf{q}=0,\omega=0)$) in sec. 3.1.2. In the following, an alternative approach for the longitudinal and transverse relaxation rates in magnetic systems will be given in order to derive the standard formula for T_1 and T_2, and to allow a direct comparison of the experimental data with theoretical calculations for the dynamic susceptibility.

As in the Redfield approach, the T_1 relaxation rate is given by the Fourier component at ω_L of the time correlation of $b_\alpha(t)$ at the nucleus site:

$$\frac{1}{T_{1z}} = \frac{\gamma_n^2}{2} \sum_{\alpha=x,y} \int_{-\infty}^{\infty} < b_\alpha(t) b_\alpha(0) > e^{-i\omega_L t} dt. \tag{89}$$

In magnetic systems, temporal fluctuations of the local fields $\mathbf{b}(t)$ at ω_L originate from fluctuating electronic spins $\delta\mathbf{S}(t)$,

$$b_\alpha(t) = \sum_\beta A_{\alpha\beta} \delta S_\beta(t), \tag{90}$$

and provide the dominant relaxation channel for nuclear spins. Here, α and β represent the crystallographic axes (x, y, z), and $A_{\alpha\beta}$ are the elements of the hyperfine coupling tensor $\overleftrightarrow{A}$. Eq. 90 demonstrates that both longitudinal and transverse fluctuating spins may contribute to the spin-lattice relaxation rate, while only transverse fluctuating fields lead to a relaxation of the nuclear spin system.

Expanding Eq. 89, and assuming independent fluctuations of the three field components, $1/T_1$ is explicitly given by the spin-spin correlation functions $< \delta S_\beta(t)\delta S_\beta(0) >$:

$$\begin{aligned}\frac{1}{T_{1z}} =& \frac{\gamma_n^2}{2}\int_{-\infty}^{\infty}((A_{xz}^2 + A_{yz}^2) < \delta S_z(t)\delta S_z(0) > + \\ &+ (A_{xx}^2 + A_{yx}^2) < \delta S_x(t)\delta S_x(0) > +(A_{xy}^2 + A_{yy}^2) < \delta S_y(t)\delta S_y(0) >)e^{-i\omega_L t}dt. \qquad (91)\end{aligned}$$

The elements of the hyperfine coupling tensor $\overleftrightarrow{A}$ are given by the sum of dipolar and Fermi contact contributions. In the case of on-site coupling, *i.e.*, magnetic and nuclear spin are on the same atom, the isotropic contact coupling will be the dominant relaxation mechanism yielding $b(t) = A\sum_{\beta=x,y}\delta S_\beta(t)$. Note, that if $\overleftrightarrow{A}$ is *non*-diagonal in the laboratory frame, both parallel and transverse (to the external field $\mathbf{B}_0||z$) spin-spin correlation functions contribute to the relaxation, while only the latter contribution is active if $\overleftrightarrow{A}$ is diagonal. In general, $A_{\alpha\beta} \neq 0$ as soon as $\mathbf{B}_0$ is not parallel to a symmetry axis of the $\overleftrightarrow{A}$-tensor, leading to a complicated angular dependence of T_1.

In order to take into account the coupling to more than one electronic spin $\overleftrightarrow{A} \cdot \delta\mathbf{S}$ has to be replaced by $\sum_{\mathbf{r}} \overleftrightarrow{A}(\mathbf{r}) \cdot \delta\mathbf{S}(\mathbf{r}) = \sum_{\mathbf{q}} \overleftrightarrow{A}(\mathbf{q}) \cdot \delta\mathbf{S}(-\mathbf{q})$. The $\mathbf{q}$-dependent spin fluctuations $\delta\mathbf{S}(-\mathbf{q})$ are obtained by expanding the spin operator δS_β with the wave vector $\mathbf{q}$ as $\delta S_\beta(t) \cdot \exp(-i\mathbf{q}\cdot\mathbf{r}) = S_\beta(\mathbf{q},t)$, yielding

$$\frac{1}{T_{1z}} = \frac{\gamma_n^2}{2}\sum_{\mathbf{q}}\sum_{\beta=x,y,z}(A_{x\beta}^2(\mathbf{q}) + A_{y\beta}^2(\mathbf{q}))\int_{-\infty}^{\infty} < S_\beta(\mathbf{q},t)S_\beta(-\mathbf{q},0) > e^{-i\omega_L t}dt \qquad (92)$$

$$= \frac{\gamma_n^2}{2}\sum_{\mathbf{q}}(F_\perp(\mathbf{q})S_\perp(\mathbf{q},\omega_L) + F_z(\mathbf{q})S_z(\mathbf{q},\omega_L)). \qquad (93)$$

Here, $S_\perp(\mathbf{q},\omega)$ and $S_z(\mathbf{q},\omega)$ are the dynamic structure factors and $F_\perp(\mathbf{q}) = \sum_{\beta=x,y}(A_{x\beta}^2(\mathbf{q}) + A_{y\beta}^2(\mathbf{q}))$ and $F_z(\mathbf{q}) = A_{xz}^2(\mathbf{q}) + A_{yz}^2(\mathbf{q})$ represent the so-called geometrical form factors in momentum space. $F_\perp(\mathbf{q})/F_z(\mathbf{q})$ modifies the sensitivity of T_1 to different $\mathbf{q}$-components of the magnetic fluctuation spectrum. For example, in the CuO_2 plane of high-T_c superconductors, oxygen (^{17}O) is situated between two copper spins, and is coupled to each of them by the same hyperfine coupling constant, in effect filtering out the antiferromagnetic component of the copper spin fluctuations in $^{17}T_1$ measurements. Antiferromagnetic fluctuations will hence only be seen in the copper $^{63}T_1$, because the on-site coupling is $\mathbf{q}$-independent. Hence, complementary information on the $\mathbf{q}$-dependence can be obtained by measuring copper spin fluctuations at different crystallographic positions [109, 110, 111, 112].

Furthermore, the comparison of $1/T_1$ with theoretical calculations for different magnetic relaxation mechanisms, *i.e.*, one-magnon, two-magnon and multi-magnon processes, yields

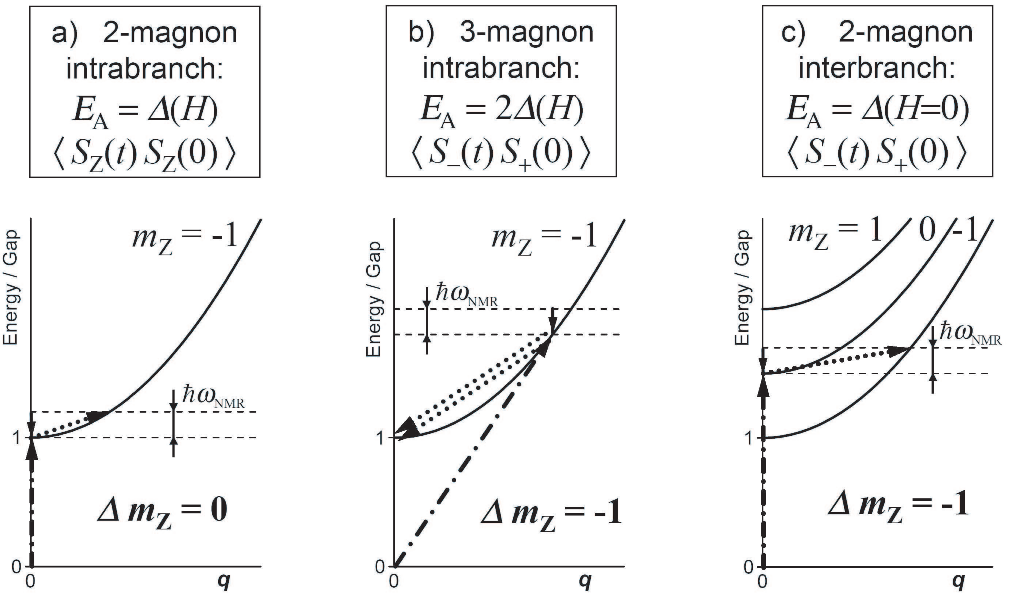

Figure 17: *The different magnon scattering processes involved in the nuclear spin-lattice relaxation rate 1/T_1 for 1D systems with a spin-excitation gap. Dash-dotted arrows indicate the incoming magnons, while solid arrows schematically denote the absorbed nuclear energy. Dotted arrows represent the outgoing magnons. The figure is taken from Ref. [115].*

important information about the relevant relaxation processes contributing to the spin-lattice relaxation rate. One-magnon processes add to the transverse dynamic structure factor $S_\perp(\mathbf{q}, \omega_L)$ and involve a single excitation whose energy must be essentially zero in order to induce a spin flip at $\hbar\omega_L$. For 1D systems with a spin excitation gap Δ, like those examined in this work, these interbranch ($\Delta m_z = \pm 1$) processes do not exist. Here, only nuclear relaxation via two- or three-magnon processes is allowed [113, 114, 115]. The different magnon scattering mechanisms are schematically depicted in Fig. 17. The most simple process is a spin-conserving two-magnon process ($\Delta m_z = 0$), which is intrabranch and couples to the longitudinal structure factor $S_z(\mathbf{q}, \omega_L)$. Other relaxation mechanisms involve spin non-conserving interbranch two-magnon processes with a spin flip, where magnons in the m_z = 0 and m_z = -1 branches couple to each other. They contribute to the transverse structure factor $S_\perp(\mathbf{q}, \omega_L)$, just as three-magnon intrabranch processes, that scatter two occupied magnons at the bottom of the m_z = -1 band into a magnon with twice the energy via a large momentum transfer. Notably, all these processes only occur for thermally activated excited states since usually $\hbar\omega_L << \Delta$.

Via the *fluctuation-dissipation theorem*

$$\begin{aligned} S_\beta(\mathbf{q}, \omega) &= 2\hbar \frac{1}{1 - e^{-\frac{\hbar\omega}{k_B T}}} \chi''_\beta(\mathbf{q}, \omega), \\ \text{with } \chi''_\beta(\mathbf{q}, \omega) &= \chi''_\beta(\omega) \exp(-i\mathbf{q} \cdot \mathbf{r}), \end{aligned} \tag{94}$$

which relates the strength of dissipation χ'' at ω in the linear response regime to spin fluctuations at ω in the absence of a driving field, one obtains the standard expression for $1/T_1$:

$$\frac{1}{T_{1z}} = \hbar\gamma_n^2 \sum_{\mathbf{q}} \frac{F_\perp(\mathbf{q})\chi_\perp''(\mathbf{q},\omega_L) + F_z(\mathbf{q})\chi_z''(\mathbf{q},\omega_L)}{1-e^{-\frac{\hbar\omega_L}{k_B T}}} \tag{95}$$

$$\approx \gamma_n^2 k_B T \sum_{\mathbf{q}} \frac{F_\perp(\mathbf{q})\chi_\perp''(\mathbf{q},\omega_L) + F_z(\mathbf{q})\chi_z''(\mathbf{q},\omega_L)}{\omega_L}. \tag{96}$$

This relation between the spin-lattice relaxation rate and the imaginary part of the dynamic susceptibility allows to test theoretical predictions for the dynamic susceptibility. Notably, in Eq. 96 $F_\perp(\mathbf{q})/F_z(\mathbf{q})$ is given in units T^2 and $\chi_\perp''(\mathbf{q},\omega_L)/\chi_z''(\mathbf{q},\omega_L)$ in units $1/J$.

For s-electron metals, which are described by the Fermi liquid theory, and under the assumption that the interaction between the nuclei and the electrons is the Fermi contact interaction, Eq. 96 yields the well-known *Korringa law*

$$T_1 T K^2 = \frac{\hbar\gamma_e^2}{4\pi k_B \gamma_n^2}. \tag{97}$$

This is understood from the fact that the spin-lattice relaxation rate is mainly due to conduction electrons, which have a finite probability at the nucleus site (see sec. 3.1.2). With the Korringa law, by plotting $1/(T_1 T)$ versus temperature, a first estimate of the degree of electron-electron correlation is possible.

For the calculation of $1/T_2$ beyond mean field theory, the reader is referred to Refs. [116, 117, 118]. Here, only the main results will be presented. In the Redfield theory, yielding $1/T_2 = 1/(2T_1) + 1/T_2'$, nuclear relaxation is only due to dynamic electronic spin moments. Relaxation processes due to indirect nuclear dipole-dipole coupling have been neglected, which, however, are usually the most important source for the decay of coherence of the nuclear spin components perpendicular to the external field. For a more appropriate treatment of the spin-spin relaxation rate an additional term, namely $1/T_{2G}$, has to be included in the calculations. It stems from nuclear dipole-dipole coupling and describes the gaussian decay of the spin-echo amplitude. Since the indirect nuclear dipole-dipole interaction is mediated through the electronic system, a measurement of T_{2G} yields important information about the electronic properties of the sample. $1/T_{2G}$ is given by [116, 117, 118]

$$(\frac{1}{T_{2G}})^2 \propto \frac{1}{N}\sum_{\mathbf{q}}(F_z(\mathbf{q})\chi_z'(\mathbf{q},\omega_L\approx 0))^2 - (\frac{1}{N}\sum_{\mathbf{q}} F_z(\mathbf{q})\chi_z'(\mathbf{q},\omega_L\approx 0))^2, \tag{98}$$

with N as the number of probing isotopes per unit cell and $\chi_z'(\mathbf{q},\omega_L\approx 0)$ as the real part of the electronic spin susceptibility along the quantization axis. Just as in the case of the imaginary part of the spin susceptibility, $\chi_z'(\mathbf{q},\omega_L\approx 0)$ is related to the dynamic structure factor via the fluctuation-dissipation theorem.

3.1.4 NMR Spectrometer

The main components of an experimental NMR setup are shown in Fig. 18. The setup consists of a cryostat containing the resonance circuit, with the sample placed inside a coil. The cryostat is inserted into a superconducting magnet supplying the external static field, with a homogeneity typically of the order of ppm. The main item of the setup is the spectrometer, generating the pulse sequences and amplifying the response signal from the sample. It is computer controlled to program the pulse sequences and to store the measured response of the studied system.

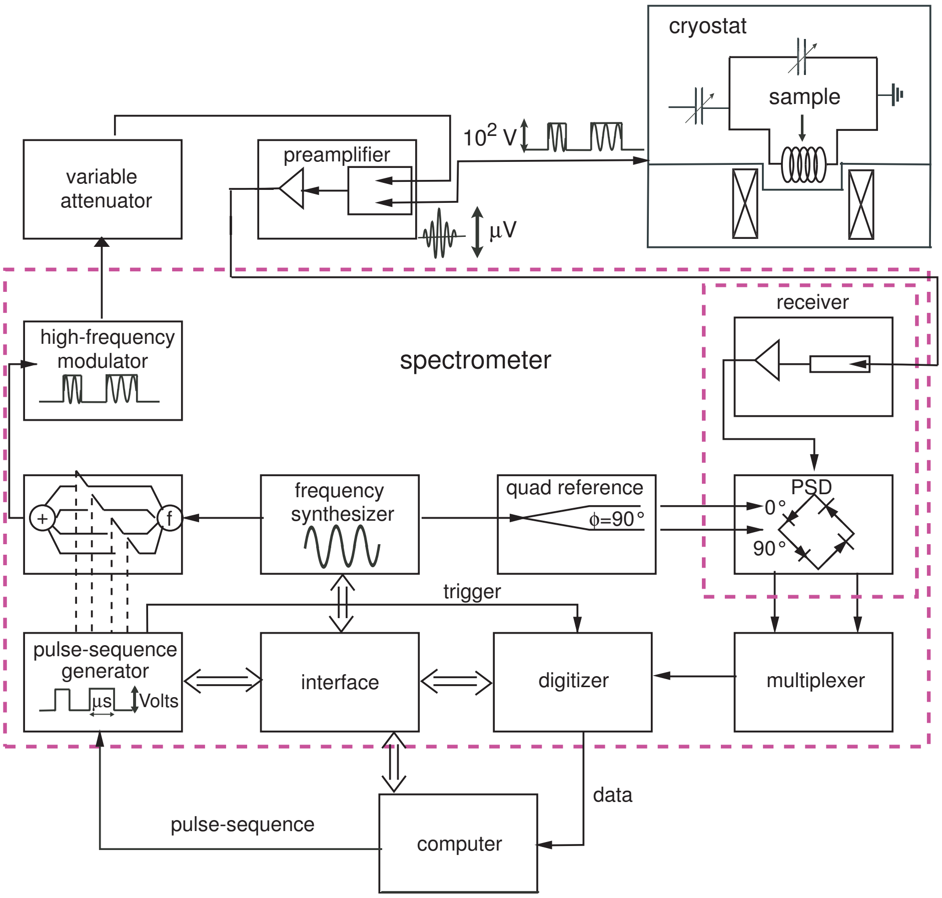

Figure 18: *Schematical representation of an experimental NMR setup.*

The cryostat

The cryostat allows to vary the temperature of the sample in order to perform measurements in a variable temperature range (here, 5 to 300 K). The temperature regulation in the flux flow cryostats, used in this work, can be realized via a gas flux of nitrogen (down to 77 K) or helium (down to ~ 5 K). The cooling from the gas flux is balanced by a heater situated next to the sample. For measurements at temperatures $T < 70$ K, one often encounters problems due to the formation of electric arcs from ionized helium gas. The effect of these electric arcs is a partial or total short circuit of the radio frequency pulses sent to the coil of the resonance circuit. As result, the response signal from the sample is reduced and deformed. In order to diminish the possibility of ionization of the helium gas, the pressure of the helium gas should be enhanced around the coil of the resonance circuit and metallic tips acting as a lightning rod should be avoided.

The emission of radio frequency pulses

In equilibrium state, the sample is only exposed to a static external magnetic field $\mathbf{B_0}$. With the application of an oscillating magnetic field $\mathbf{B}_1$ perpendicular to $\mathbf{B}_0$, a perturbation of the nuclear spin ensemble of the sample is achieved. This oscillating field is produced via rectangular pulses of variable frequency and duration inside the coil of the resonance circuit. Typical $\mathbf{B}_1$ pulses last a few μs, with an amplitude of the order of 100 Gauss. The pulses are produced by a frequency generator with $\omega \approx \omega_L$, and are enveloped into a rectangular signal of duration τ. In order to measure a signal of maximum intensity afterwards, one has to use $\pi/2$-pulses to turn the average nuclear magnetization into the plane of the coil, which is perpendicular to the static external field. The conditions for $\pi/2$-pulses depend on the gyromagnetic ratio of the nucleus, on the amplitude of $\mathbf{B}_1$ and the duration τ ($\theta = \gamma_n B_1 \tau$). To adjust it adequately, one can either tune the length of the pulse or the magnitude of $\mathbf{B}_1$ by using an adjustable attenuator. The Fourier transformation of the rectangular pulse of duration τ is given by

$$F(\nu) = F_0 \frac{\sin(\pi(\nu - \nu_o)\tau)}{\pi(\nu - \nu_0)\tau}, \tag{99}$$

with ν_0 as the frequency of the radio frequency pulse. For example, for a pulse of 3 μs, the spectral width at half maximum of $F(\nu)$ is approximately 300 kHz, leading to an excitation of all nuclei precessing at $\omega_L \pm$ 300 kHz. By the application of longer pulses, the excitation spectrum is reduced. Therefore, exact $\pi/2$-pulses are usually adjusted by an attenuation of the magnitude of $\mathbf{B}_1$.

The detection of the nuclear response

After the transmission of the radio frequency pulses, the nuclear spins precess back into their equilibrium state and induce a signal into the coil of the resonance circuit. This process is detected and sent to the receiver. The resonance circuit for excitation is the same as for detection. It is a "LC-C"-circuit, consisting of the coil with the sample, and two variable capacitors, which allow to adjust the resonance frequency of the circuit and to adapt it to the impedance of 50 Ω of the coaxial line. Notably, before each detection one has to wait for a certain delay, the deadtime of the electronic system, which is caused by the transistor signal at the end of the last pulse. While this last pulse is of the order of 100 V, the response signal of the nuclear spins is just of the order of μV. In order to protect the electronic devices to measure the response signal, they have to be decoupled from the circuit for some μs after

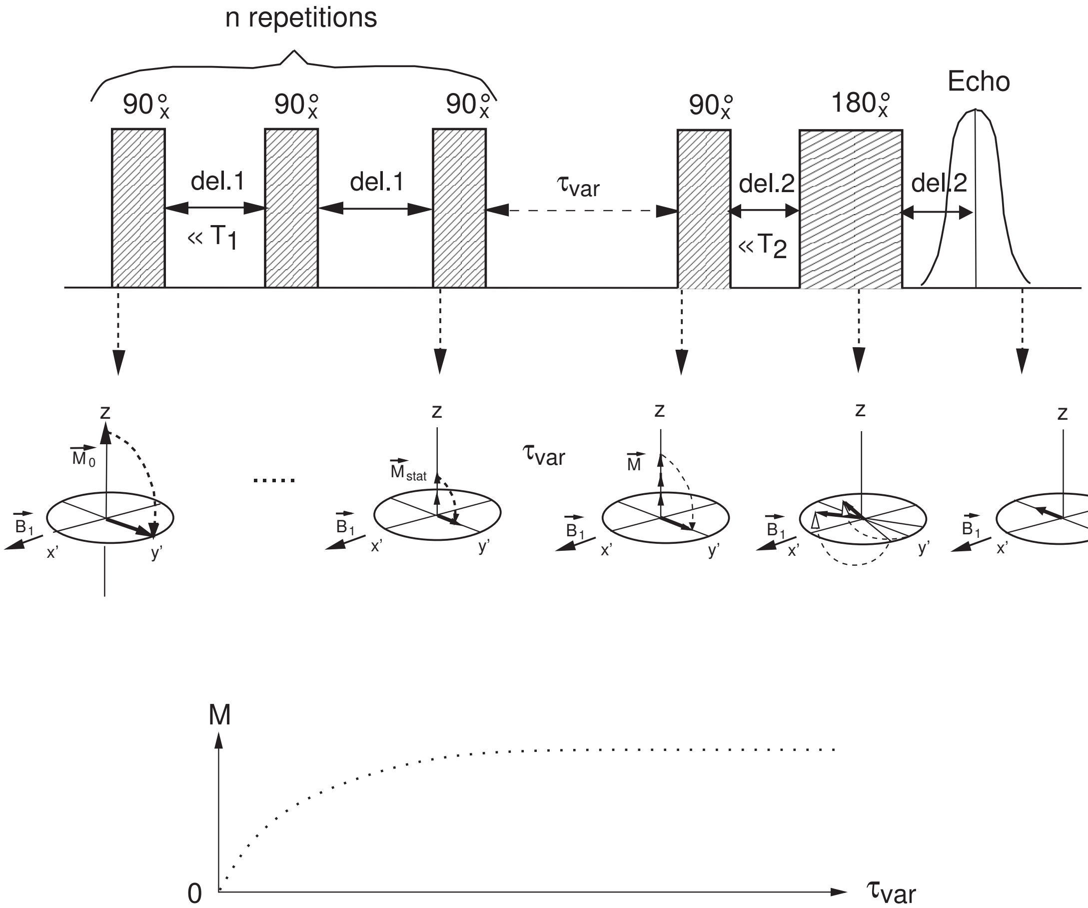

Figure 19: *The progressive-saturation pulse sequence to determine the spin-lattice relaxation time T_1 (shown in the rotating frame of reference). In the lower panel the nuclear magnetization as function of τ_{var} is illustrated.*

the last pulse. To overcome this problem the *Hahn spin-echo method* can be used, allowing a retardation of the precession of the nuclear spins back into their thermodynamic equilibrium. The Hahn spin-echo method consists of a $\pi/2$-τ-π sequence, which refocusses the transverse nuclear magnetization after the time $\tau > \tau_{dead}$. Notably, by using this method inhomogeneities of the external field are eliminated due to the interplay of the induced defocussing and refocussing of the nuclear spins.

After the detection of the small response signal of the nuclear spin ensemble, it is amplified. The method of phase-sensitive detection (PSD) demodulates the response with the reference frequency of the frequency synthesizer and divides it into two signals of low frequencies around zero, which are shifted by 90^0. This procedure is necessary to obtain a complex signal of the Fourier transformed response with a real (absorption curve $\chi\prime(\omega)$) and an imaginary part (dispersion curve $\chi\prime\prime(\omega)$).

In the following some specific features of common pulse sequences will be discussed, *i.e.*, the *phase cycling* and the *progressive-saturation method*, the latter being used to measure the spin-lattice relaxation rate. Phase cycling is used to cancel parasitic signals, either from multi-pulse experiments yielding phantom echoes, from transient responses of high-frequency pulses or imperfect hardware. The basic idea is that rotation around different axes affect the component of the magnetization vector in a different way. It takes advantage of the fact that parasitic signals have a constant/different phase than the signal stemming from nuclei of the sample. The special pulse sequence, which is used for phase cycling experiments consists of at least four pulses with different phases. Whereas the sequence of emission is represented by the transmitter phases (0°, 90°, 180°, 270°), the phase of detection is shifted by 180° for every second pulse yielding (0°, 270°, 180°, 90°) for the receiver phases. This way, it is guaranteed that an addition of the four responses eliminate parasitic signals whereas signals from the sample survive and add up to the measured response.

For the determination of the spin-lattice relaxation time T_1, a large quantity of different techniques exist, *i.e.*, the *inversion-recovery*, *the saturation-recovery*, *the progressive-saturation* method, to name a few. Since the latter was used in this work, it will be briefly discussed here. In the progressive-saturation method a series of $\pi/2$-pulses is used, the single pulses being quickly sent one after another relatively to the absolute value of T_1 of the examined system (Fig. 19). If the pulses are exact $\pi/2$-pulses, an equilibrium state between excitation and relaxation will be reached very quickly, represented by the stationary magnetization M_{stat}, which is a function of $del.1$, the interval between the $\pi/2$-pulses. In the limit $del.1 \rightarrow 0$, the magnetization along the z-direction cancels out after n repetitions. After another interval τ_{var} one can either detect the FID (free induction decay) or add a spin-echo subsequence, *i.e.*, a $\pi/2$ - $del.2$ - π - $del.2$ subsequence, such that the $\pi/2$-pulse rotates the magnetization vector $\mathbf{M}(\tau_{var})$ onto the xy-plane once more. Due to inhomogeneities of the local field each nuclear spin experiences a somewhat different field and precesses at a slightly different frequency, leading to a loss of coherence of the nuclear spins. After a second constant delay $del.2 \ll T_2$, a π-pulse inverts the direction of the spins leading to a refocussing, which can be detected as an echo response at 2*$del.2$ (neglecting the duration of the π-pulse). Only for large values of τ_{var} the maximal value of the magnetization, which is proportional to the magnetization in equilibrium state M_0, is detected. Hence, T_1 is determined by repeating the experiment with variable τ_{var}. The equation of motion is written as

$$M_z(\tau) = M_0 \cdot (1 - \exp(\frac{-\tau_{var}}{T_1})). \tag{100}$$

The progressive-saturation method is restricted to systems with $T_2 \ll T_1$. Otherwise, due to a remaining transverse component of the magnetization along the y-direction after the delay $del.1$, a second pulse would switch the magnetization along the z-axis and hence refocus the nuclear spins, destroying the validity of Eq. 100.

3.1.5 NMR under Pressure

In this section the specific features of NMR experiments under pressure will be discussed. Particular emphasis will be given to the clamp pressure cell for high hydrostatic pressures used in this work. In general, the maximal possible pressure, that can be produced by a cell, depends on the elastic limit and tensile strength of the material of the pressure cell as well as on the diameter of the pressurized sample space. Whereas 14 kbar can be achieved in the pressure cells consisting of CuBe used in this work, those made of Ni-Cr-Al alloy bear up to 40 kbar without any permanent deformation.

The cell, which has been specially designed for NMR investigations by the group of D. Jérome, LPS Orsay, is shown in Fig. 20. The outer cell diameter is 35 mm, the inner diameter of the sample space is 5 mm, leading to a volume of approximately 100 mm^3 for pressurization. The sample is placed inside a polycarbonate cylinder, filled with a liquid (Fluorinert) as pressure transmitter, closed with a CuBe cap and inserted into the borehole of the pressure cell. The cell is pressurized at ambient temperature using a press and a hydraulic jack with a multiplication factor of $\sim$ 300, then fixed with a screw.

In Fig. 21 the bottom sealing is shown in detail, illustrating the construction of the feedthrough for the electric leads of the rf-coil for NMR measurements. The sealing has a cylindric hole for the leads. They are fixed and the hole is closed by Stycast, the latter guaranteeing the sealing and the electric isolation under solidification.

For NMR measurements the CuBe pressure cell has an important advantage in comparison to other types of cells, *i.e.*, the minimal disturbance of the external magnetic field seen by the sample. The susceptibility of CuBe, which is only weakly paramagnetic due to traces of Ni and Fe, varies between $\chi = 2.2 \cdot 10^{-8}$ cm^3/g at room temperature and $\chi = 3 \cdot 10^{-6}$ cm^3/g at 4.2 K. In comparison, the susceptibility of the Ni-Cr-Al alloy, which is also used for pressure cells, varies between $\chi = 3.5 \cdot 10^{-6}$ cm^3/g and $\chi = 9 \cdot 10^{-6}$ cm^3/g in the same temperature interval.

On the other hand, for NMR experiments under pressure a couple of inherent problems have to be solved. The quality factor of the resonance circuit, $Q = 1/R \cdot \sqrt{L/C}$, is reduced

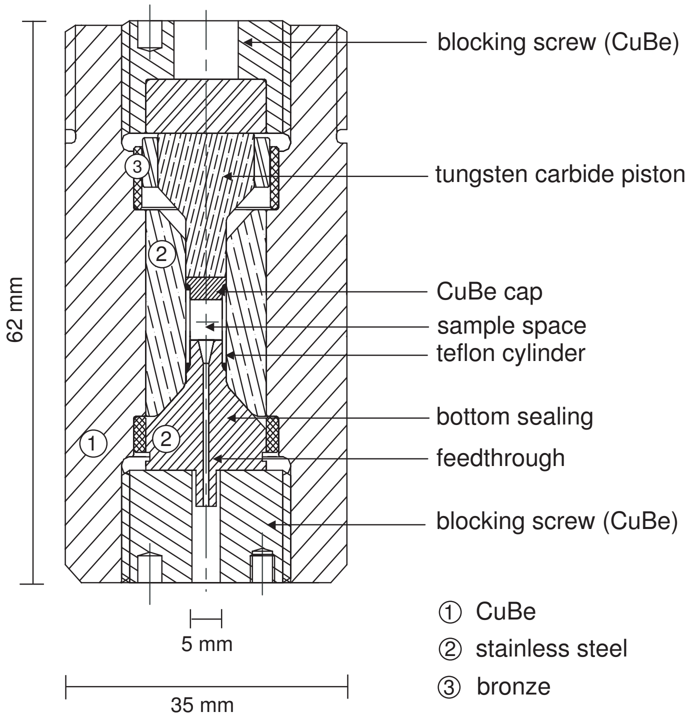

Figure 20: *The CuBe clamp pressure cell designed by the group of D. Jérome, LPS Orsay* (P_{max} *= 14 kbar) [119].*

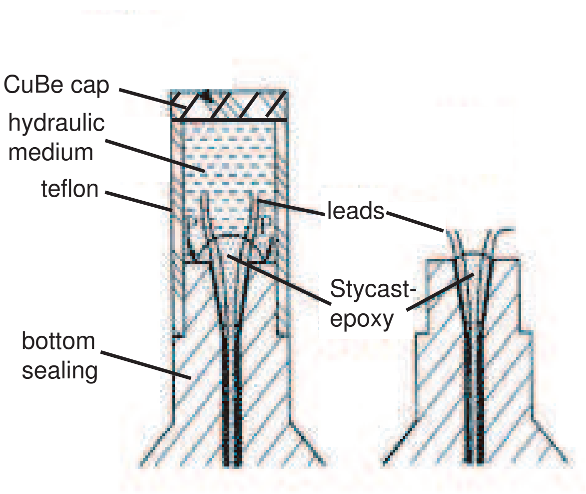

Figure 21: *A detailed drawing of the feedthrough for the leads inside the clamp pressure cell [119].*

by using this type of cell, since the bottom sealing of the pressure cell works as a parasitic capacitance, interfering parallel to the rf-coil. Furthermore, due to the small sample space containing only the rf-coil with the sample, the NMR signal is reduced, which may pose a problem in NMR experiments on low abundance nuclei such as ^{13}C. By optimizing the filling factor of the coil, sufficiently large signals can usually be obtained even on not isotopically enriched materials.

Particular attention needs to be paid to the pressure transmitting medium because most of the liquids contain protons or carbon, yielding additional NMR lines in the respective proton or carbon spectrum. In this ^{13}C-NMR work Fluorinert was used, a liquid which does not contain hydrogen but carbon. The corresponding parasitic lines could be distinguished from the broader signal of the sample due to their very sharp appearance and their small intensity, stemming from long spin-lattice relaxation times T_1 at low temperatures for liquid materials. Sometimes the additional lines can even be helpful and serve as a gauge for the applied pressure, since they are known to shift significantly under solidification at 14 kbar and room temperature.

The most important disadvantage of the CuBe pressure cell used in this work is that the pressure in the sample space cannot be determined directly. The absolute pressure value is estimated based on a preceding calibration process, which is reproducible for each pressure cell. For the calibration, the sample is replaced by a manganin wire with a known linear dependence of its resistance on pressure at room temperature. During the pressurization the applied pressure of the press as well as the displacement of the hydraulic jack are recorded as function of the pressure, as measured by the manganin gauge. For each following pressurization, the relation between the displacement of the hydraulic jack and the pressure in the pot has to be observed in order to check that there is neither a leak of the hydraulic fluid nor any anomalous deformation inside the cell, which would be reflected in disproportionately rapid displacements of the hydraulic jack. Then, empirical values for the loss of pressure due to cooling need to be taken into account, being 1-2 kbar for $P \leq 5$ kbar, < 1 kbar for 5 kbar$<P\leq$10 kbar and negligible small for pressures higher than 10 kbar.

3.2 Magnetization Measurements in Pulsed Magnetic Fields

In this section a brief overview of the calculation of the magnetization in statistical mechanics, the experimental setup, which has been used for the experimental determination of the magnetization performed at the Laboratoire National des Champs Magnétiques Pulsés (LNCMP) in Toulouse, and the requirements for the generation of pulsed high magnetic fields will be given.

The generation and use of pulsed magnetic fields was invented by P. Kapitza in Cambridge in 1924. Its first implementation in Toulouse dates back to 1965, when 40 T were generated in a small reinforced Cu coil driven by a 100 kJ capacitor bank. Later, the bank was upgraded to 1.25 MJ, which in 1987 permitted the generation of 61 T, with a pulse length of 0.2 s in a coil wound with NbTi-reinforced Cu wire. In the beginning of the 1990s the laboratory in Toulouse built up a 14 MJ generator and developed new high strength Cu-stainless steel conductors, which allow long pulse fields in excess of 60 T.

3.2.1 Magnetization in a Statistical Mechanics Approach

For the calculation of the magnetization of a paramagnetic material, one considers the additional magnetic energy of its atoms subjected to a magnetic field **B**. Here, only pure spin states will be treated, since the orbital momenta of the magnetic ions in the systems studied in this work are negligible. The remaining small orbital contributions are taken into account by using the experimentally determined g-tensor, which deviates from the value of the free electron. The Hamiltonian of the spin ensemble is written as

$$\mathrm{H} = -\boldsymbol{\mu} \cdot \mathbf{B}, \tag{101}$$

where $\boldsymbol{\mu} = -g\mu_B\mathbf{S}$ is the operator of the electron magnetic moment, g the Landé factor and μ_B the Bohr magneton. The spin operator is a vector operator with the components S_x, S_y, S_z, which do not commute with each other but with $\mathbf{S}^2$. The eigenvalues of S_x, S_y and S_z are $m = -S, -S+1, ..., S-1, S$ (m: magnetic quantum number). For the magnetic field **B** along the z-direction the stationary states of the spins in the magnetic field are the eigenstates of the S_z-operator. The eigenvalues of the energy are $g\mu_B mB$, reflecting $2S{+}1$ different energy levels.

The thermodynamic properties can be obtained from a partition function, Z, which depends on both the magnetic field and the temperature, since the energy levels are occupied according to the Boltzmann distribution:

$$\begin{aligned} Z &= \sum_{m=-S}^{+S} e^{-\beta g\mu_B Bm} \\ &= \sum_{j=0}^{2S} e^{-\beta g\mu_B B(j-S)} \\ &= e^{\beta g\mu_B BS} \sum_{j=0}^{2S} e^{-\beta g\mu_B Bj}, \end{aligned} \tag{102}$$

with $\beta = 1/k_BT$. By using the formula $\sum_{j=0}^{n} q^j = \frac{1-q^{n+1}}{1-q}$, one obtains another expression for the partition function

$$Z = \frac{sinh(\beta g\mu_B B(S+\frac{1}{2}))}{sinh(\beta g\mu_B B/2)}. \tag{103}$$

The free energy of a spin system is calculated by $F = -\frac{1}{\beta} lnZ$, its derivative (-$\frac{\partial F}{\partial B}$) yielding the statistical average of the magnetic moment $<\mu_z>$:

$$\begin{aligned} <\mu_z> &= \frac{1}{Z}\sum_{m=-S}^{+S}\mu_z(m)e^{-\beta(-\mu_z(m)B)} \\ &= \frac{1}{Z}\frac{1}{\beta}\frac{\partial}{\partial B}\sum_{m=-S}^{+S}e^{+\beta\mu_z(m)B} \\ &= \frac{1}{\beta}\frac{1}{Z}\frac{\partial Z}{\partial B} = \frac{1}{\beta}\frac{\partial lnZ}{\partial B} = \frac{\partial}{\partial B}(\frac{lnZ}{\beta}) \\ &= -\frac{\partial F}{\partial B}. \end{aligned} \tag{104}$$

For a system with N independent spins the total magnetic moment $M = N<\mu_z>$ is given by

$$\begin{aligned} M = N<\mu_z> &= -N\frac{\partial F}{\partial B} \\ &= -N\frac{\partial(g\mu_B B)}{\partial B}\frac{\partial F}{\partial(g\mu_B B)} = N\frac{g\mu_B}{\beta}\frac{\partial lnZ}{\partial(g\mu_B B)} \\ &= Ng\mu_B S B_S(x). \end{aligned} \tag{105}$$

Here

$$B_S(x) = \frac{2S+1}{2S}coth(\frac{2S+1}{2S}x) - \frac{1}{2S}coth(\frac{1}{2S}x),\ x = \beta g\mu_B SB, \tag{106}$$

is the Brillouin function, which for large values of S turns into the classical Langevin function $L(x') = coth(x') - \frac{1}{x'}$, $x' = \beta g\mu_B B$. For a single spin $S = 1/2$, $B_S(x) = tanh(x)$. For small values of the argument of B_S, *i.e.*, low magnetic fields and high temperatures, the Brillouin function can be expanded using the expression $x\,coth(x) = 1 + \frac{1}{3}x^3 - \frac{1}{45}x^4 + ...$, yielding

$$M = N\frac{(g\mu_B)^2 S(S+1)}{3k_B}\frac{B}{T}. \tag{107}$$

Then, the magnetic susceptibility of a non-interacting spin ensemble with N magnetic moments is given by

$$\chi = \frac{\mu_0 M}{B} = \mu_0\frac{Ng^2\mu_B^2 S(S+1)}{3k_B T} = \frac{C}{T}, \tag{108}$$

with C as the Curie constant.

In the case of metallic materials, in addition the contribution of the conduction electrons needs to be taken into account in the magnetization, *i.e.*, the Pauli paramagnetism $M_{Pauli} = (N_+ - N_-)\mu_B$, where N_+ and N_- are the number of conduction electrons per volume with the magnetic moment parallel and antiparallel to the external magnetic field, respectively. By using the density of states for the conduction electrons per volume (see sec. 3.1.2), M_{Pauli} follows to

$$M_{Pauli} = \frac{3}{2}\frac{N\mu_B^2}{k_B T_F}B. \tag{109}$$

Notably, M_{Pauli} is temperature independent for $T << T_F$, since the excess of electrons with the magnetic moment parallel to the external field only stems from possible states near the Fermi level $E_F = k_B T_F$.

For magnetically ordered systems with spins coupled to each other via an exchange interaction, the Hamiltonian of the spin ensemble in an external magnetic field $\mathbf{B}$ is given by

$$\mathrm{H} = -\sum_{i,j} J_{ij}\mathbf{S_i S_j} - \sum_{j} g\mu_B \mathbf{S_j B}, \tag{110}$$

with J_{ij} as the exchange parameter. The first term represents the exchange coupling, which yields a favorable parallel arrangement of two spins if J_{ij} >0, and an antiparallel arrangement if J_{ij} <0, respectively. The second term in Eq. 110 stands for the Zeeman energy of the magnetic moments in the external magnetic field. In the ordered case, the magnetization is often calculated in a mean field approach, where the exchange coupling is replaced by an internal field $\mathbf{B}_i$, offering the advantage of a treatment just as in the case of free paramagnetic electrons.

3.2.2 Experimental Setup for Magnetization Measurements

Magnetization measurements in pulsed magnetic fields are carried out by determining the magnetic induction in a stationary pick-up coil system surrounding the sample, which is located inside the borehole of the external magnet. The field pulse causes a change of the magnetic flux $d\phi/dt$ and induces a voltage in the pick-up coil. To obtain a signal proportional to the magnetic moment of the sample, the signal induced by the pulsed field has to be compensated by at least one additional compensation coil.

For an optimum signal a good filling factor $F \propto L^3/r^3$ is critical, L being the size of the sample and r the radius of the pick-up coil. Of course, large samples improve the relative sensitivity, whereas the absolute sensitivity depends on the experimental equipment and the specific level of both field and thermal noise. For a pick-up system in the center of the external magnet coil, the magnitude of the field noise scales with the effective coil area Nr^2. With axial displacement of the pick-up coil the field noise level increases like Nr^4. The thermal noise is given by the metallic material of the pick-up coil and scales like $(RT)^{1/2}$, where R is the resistance of the coil. Whereas it decreases by two orders of magnitude for a reduction of temperature from room to liquid helium temperatures, it increases by a reduction of the radius of the coil. Hence, thermal and field noise are competing effects, the latter being decreased by a reduction of the radius of the coil.

The geometrical arrangement of pick-up and compensation coil can be axial or coaxial. Whereas axial pick-up arrangements usually have a high degree of compensation of the induced signal, coaxial pick-up systems have the advantage of a small sensitivity to a displacement relative to the external field coil. In contrast, axial pick-up systems are very sensitive to such a displacement, *e.g.*, by vibrations during the field pulse or by a thermal expansion of the sample holder. In order to reduce this effect, an axial compensation coil is often divided into two coils localized symmetrically above and below the pick-up coil. If furthermore the pick-up coil is divided into two halves with an optimized distance to the center, the influence of a displacement of the sample from the center of the coil on the measured signal is minimized, now only stemming from a varying sensitivity of the pick-up system along the coils. For an axial coil arrangement the sensitivity is rotationally symmetric and has a saddle point in its center. Whereas there is a large reduction of the sensitivity along the axis of the external field, a large increase exists along the perpendicular directions.

The voltage induced by the magnetic field pulse is given by

$$\begin{aligned} U_{ind} = U_{pu1} - U_{pu_2} &\propto -N_1 A_1 \frac{\partial B}{\partial t} + N_2 A_2 \frac{\partial B}{\partial t} \\ &= \eta\Omega(\frac{\partial}{\partial t}(M+H) - \frac{\partial}{\partial t}H) \\ &= \eta\Omega\frac{\partial M}{\partial t}. \end{aligned} \tag{111}$$

Here, η represents a coupling constant which reflects the specific parameters of the pick-up coil, like the number of turns and coil area, but also the geometry and position of the sample. Ω is the volume of the sample. Due to a varying sensitivity of the pick-up system along the coils, bar- or disc-shaped samples may exhibit geometry effects in the measured signal.

In the experiment the resulting magnetization $M(H)$ of the sample is obtained by a numerical integration of the induced voltage U_{ind} (Eq. 111). Strictly speaking, the induced voltage is determined by $U_{ind} = \eta\Omega\frac{\partial B}{\partial t}\frac{\partial M}{\partial B}$, the rate of change of magnetic field $\partial B/\partial t$ being measured simultaneously with U_{ind} using a separate pick-up coil. Then the resulting magnetization of the sample is subsequently found by a numerical integration of the induced voltage U_{ind} after the numerical integration of $\partial B/\partial t$.

For the magnetization measurements at the LNCMP in Toulouse an axially compensated pick-up system, concentrically wound around the sample, was used, enabling a determination of the magnetization of the sample as function of external field. In order to perform temperature dependent measurements, the complete arrangement, *i.e.*, the pick-up coils and the holder plus sample, were placed inside a ^{4}He cryostat located inside the borehole of the external field coil producing up to 60 T. Due to a homogeneity (dB/B) of the pulsed fields (40T) of about 10^{-3} inside a sphere of 10 mm diameter, and $1.3{\cdot}10^{-3}$ inside a sphere of 5 mm diameter for the 60 T magnets, the pick-up system has to be centered very carefully to avoid large field noise. Still, the remaining imperfect compensation of the pick-up coils brought about the necessity of a repetition of the magnetization measurements without sample to correct for the small residual background signal.

3.2.3 Generation of Pulsed Magnetic Fields up to 60 T

High strength conductors

The conductor materials used for pulsed high magnetic field coils need to be adapted to specific requirements, *i.e.*, a maximum mechanical strength to guarantee the highest possible

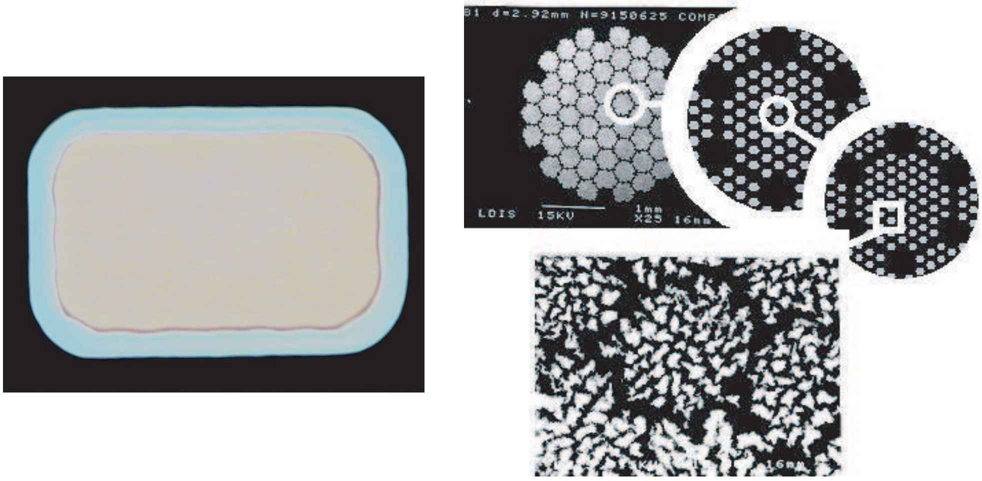

(a) (b)

Figure 22: *Image of (a) the section of a copper/stainless steel macro-composite conductor for pulsed fields < 70 T and (b) the multi-ladder structure of a copper/niobium nanofilamentary conductor used for pulsed magnetic fields > 70 T [122].*

peak field, together with a large specific heat and low resistivity to permit the longest possible pulse duration. For square coils, for example, the accumulated stress during a pulse due to the magnetic pressure $P_{mag} = B_0^2/(2\mu_0)$ exceeds more than 860 MPa at 60 T, a value that has to be met by the elastic limit of the conductor material in order to be non-destructive [120]. Furthermore, the coil performance is limited by heating as determined by the integral $\int_0^{t_1} j^2 dt = \int_{T_0}^{T_1} c_V/\rho dT$, where j is the current density, c_V the specific heat and ρ the resistivity of the coil conductor material. The first part of the equation indicates that for a given pulse shape, the heating can be adjusted via the pulse duration.

For pulsed magnetic fields up to 70 T, stainless steel reinforced Cu macro-composites are used (Fig. 22(a)), which are produced by cold drawing associated to heat treatment [120, 121]. The basic idea behind this type of conductors is to develop a highly conducting matrix, which is reinforced with a material with good mechanical properties. Since the distance between dislocations is negligible compared to the size of the materials ($> 100\ \mu m$), each component can be considered as bulk material. The mechanical properties of the macro-composite are then defined by the rule of mixtures. The electrical conductivity is governed by parallel conduction while - in the worst case - the heating occurs adiabatically in each component. For a composite of 60 % copper and 40 % stainless steel (SS), the universal tensile strength of insulated wires with a cross section of 6 mm^2 is approximately 1 GPa. The electrical isolation is performed with a polyimide film (Kapton).

For a non-destructive generation of more than 70 T, nanofilamentary conductors with a tensile strength exceeding 2 GPa are used. Here, Nb filaments are embedded in a Cu matrix, essentially behaving like nanowhiskers (Fig. 22(b)). The preparation of these sophisticated wires is based on the plastic deformation of metals by hot extrusion and cold drawing applied

	40T, 1.25 MJ	60T, 1.2 MJ	55T, 3.3 MJ
inner diameter	28 mm	13 mm	28 mm
outer diameter	206 mm	284 mm	200 mm
length	204 mm	304 mm	206 mm
conductor	Cu	Cu 60%/SS 40 %	Cu 60%/SS 40 %
total time	1.2 s	0.15 s	0.25 s
rising time	90 ms	25 ms	43 ms
frequency of shots	1/hour	1/hour	1/3 hour

Table 1: *The different types of magnetic coils used at the LNCMP in Toulouse.*

to bundling stages in order to reduce the fiber size [120, 121]. The strength of the whisker-like fibers is inversely proportional to their diameter and approaches the theoretical predicted value for perfect crystals $G/(2\pi)$, G being the shear modulus. The mechanical properties of these nanostructures can be improved by using a reinforced metal with a shear modulus higher than that of Nb ($G_{Nb} = 40$ GPa), like for instance Ta ($G_{Ta} = 69$ GPa).

Coil characteristics

After winding, the coils are rectified, fit into a reinforcing cylinder of a few centimeters thickness and then axially compressed between G10 discs. G10 is a highly compressed epoxy resin and glass fiber composite, which is exceptionally strong and has good thermal and electrical insulating properties. The complete setup is rigidly bolted to the bottom of specially designed superinsulated LN2-cryostats, representing the ground connection of the coil. At the LNCMP in Toulouse three different types of magnets are used at the moment, varying in the maximum attainable field, total pulse duration, rising time for B_{max} and coil dimensions. The main properties of the magnets are summarized in Tab. 1. For the present work, both the 40 T, 1.25 MJ as well as the 60T, 1.2 MJ magnets have been used.

Fig. 23 depicts a typical field pulse with 60.5 T peak field, 25 ms rising time and 150 ms total pulse duration. The graph also includes the results of a numerical calculation of the heating of the conductor material with the field pulse. The temperature of the coil increases by at least 170 K during the pulse. Therefore, the coil needs to be cooled with liquid nitrogen and the frequency of shots is reduced to 1/hour in the case of the 1.2 MJ-operated 40 and 60 T solenoids. An excellent agreement between the numerical simulations and experimental results for the heat exchange between the Cu and stainless steel components of the wire demonstrates that the coil is operated in reasonable proximity to the isothermal limit (perfect heat exchange) and that no overheating of the Cu core occurs during the pulse [120].

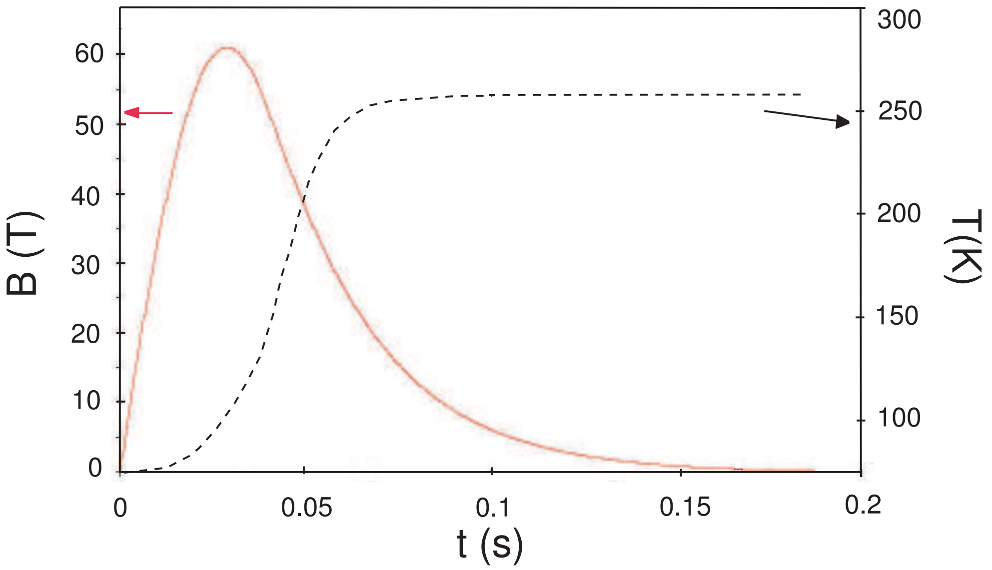

Figure 23: *The time dependence of a typical field pulse of the 60 T coil at the LNCMP (red curve), together with a numerical simulation of the heating of the conductor material with the pulse (black curve).*

The 14 MJ capacitor bank

The coils are driven by a 24 kV, 14 MJ capacitor bank. The 600 capacitors are divided into 10 modules that can be used separately and with different polarity. For safety reasons, in case of accidental short circuits the maximum current leaving each module is limited by an additional inductance to 6.5 kA. Crowbar circuits with three different resistance settings permit the individual adjustment of the pulse shape for the different coils. The discharging of the capacitor bank into the coil is realized via stacks of optically triggered thyristor switches.

The capacitor bank control is divided into two parts: a central unit monitors and controls the polarity, charging and triggering of capacitor modules and the connection of the 10 measurement stations. A secondary control attached to each of these stations permits remote communication with the central unit and determines the admissible charging parameters as a function of the cryogenic state of the magnet (temperature and pressure in the pumped cryostat). The charging time of the capacitor bank is approximately 5 minutes, which is negligible in comparison to the time needed to cool the magnet after each shot.

In Fig. 24 the circuit of a single 1.44 MJ capacitor module as well as a scheme of the entire capacitor bank is depicted. The drawing shows the charging resistors and the crowbar in parallel to the capacitors. The current limiting inductances are connected in series. The module consists of two parts that are connected via the same thyristor stack with the main discharge circuit. All components are designed to permit reversal of the current direction.

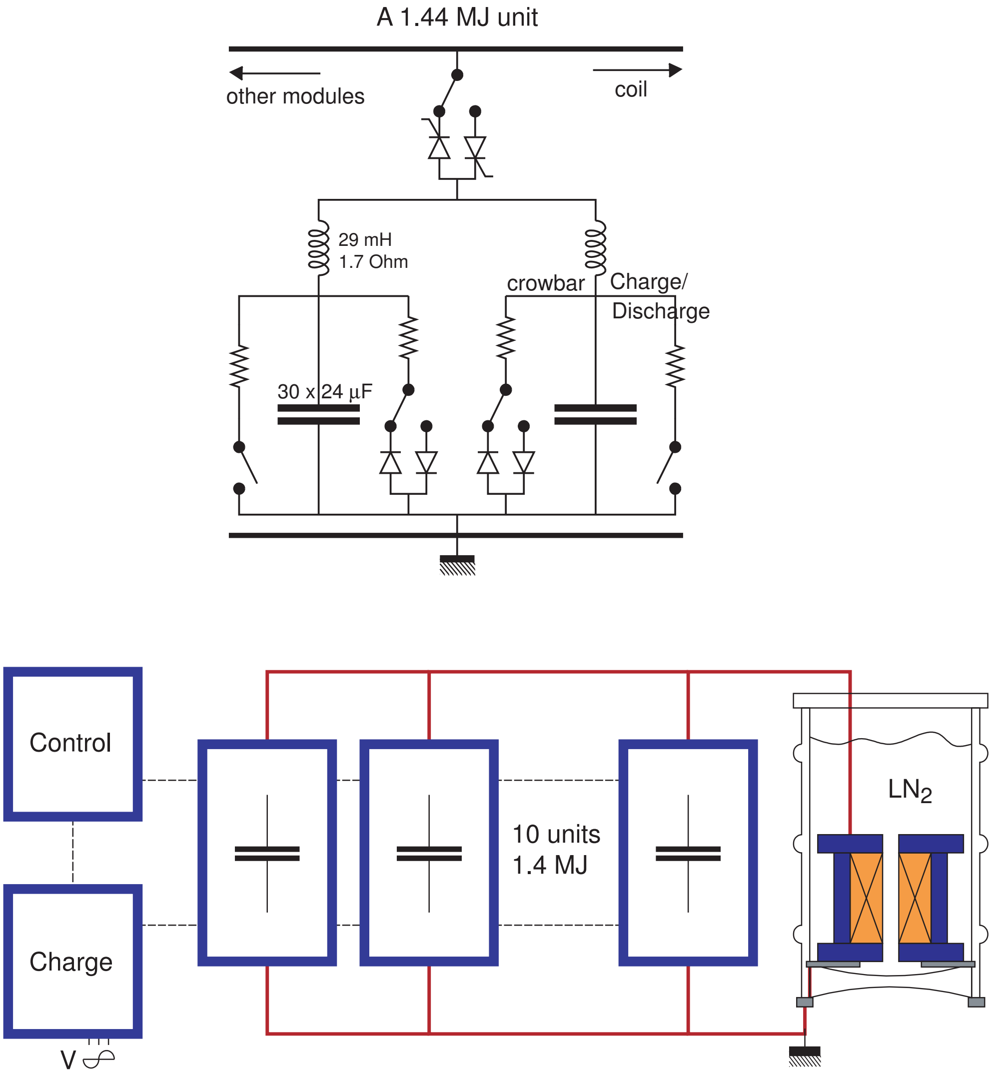

Figure 24: *The circuit of a single 1.44 MJ capacitor module as well as a scheme of the entire capacitor bank. Parts of this figure are taken from Ref. [120].*

4 Two Staggered $S = 1/2$ AFHCs: CuPM and Copper Benzoate

The samples studied in this work belong to the class of molecule-based $S = 1/2$ antiferromagnetic Heisenberg chains with alternating local symmetry. The corresponding model Hamiltonian has already been introduced and motivated in Chapter 2. This model by Oshikawa and Affleck [39, 40] has successfully been applied to four different compounds, *i.e.*, copper benzoate $Cu(C_6H_5COO)_2 \cdot 3H_2O$ [39, 40, 42, 43, 48, 123], Yb_4As_3 [55, 56, 57, 124, 125, 126], copper pyrimidine dinitrate $Cu(C_4N_2H_4)(NO_3)_2(H_2O)_2$ [52, 54] and copper chloride dimethyl sulfoxide $CuCl_2((CH_3)_2SO)_2$ [53].

Based on the temperature dependence of the susceptibility, copper chloride dimethyl sulfoxide (CDC) has been identified as an antiferromagnetic $S = 1/2$ chain system with an exchange coupling constant $J/k_B \approx 17.6$ K [127]. Very recently, inelastic neutron scattering experiments in high magnetic fields by Kenzelmann et al. [53] yielded clear evidence in CDC for soliton/antisoliton and breather creation at $q = \pi - 2\pi < S_z >$ and $q = \pi$, respectively. The ratios of the field dependent excitation energies are in excellent agreement with the predictions derived from the quantum sine-Gordon model under the condition of a renormalized soliton mass gap. Kenzelmann et al. [53] attributed the renormalization effect to non-negligible interchain interactions in CDC, which suppress the effective staggered field close to a critical field H_c.

The second compound within this class of materials, Yb_4As_3, first attracted attention due to the similarity of its macroscopic properties to those of heavy fermion materials [128]. Later, however, it has been found that its large coefficient of the T-linear specific heat, $\gamma = 205$ mJ/mol K^2, and its T^2 dependence of the low temperature resistivity are not due to a Kondo lattice mechanism, but have been attributed to 1D spin excitations in the Yb^{3+} chains [129]. In contrast to copper benzoate and copper pyrimidine dinitrate, the magnetically one-dimensional character of Yb_4As_3 is not due to an anisotropic crystal structure, but stems from a different physical process. A charge ordering in Yb_4As_3, which occurs below $T_{co} \sim 295$ K, gives rise to the formation of one-dimensional chains of Yb^{3+} ions. The chains are well separated from each other by nonmagnetic Yb^{2+} and As ions. Shiba et al. [130] demonstrated that the effective Hamiltonian for the crystal field ground state doublets of Yb^{3+} ions in Yb_4As_3 can be mapped onto the $S = 1/2$ AFHC model.

When Helfrich et al. [55] observed a field-induced gap in the specific heat of Yb_4As_3 due to a staggered field introduced through the DM interaction, Yb_4As_3 was finally added to the list of staggered $S = 1/2$ AFHCs. Further, distinct field anomalies in the thermal expansion and thermal conductivity of Yb_4As_3 were found, which are well described by the quantum SG model [57]. Inelastic neutron scattering investigations in applied fields also confirmed the staggered $S = 1/2$ chain behavior of Yb_4As_3. Here, the excitation spectrum at the antiferromagnetic wave vector changes drastically from a broad one, corresponding to the spinon excitation continuum of the uniform $S = 1/2$ AFHC, to a sharp one at a finite energy, indicating the opening of an energy gap in the system.

The antiferromagnetic $S = 1/2$ spin chains in Yb_4As_3, however, do not form an ideal insulating 1D Heisenberg antiferromagnet. *Ac* susceptibility investigations yield indications for a spin-glass freezing in Yb_4As_3 at $T = 0.12$ K, caused by disorder and the interplay between antiferromagnetic intrachain coupling together with a weak interchain coupling, the latter leading to frustration along the chains [125]. Further, the $J = 7/2$ multiplet of the Yb^{3+} ions adds a large Van Vleck-type contribution to the uniform and staggered magnetization of the effective $S = 1/2$ AFHC and prevents a saturation of the magnetization in high magnetic field experiments. The saturation field of roughly 400 T is far beyond the accessible range for magnetic fields nowadays, making an extensive high-field magnetization study impossible.

On the contrary, copper benzoate and copper pyrimidine dinitrate (CuPM), represent ideal model systems for investigating the physical properties of the staggered $S = 1/2$ AFHC. In particular, CuPM faithfully realizes the spin Hamiltonian in Eq. 27. Its intrachain exchange constant J/k_B is twice as large and its interchain coupling constant smaller than those in copper benzoate. This indicates *(i)* good experimental conditions that are necessary to access a wide range of normalized temperatures k_BT/J, normalized fields $g\mu_BH/J$, and normalized energy transfer $\hbar\omega/J$, and *(ii)* a highly one-dimensional material, where interchain interactions can safely be neglected. Hence, CuPM is probably the best realization of the quantum sine-Gordon spin chain model known to date. Copper benzoate, on the other hand, seems to be the second best realization due to its negligible interchain interactions and ideal insulating 1D Heisenberg antiferromagnetic behavior in contrast to CDC and Yb_4As_3, respectively.

Therefore, copper benzoate and copper pyrimidine dinitrate have been chosen for this work to investigate the theoretically predicted, but experimentally unexplored magnetic properties of the staggered $S = 1/2$ AFHC. The following sections 4.1 and 4.2 will provide a short characterization of the investigated samples copper pyrimidine dinitrate and copper benzoate, respectively, including their crystallographic structure and their basic magnetic properties reported so far.

4.1 Copper Pyrimidine Dinitrate $CuPM(NO_3)_2(H_2O)_2$

Antiferromagnetic interactions in linear polymers have been studied for decades, like for instance in copper pyrazine dinitrate $CuPZ(NO_3)_2$ and copper pyrazine dihexafluoro-pentanedionate $CuPZ(hfac)_2$ (PZ = pyrazine= $C_4N_2H_4$) [131, 132, 133]. When Ishida et al. [134, 135] synthesized new pyrimidine-bridged copper(II) complexes by replacing pyrazine with pyrimidine (pyrimidine = PM = $C_4N_2H_4$), they intended to change the magnetic coupling from an antiferromagnetic to a ferromagnetic one. The principal idea behind pyrazine and pyrimidine bridges to act as an antiferro- and ferromagnetic exchange pathway between neighboring magnetic ions is illustrated in Fig. 25. Whereas the magnetic exchange is mediated through three atoms in the case of pyrimidine bridges, yielding a preferred ferromagnetic exchange

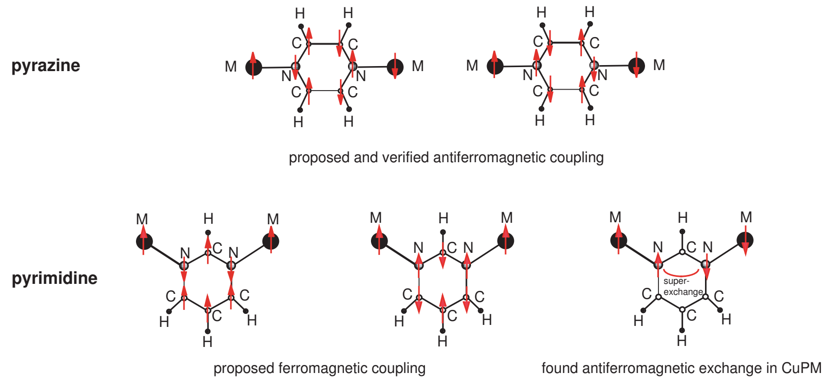

Figure 25: *Proposed model and real situation of the coupling scheme of pyrazine and pyrimidine molecules, acting as antiferro- and ferromagnetic exchange bridges, respectively [134, 135]. The red arrows indicate the spin polarization, M denotes the intermetallic ions.*

between the intermetallic ions, four atoms constitute the magnetic exchange path in pyrazine and provide a preferred antiferromagnetic exchange. Indeed, some of the pyrimidine compounds by Ishida et al. [135] show a ferromagnetic interaction between the Cu^{2+} spins, such as $CuPM_2(NO_3)_2$ with an exchange coupling along the chains of $J/k_B = 0.89$ K [135]. For the solvent containing complex copper pyrimidine dinitrate $CuPM(NO_3)_2(H_2O)_2$, however, an antiferromagnetic behavior has been observed, indicating that pyrimidine rings do not necessarily play the role of ferromagnetic couplers. The crucial difference between the structures of $CuPM_2(NO_3)_2$ and $CuPM(NO_3)_2(H_2O)_2$ are the axial/equatorial positions of the nitrogen atoms of bridging pyrimidines, defining the nature of the magnetic exchange. In CuPM, a pyrimidine molecular orbital in which atomic orbitals from both nitrogen atoms largely contribute may work as an antiferromagnetic coupler through the appreciable overlap due to the equatorial coordination on both sides.

4.1.1 Crystallographic Structure of Copper Pyrimidine Dinitrate

$CuPM(NO_3)_2(H_2O)_2$ crystallizes in a monoclinic structure, space group $C2/c$, with four formula units per unit cell. Powder x-ray diffraction yields lattice parameters of $a = 12.3760$ Å, $b = 11.4972$ Å, $c = 7.5051$ Å, $\beta = 114.97°$ at room temperature and $a = 12.1405$ Å, $b = 11.4376$ Å, $c = 7.4557$ Å, $\beta = 113.82°$ at 10 K [54]. Rietveld refinements of the powder diffraction data show that the low-temperature structure is essentially the same as at room temperature. A projection of the crystallographic structure of CuPM onto the ab-plane is shown in Fig. 26. All Cu ions are crystallographically equivalent. They form uniformly spaced chains parallel to the short ac-diagonal. The Cu ions are linked by the N–C–N moieties of the pyrimidine molecule, which represents the intrachain magnetic exchange pathway. The distance between neighboring copper ions along the chain is $d_{Cu-Cu} = 5.71$ Å at 10 K, while the interchain Cu-Cu distance is given by $d_{chain-chain} = 6.84$ Å.

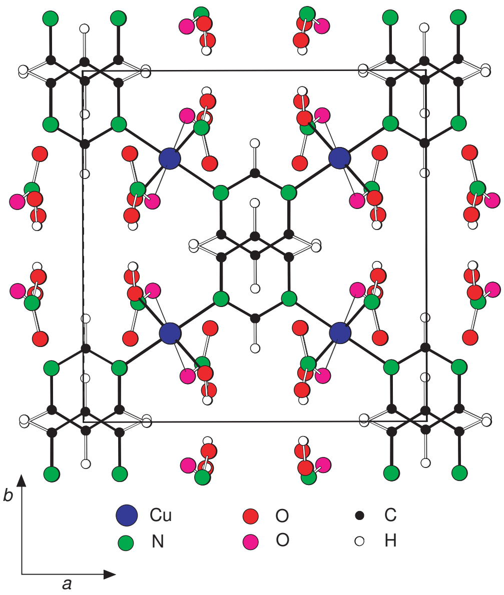

Figure 26: *Projection of the crystallographic structure of CuPM(NO_3)$_2$(H_2O)$_2$ onto the ab-plane. Note, that neighboring copper chains along the b direction are shifted by the amount of the lattice parameter a, while neighboring chains along the c-axis are directly stacked on top of each other.*

The local symmetry of the Cu ions is a distorted octahedron with N–O–N–O equatorial planes and O in the axial positions, as indicated in Fig. 27. The main axis of the octahedron is tilted by ± 29.4° out of the ac-plane. As this axis coincides with the g-tensor's principal axis, neighboring Cu atoms are crystallographically but not magnetically equivalent. The perpendicular bisector of two such neighboring principal axes is denoted c' and is shown in Fig. 27(a), where a' is taken to be perpendicular to b and c'. The principle axis for the nearest neighbor spin-spin interaction results from a combination of the anisotropic exchange interaction and the DM interaction, both being roughly of the same order of magnitude. Whereas the exchange interactions are determined by the g-tensor and thus are parallel to c', the DM interactions are essentially parallel to the copper chain direction. Therefore, the principle axis of the nearest neighbor spin-spin interaction approximately bisects c' and the chain direction. It is denoted c'', with a'' being perpendicular to b and c'' directions. The main directions of spin space anisotropy, a'' and c'', are depicted in Fig. 27(a). In the coordination frame $a''bc''$, the g-tensor of copper pyrimidine dinitrate assumes the form[8]

$$\overleftrightarrow{g} = \begin{pmatrix} 2.140 & \mp 0.071 & -0.099 \\ \mp 0.071 & 2.149 & \pm 0.105 \\ -0.099 & \pm 0.105 & 2.220 \end{pmatrix} = \overleftrightarrow{g}_u \pm \overleftrightarrow{g}_s, \tag{112}$$

---

[8] The g-tensor in the coordination frame $a''bc''$ was obtained by a transformation of the g-tensor from Ref. [54], *viz.*, a rotation around the b-axis by an angle of +34° (see Fig. 27).

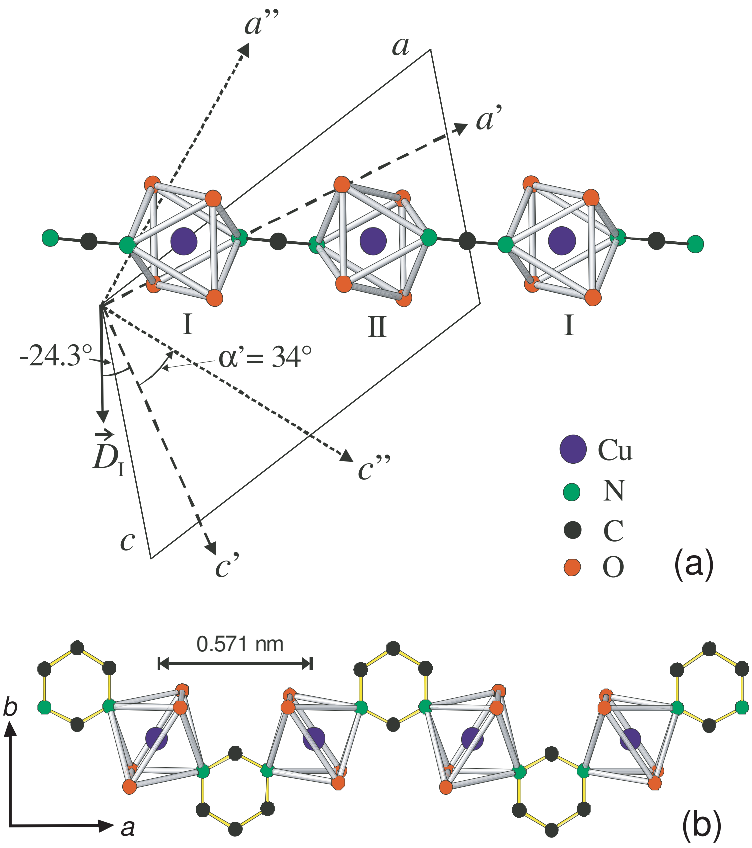

Figure 27: *(a) A single chain of CuPM(NO$_3$)$_2$(H$_2$O)$_2$ in a view onto the ac-plane. For clarity, only the ions forming the distorted octahedra around the Cu ions and the N–C–N bridges are shown. The definition of the axes a', c' and a'', c'' is given in the text. For the orientation of the DM vector* **D** *see section 4.1.2. (b) A single chain of CuPM(NO$_3$)$_2$(H$_2$O)$_2$ in a view onto the ab-plane. The pyrimidine complex C$_4$N$_2$H$_4$ connects two Cu ions along the chain, as is indicated in the figure. Note that figure (a) is taken from Ref. [54].*

with ± referring to the two inequivalent Cu sites. The effective g-value for an arbitrary field direction is given by $g = |\overleftrightarrow{g} \cdot \mathbf{H}|/|\mathbf{H}|$.

4.1.2 Magnetic Properties of Copper Pyrimidine Dinitrate

A preliminary report of the single-crystal susceptibility $\chi(T)$ of copper pyrimidine dinitrate has been given in Ref. [136]. In that work Feyerherm et al. [136] showed that for temperatures $T > 10$ K the susceptibility data of CuPM is well reproduced by the uniform $S = 1/2$ antiferromagnetic Heisenberg chain model calculated first by Bonner and Fisher [80]. From a fit to the data, an exchange coupling constant $J/k_B = 36$ K has been obtained, which was found to be isotropic within the experimental uncertainty (± 2%). Further, an upturn of $\chi(T) \propto 1/T$ was reported for $T < 10$ K, which exhibits a strong dependence on the magnetic field direction, and therefore was interpreted as an intrinsic property of the copper chains.

In a subsequent work Feyerherm et al. [54] improved the analysis of the low-temperature susceptibility and applied the staggered AFHC model by Oshikawa and Affleck [40] to their data. This way, they obtained a quantitative description of their experimental results for $\chi(T)$ in terms of the effect by the staggered field h_s, resulting from the staggered g-tensor and the alternating DM interaction in CuPM.

Figure 28(a) shows the susceptibility data for CuPM for two different magnetic field orientations close to the magnetic principal axes a'' and c'' in the ac-plane. The solid lines are fits to the sum of the uniform susceptibility $\chi_u(T)$ given by Eq. 17 and the longitudinal component of the staggered susceptibility $\chi_{s||} = (cg)^2\chi_s(T) = C_s/T$. Note, that a logarithmic correction for $T \ll J/k_B$ has been neglected in this approach (see sec. 2.3.1). While $\chi_{s||}(T)$ is most pronounced in the direction $\alpha' = 39°$, it vanishes almost completely in the perpendicular direction $\alpha' = 129$ °. The staggered coefficient C_S derived from the susceptibility data for various field directions is depicted in Fig. 28(b). Whereas the maximum of $C_s(\alpha')$ is located at $\alpha' = 34°$, corresponding to the c'' direction, the minimum is observed at $\alpha' = 124°$, *i.e.*, the a'' direction. The small deviation of C_s from zero for a'' has been attributed to be an artefact resulting from an inaccurate description of the actual case of zero staggered field by Eq. 17 due to the difference between the susceptibility for the uniform $S = 1/2$ AFHC and the uniform susceptibility component χ_u for the staggered S =1/2 AFHC (for details see section 2.3.1). It is not clear how strong the C_s values for the other orientations are affected, but the corresponding systematic error is presumably smaller [54].

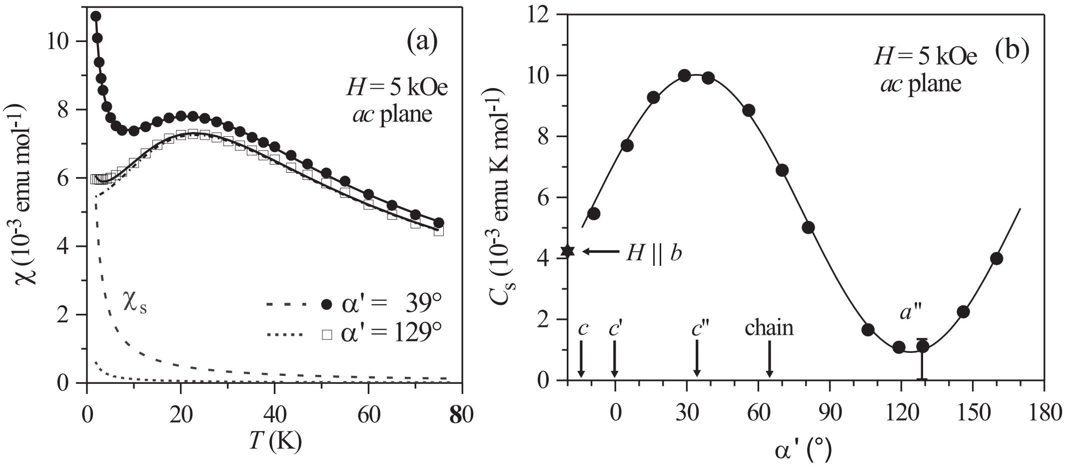

Figure 28: *(a) The temperature dependent susceptibility $\chi(T)$ of CuPM for two orientations in the ac-plane. The solid lines are fits of the data to the model by Oshikawa and Affleck [39, 40]. The dashed lines represent the longitudinal component of the staggered susceptibility $\chi_{s||}(T) = C_s/T$ as obtained from the fits for both orientations. For $\alpha' = 129°$ the behavior assuming $\chi_{s||}(T) = 0$ is marked as a dash-dotted line. (b) Angular dependence of the staggered coefficient C_s in the ac-plane obtained from fits to $\chi(T) = \chi_u(T) + C_s/T$ for various field directions. The solid line is a fit to a $(\cos(\alpha'))^2$ angular dependence. The error bar refers to a possible systematic error (see text). The figure is taken from Ref. [54].*

From a comparison of C_s obtained from the fits and $(cg)^2\chi_s(T)$, using the expression for $\chi_s(T)$ with a logarithmic correction factor of $\ln^{1/2}(J/k_BT)$ from Eq. 37, Feyerherm et al. [54] determined the ratio $c = h_s/H$ for the magnetically principle directions b and c'' to $c_b = 0.152$ and $c_{c''} = 0.235$. For the definition $c = h_s/(gH)$ used in the present work, these values translate into $c_b = 0.071$ and $c_{c''} = 0.106$. They agree to within 20% with the c values obtained from specific heat data along the b and c'' directions [54], $c_b = 0.085$ and $c_{c''} = 0.128$, respectively (see below). The variance has been attributed to the uncertainty of the magnitude of the logarithmic corrections for the two different experiments. From the experimental values for c from the susceptibility data the DM vector **D** has been resolved. Since neighboring Cu ions are symmetry related by a rotation about the twofold axis parallel to b, bisecting the connecting line between neighboring Cu ions, **D** must lie in the ac-plane and alternate along the chain. Feyerherm et al. [54] obtained

$$\mathbf{D} = 0.139J(-0.4115, 0.0, 0.9114) \tag{113}$$

in the $a'bc'$ coordinate frame. The orientation of **D** is approximately perpendicular to the copper chain direction, which is in perfect agreement with the rules by Moriya [78].

The field dependence of the staggered susceptibility has been studied for various magnetic fields in the range of $0.005\ \mathrm{T} \leq \mu_0 H \leq 9\ \mathrm{T}$, with the external field approximately parallel to the c'' direction [54]. Whereas the $\chi(T)$ curves for 0.005 T and 0.5 T show no variation due to the different applied fields, magnetic fields of 5 T and 9 T strongly reduce the upturn of the susceptibility at low temperatures (Fig. 29). Here, the staggered susceptibility is reduced by about 25% for $\mu_0 H = 5$ T and by almost 50% for $\mu_0 H = 9$ T. Feyerherm et al. [54] associated this effect with the saturation of the staggered magnetization.

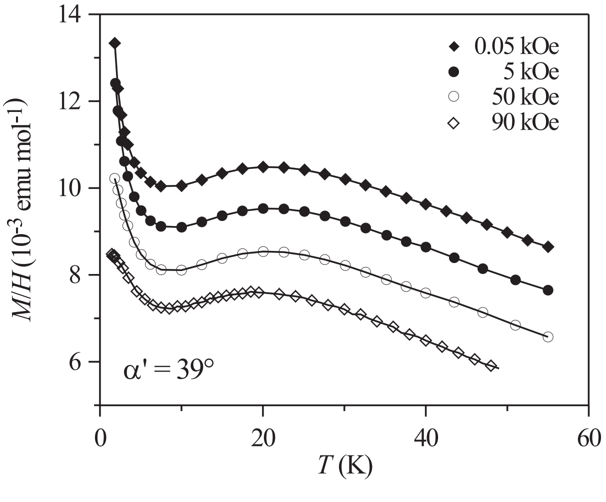

Figure 29: *The temperature dependence of the susceptibility of CuPM for H approximately parallel to the c'' direction and for different magnetic field values. Note, that the curves for $\mu_0 H$ = 0.005 T, 0.5 T and 5 T are shifted upwards by a factor 10^{-3}, 2×10^{-3} and 3×10^{-3} emu/mole. The solid lines are guides to the eye. This figure is taken from Ref. [54].*

The temperature dependence of the electronic specific heat coefficient $C(T)/T$ of CuPM has also been determined by Feyerherm et al. [54] for different values and orientations of the external magnetic field and is depicted in Fig. 30(a) and (b). Obviously, the zero-field electronic specific heat coefficient $C(T)/T$ is perfectly described by the sum of a constant term for the uniform $S = 1/2$ antiferromagnetic Heisenberg chain, as discussed in section 2.2.1, and a term proportional to T^2 from the thermal excitation of lattice vibrations, which mainly contribute at higher temperatures. Remarkably, the specific heat data by Feyerherm et al. [54] showed no indications for three-dimensional long-range ordering down to 0.38 K. From this observation an upper limit of the interchain interaction J' in CuPM can be estimated using the relation [137]

$$J'/k_B = \frac{T_N}{1.28\sqrt{\ln(5.8J/(k_B T_N))}}, \tag{114}$$

which results in $J'/k_B < 0.36$ K, indicating that the interchain interactions J'/k_B is at least two orders of magnitude smaller than the intrachain coupling constant J/k_B.

In the presence of an external magnetic field the low-temperature behavior of the specific heat $C(T)$ changes dramatically from a T-linear to an exponential one, revealing the existence of a magnetic field-induced spin excitation gap Δ [54] as predicted by the staggered $S = 1/2$ AFHC model by Oshikawa and Affleck [39, 40]. This is shown in Figs. 30(a) and (b), where the electronic specific heat coefficient $C(T)/T$ exhibits a broad peak at temperatures $k_BT \approx 0.4\ \Delta$, and a sharp exponential decrease due to the gap below $k_BT \approx 0.3\ \Delta$ for $H > 0$. For temperatures $k_BT > \Delta$ the electronic specific heat coefficient approaches the uniform chain behavior asymptotically. As expected from the angular dependence of the staggered susceptibility, the field-induced gap does not only depend on the magnitude of the external magnetic field (Figs. 30(a), (c)) but is also strongly dependent of the field orientation (Figs. 30(b), (d)).

Feyerherm et al. [54] described their specific heat data by a fit to the numerical solution for $C(T)$ in the sine-Gordon model (Eq. 31) and obtained the soliton gap values Δ_S for the corresponding external fields of 3, 5, 7 and 9 T for $H \parallel a''$-5°, a', c' and c'', respectively. Their results are depicted in Fig. 30(c), where the solid lines represent fits to the equation $\Delta_S = aH^{2/3}$. This way, they verified the predicted scaling of the gap with the external field as $\Delta_S \propto H^{2/3}$ in copper pyrimidine dinitrate. Their maximum field-induced soliton gap has been determined to $\Delta_S/k_B = 9.1$ K in a field of 9 T parallel to the c'' direction. For $H \parallel a''$, however, Eq. 31 does not describe the data appropriately. Here, the gap is so small that the activated behavior cannot be observed experimentally. Feyerherm et al. [54] associate the observed residual gap to a small misalignment error, which due to the steep angular dependence close to the minimum (see Fig. 30(d)) would already lead to a measured gap of about 10% of the maximum value.

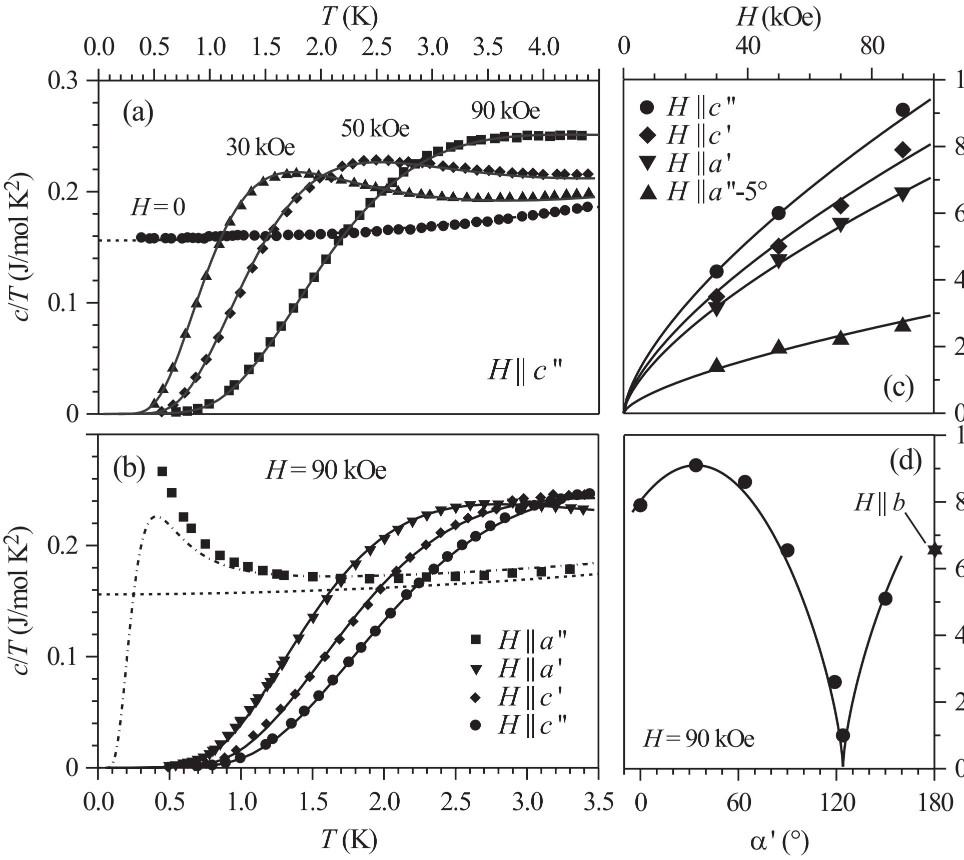

Figure 30: *(a) The temperature dependence of the electronic specific heat coefficient $C(T)/T$ of CuPM for different values of the external magnetic field $H \parallel c''$. (b) Temperature dependence of $C(T)/T$ for an applied field of $\mu_0 H = 9$ T and different field orientations. The solid lines in (a) and (b) are fits to the uniform and staggered $S = 1/2$ AFHC model for zero and nonzero external field, respectively, as described in the text. The dash-dotted line in (b) for $H \parallel a''$ is a calculation for $\Delta_S = 1$ K. (c) Field dependence of the soliton gap Δ_S determined from the fits shown in (a) and (b). The solid lines are fits $\propto H^{2/3}$. (d) Angular dependence of the soliton gap in the ac-plane for an external magnetic field $\mu_0 H = 9$ T. The solid line is a fit to the expected $(\cos(\alpha'))^{2/3}$ angular dependence. This figure is taken from Ref. [54].*

4.2 Copper Benzoate $Cu(C_6H_5COO)_2 \cdot 3H_2O$

4.2.1 Crystallographic Structure of Copper Benzoate

The crystallographic structure of copper benzoate was first determined by Koizumi et al. [138]. This compound crystallizes in a monoclinic structure, space group $I2/c$, with four formula units per unit cell. The lattice constants are $a = 6.98$ Å, $b = 34.12$ Å, $c = 6.30$ Å and $\beta = 89.5°$ at room temperature. The unit cell parameter b is so large that one may neglect the exchange coupling between the ac-planes. The crystallographic structure of copper benzoate is shown in Fig. 31. As is easily seen from the figure, a strong superexchange interaction can be expected between copper spins along the c-axis, whereas exchange interactions along the a-axis via the path Cu-H_2O-H_2O-Cu may be negligible as compared with the coupling along the chain. A schematic picture of the relevant exchange pathway is also illustrated in Fig. 32(a).

The Cu coordination is a distorted octahedron, consisting of four oxygen atoms from water molecules and two oxygen atoms from benzoate groups (Fig. 32(a), (c)). The octahedra are linked, by sharing two oxygen atoms from water molecules, into a column parallel to the c-axis. In this tetragonal local symmetry, the local principal axis of neighboring octahedra is tilted out of the ac-plane by $\sim \pm 10\,°$, resulting in two inequivalent tetragonal axes I and II as shown in Fig. 32(b). Since axes I and II coincide with the g-tensor's principal axis, for a pair of Cu nearest neighbors the local g-tensors are staggered. The resultant principal axis for the anisotropic exchange interaction is c', the perpendicular bisector of axes I and II, where c' is defined as in Fig. 32(b) and a' is chosen to be perpendicular to b and c'. Further, the DM interaction is roughly of the same order of magnitude, with its principal axis essentially parallel to the c-axis. Combining these two types of contributions to the nearest neighbor spin-spin interaction, one obtains a principle axis which approximately bisects c' and c, and is denoted c'' (Fig. 33). In this coordinate system $a''bc''$, with a'' being perpendicular to b and c'', the g-tensor of copper benzoate takes the form [40]

$$\overleftrightarrow{g} = \begin{pmatrix} 2.115 & \pm 0.0190 & 0.0906 \\ \pm 0.0190 & 2.059 & \pm 0.0495 \\ 0.0906 & \pm 0.0495 & 2.316 \end{pmatrix} = \overleftrightarrow{g}_u \pm \overleftrightarrow{g}_s, \tag{115}$$

with ± referring to the two inequivalent Cu sites. The effective g-value for an arbitrary field direction is given by $g = |\overleftrightarrow{g} \cdot \mathbf{H}|/|\mathbf{H}|$. $\overleftrightarrow{g}_u$ and $\overleftrightarrow{g}_s$ denote the uniform and staggered parts of the g-tensor, respectively. Whereas the staggered component produces an effective staggered field $\pm\overleftrightarrow{g}_s \cdot \mathbf{H}$, the uniform part produces an effective uniform field $\overleftrightarrow{g}_u \cdot \mathbf{H}$. In the special case of $\mathbf{H} \,||\, b$ or $\mathbf{H}$ in the $a''c''$-plane, the effective staggered field is perpendicular to both the applied field $\mathbf{H}$ and to the uniform field $\overleftrightarrow{g}_u \cdot \mathbf{H}$. For general directions of the external field they are almost perpendicular (to within a few %).

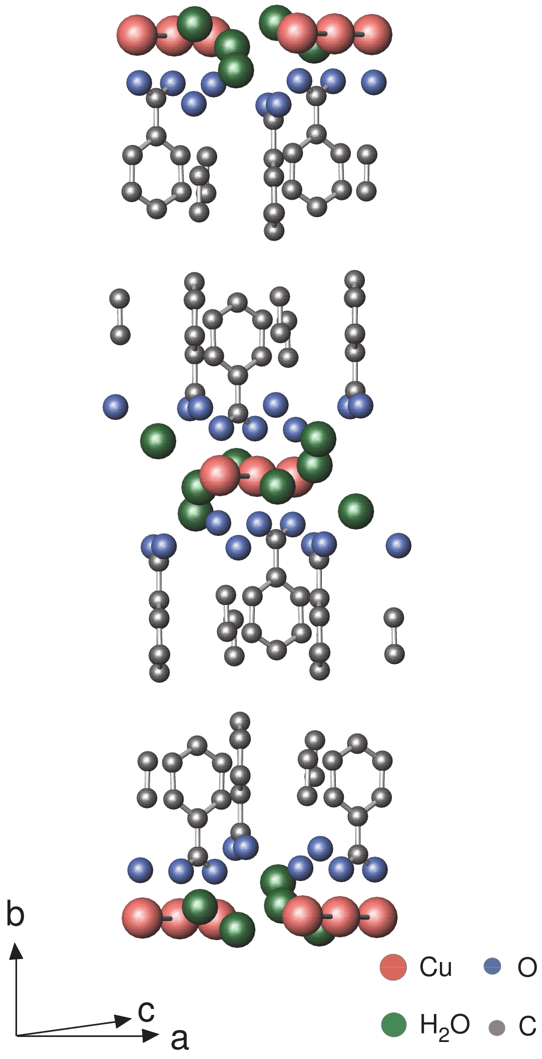

Figure 31: *The crystallographic structure of copper benzoate* $Cu(C_6H_5COO)_2{\cdot}3H_2O$*. Note that the protons on the benzoate groups are not shown for simplicity.*

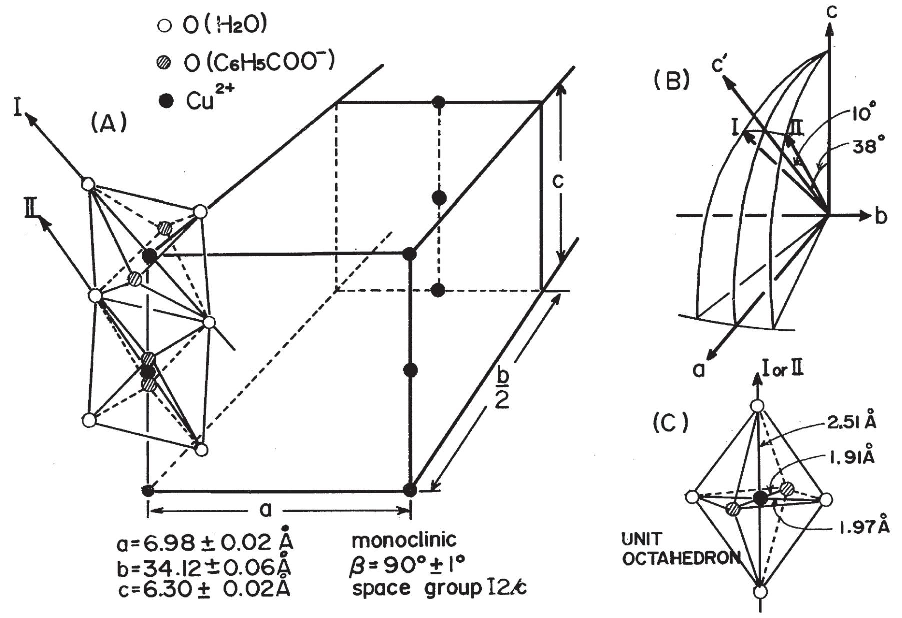

Figure 32: *(a) Schematic view of the crystallographic structure of copper benzoate* $Cu(C_6H_5COO)_2{\cdot}3H_2O$*. (b) The two inequivalent principal axes I and II of the Cu* $^{2+}$ *local symmetry. (c) A copper ion in local tetragonal symmetry. This figure is taken from Ref. [139].*

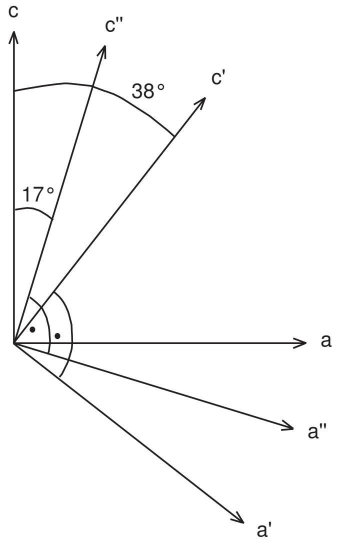

Figure 33: *Local principle axes* a'' *and* c'' *of the combined magnetic interactions in copper benzoate, shown in the ac-plane.*

4.2.2 Magnetic Properties of Copper Benzoate

The magnetic susceptibility of copper benzoate was first measured with the external magnetic field applied along the crystallographic axes a, b and c by Date et al. [140]. The experimental results were compared with the magnetic susceptibility of the uniform $S = 1/2$ antiferromagnetic Heisenberg chain calculated by Bonner and Fisher [80], yielding a very good agreement for temperatures $T > 8$ K and an exchange coupling constant along the chain $J/k_B = 17.2 \pm 2.0$ K. Unexpectedly by that time, a deviation from the Bonner Fisher theory was observed for all three crystallographic directions below ~ 8 K. In this temperature region the observed susceptibility is larger than the theoretically predicted value and increases with decreasing temperature. Since the upturn varies strongly with the external field direction, it cannot be attributed to magnetic impurities but has to be intrinsic[9]. Additional Knight shift investigations by proton NMR [140] confirmed both the broad maximum of $\chi(T)$ at 12.5 ± 1.0 K ≈ 0.640851 J/k_B, which is typical for a $S = 1/2$ AFHC, and the Curie-like upturn at low temperatures. However, an interesting quantitative disagreement between the static and NMR susceptibilities appeared below 8 K in particular in the case of $H \parallel c$. While the NMR susceptibility increases quickly with decreasing temperature, the corresponding static susceptibility varies rather slowly with T. The origin of the Curie-like upturn as well as the discrepancy between the static and NMR susceptibilities at low temperature were not clear by that time.

In 1996 Dender et al. [36] confirmed the anisotropic temperature dependence of the susceptibility of copper benzoate. Whereas their data for $H \parallel a$ can be described by a fit of the uniform $S = 1/2$ antiferromagnetic Heisenberg chain, the low temperature upturn was verified along the other two crystallographic axes b and c. In addition, they found a ferromagnetic contribution to the susceptibility for small fields below $T = 0.8$ K, which is suppressed in larger external fields. This weak ferromagnetic contribution was argued to result from a spin canting in the three-dimensional antiferromagnetic state at very low T, and thus has little consequence for $g\mu_B H/J > 0.1$. The deviations of the *dc* susceptibility from the uniform $S = 1/2$ AFHC behavior for $T < 8$ K and $H \parallel b$, c were explained in context of the remanence of the weak ferromagnetic behavior at low temperatures and low fields. From a fit of the susceptibility data an exchange coupling constant along the chain $J/k_B = 18.2 \pm 0.1$ K has been determined, in agreement with previous results by Date et al. [140].

Whereas specific heat investigations of copper benzoate in zero external field verified the T-linear behavior of a uniform $S = 1/2$ antiferromagnetic Heisenberg chain, such experiments in applied magnetic fields up to 7 T revealed an unexpected field-induced spin excitation gap Δ. The specific heat data by Dender et al. [48] for zero as well as several applied magnetic fields $\parallel b$ are depicted in Fig. 34. For $H \neq 0$, the solid lines are fits to a simple activated

---

[9] The temperature dependent magnetic susceptibility curves $\chi(T)$ for the single crystals of copper benzoate used in this work are shown in section 5.2.

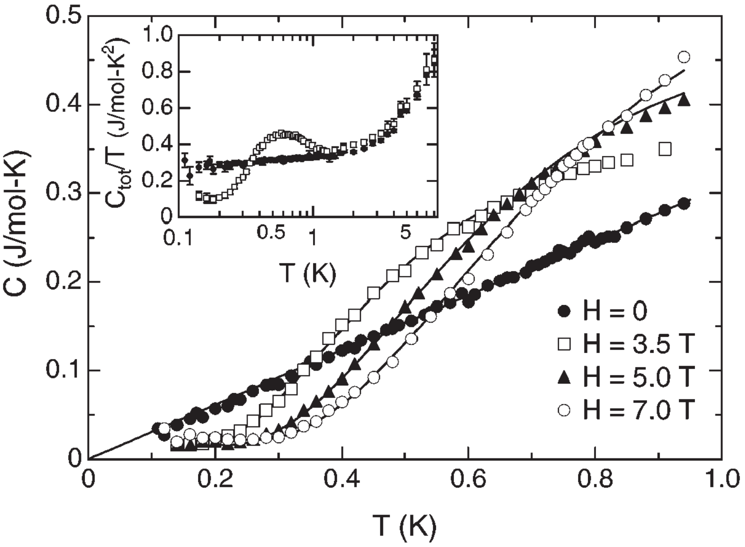

Figure 34: *The temperature dependence of the magnetic specific heat, i.e., the total specific heat after subtraction of phonon contributions, of copper benzoate for zero and applied field H parallel to the crystallographic b-axis. In the inset, the electric specific heat coefficient* $C_{tot}(T)/T$ *for zero external field and* $\mu_0 H$ *= 3.5 T is shown. Solid lines are fits as described in the text. This figure is taken from Ref. [48].*

behavior $\propto (\Delta/k_B T)^{3/2} exp(-\Delta/k_B T)$ (see Eq. 31). Motivated by the field-induced gap in copper benzoate, Oshikawa and Affleck [39, 40] developed their model of the staggered $S = 1/2$ AFHC (see section 2.3), proposing that the primary mechanism of the gap formation is an effective staggered field due to the alternating g-tensor and the DM interaction present in copper benzoate. In the framework of this model, Essler [42] reanalyzed the specific heat data by Dender et al. [48], using the activated behavior of Eq. 31 as fit function for the magnetic specific heat $C(T)$ of copper benzoate. This way, Essler verified the predicted soliton mass gap dependence $\Delta_S \propto H^{2/3}$ for two different crystallographic directions $H \,||\, b$ and c'' (Fig. 35). For $H \,||\, a''$, however, the magnetic specific heat of copper benzoate was found to be nearly linear as predicted for the uniform $S = 1/2$ AFHC, indicating a cancellation of the effective staggered field h_s by the combination of the staggered g-tensor and the DM interaction.

The value and direction of the DM vector have been estimated by Essler [42]. Since neighboring Cu ions are symmetry related by a rotation about the twofold axis parallel to the b-axis bisecting the connecting line between neighboring Cu ions, $\mathbf{D}$ must lie in the ac-plane. Further, it alternates along the chain, which is included in the Hamiltonian (Eq. 27) via $(-1)^i$. Oshikawa and Affleck [40] confirmed the results of Essler [42] and determined the DM vector in copper benzoate to

$$\mathbf{D} = J(0.13, 0.0, 0.02) \tag{116}$$

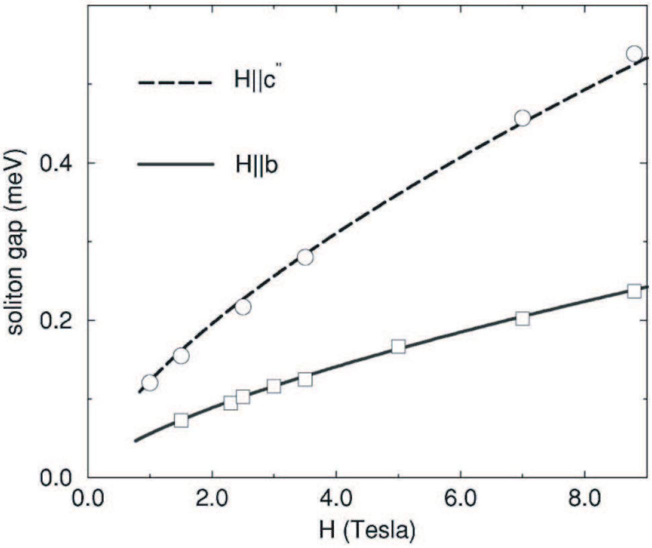

Figure 35: *The field dependence of the soliton mass gap Δ_S in copper benzoate for the applied magnetic field H || b and || c''. The solid lines are fits to the scaling law $\Delta_S \propto (H/J)^{2/3}$, neglecting the logarithmic factor $|ln(J/g\mu_B H)|^{1/6}$. The figure is taken from Ref. [42].*

in the $a''bc''$ coordination system. Hence, **D** lies close to the a''-axis of copper benzoate, which is in perfect agreement with the rules by Moriya [78]. The proportionality constant c between the staggered field h_s and the uniform applied field H, which strongly depends on the external field direction[10], was obtained from the specific heat data for H || c'', $c_{c''}$ = 0.111 [40].

Inelastic neutron scattering experiments on copper benzoate in zero external field [48] revealed a bounded continuum of excited states, as it has been predicted for the uniform S = 1/2 antiferromagnetic Heisenberg chain. The zero-field dynamic spin correlation function for copper benzoate is shown in Fig. 36. The solid lines are the boundaries of the spinon continuum $\epsilon_1(q)$ and $\epsilon_2(q)$ for the uniform $S = 1/2$ AFHC as described in section 2.2.2, using the value $J/k_B = 18.2$ K from susceptibility measurements. Whereas the data are insufficient to identify an upper bound of the continuum, the data clearly show a lower edge following the des Cloiseaux-Pearson boundary $\epsilon_1(q)$ and the existence of a spinon continuum. Inelastic neutron scattering experiments in magnetic fields up to 7 T || b [48], however, provided evidence for a field-induced gap in the excitation spectrum both at commensurate and at incommensurate wave vectors. The lowest breather mass gap Δ_{B1} at $q = \pi$ as well as the soliton mass gap Δ_S at $q = \pi\text{-}2\pi< S_z >$ were extracted for an external field of 7 T, their average value nicely fitting with the value observed from the single-exponential fit of the specific heat data by Dender et al. [48].

---

[10] The additional logarithmic factor $|ln(J/g\mu_B H)|^{1/6}$ as predicted from the SG model (see section 2.3.2) was expected to be close to unity and hence neglected in this approach. Taking into account the logarithmic factor would reduce the extracted c value by 10%.

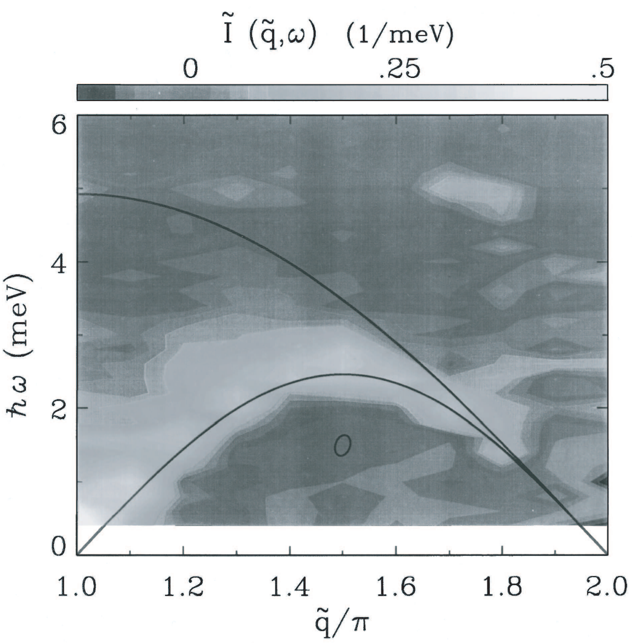

Figure 36: *The zero-field dynamic spin correlation function for the staggered $S = 1/2$ AFHC copper benzoate at T = 1.8 K. The solid lines are boundaries of the spinon continuum as predicted for the uniform $S = 1/2$ antiferromagnetic Heisenberg chain, using a value of J/k_B = 18.2 K. This figure is taken from Ref. [36].*

In contrast to the specific heat and inelastic neutron scattering experiments, no extensive magnetization study of copper benzoate has been performed so far. In 1980 Mollymoto et al. [141] determined the field dependence of the magnetization $M(H)$ at 1.3 K and 4.2 K under pulsed high fields up to 40 T parallel to the crystallographic c-axis. A saturation was found in the high magnetic field region $\mu_0 H > 35$ T, and the estimated g-value, g_c = 2.26, agrees well with the one obtained from ESR (Eq. 115). Using an exchange coupling constant along the chain of $J/k_B = 17.8$ K, Mollymoto et al. [141] determined the saturation field at $T = 0$, $H_{sat} = 2J/(g\mu_B)$, to 26.6 T for $H \parallel c$. A comparison of their experimental data at 4.2 K with theoretical calculations for the isotropic $S = 1/2$ Heisenberg chain at finite temperatures $T \neq 0$ by Inawashiro and Katsura [142] yields a perfect agreement for fields $\mu_0 H < 30$ T. The discrepancy for higher fields was tentatively attributed to magnetic anisotropies including the DM interaction, but has not been considered further at that time.

5 High-Field Magnetization Experiments on Staggered $S = 1/2$ AFHCs

According to the staggered $S = 1/2$ antiferromagnetic Heisenberg chain model by Oshikawa and Affleck [39, 40], the experimentally observable magnetization m_{phys} consists of two different contributions, *i.e.*, the uniform magnetization m_u and the staggered magnetization m_s due to the uniform and induced staggered field, respectively. While the staggered field h_s is practically perpendicular to the external uniform field H, the staggered magnetization m_s is slightly canted against the staggered field, yielding a large staggered magnetization component in the direction of the staggered field, $m_{s\perp}$, and a small one in the direction of the uniform field, $m_{s||} = (cg)\, m_s$.

The staggered component of the magnetization m_s brings about an additional staggered contribution (χ_s) to the susceptibility. Its projection on the uniform field, $\chi_{s||} = (cg)^2\chi_s$, has been observed in four compounds: copper benzoate [36, 140], Yb_4As_3 [56, 126], copper chloride dimethyl sulfoxide [127] and copper pyrimidine dinitrate [54]. In particular in the latter compound the temperature dependence of this longitudinal staggered susceptibility has been studied in detail and has been compared to the predictions of the staggered $S = 1/2$ AFHC model [54]. Here, the behavior of $\chi_{s||} \propto 1/T$ has been verified for low fields and temperatures $T \geq \Delta$.

Recently, Shibata and Ueda [94], Lou et al. [95] and Capraro and Gross [143] extended the model of Oshikawa and Affleck [39, 40] by calculating the high-field magnetization of the staggered $S = 1/2$ AFHC for $0 \leq g\mu_B H/J \leq 2$. Experiments on Yb_4As_3 [125] to obtain the field dependence of the staggered magnetization component $m_{s||}$ in pulsed fields up to 55 T could not be compared to these theoretical predictions, since $m_{s||}$ could not be extracted from the data due to the single-ion CEF excitations of the $J = 7/2$ multiplet of the Yb^{3+} ions. The CEF excitations yield a large Van Vleck-type contribution, which should not saturate up to very high magnetic fields of roughly 400 T. Hence, the absence of an experimental verification of the theoretical predictions for the field dependence of $m_{s||}$ inspired the magnetization study on CuPM and copper benzoate in this thesis.

In this chapter, high-field magnetization experiments will be presented which address the field and temperature dependence of the magnetization of two staggered $S = 1/2$ antiferromagnetic Heisenberg chains. The following section 5.1 deals with the magnetization investigations on $CuPM(NO_3)_2(H_2O)_2$ at temperatures $T = 1.6$ K and 4.2 K, covering the entire field range up to saturation, *i.e.*, $\mu_0 H \simeq 53$ T. Temperature dependent pulsed-field magnetization measurements of $Cu(C_6H_5COO)_2 \cdot 3H_2O$ in the range of $0.09 < k_B T/J < 1.4$ will be given in section 5.2. In contrast to the analysis of CuPM, emphasis will be laid upon the temperature dependence of the staggered magnetization for Cu benzoate.

5.1 Longitudinal Magnetization of $CuPM(NO_3)_2(H_2O)_2$

In section 4.1, $CuPM(NO_3)_2(H_2O)_2$ has been introduced as a staggered antiferromagnetic $S = 1/2$ Heisenberg chain with an exchange parameter $J/k_B = 36$ K along the chain. The field-induced spin excitation gap and the Curie-like staggered contribution to the susceptibility at low temperatures are largest for the same orientation c''. Along a'', the direction perpendicular to c'', the field-induced gap vanishes and the crystal shows the behavior of an ideal, uniform Heisenberg chain. In this chapter, the qualitatively different behavior of the high-field magnetization data of CuPM in the directions of maximum and zero spin excitation gap, *viz.*, along c'' and a'', is revealed. The data are analyzed via exact diagonalization of a linear spin chain with up to 20 sites for $T = 0$ and on basis of the Bethe ansatz equations for finite temperatures, respectively. For both directions a very good agreement between experimental data and theoretical calculations has been found. The characteristic properties, *i.e.*, the magnetic coupling strength along the chain direction J/k_B, the ratio between the staggered and uniform field $c = h_s/(gH)$ and the field dependence of the staggered magnetization $m_s(H)$ have been determined.

5.1.1 Experimental Details

The single crystals of copper pyrimidine dinitrate $CuPM(NO_3)_2(H_2O)_2$ used for the pulsed-field magnetization measurements have been grown by R. Feyerherm from the Hahn-Meitner-Institute in Berlin. The single crystals have been obtained by slow evaporation of the equimolar aqueous solution of copper nitrate and pyrimidine [135]. All the crystals show well-defined facets and the principal crystallographic axes a, b and c can be identified easily. According to Fig. 27, the principal magnetic axes a'' and c'' follow from a rotation of the crystal in the ac-plane by 24° and 48° with respect to the a- and c-axis, respectively. For the high-field magnetization measurements the oriented samples had to be cut along the c-axis to a typical dimension of $1.5 \times 1 \times 2$ mm^3. They were glued to the tip of a plexiglass rod and placed inside a thin walled teflon cylinder. The magnetization signal of the sample holder was negligible.

It was checked by low-field investigations in a commercial SQUID magnetometer that the magnetic susceptibilities of the single crystals matches those published in Ref. [54]. The temperature dependence of the susceptibility $\chi(T)$ of the crystals oriented along the a'' and c'' direction are depicted in Figs. 37(a) and (b), respectively. Fits of the data to the staggered $S = 1/2$ AFHC model with $\chi_{phys} = \chi_u + (cg)^2\chi_s + \chi_{corr}$, using Eq. 17 by Eggert et al. [82] for the uniform susceptibility and $(cg)^2\chi_s = C_s/T$ for the longitudinal staggered susceptibility, yield the staggered coefficient C_s for $H \parallel a''$ and $\parallel c''$. Since neither the susceptibility nor the magnetization data were corrected for sample holder contributions, the corrections had to be accounted for by a small constant term χ_{corr} in the fit. Values of $C_{s,a''} = 0.5$ memu K mole^{-1} and $C_{s,c''} = 11$ memu K mole^{-1} have been obtained, which are in perfect agreement with the values $C_{s,a''} = 1 \pm 1.25$ memu K mole^{-1} and $C_{s,c''} = 10 \pm 1.25$ memu K mole^{-1}

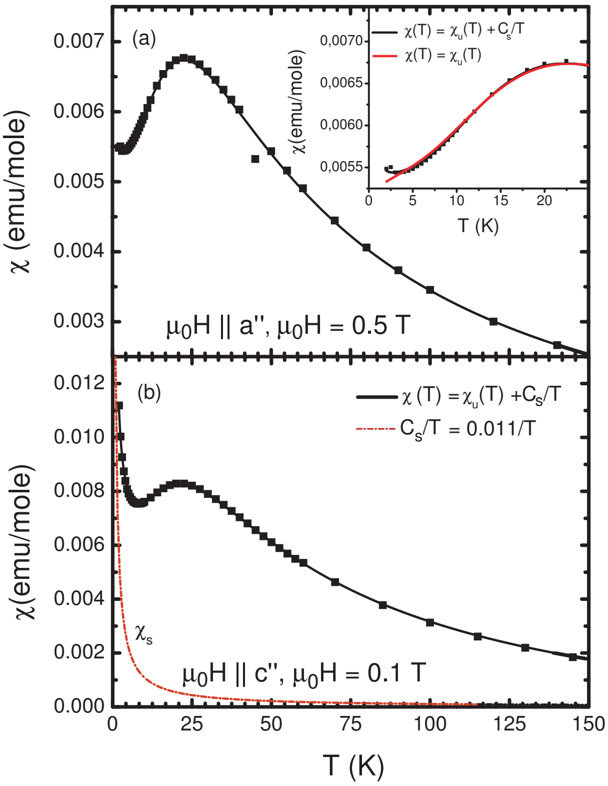

Figure 37: *The temperature dependence of the susceptibility of the single crystals of CuPM used in this work, with the external magnetic field (a) parallel to* a'' *and (b) parallel to* c''*. The solid lines are fits to the staggered* $S = 1/2$ *AFHC model. The red dash-dotted line in (b) represents the longitudinal staggered susceptibility component* $\chi_{s||} = C_s/T$ *obtained from the fit. In the inset of (a) the low temperature regime* $T \leq 30$ *K is shown, indicating a maximum misorientation of the sample by ± 5°.*

from Ref. [54]. Hence, the maximal misalignment of the samples with respect to the magnetically principal axes a'' and c'' is estimated to be less than ± 5°.

Magnetization measurements of CuPM in a SQUID magnetometer in fields up to 5 T reveal a magnetization linear in field along the direction of ideal Heisenberg behavior (Fig. 38(a)), whereas a slight curvature of $m(\mu_0 H)$ is seen in the gapped regime along c'' for lowest temperatures (Fig. 38(b)).

High-field magnetization investigations were carried out at the Laboratoire National des Champs Magnétiques Pulsés in Toulouse in pulsed magnetic fields up to $\mu_0 H = 53$ T with experimental support by H. Rakoto and M. Costes. Pulsed fields were obtained by discharging a capacitor bank in a solenoid according to a crowbar (see section 3.2.3). For the 53 T experiments the pulse duration was about 200 ms, with an increasing time of 25 ms, while it was about 1.2 s, with an increasing time of 90 ms for the 40 T equipment. The magnetization was detected as a voltage V induced in a compensated arrangement of pick-up coils wound concentrically around the sample and coupled to it with the coupling constant η, such that $V = \eta\Omega\partial M/\partial t$ (Ω: sample volume). The absolute magnetization was obtained by a numeri-

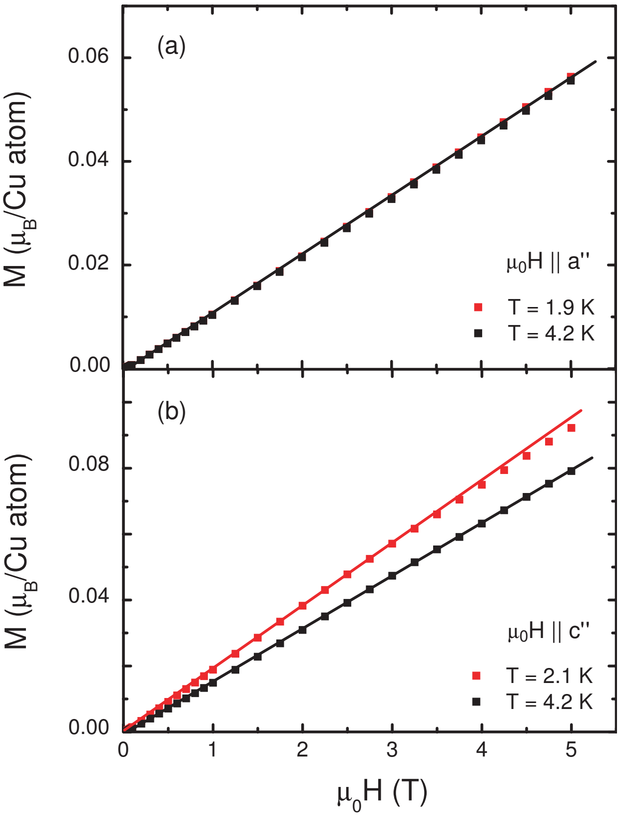

Figure 38: *The field dependence of the magnetization of the single crystals of CuPM used in this work, oriented along the a'' (a) and c'' direction (b) for temperatures of 1.9 K/2.1 K and 4.2 K. The solid lines are guides to the eye.*

cal integration of the voltage V. Measurements were made for increasing and decreasing field. No hysteresis has been observed. For clarity, because of a higher signal-to-noise ratio, only data taken for decreasing field will be presented here.

Due to the limited sample space, with a diameter < 1.6 mm, the weight of the sample (≈ 3 mg), and thus the absolute signal was small ($< 10^{-5}$ Am^2). Further, a remaining imperfect compensation of the pick-up coils brought about the necessity of a repetition of the magnetization measurements without sample after each "shot", in order to correct the signal for the small residual background. But with the pick-up system being very sensitive to a displacement of the sample from the center of the pick-up coils as described in section 3.2.2, each (un)mounting of the sample holder may cause small variations of the absolute signal. Hence, to achieve a higher accuracy of the signal calibration, the high-field data have been calibrated by the additional magnetization measurements in a SQUID magnetometer in fields up to 5 T. Note, that the low-field data for the calibration at $T = 1.6$ K are obtained from an extrapolation of fits to additional susceptibility data at various fields in the range of 0.1 T $\leq \mu_0 H \leq 5$ T and temperatures 1.8 K - 30 K (not shown). This way, the susceptibility at $T = 1.6$ K was obtained for different external fields between 0.1 T and 5 T and for both constellations $H \parallel c''$ and $\parallel a''$. Then, the magnetization curve at $T = 1.6$ K was derived from these extrapolated susceptibility data as $m \simeq \chi H$.

5.1.2 Results and Discussion

The magnetization curve of CuPM$(NO_3)_2(H_2O)_2$ as function of field at 1.6 and 4.2 K is presented in Fig. 39 for the two characteristic orientations, *i.e.*, $H||a''$ (Fig. 39(a)) and $||c''$ (Fig. 39(b)), respectively. Comparing the magnetization along the two directions, an anisotropic response is observed. At $T = 1.6$ K and for $H||a''$ the archetypal behavior of the uniform $S = 1/2$ AFHC is found [35, 80, 85, 86]. In contrast, for fields parallel to the c''-axis an additional low-field contribution and a delayed saturation of the magnetization occurs. To emphasize this difference the derivatives of the magnetization, $dM/d(\mu_0 H)$, are plotted in the insets of Figs. 39(a) and (b) for $T = 1.6$ K. For small fields $||c''$ the initial slope is more than twice as large as for the a''-axis. At high fields (> 35 T), the saturation of the magnetization for $H||c''$ is suppressed compared to the a''-axis response, as it is indicated by a smaller, broader feature in $dM/d(\mu_0 H)$. Increasing the temperature to $T = 4.2$ K reduces the difference in the $M(\mu_0 H)$ curves between the two directions, but does not completely suppress it.

The deviation from the uniform $S = 1/2$ AFHC behavior along the c'' direction is attributed to an additional magnetization component. It increases much faster and passes through a maximum at a lower field than the uniform saturation field $\mu_0 H_{sat}$. Since the second component is not present along a'', it is ascribed to the longitudinal component of the staggered magnetization $m_{s||}$.

The g-tensor of CuPM has been derived from ESR measurements [54] and is given in Eq. 112. In the uniform $S = 1/2$ AFHC model the saturation field is calculated according to the formula $H_{sat} = 4JS/g\mu_B$. For zero temperature, and using $J/k_B = 36 \pm 0.5\,\mathrm{K}$, $g_{a''} = 2.14 \pm 0.02$ and $g_{c''} = 2.21 \pm 0.02$ from Ref. [54], the following values for the saturation field along a'' and c'' have been calculated to $\mu_0 H_{sat} = 50.1 \pm 0.8\,\mathrm{T}$ and $48.5 \pm 0.8\,\mathrm{T}$, respectively. The saturation magnetization m_{sat} is calculated to $m_{sat,a''} = 1.07 \pm 0.01\,\mu_B$/Cu atom and $m_{sat,c''} = 1.11 \pm 0.01\,\mu_B$/Cu atom. Thus, for the uniform $S = 1/2$ AFHC at $T = 1.6$ K $\ll J/k_B$ the saturation magnetization should be approached at highest experimental applied field. Indeed, for $H||a''$ (Fig. 39(a)) the $T = 1.6$ K curve has an initial slope lower than at $T = 4.2$ K. With increasing field the curvature becomes larger, crosses the 4.2 K curve near $\mu_0 H = 38$ T and almost reaches saturation at ≈ 53 T. The data for both temperatures become nonlinear with field for $\mu_0 H > 15$ T. Moreover, with decreasing temperature the data sets approach the $T = 0$ curve for the uniform $S = 1/2$ AFHC, in full agreement with previous experimental work [35].

From a theoretical point of view, the magnetization curve of the uniform $S = 1/2$ AFHC has been computed for $T = 0$ by the Bethe ansatz [81]. However, the measurements have been carried out at temperatures $T > 0.04 J/k_B$, where thermal fluctuations lead to a substantial

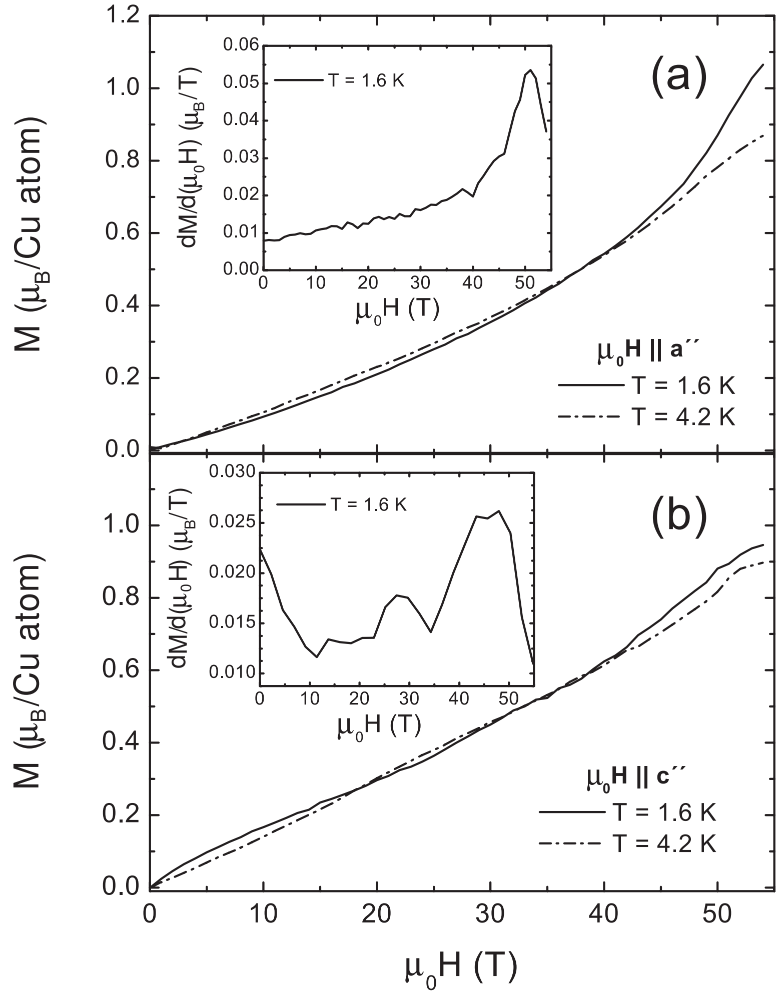

Figure 39: *The field dependence of the magnetization of CuPM(NO$_3$)$_2$(H$_2$O)$_2$, with the external field aligned along the a'' (a) and the c'' direction (b). In the insets the field derivative $dM/d(\mu_0 H)$ is displayed.*

rounding of the cusp at the saturation field in the $T = 0$ magnetization curve. On the other hand, at 1.6 K one has $T < 0.05J/k_B$, substantially smaller than the lowest corresponding temperature studied in Ref. [35] for copper pyrazine dinitrate. Even at $T = 0.05J/k_B$, the magnetization curve computed for the uniform $S = 1/2$ AFHC on a ring with N=16 sites still exhibits clear finite-size effects (not shown), precluding an analysis along the lines of Ref. [35]. Therefore results obtained by the thermodynamic Bethe ansatz in the thermodynamic limit $N = \infty$ and at arbitrary temperature T are used to describe the magnetization curve for $H \parallel a''$ [85]. These calculations have been carried out by A. Klümper from the Physics Department, University Wuppertal.

The situation for $H \parallel c''$ is quite different. On the one hand, the Hamiltonian in Eq. 27 cannot be solved exactly with a non-zero staggered field h_s and therefore one has to rely on a numerical treatment. Whereas the z-component S^z of the total spin is conserved for

h_s=0, even this is not the case anymore for $h_s \neq 0$. This has two consequences: (*i*) The reduced symmetry of the Hamiltonian (27) restricts the system size N that can be accessed, and (*ii*) each new set of magnetic fields H and h_s requires a new numerical determination of the ground state. On the other hand, the field-induced opening of a gap [39, 40] leads to the following two simplifications: (*i*) For the high magnetic fields studied here, the gap is sufficiently large to suppress thermal excitations at low temperatures. Therefore, finite temperature is expected to have only a comparatively small effect. Indeed, this is confirmed by the difference of the $T = 1.6\,\mathrm{K}$ and $4.2\,\mathrm{K}$ curves in Figs. 39(a) and (b) which is noticeably smaller along the c'' direction than for the a'' one. This permits to compare a measurement at low but finite T (here 1.6 K) with a computation at $T = 0$. (*ii*) In most field ranges considered here, the correlation length turns out to be sufficiently short such that finite-size effects can be neglected already for systems with only $N = 20$ sites. More precisely, the correlation length is large only for a small staggered field h_s and thus only the low-field region suffers from finite-size effects. These lead to an artificial low-field peak in the staggered magnetization m_s (see *e.g.* dashed curve in Fig. 40(b)) whose position roughly determines the region up to which finite-size effects are still relevant, as evidenced by a comparison with results for $N \leq 16$. Due to the fast disappearance of finite-size effects for higher magnetic fields, it is completely sufficient for this purpose to apply the Lanczos diagonalization procedure to rings with $N \leq 20$ sites. Therefore, the additional effort of a density matrix renormalization group procedure (DMRG) [94, 95, 123, 143] is not necessary here. The calculations for $H \parallel c''$ on basis of the staggered $S = 1/2$ AFHC model have been performed by A. Honecker from the Institute of Theoretical Physics, TU Braunschweig.

A final remark is in order before the numerical results are presented and compared with the experiment. According to Eq. 34, in the presence of a staggered field h_s the physical magnetization m_{phys} is given by the superposition of the uniform and longitudinal staggered magnetization components: $m_{phys} = m_u + (cg)\, m_s$. While previous numerical works [94, 95, 123, 143] only showed m_u and m_s separately, numerical results for the combination m_{phys} had not been published. During this study on CuPM, Asano et al. [144] reported on high-field magnetization experiments on CuPM for the arbitrary orientation $\mu_0 H \parallel c$ at $T =$ 1.3 K, prohibiting a detailed analysis. While their data also show distinct deviations from the uniform $S = 1/2$ antiferromagnetic Heisenberg chain behavior due to the effect of the staggered field, no quantitative analysis of their experimental data on basis of the staggered $S = 1/2$ AFHC model has been performed.

For the magnetization along a'' (Fig. 40(a)), using $\mu_0 H_{sat} = 50.6\,\mathrm{T}$, $g_{a''} = 2.14$, and taking into account the finite experimental temperature, a very good agreement between the experimental data and the Bethe ansatz result is found [85]. The deviations for fields $\mu_0 H > 50$ T can be attributed to the misalignment of the crystal, while for smaller fields experimental data and calculated result match within 2 %. Thus, for this field direction the uniform $S = 1/2$ AFHC is established.

Fig. 40(b) depicts the field dependence of the magnetization along c''. For fields $\mu_0 H > 10\,\mathrm{T}$

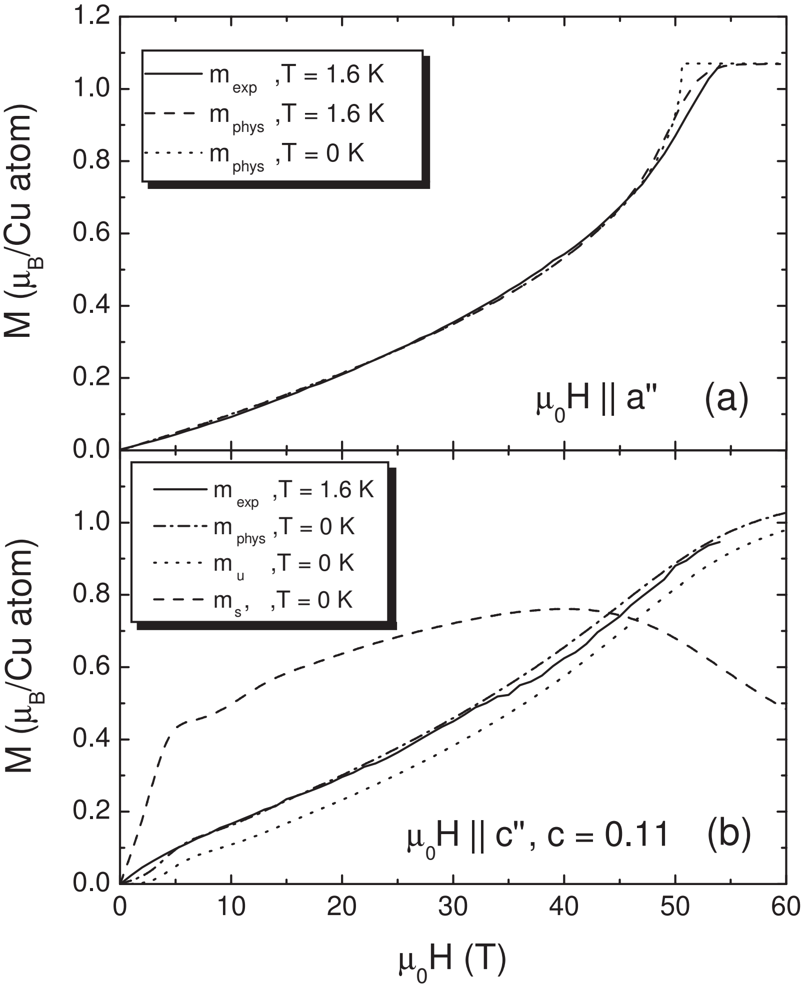

Figure 40: *Experimental and theoretical magnetization curves for CuPM$(NO_3)_2(H_2O)_2$ at $T = 1.6$ K for different field directions. (a) $\mu_0 H || a''$: solid line - experimental data, dashed line - fit assuming uniform $S = 1/2$ AFHC behavior for $T = 1.6\,K$, dotted line - $T = 0$ calculations. (b) $\mu_0 H || c''$: solid line - experimental data, dash-dotted line - calculated physical magnetization m_{phys} for $c = 0.11$, dotted line - uniform magnetization m_u, dashed line - staggered magnetization m_s.*

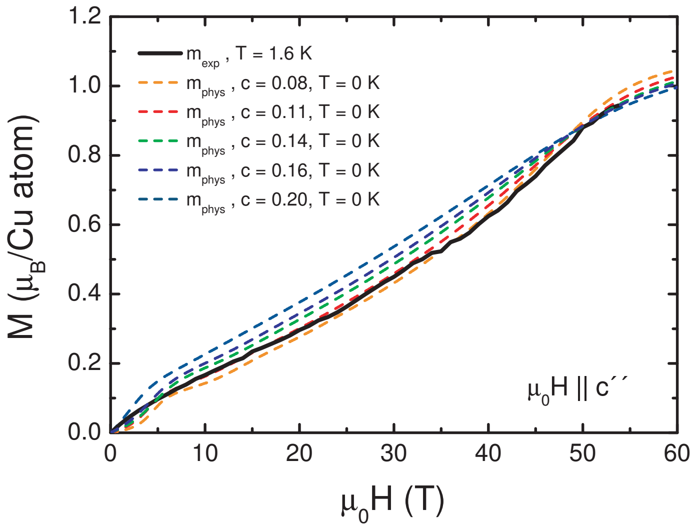

Figure 41: *Experimental and theoretical magnetization curves of $CuPM(NO_3)_2(H_2O)_2$ for the external field $\mu_0 H \parallel c''$ and different anisotropy parameters $c = h_s/(gH)$. The numerical calculations have been performed by A. Honecker from the Institute for Theoretical Physics, TU Braunschweig. Note that the calculations for c = 0.14 and 0.16 have been performed for N = 16 sites.*

these data are fully described by the calculations on basis of the staggered $S = 1/2$ AFHC model, using $\mu_0 H_{sat} = 49.3\,\mathrm{T}$, $g_{c''} = 2.19$ and an anisotropy parameter $c = 0.11$. This value has been obtained from a comparison of the data and calculations for $c \in [0.08;0.12]$, step size 0.01, as the optimum solution. The values $\mu_0 H_{sat}$ along a'' and c'' are fully consistent within their error bars with those predicted from the formula above: $H_{sat} = 4JS/g\mu_B$. On average, the saturation fields $\parallel c''$ and $\parallel a''$ correspond to a magnetic coupling strength J/k_B = 36.3(5) K.

With the value of the anisotropy parameter c according to Eq. 34, the physical magnetization m_{phys} can be decomposed into the uniform (m_u) and staggered (m_s) component. Both m_u and m_s are included in Fig. 40(b). Their field dependence closely resembles the ones obtained in Ref. [95] for the case $h_s = 0.1\,gH$. Specifically, the data show that m_s traverses a maximum at $\sim 40\,\mathrm{T}$, while m_u and m_s approach finite but nonsaturated values for largest fields. This way, the high-field magnetization analysis establishes the staggered $S = 1/2$ AFHC for the c''-axis of $CuPM(NO_3)_2(H_2O)_2$.

Further, calculations for c-values in the range 0.08 - 0.28 have been performed by A. Honecker. The cases $c =$ 0.08, 0.11, 0.14, 0.16 and 0.2 are depicted in Fig. 41. From these data it appears that for decreasing parameter c the curvature of m_{phys} increases and approaches the uniform $S = 1/2$ AFHC magnetization behavior for vanishing staggered field h_s, as expected. With the slightly different definition of the c-value in Ref. [54], $c = h_s/H$, the anisotropy parameter $c = 0.11$ from this work translates into a value 0.24. Thus, a perfect

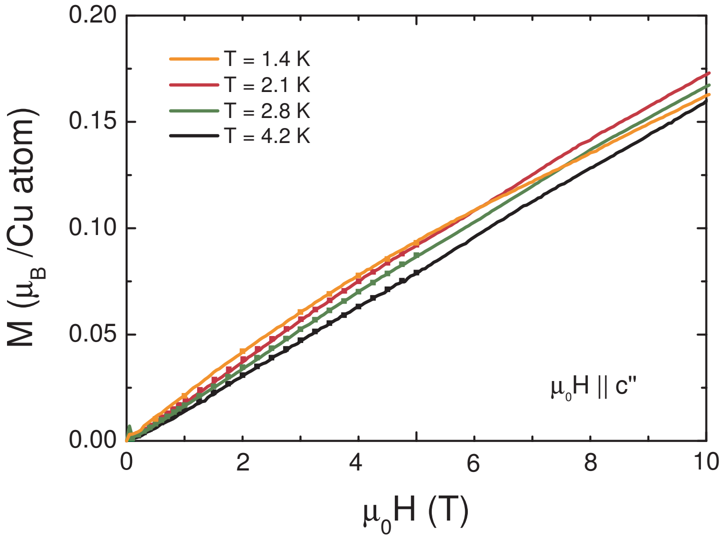

Figure 42: *The temperature dependent magnetization curves of CuPM(NO_3)$_2$(H_2O)$_2$ for the external field $\mu_0 H \parallel c''$. The solid lines represent the magnetization data for $0 \leq \mu_0 H \leq$ 10 T obtained in pulsed fields up to 35 T, while the data points are the SQUID results for fields up to 5 T.*

agreement of the c-value from high-field magnetization with the one obtained from magnetic susceptibility measurements in Ref. [54], *i.e.*, $c = 0.235$, is found. In contrast, a discrepancy with the value recently obtained from ESR investigations by Zvyagin et al. [52], $c = h_s/(gH)$ $= 0.08$, is noticed, but whose origin is not clear at present.

5.1.3 Conclusions and Outlook

In conclusion, high-field magnetization experiments on CuPM(NO_3)$_2$(H_2O)$_2$ have been performed at temperatures $T = 1.6$ and 4.2 K and the external field H parallel to the principal directions a'' and c''. With this study of the magnetization along a'' and c'' the contrasting behavior along the two directions has been established, the first representing the uniform and the latter the staggered $S = 1/2$ antiferromagnetic Heisenberg chain. The behavior of the uniform $S = 1/2$ AFHC has been evaluated on basis of the Bethe ansatz equations [85, 86]. In contrast, for the staggered $S = 1/2$ AFHC the data has been analyzed by means of exact diagonalization of linear chains with up to $N = 20$ spins for $T = 0$, based upon the staggered field theory by Oshikawa and Affleck [39, 40].

Comparing the finite-size calculations to previous density matrix renormalization group studies [94, 95, 123, 143] for the Hamiltonian (27), a perfect agreement between the results shown in this work and those of other groups has been found. Only for low fields finite-size effects are present. The advantage of finite-size calculations compared to the DMRG method lies in its simplicity and short computation time. The very good agreement between the experimental data and the theoretical calculations verifies the predictions for the uniform and staggered $S = 1/2$ AFHC models. This way, the characteristic parameters, *i.e.*, the coupling constant J/k_B, the ratio between the staggered and uniform field $c = h_s/(gH)$ and the longitudinal staggered magnetization component $m_{s||}(\mu_0 H)$ have been extracted.

Furthermore, temperature dependent magnetization studies have been performed on CuPM for $H \; || \; c''$ in the temperatures range $1.4 \text{ K} \leq T \leq 4.2 \text{ K}$. The results are depicted in Fig. 42. Clearly, the effect of the additional longitudinal staggered magnetization component $m_{s||}$ is visible in the curvature of $m_{phys}(\mu_0 H)$ for temperatures $T < 4.2$ K, most pronounced for lowest temperatures $T = 1.4$ and 2.1 K. A numerical analysis for $T = 0$ with $N = 20$ spins as presented above fails to work in this case due to finite-size effects for $\mu_0 H <$ 10 T and thermal fluctuations for $T > 0.05 \; J/k_B$. Here, in order to improve the description of the magnetization it would be useful to carry out experiments in a wider range $k_B T/J$ and up to the saturation field. This, however, is a difficult task for CuPM because of the large J-value. Therefore, instead, a study on a material with a smaller J-value, that is Cu benzoate, was initiated.

5.2 Longitudinal Magnetization of $Cu(C_6H_5COO)_2 \cdot 3H_2O$

$Cu(C_6H_5COO)_2 {\cdot} 3H_2O$ has been characterized as a staggered antiferromagnetic $S = 1/2$ Heisenberg chain with an exchange parameter $J/k_B = 18.2$ K along the chain [36, 39, 40, 42, 48, 140]. Just as in the case of CuPM, the field-induced spin excitation gap and the Curie-like staggered contribution to the susceptibility at low temperatures are largest for the same orientation c'' and vanish along a'', the direction perpendicular to c''.

In this section, as an extension of the study of CuPM, a detailed investigation of the temperature dependence of the magnetization for $H \; || \; a''$ and $|| \; c''$ of Cu benzoate is presented. With its exchange coupling constant J/k_B being a factor 2 smaller than that of copper pyrimidine dinitrate, the saturation field $\mu_0 H$ is in the easily accessible range of $\sim$ 26.5 T. On Cu benzoate, magnetization measurements up to 38 Tesla have been performed at temperatures $0.09 < k_B T/J < 1.4$ and along the two characteristic magnetic orientations a'' and c'' of the sample. This way, the different characteristic temperature regions are covered, *i.e.*, that of a dominant staggered magnetization (below $\sim$ 5 K), of strong antiferromagnetic correlations (up to $\sim$ 18 K) and of the high-temperature paramagnetic state. The data for $H \; || \; a''$ are analyzed on basis of the thermodynamic Bethe ansatz and via exact diagonalization of a linear spin chain with 20 sites by A. Klümper, University Wuppertal, and by A. Honecker from the TU Braunschweig, respectively. For $H \; || \; c''$ the data are compared to recent transfer matrix renormalization group (TMRG) calculations by S. Glocke from the Physics Department, University Wuppertal, incorporating now the effect of temperature. These calculations are based on preceding work by A. Klümper, and are discussed with respect to the relevance of magnetocaloric effects, which have recently been proposed to play a role in $S = 1/2$ AFHCs [145].

5.2.1 Experimental Details

Single crystals of copper benzoate have been grown by the diffusion method as described in Ref. [140]. The reagents $CuSO_4{\cdot}5H_2O$ and C_6H_5COONa were put separately into two beakers, with the smaller beaker A placed inside the bigger one B. Then, water was slowly poured into both beakers until the water level was far up beyond the edge of beaker A. By the chemical reaction between slowly diffused Cu^{2+} and $C_6H_5COO^-$ ions flat plate-like crystals have been grown on the rim of the beakers within a few days to weeks, depending on the solvent temperature. In this work, several attempts have been undertaken at varying temperatures between 277 and 293 K. When the growth process is too fast, there is a risk of obtaining a big agglomerate of single crystals. Then, their separation is hardly possible without breaking them. Further, there seems to be a tendency of crystals to be twinned when the temperature is too high. All crystals show a perfect cleavage parallel to the *ac*-plane with well-defined edges parallel to the *c*-axis. Typical crystal dimensions are $4 \times 0.4 \times 12$ mm^3 along the *a*-, *b*- and *c*-axis, respectively. The magnetically principle axes a'' and c'' have been identified by a rotation of the crystal in the *ac*-plane by 17° with respect to the crystallographic *a* and *c*-axis, respectively (see Fig. 33).

Each single crystal has been characterized by determining the temperature dependence of the susceptibility with a SQUID magnetometer in an external field $\mu_0 H = 1$ T. Variations of the magnetic exchange coupling and of the longitudinal staggered susceptibility have been found, with $J/k_B = 17.3 \pm 1.6$ K and $\chi_{s||}$ of up to 15%. Note, that a subroutine for a direct background substraction of the raw data, implemented in the SQUID software, has been used for these investigations on copper benzoate. This way, a correction term could be neglected in the fit of the data. Nevertheless, the sample holder contributions were checked for their order of magnitude, being $< 5\%$ of the absolute signal in an external field of 1 T.

In order to obtain a reasonable signal in pulsed-field magnetization experiments, several oriented, plate-like single crystals have been glued into the borehole of a plexiglass rod, which was well-fixed inside a gel capsule and then placed inside a thin walled teflon cylinder. Since the sample diameter was restricted to 4 mm, the single crystals had to be cut along the a'' and c'' directions, respectively. This way, an optimal filling factor and hence absolute signal was guaranteed for the high-field magnetization experiments. The resulting $\chi(T)$ for the stack of samples, typically consisting of about eight single crystals oriented along the a'' or c'' direction, are depicted in Figs. 43(a) and (b), respectively. Fits of the susceptibility data to the staggered $S = 1/2$ AFHC model with $\chi_{phys} = \chi_u + C_s/T$ yield an averaged $J/k_B = 18.7(5)$ K, $C_{s,a''} \approx 0$ and $C_{s,c''} = 7$ memu K mole^{-1}. Hence, an almost perfect alignment of the prepared samples along a'' has been achieved.

A comparison of the staggered susceptibility component for the stacked samples aligned along c'' with unpublished data by Feyerherm [146] also reveals pronounced sample-to-sample variations. Feyerherm obtained $C_{s,c} = 18$ memu K mole^{-1} from a fit of the susceptibility data, which even for an orientation parallel to the c direction is much larger than the value for the samples used in this work. The origin of this discrepancy is not clear at present. It may be caused by chain defects, stemming for instance from partial dehydration of the samples from Feyerherm [146], since a Curie-like upturn with $C_{s,a} = 7$ memu K mole^{-1} has even been detected for the same single crystal of Ref. [146] for external field parallel to the a-axis. The susceptibility data by Dender et al. [36] and Date et al. [140] provide further examples for pronounced sample dependencies. No quantitative analysis of the staggered contribution is given here, but from the published data it can be seen that the Curie-like contributions at low temperatures differ a lot. While the staggered contribution for $H \parallel c$ from Ref. [36] is even smaller than the one for the samples of this work, it is much more pronounced in the data by Date et al. [140].

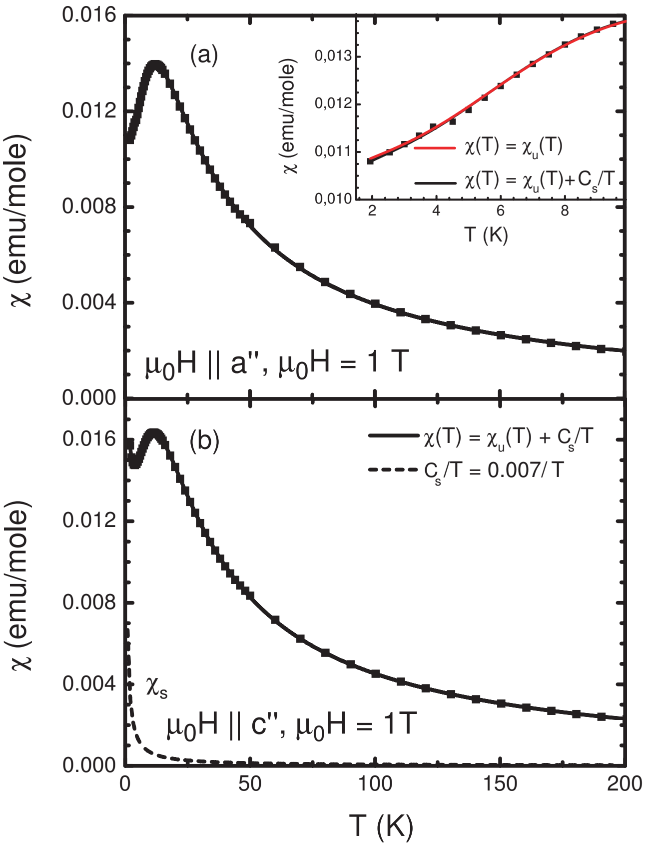

Figure 43: *The temperature dependence of the susceptibility of the stacked crystals of copper benzoate used in this work with the external magnetic field (a) parallel to a″ and (b) to c″. The solid lines are fits to the staggered* $S = 1/2$ *AFHC model. The dashed line in (b) represents the longitudinal staggered susceptibility component* $\chi_{s||} = C_s/T$ *as obtained from the fit. In the inset of (a), the low temperature regime* $T \leq 10$ *K is shown, indicating an almost perfect orientation (within ±1°) of the sample along a″.*

Magnetization experiments of copper benzoate in a SQUID magnetometer are depicted in Figs. 44(a) and (b) for H parallel to the a''- and c''-axis, respectively. Here, even for the lowest temperature $T = 2.0$ K a linear dependence of $M(\mu_0 H)$ is detected for both directions, indicating a less pronounced influence of the staggered field for copper benzoate than for CuPM in the same temperature interval.

High-field magnetization measurements were carried out at the Laboratoire National des Champs Magnétiques Pulsés in Toulouse as described in sections 3.2 and 5.1.1. For copper benzoate, the experiments have been performed in pulsed magnetic fields up to $\mu_0 H = 38$ T with experimental support by H. Rakoto and J. M. Broto. The pulse duration was about 1.2 s with an increasing time of 90 ms. The determination of the absolute value of the temperature at the sample site has been determined via a Si diode. In general, the accuracy of these temperature sensors is reduced above ~ 20 K due to the shape of their characteristic resistivity curve. In effect, a difference between the real and the displayed temperature value of ~ 1-2 K is possible for 20 K $\leq T \leq$ 300 K, in contrast to lower temperatures, where the matching is quite good.

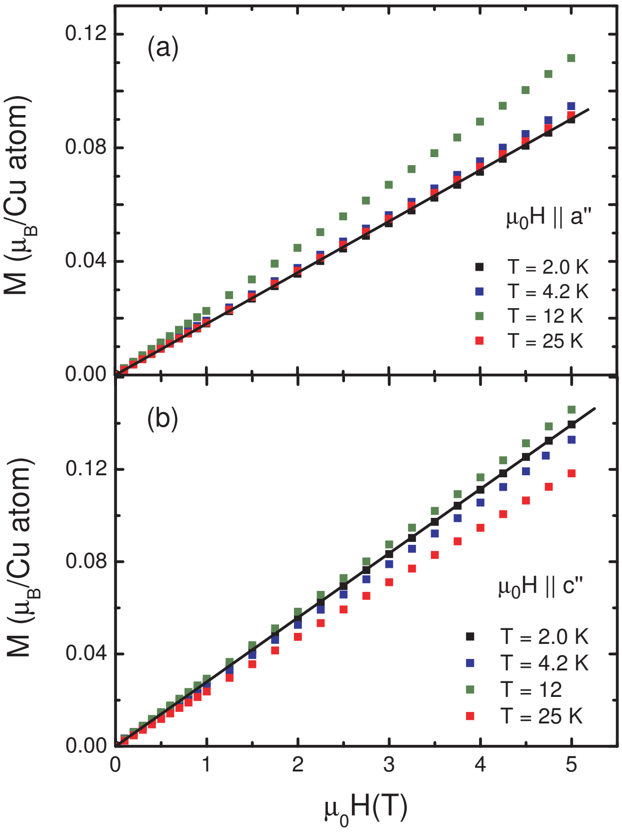

Figure 44: *The field dependence of the magnetization of the stacked crystals of copper benzoate used in this work, oriented along the a'' (a) and c'' direction (b) for temperatures 2.0 K, 4.2 K, 12 K and 25 K. The solid lines are guides to the eye.*

Due to the preparation of the stack of samples, which have been glued into the borehole of a plexiglass rod, one has to take into account the diamagnetic background contribution, adding up to the signal of the sample. In order to determine its absolute signal, the magnetization signal of the sample holder was measured separately in fields up to $\mu_0 H = 38$ T and corrected for in the data analysis for $T = 12$ K and 25 K, where it amounted to approximately 5 % of the total measured signal. Note, that the low-field SQUID magnetization data for a calibration at $T = 1.7$ K follow from an extrapolation as described in section 5.1.1.

5.2.2 Results and Discussion

In Figs. 45 and 46 the overall field dependence and the low-field range of the magnetization of $Cu(C_6H_5COO)_2 \cdot 3H_2O$ is plotted for $\mu_0 H \parallel a''$ and temperatures $T = 1.7$ K, 4.2 K, 12 K and 25 K. While the solid lines represent the experimental data, the markers denote the calculations based on exact diagonalization of a linear spin chain with 20 sites, which have been performed by A. Honecker. The temperature dependence is that expected for a uniform S = 1/2 AFHC [35, 80, 85, 86], with the pronounced rounding in $M(\mu_0 H)$ at the saturation field H_{sat} at low but finite temperatures, while at highest temperatures a Brillouin-like behavior is observed ($T = 12$ K and 25 K).

Quantitatively, the data can be perfectly described at all temperatures by means of exact diagonalization of a linear spin chain with 20 sites. For the comparison the g-tensor of copper

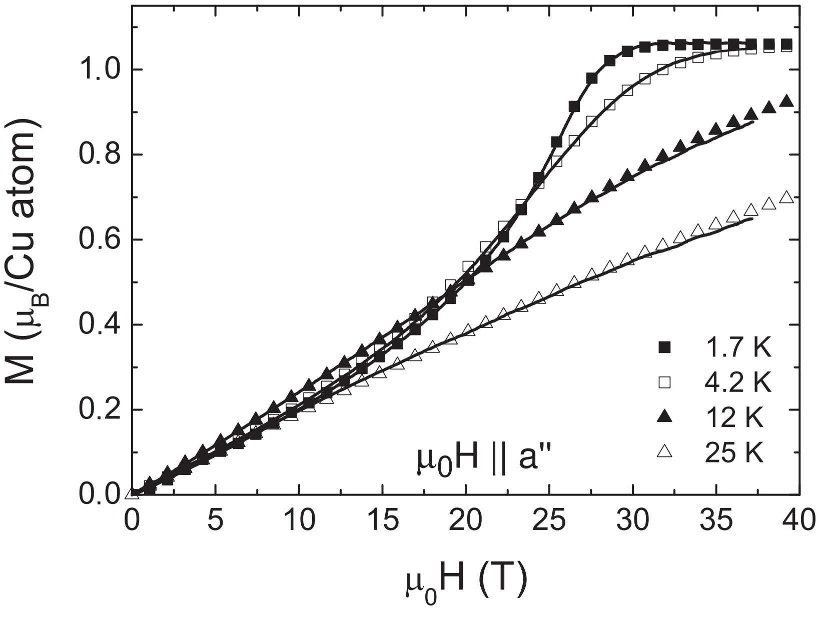

Figure 45: *The magnetization $M(\mu_0 H)$ of $Cu(C_6H_5COO)_2 \cdot 3H_2O$ as function of temperature with the external field aligned along the a'' direction. The experimental data is represented by solid lines, while the markers denote the calculated magnetization based on exact diagonalization of a linear spin chain with 20 sites.*

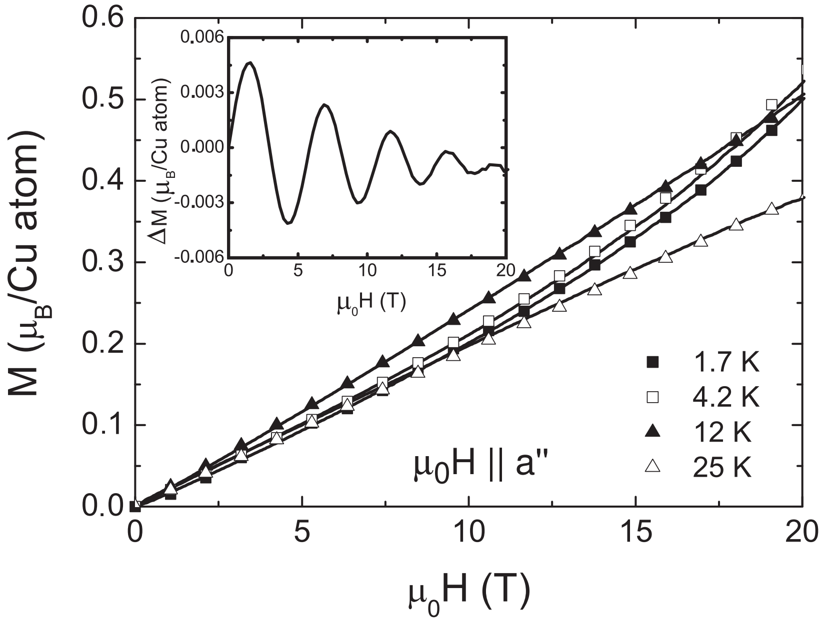

Figure 46: *The low-field range of the magnetization data from Fig. 45. In the inset the difference of the calculated magnetization based on the thermodynamic Bethe ansatz and exact diagonalization of a linear spin chain with 20 sites is shown.*

benzoate needs to be taken into account, which has been derived from ESR measurements [40] and is given in Eq. 115. For zero temperature, and using $g_{a''} = 2.117 \pm 0.01$ and $J/k_B = 18.7 \pm 0.5\,\mathrm{K}$ from susceptibility investigations, the saturation field along a'' is determined to $\mu_0 H_{sat,a''} = 4JS/g\mu_B = 26.3 \pm 0.7$ T. The saturation magnetization m_{sat} is calculated to $m_{sat,a''} = 1.06 \pm 0.005\,\mu_B$/Cu atom. Thus, for the uniform $S = 1/2$ AFHC at $T = 1.7$ K $\ll J/k_B$ the saturation magnetization should be approached at high fields. Indeed, for $H \mid\mid a''$ the curve for 1.7 K has an initial slope lower than at 4.2 K and 12 K. With increasing field the curvature becomes larger, crosses the 4.2 K and 12 K curves near $\mu_0 H = 21$ T, and reaches saturation at $\sim$ 30 T.

From the comparison between the experimental data and theoretical calculations for $H \mid\mid a''$, values of $g_{a''} = 2.117$ and $J/k_B = 18.8$ K have been extracted for copper benzoate, leading to a saturation field $H_{sat,a''} = 26.5$ T, which is in good agreement with previous reports [36].

Recently, high-field magnetization measurements on a related $S = 1/2$ antiferromagnetic Heisenberg chain system, *i.e.*, the coordination polymer complex Cu(II)-2,5-bis(pyrazol-1-yl)-1,4-dihydroxybenzene [145], have been interpreted as evidence for magnetocaloric effects in this system: $(\partial T/\partial B)_S = -(T/C)(\partial M/\partial T)_H$, C: specific heat. With regard to pulsed-field experiments, such might occur in the high-field range (large $(\partial M/\partial T)_H$) and at low temperatures (small C). In Ref. [145] a comparison between the experimental data and numerical calculations indicated that a description of the data taken at $T_B = 1.5$ K is only possible with numerical results corresponding to an average sample temperature of $T_{av} =$ 4.3 K, implying that throughout the pulsed-field experiment the sample has been subject to a magnetocaloric effect of +2.8 K at a bath temperature of 1.5 K. At higher temperatures this effect is less pronounced and vanishes at $T_B \sim 7.5$ K. For copper benzoate the fact that there is a perfect matching between theory and experiment at all temperatures implies that in our pulsed-field experiments magnetocaloric effects play no role.

Further, an additional comparison of our experimental data with calculated results obtained via the thermodynamic Bethe ansatz [85, 86] by A. Klümper has been performed. Overall, the matching between the Bethe ansatz results and the experimental data is as good as via exact diagonalization. In comparison, only for $T \leq 0.1\ J/k_B$ small finite-size effects are observable in the exact diagonalization approach. This is illustrated in the inset of Fig. 46, where the difference between exact diagonalizations of finite chains with 20 sites and the thermodynamic Bethe ansatz is plotted for $T = 1.7$ K. As can be seen from the figure, the difference is less than $\sim 0.005\ \mu_B/$ Cu atom and vanishes above 20 T. For higher temperatures $T > 0.1\ J/k_B$ finite-size effects become negligible, as it has been tested for the results at $T = 4.2$ K, 12 K and 25 K.

The magnetization curve $M(\mu_0 H)$ of copper benzoate with the external field aligned along the c'' direction is presented in Fig. 47(a) for temperatures $T = 1.7$ K, 4.2 K, 12 K and 25 K. For a quantitative comparison with theoretical calculations the g-factor of copper benzoate has been derived from the g-tensor in Eq. 115 to $g_{c''} = 2.32 \pm 0.01$. Then, the saturation magnetization is calculated to $m_{sat,c''} = 1.16 \pm 0.005\,\mu_B/\mathrm{Cu}$ atom. For zero temperature, and using $J/k_B = 18.8 \pm 0.5\,\mathrm{K}$ the saturation field has been obtained according to the formula of the uniform $S = 1/2$ AFHC: $\mu_0 H_{sat,c''} = 23.9 \pm 0.7\,\mathrm{T}$.

Fig. 47(a) includes the calculated field dependence of the magnetization along c'', which has been performed via the TMRG method by S. Glocke, University of Wuppertal. For the whole field regime the experimental data are fully described by these calculations, using J/k_B = 18.9 K, $g_{c''} = 2.32$, $\mu_0 H_{sat} = 24.2\,\mathrm{T}$ and an anisotropy parameter $c = h_s/(gH) = 0.043$. This value has been obtained from a comparison of the experimental data and calculations for $c = 0.043$, 0.083 and 0.1 as the optimum solution. The absolute values for c have been chosen by S. Glocke based on the experimental work in Ref. [40]. Note that the experimental data for $T = 25$ K has been compared with calculations for a slightly lower temperature $T =$ 23.7 K. As discussed, this difference can be accounted for as being the result of the reduced accuracy of the temperature sensor above 20 K. Altogether, from this analysis a very good agreement between the experimental and theoretical data set is achieved.

Comparing the anisotropy parameter $c = 0.043$ for copper benzoate with the one for CuPM, $c = 0.11$, the staggered field contribution for copper benzoate turns out to be considerably smaller. Therefore, the difference in the magnetization curves for the two magnetically main axes of copper benzoate, *i.e.*, the additional low-field contribution and the delayed saturation of the magnetization $\parallel c''$, are washed out. This can be seen from a comparison of Figs. 40(a) and (b) with Figs. 45 and 47(a) for CuPM and copper benzoate, respectively.

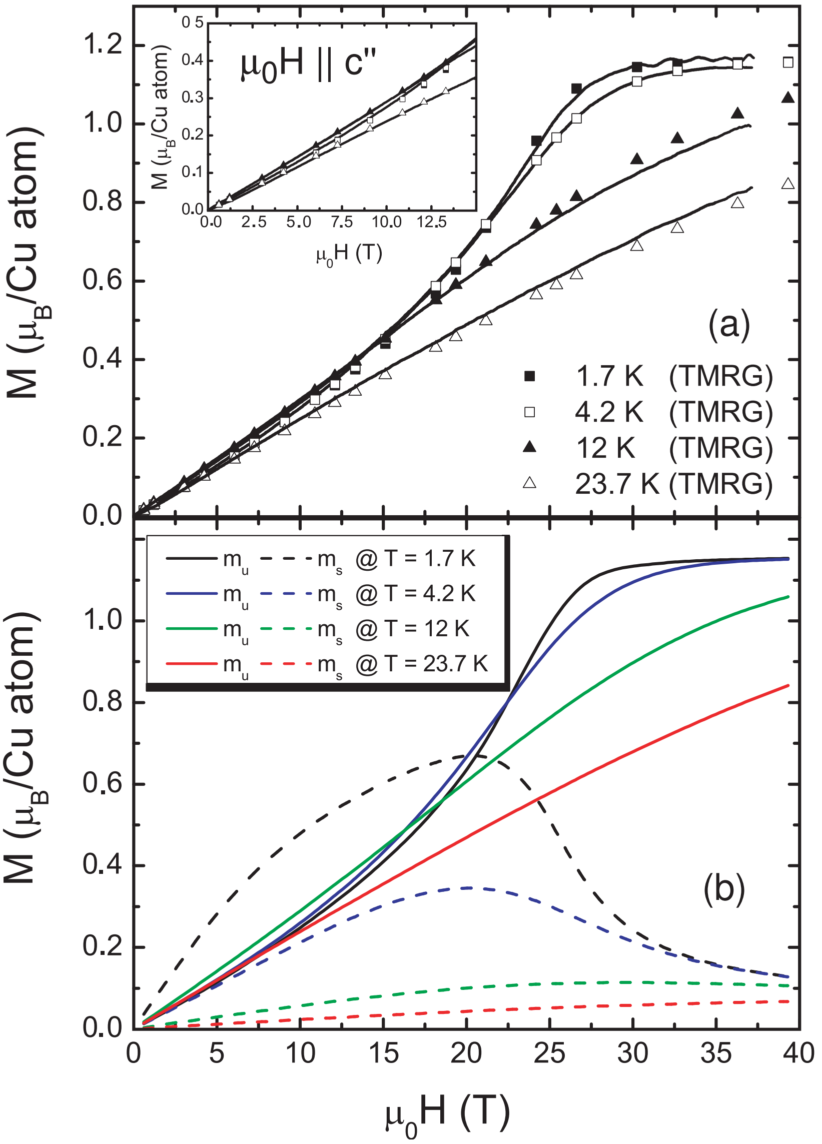

Figure 47: *(a) Experimental and theoretical magnetization curves for* $Cu(C_6H_5COO)_2 \cdot 3H_2O$ *at* $T = 1.7$ *K, 4.2 K, 12 K and 25 K with the external magnetic field aligned along the* c'' *direction. The solid lines are the experimental data, and the markers represent the calculated physical magnetization* $m_{phys} = m_u + (cg)\, m_s$ *for an anisotropy constant* $c = 0.043$ *and temperatures* $T = 1.7$ *K, 4.2 K, 12 K and 23.7 K. The calculations have been performed via the TMRG method by S. Glocke. (b) Plot of the temperature dependent TMRG results for* $c = 0.043$*, with the separation into the uniform (*m_u *- solid lines) and staggered (*m_s *- dashed lines) magnetization components for copper benzoate.*

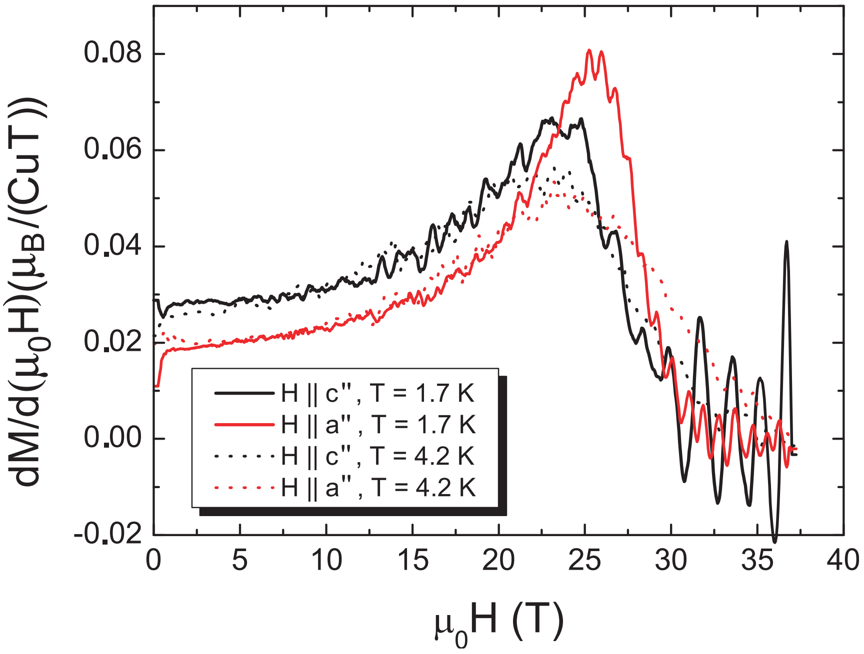

Figure 48: *The field derivative* $dM/d(\mu_0 H)$ *of* $Cu(C_6H_5COO)_2 \cdot 3H_2O$ *for* $T = 1.7$ *K and 4.2 K with the external field* $\mu_0 H \parallel a''$ *(solid and dotted red lines) and* $\parallel c''$ *(solid and dotted black lines).*

To emphasize the difference between the response for the two magnetically main axes of copper benzoate the derivatives of the magnetization, $dM/d(\mu_0 H)$, are plotted in Fig. 48 for $\mu_0 H \parallel a''$ and $\parallel c''$. For small fields $\parallel c''$ the initial slope is increased by approximately 50% compared to the a''-axis. At high fields (> 20 T), the saturation of the magnetization for $H \parallel c''$ is suppressed, as it is indicated by a smaller, broader feature in $dM/d(\mu_0 H)$ compared to the a''-axis response. Increasing the temperature to $T = 4.2$ K reduces the difference in the $M(\mu_0 H)$ curves between the two directions, but does not completely suppress it.

The reduction of the anisotropy parameter in copper benzoate is in agreement with its susceptibility data in section 5.2.1, where the staggered contributions $\chi_{s||}T = C_{s,c''} = 7$ memu K mole^{-1} have been determined to be considerably smaller than in CuPM, where $C_{s,c''} = 11$ memu K mole^{-1}. It has to be noted, however, that a remaining discrepancy between the value in this work and the one proposed in Ref. [40], *i.e.*, $c = 0.1$, is still a matter of debate. Possibly, it might be attributed to the pronounced sample dependency of C_s, which may stem for instance from dehydration leading to micro cracks in the sample. In our analysis, however, a perfect agreement between experimental results obtained from both susceptibility and high-field magnetization experiments with theoretical calculations has been achieved.

With the value of the anisotropy parameter c, the physical magnetization m_{phys} can be decomposed into the uniform (m_u) and staggered (m_s) component, according to Eq. 34. Both m_u and m_s are included in Fig. 47(b) for temperatures $T = 1.7$ K, 4.2 K, 12 K and 23.7 K. Qualitatively their field dependencies closely resemble the ones obtained for CuPM. More specifically, the data show that m_s traverses a maximum at $\sim 21\,\mathrm{T}$, while m_u monotonically approaches the saturation magnetization for $T = 1.7$ K and 4.2 K at large fields $\mu_0 H \approx$ 30-35 T. In addition to the analysis for CuPM, the temperature dependence of m_u and m_s is included in this figure. A detailed analysis by S. Glocke reveals a behavior $m_s \propto h_s^{\frac{1}{3}}$ for $T = 1.7$ K and 3 T $\leq \mu_0 H \leq$ 18 T and $m_s \propto h_s$ for higher temperatures in the low and intermediate staggered field regime. Thus, for the c'' data of $Cu(C_6H_5COO)_2 \cdot 3H_2O$ the high-field magnetization analysis verifies the predictions of the staggered $S = 1/2$ AFHC model.

5.2.3 Conclusions and Outlook

Summarizing, high-field magnetization experiments on $Cu(C_6H_5COO)_2 \cdot 3H_2O$ have been performed at temperatures $0.09 < k_B T/J < 1.4$, with the external field H parallel to the principal directions a'' and c''. From a comparison of experiment and theory, the behavior of the uniform $S = 1/2$ AFHC has been established for $H \parallel a''$, which has been evaluated via exact diagonalization of a linear chain with 20 sites and on basis of the thermodynamic Bethe ansatz equations [85, 86]. A perfect matching between theory and experiment at all temperatures implies that in the pulsed-field experiments on copper benzoate magnetocaloric effects, which have recently been discussed for a similar $S = 1/2$ antiferromagnetic Heisenberg chain, Cu(II)-2,5-bis(pyrazol-1-yl)-1,4-dihydroxybenzene [145], play no role.

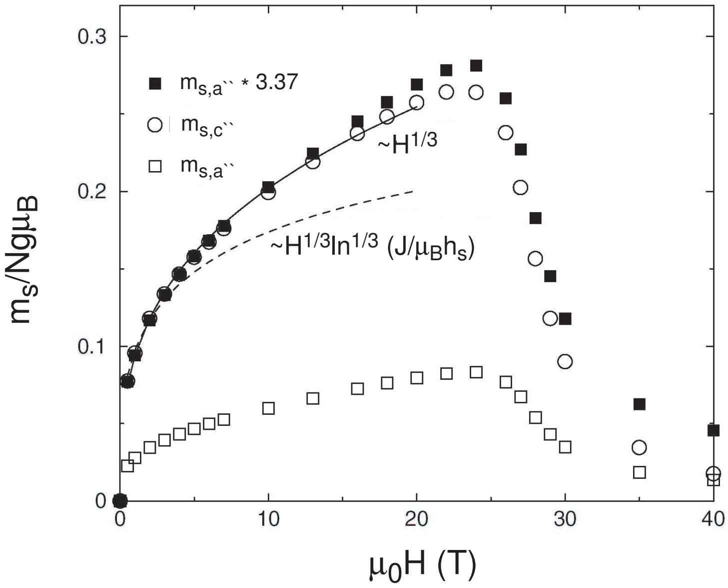

Figure 49: *The calculated staggered magnetization $m_s(\mu_0 H)$ of copper benzoate as function of the external field with $H \parallel b$, as obtained by means of DMRG calculations for $T = 0$; figure after Ref. [123].*

In contrast, for the staggered $S = 1/2$ AFHC direction, *i.e.*, $H \mid\mid c''$, the data has been analyzed by the transfer matrix renormalization group method based upon the staggered field theory by Oshikawa and Affleck [39, 40]. The very good agreement between the experimental data and the theoretical calculations fully verifies the predictions for the staggered $S = 1/2$ AFHC model. This way, TMRG calculations for such systems incorporating the effect of temperatures have been successfully tested for the first time. The characteristic parameters of copper benzoate have been extracted, *i.e.*, the coupling constant $J/k_B = 18.9(1)$ K and the ratio between the staggered and uniform field, $c = h_s/(gH) = 0.043$.

Recently, for the staggered $S = 1/2$ AFHC model a low-field/high-field crossover in the staggered magnetization has been predicted [123], which modifies both the spin excitation gap as function of external field and the staggered magnetization component for large external field values (see Fig. 49). These calculations for $H \mid\mid b$ imply that deviations from the staggered behavior in the field range $\mu_0 H > 20$ T should occur. To verify the predictions from Ref. [123], it would be interesting to perform analogous magnetization studies on copper benzoate for the external field aligned along the crystallographic b direction.

Furthermore, a direct experimental test of the finite-size effects in $S = 1/2$ antiferromagnetic Heisenberg chains with a finite number of sites seems to be a very interesting topic. Finite chains can be realized by doping nonmagnetic defects, which may disturb the correlated ground state of the bulk and locally restore magnetic behavior. This way, the exact diagonalization results for finite spin chains should be directly comparable to the experiment.

6 ^{13}C-NMR Experiments of the Staggered $S = 1/2$ AFHC CuPM

The vectorial picture of the uniform and staggered magnetization components of staggered $S = 1/2$ antiferromagnetic Heisenberg chains, including the canting of the staggered magnetization m_s against the induced staggered field h_s, which results in a large staggered magnetization component in the direction of the staggered field, $m_{s\perp}$, and a small uniform component in the direction of the uniform field, $m_{s||}$, has already been introduced in Chapter 5. While the longitudinal magnetization $m_{s||}$ has been extensively studied and compared to the staggered $S = 1/2$ AFHC model [39, 40] for two compounds, CuPM$(NO_3)_2(H_2O)_2$ and $Cu(C_6H_5COO)_2 \cdot 3H_2O$, generic features of this model, *i.e.*, the magnitude and direction of $m_{s\perp}$ and its temperature dependence, have not been verified experimentally. This motivated the detailed NMR shift investigations of copper pyrimidine dinitrate presented here.

NMR is a powerful tool to address these open questions in the field of staggered $S = 1/2$ AFHCs, since it allows new insight into the microscopic physics of compounds, and which are not accessible with conventional bulk techniques. Essential differences arise because NMR greatly profits from the local character of the probing nucleus, which is highly sensitive to small magnetic moments as well as to a canting of the investigated magnetic moments in the specific system. As opposed to bulk investigations, the interpretation of NMR data often requires reliable predictions about nonmagnetic quantities such as the chemical shift of the specific compound, in order to subtract the Knight shift from the absolute value of the measured shift. In the absence of such information, a determination of the chemical shift is possible using an extrapolation scheme by combining experimental NMR shift and bulk susceptibility data, *i.e.*, the *Clogston-Jaccarino* plot [147]. Further, choosing an adequate probing nucleus is crucial, since on-site/transferred hyperfine coupling between the nuclear and the electronic spins and the form factor are of great importance to derive the required information.

For this study, ^{13}C has been chosen as the probing nucleus, combining the advantage of a limited number of inequivalent sites with a strong anisotropic transferred hyperfine coupling to the electronic copper spins. This way, detailed information about the magnitude and direction of the transverse staggered moments can be achieved. In contrast, for ^{63}Cu and ^{65}Cu the main contributions to the Knight shift can generally be attributed to an isotropic on-site coupling, which is not sensitive to an alternation of transverse magnetic components. Further, ^{63}Cu, ^{65}Cu and ^{17}O have a nuclear spin $I > 1/2$, yielding not only magnetic but also quadrupolar contributions to the static and dynamic NMR data, which are usually not easy to separate. Even the ^{1}H nucleus, with a nuclear spin $I = 1/2$ and an ≈ 100 times higher natural abundance than ^{13}C, is not favorable in this case due to the large number of inequivalent sites either belonging to the pyrimidine or the water molecules.

The observation of a breather excitation in copper benzoate by electron spin resonance (ESR) [43] represents the first direct proof for the existence of the particle-like excitations predicted for the staggered $S = 1/2$ AFHC by the quantum sine-Gordon model. The nonlinear frequency-field dependence, found for copper benzoate, agrees well with the results of the previously reported specific heat measurements and establishes the validity of the mass formula for the first breather mode at $q = 0$ in a wide field range. These new results induced analogous tests for copper pyrimidine dinitrate, which have been performed by means of temperature dependent spin-lattice relaxation investigations. During the preparation of this thesis, a detailed study of the elementary excitation spectrum in copper pyrimidine dinitrate has been reported using submillimeter wave electron spin resonance spectroscopy [52], allowing to directly compare the results concerning the detection of particle-like soliton and breather excitations by means of ESR and NMR.

In this chapter, ^{13}C-NMR investigations on CuPM will be presented to verify mentioned fundamental properties of the staggered $S = 1/2$ AFHC. In the following section 6.1 the static part, *i.e.*, the temperature and orientation dependence of the NMR shift, will be shown. From the local susceptibility measured by NMR the magnitude and direction of the staggered magnetization is deduced, providing a quantitative test of the predictions by Oshikawa and Affleck [39, 40]. The data also yield basic information on the hyperfine coupling mechanism in CuPM. NMR experiments probing the spin excitations will be discussed in section 6.2. Their interpretation will be discussed in the framework of the quantum sine-Gordon model. Finally, section 6.3 deals with pressure dependent Knight shift and spin-lattice relaxation investigations of CuPM. This way, one possible extension of the parameter space has been introduced, and which might represent a direction to follow up in future studies.

6.1 Knight Shift Investigations of Cu Pyrimidine Dinitrate

As discussed previously, in Fig. 50 a schematic picture of the different terms of the magnetization induced by either the external or the induced staggered field is presented. Here, m_u represents the uniform magnetization induced by the external field H. Following Ref. [54] m_s denotes the total magnetization induced by the staggered field, which has both a staggered ($m_{s\perp}$) and a uniform ($m_{s||}$) component. As indicated, the perpendicular component ($m_{s\perp}$) cannot be detected by conventional bulk techniques. Since in CuPM $m_{s||}$ is predicted to be only ≤ 0.11 of m_s, it remains a necessity to prove the existence of the perpendicular component $m_{s\perp}$.

Therefore, in this chapter a combined experimental and theoretical study on copper pyrimidine dinitrate is presented. From the local susceptibility measured by ^{13}C-NMR at the three inequivalent carbon sites in the pyrimidine molecule a giant spin canting, *viz.*, an additional staggered magnetization perpendicular to the applied external field at low temperatures, is deduced. The magnitude of the transverse staggered magnetization $m_{s\perp}$, the spin canting of $(52\pm4)^\circ$ at 10 K and 9.3 T and its temperature dependence are in excellent agreement with exact diagonalization calculations on basis of the staggered $S = 1/2$ AFHC model by A. Honecker from the Institute of Theoretical Physics, TU Braunschweig.

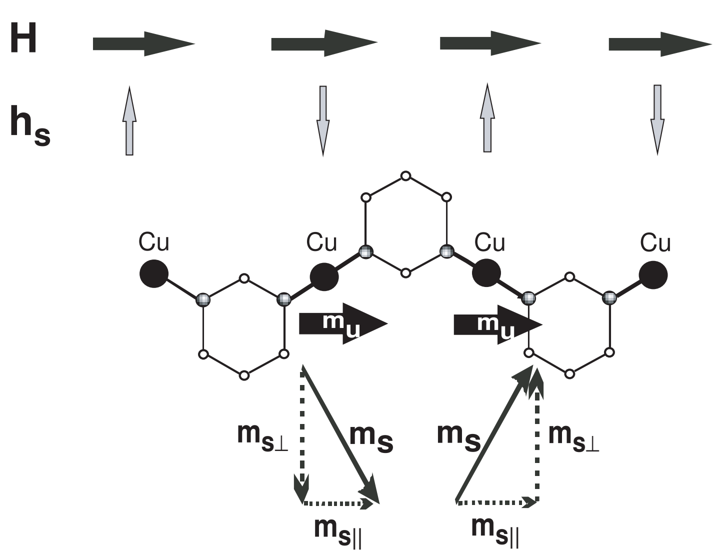

Figure 50: *A chain segment of* $CuPM(NO_3)_2(H_2O)_2$ *in a view onto the ab-plane. For clarity, only the Cu ions and the pyrimidine molecules are shown. The directions of the different components to the magnetization, i.e.,* m_u, $m_s = m_{s||}+m_{s\perp}$, *are illustrated on the middle chain segment. Note that the different staggered components are not to scale.*

6.1.1 Experimental Details

The single crystal of copper pyrimidine dinitrate $CuPM(NO_3)_2(H_2O)_2$ used for the determination of the transverse staggered magnetization has been grown by T. Ishida from the Department of Applied Physics and Chemistry, University of Electro-Communications in Tokyo. The size of the sample is about $6 \times 4 \times 15$ mm^3 along the crystallographic a, b and c direction, respectively. For the NMR experiments, the single crystal was oriented with the ac-plane parallel to the external field and placed inside a polycarbonate tube, which was stuck onto a sample holder, that could be rotated around an axis perpendicular to the external field direction. Since polycarbonate contains ^{13}C, the NMR signal had to be properly separated into components from ^{13}C atoms belonging to either the sample or the tube. This has been achieved by comparing the different widths and temperature dependencies of the lines, the shift of the single line of the amorphous polycarbonate tube being nearly temperature independent and its width being a factor 10 larger than the sharp lines of CuPM. Further, the intensity of the lines from the polymer is expected to be small, since the spin-lattice relaxation rate T_1 of such materials is much longer compared to non-amorphous solids like CuPM.

^{13}C-NMR shift experiments have been performed using a home-built spectrometer in quadrature detection and a superconducting magnet operating at a constant field of 9.30 T at temperatures between 5 and 200 K. The frequency spectra of ^{13}C were obtained using a progressive-saturation sequence with constant delay $\tau_{var} = 500\,\mathrm{ms}$ and an echo subsequence at the end, *($\pi/2$ - del.1)$_n$ - τ_{var} - $\pi/2$ - del.2 - π - del.2 - acq.*. Phase cycling has been used to cancel possible overlapping parasitic signals, either from multi-pulse experiments yielding phantom echoes, from transient responses of high-frequency pulses or imperfect hardware. Typical conditions of excitation were $\pi/2 = 14\,\mu$s and $\pi = 28\,\mu$s for a 90°– and 180°–pulse, respectively. The delay *del.1*$=250\mu$s was set to be much shorter than T_1 and *del.2*$=10\,\mu$s to be shorter than T_2. Repetition rates were in the range 0.005 – 0.05 kHz. The spectra were recorded piecewise by 30 kHz sections, using Fourier transform NMR at 9.30 T and summation over the frequency range between 99.35 – 99.95 MHz.

The ^{13}C-NMR shift δ is defined as the normalized difference between the observed resonance frequency ω_{res} and the calculated value for the bare nucleus, $\delta = \frac{\omega_{res} - {}^{13}\gamma\mu_0 H_0}{{}^{13}\gamma\mu_0 H_0}$. ${}^{13}\gamma_n = 6.726 \cdot 10^7\,\mathrm{s^{-1}T^{-1}}$ is the gyromagnetic ratio of the nucleus. H_0 was determined from the ^{1}H-NMR resonance frequency of water at room temperature.

6.1.2 Results and Discussion

As illustrated in Fig. 51(a) the intrachain magnetic exchange pathway in CuPM is provided by the N-C-N moieties of the pyrimidine ring $C_4N_2H_4$, which connect two neighboring Cu ions. The C atom on the magnetic exchange pathway, labelled C1, as well as the one on the opposite side of the pyrimidine ring (C2) are symmetrically sited with respect to the two Cu ions, while the atoms C3a and b are not. As is evident from the plot, for the situation where the crystallographic *ac*-plane is parallel to the external magnetic field C1, C2 and C3 are inequivalent, while the carbon sites C3a and b remain crystallographically equivalent. To each of the C atoms one hydrogen atom is bound, which may have either spin up or down, leading to two different eigenstates in the Hamiltonian (73). In consequence, in a ^{13}C-NMR study six distinct lines are observed, that is, three sets of double pairs of lines from the three inequivalent carbon sites, and with the line splitting caused by the hydrogen spin direction (see section 3.1.2). A set of representative NMR spectra, taken with the external field along the copper chain direction at temperatures between 5 and 120 K, is depicted in Fig. 51(b). Note the approximately doubled intensity of line pair 3 in comparison with the intensity of pair 1 or 2, which is in perfect agreement with the number of ^{13}C nuclei for each inequivalent site.

The splitting due to the nuclear coupling of the ^{13}C and ^{1}H nuclei can be calculated according to Eq. 73, with $J_{zz} = \frac{1}{2}\omega_d(1 - 3cos^2\theta)$ as the coupling constant, $\hbar\omega_d = \frac{\mu_0}{4\pi}\frac{\hbar^2\gamma_{n1}\gamma_{n2}}{r^3}$ as the characteristic coupling energy and θ representing the angle between the external field H and the vector spanning from the one to the other nucleus. There are four states and four transitions in a two-spin system, the difference between a homonuclear and heteronuclear situation being that in the latter they are at very different frequencies: for a ^{13}C-^{1}H system two transitions are close to the carbon resonance frequency $\omega_L(^{13}\mathrm{C})$ and the other two are close to the proton resonance frequency $\omega_L(^1\mathrm{H})$. Thus, in a $|^{13}\mathrm{C},^1\mathrm{H}>$ basis the observable transitions near the ^{13}C frequency are $|+->\leftrightarrow|-->$ and $|++>\leftrightarrow|-+>$, with

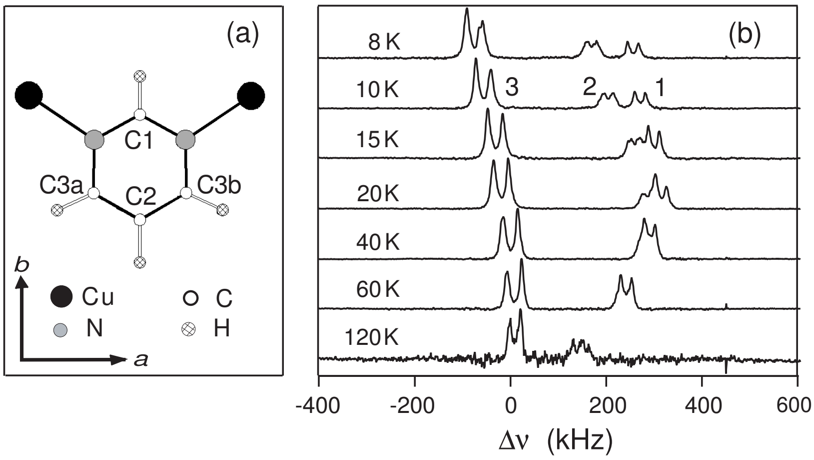

Figure 51: *(a) Schematic picture of the magnetic exchange pathway in CuPM(NO_3)$_2$(H_2O)$_2$ provided by the N-C-N moieties of the pyrimidine ring $C_4N_2H_4$. (b) The temperature dependence of the ^{13}C-NMR spectra in CuPM(NO_3)$_2$(H_2O)$_2$ in an external field of 9.3 T applied along the copper chain direction. The line pairs labelled 1,2 and 3 are associated to the corresponding sites on the pyrimidine molecule. For details see text.*

resonance frequencies $\omega_{1,2} = 2\pi\nu_{1,2} = \omega_L(^{13}\mathrm{C}) \pm J_{zz}$.

The values for J_{zz} have been determined by using the absolute value for the distance between the carbon and their adjacent proton positions as obtained from neutron powder diffraction by R. Feyerherm et al. [54]. In an experimental situation with H parallel to the copper chains, as it is shown in Fig. 51(b), the calculations yield J_{zz} (C1) $= \nu_d/2 = 16$ kHz, J_{zz} (C2) $= \nu_d/2 = 11.5$ kHz and J_{zz} (C3) $= 19.5$ kHz. On the contrary, experimentally we find slightly smaller values for all three sites: J_{zz} (C1) $=$ (11±1) kHz, J_{zz} (C2) $=$ (10.5±1) kHz and J_{zz} (C3) $=$ (16±1.5) kHz. Since a misalignment of the single crystal of $> 20°$ out of the ac-plane can be excluded[11], which would yield an increase of J_{zz} by the desired amount for site C1 and C3, the discrepancy is attributed to indirect contributions from the electronic environment of H and C. For the calculation only dipolar contributions have been taken into account, while the spin-density distribution of CuPM (see sec. 6.1.3) demonstrates the covalent character of the CuPM bonds, leading to additional indirect hyperfine contributions at all three carbon sites C1, C2 and C3.

Remarkably, in Fig. 51(b) an additional splitting of the line pair 3 is observed for $T \leq$ 10 K. The temperature dependence of this splitting $\Delta\delta$ is depicted in Fig. 52. An increase of $\Delta\delta$ is discernable for decreasing temperature, indicating an inequivalence of carbon sites C3a and C3b for temperatures below $T \sim 15$ K and thus different local magnetic fields at the two sites. The origin of this splitting will be discussed in section 6.2.

---

[11] Such a scenario can be excluded since in that case *(i)* the carbon sites C3a and C3b would become crystallographically inequivalent, which would be reflected in four instead of two NMR lines and *(ii)* the value J_{zz} for site C2 would be reduced by the same amount as for C1 and C3.

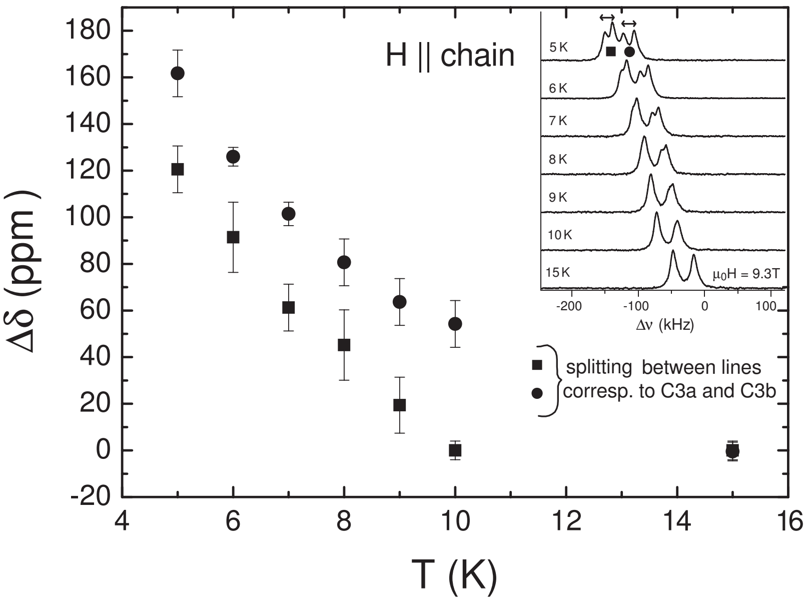

Figure 52: *The temperature dependence of the splitting* $\Delta\delta$ *between the NMR lines corresponding to carbon sites C3a and C3b. In the inset the NMR spectra of lines C3a and C3b are shown. The site assignment has been derived from angular dependent NMR shift measurements (see text).*

To establish the correlation between the pairs of NMR lines and the inequivalent C sites angular dependent NMR shift measurements have been performed in the paramagnetic regime at 200 K, which are depicted in Fig. 53. The angular dependence can be modeled taking into account the sum of chemical shift, isotropic and dipolar contributions of both Cu and N moments located within a sphere of radius $R = 30\,\text{Å}$ from the carbon atom. In order to adequately describe the data, a finite moment transfer of 10% to the nitrogen atoms of the pyrimidine molecules needs to be taken into account. From this analysis, which includes the angular dependence of the magnetic moment at the copper site [54], an angular dependence of the NMR shift is obtained as indicated by the solid lines in Fig. 53. The matching of lines and experimental data implies a correspondence of the line pairs to the carbon sites C1, C2 and C3 as denoted in Figs. 51, 52 and 53. In the modeling of the angular dependent shift, for the parametrization of the coupling between proton and carbon nuclear magnetic moments we have used the experimental values. A more extensive description of the analysis will be given below.

The angular dependent data in Fig. 53 clearly prove the experimental situation with the external field H in the ac-plane, since a misalignment of the field out of the ac-plane yields an angular variation of the typical splitting constant for all three sites C1, C2 and C3. Here, with the field in the ac-plane and the vector spanning from the carbon to the proton nucleus being parallel to the b direction for C1 and C2, J_{zz} becomes constant for these sites. For site C3, on the contrary, a strongly varying splitting is discernable, which is due to $\overrightarrow{C_3H}$ not being perpendicular to the ac-plane. Then, the angular dependence of $J_{zz} = \frac{1}{2}\,\omega_d(1 - 3cos^2\theta)$

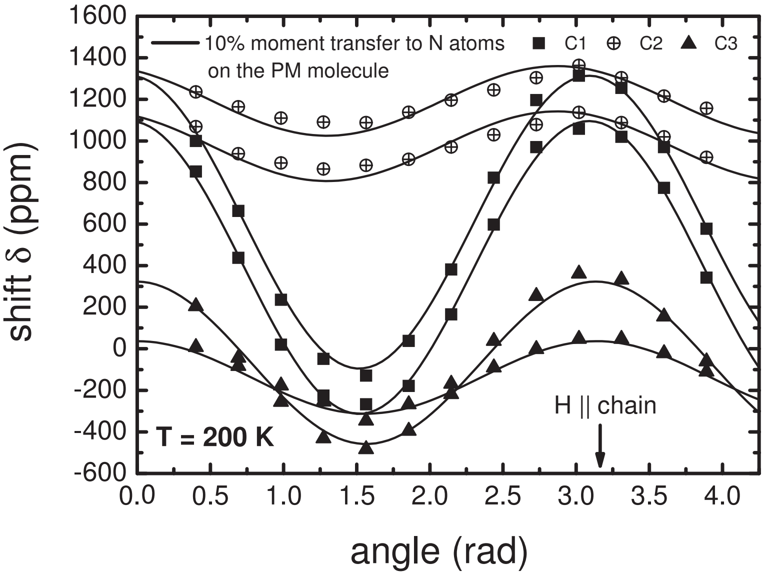

Figure 53: *The angular dependence of the NMR shift δ of the ^{13}C–NMR lines of $CuPM(NO_3)_2(H_2O)_2$ at 200 K with H parallel to the ac-plane. The line pairs are associated to the corresponding sites on the pyrimidine molecule (Fig. 51(a)). The solid lines represent fits of the data with a model taking into account the sum of chemical shift, dipolar and isotropic contributions as described in the text.*

results in a crossing between the two lines belonging to C3 for $\theta = \pm 54.74°$, corresponding to $\approx 124°$ (2.16 rad) and 226° (3.94 rad) in Fig. 53.

From the NMR spectra as depicted in Fig. 51 the temperature dependence of the NMR shift δ has been obtained for carbon sites C1, C2 and C3 for two different directions H || and $\perp$ chain. In Fig. 54 a direct comparison between the T-dependent shift δ of CuPM and the macroscopic bulk susceptibility is shown for all three carbon sites. Note that in the following, each set of hyperfine doublets is represented by its average shift, which can be described by the sum of the chemical shift σ_0 and the Knight shift K. While σ_0 represents the temperature independent chemical shift due to closed electronic shells, $K = A\cdot\chi(\mathrm{T})$ describes the hyperfine coupling to the paramagnetic electronic moments mainly residing on the Cu sites. Here, A is the hyperfine coupling constant, which can either have positive or negative sign, and $\chi(\mathrm{T})$ is the magnetic susceptibility. The shift and proportionality constants between the scales for δ and χ in Fig. 54 give the chemical shift and hyperfine coupling constants $A_{||}$ and $A_{\perp}$ for each carbon site for H || and $\perp$ chain, respectively.

For H || chain, the lines for C1 and C2 show a similar temperature dependence. Both have a positive NMR shift and their T dependencies agree with the bulk susceptibility for $T >$ 30 K. For lower temperatures, however, distinct deviations can be observed. In contrast, the third line for site C3 exhibits a different behavior. Here, a negative NMR shift is found, and the temperature dependence does not resemble the staggered $S = 1/2$ AFHC susceptibility

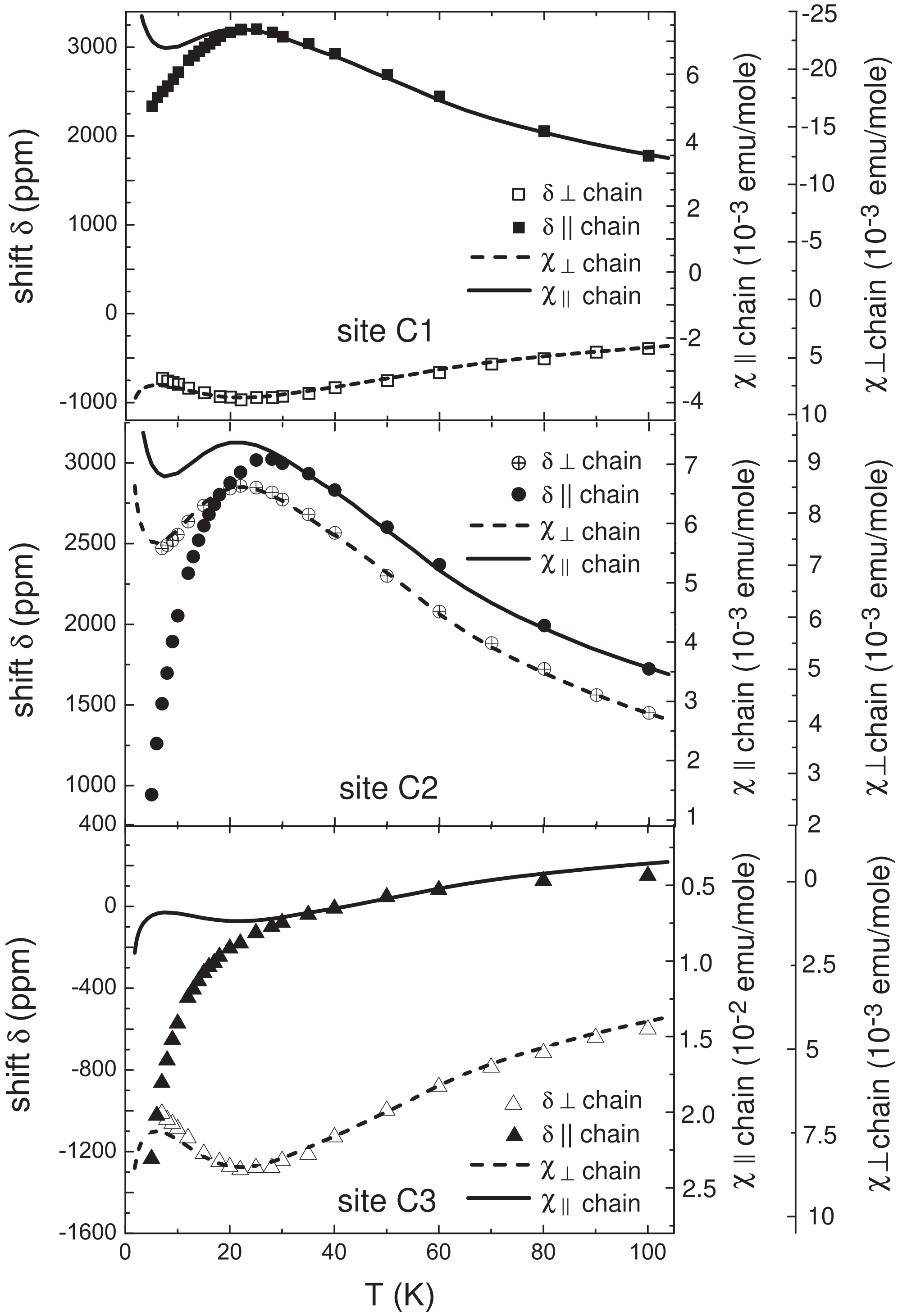

Figure 54: *The temperature dependence of the NMR shift δ of CuPM for H || and ⊥ chain for carbon sites (a) C1, (b) C2 and (c) C3. The solid and dashed lines represent the corresponding experimental bulk susceptibility* $\chi(T)$.

with the broad maximum at $\approx 0.64\ J/k_B$, but rather appears to be Curie–Weiss like.

In general, two different contributions are expected to the shift, *i.e.*, the Bonner-Fisher term for an ideal $S = 1/2$ Heisenberg chain and additional longitudinal and transverse contributions at low temperatures resulting from the staggered field. Then, the maximum in the NMR shift at about $\sim 25\,\mathrm{K}$ for sites C1 and C2 indicates that the 1D Bonner-Fisher contributions are dominant for temperatures $T \geq 25$ K. Due to the negative hyperfine coupling for site C3 the susceptibility maximum would correspond to a minimum in the NMR shift, which in fact is compensated by the strong negative staggered field contribution. In that sense, the NMR shift directly probes the staggered magnetization. Depending on the distance and angle between the carbon nucleus and copper atoms on their own and on neighboring chains, the hyperfine coupling can change sign and amplitude independently for uniform and staggered contributions. It leads to the variation of the NMR shift for inequivalent carbon sites in the low temperature region.

In contrast, for $H \perp$ chain all three lines resemble the bulk susceptibility with negative hyperfine coupling constants for sites C1 and C3. Small deviations are only present for temperatures $T \leq 10$ K. Here, the NMR shift data does not follow the Curie-like upturn of the bulk susceptibility, but remains at slightly smaller values. This very small deviation is attributed to compensating longitudinal and transverse staggered contributions for this geometry, mimicking an almost uniform $S = 1/2$ Heisenberg chain behavior. Although the transverse staggered component is predicted to be much larger than the small longitudinal one, which would prohibit a complete compensation, dipole calculations revealed that for $H \perp$ chain the dipole coupling constant for a transverse spin polarization is nearly zero, reducing the additional transverse staggered Knight shift $K_{s\perp}$ in this case.

A further comparison of the NMR shift $\delta(\mathrm{T})$ with $\chi(\mathrm{T})$ for all three carbon sites is shown in Fig. 55. The advantage of this so-called *Clogston-Jaccarino* [147] plot lies in the possibility to determine the nonmagnetic chemical shift contributions σ_0 by an extrapolation of the magnetic susceptibility for $\chi \to 0$. In Fig. 55 the solid lines represent linear fits of the form $\delta(\mathrm{T}) = \sigma_0 + A \cdot \chi(\mathrm{T})$ for $T \geq 30$ K. Whereas for $H \perp$ chain this linear relation is obeyed in the full temperature range (5-120 K), a large deviation is observed below 30 K for $H \parallel$ chain. In this geometry the transverse component of the staggered magnetization $m_{s\perp}$ results in an additional Knight shift $K_{s\perp}$, which due to its transverse character is not detectable in bulk susceptibility investigations.

$K_{s\perp}$ is extracted from the data via $K_{s\perp}(T) = \delta(T) - \sigma_0 - A \cdot \chi(T)$ and is shown in Fig. 56 (a) for sites C1, C2 and C3. The solid lines represent fits to $K_{s\perp}(\mathrm{T}) = A_{dip,\uparrow\downarrow} \cdot C_s^* / \mathrm{T} + K_{s,corr}$. The hyperfine coupling constant for a staggered magnetization along the b-axis, $A_{dip,\uparrow\downarrow}$, is calculated in localized dipole approximation within a sphere of 120 Å centered at the respective carbon site. The FORTRAN programme as well as the results for tensors $\overleftrightarrow{A}_{dip,\uparrow\downarrow}$ for carbon sites C1, C2 and C3 are listed in the Appendices A and B. A small offset $K_{s,corr}$ = -250 ppm had to be included since in this analysis the experimental value $K_{s\perp}(30\mathrm{K})$ is fixed to zero. From the fitted parameters C_s^* for the three carbon sites independent values

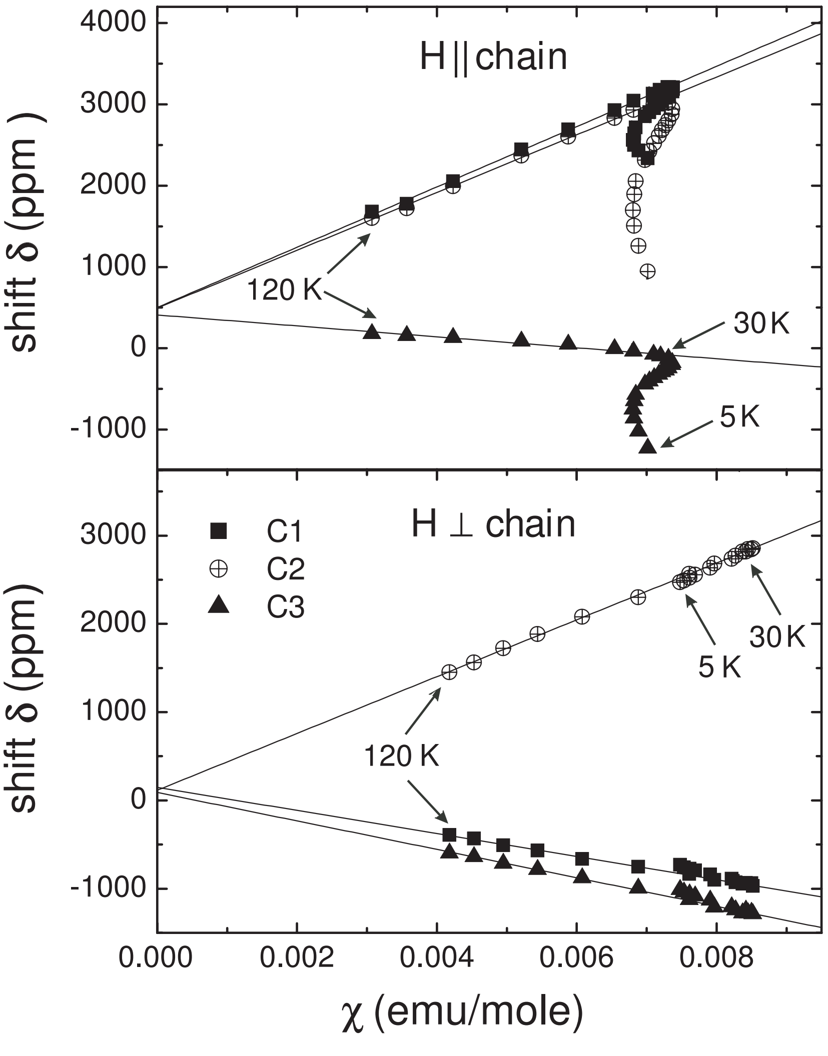

Figure 55: *NMR shifts $\delta(T)$ versus the experimental magnetic bulk susceptibility $\chi(T)$ for CuPM, with the external field H $||$ and $\perp$ to the Cu chain in the ac-plane. The solid lines are fits of the form $\delta(T)=\sigma_0+A\cdot\chi(T)$ for $T \geq 30K$.*

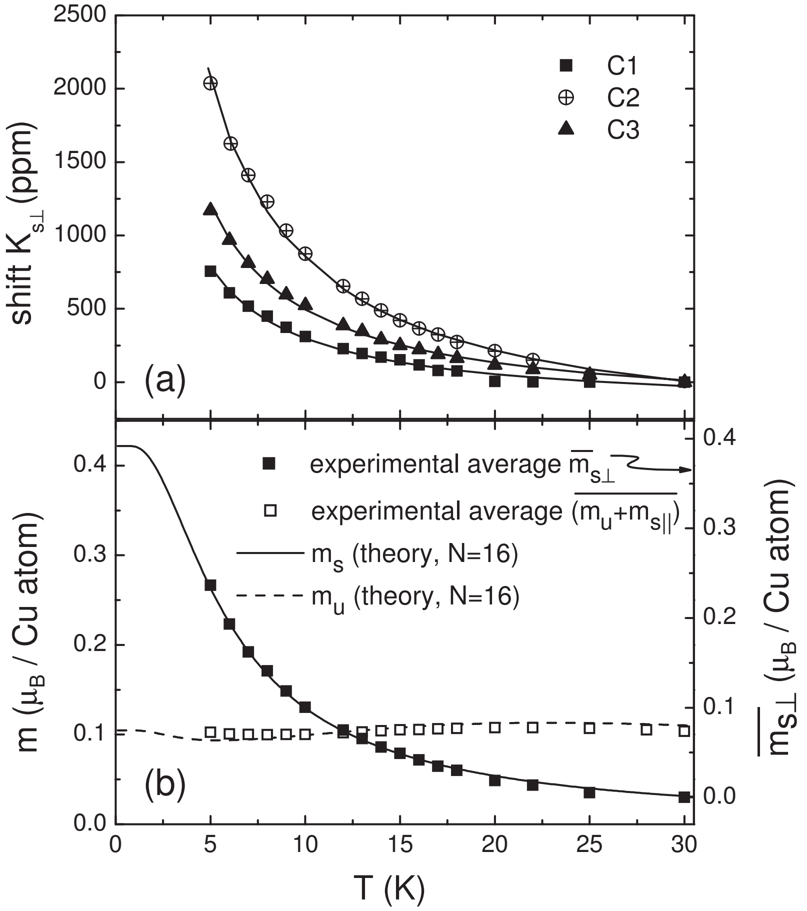

Figure 56: *(a) The temperature dependent transverse staggered contribution to the Knight shift, $K_{s\perp}$, in CuPM, with the external field H || to the Cu chains. The solid lines are a parametrization to $K_{s\perp} = A_{dip,\uparrow\downarrow}{\cdot}C_s^*/T{+}K_{s,corr}$. (b) The experimental average of the staggered and total uniform components for the three carbon sites, $\overline{m_{s\perp}}$ and $\overline{(m_u + m_{s||})}$, respectively, in comparison with exact diagonalization calculations of a linear chain with N = 16 spins for both the staggered magnetization m_s and for m_u. Note that the small offset between the experimental and calculated magnetization $m_{s\perp}$ (-0.03 μ_B/Cu atom) results from the analysis which sets $K_{s\perp}$(30 K) = 0.*

for $m_{s\perp}$, namely $m_{s\perp}$(C1) = (0.07±0.01)μ_B, $m_{s\perp}$(C2) = (0.16±0.01)μ_B and $m_{s\perp}$(C3) = (0.07±0.01)μ_B, are deduced for 10 K in 9.3 T external field || to the Cu chains.

In Fig. 56(b) the average of the experimental results obtained from the three carbon sites, $\overline{m_{s\perp}}$ and $\overline{(m_u + m_{s||})}$, is compared with results for the uniform z-component m_u and the staggered x-component m_s of the magnetization obtained by full diagonalization of the staggered S=1/2 AFHC chain Hamiltonian in Eq. 27, with N=16 sites and periodic boundary conditions. The calculations have been performed by A. Honecker from the Institute of Theoretical Physics, TU Braunschweig. Here, a value of J/k_B = 36.5 K, a ratio of the staggered and uniform field $h_s/(gH) = 0.083$ and $g = 2.117$ for H || chain [54] have been used. A comparison with results for $N < 16$ and for N=20 at $T = 0$ (see section 5.1) indicates that the data for N=16 yield a good approximation to the thermodynamic limit at all temperatures. An excellent agreement is found between experiment and theory in the whole temperature range. At 10 K and 9.3 T || chain the ratio of the staggered magnetization, $\overline{m_{s\perp}} = 0.13\ \mu_B$, to the total uniform one, $\overline{(m_u + m_{s||})} = 0.10\ \mu_B$, corresponds to a giant spin canting of (52±4)° with respect to the external field. With decreasing temperature the spin canting increases even further, extrapolating to $\sim 75°$.

In an independent approach to extract $m_{s\perp}$ the angular dependence of δ in the ac-plane was measured at 30 K and 10 K (Fig. 57). Taking into account an anisotropic dipolar and isotropic Fermi contact hyperfine coupling to the longitudinal susceptibility $\overleftrightarrow{\chi}_u + \overleftrightarrow{\chi}_{s||}$, an anisotropic dipolar coupling to the transverse susceptibility $\overleftrightarrow{\chi}_{s\perp}$, and the chemical shift $\overleftrightarrow{\sigma}$, the angular dependent shift δ can be expressed as

$$\begin{aligned}\delta \;&=\; \frac{1}{H^2}\mathbf{H} \cdot (\overleftrightarrow{A}_{dip,\uparrow\uparrow} \cdot (\overleftrightarrow{\chi}_u + \overleftrightarrow{\chi}_{s||}) + A_{iso}(\overleftrightarrow{\chi}_u + \overleftrightarrow{\chi}_{s||}) + \\ &\quad + \overleftrightarrow{A}_{dip,\uparrow\downarrow} \cdot \overleftrightarrow{\chi}_{s\perp} + \overleftrightarrow{\sigma}) \cdot \mathbf{H}. \qquad (117)\end{aligned}$$

Following Refs. [148, 149] the general form of the susceptibility tensors $\overleftrightarrow{\chi_u}$, $\overleftrightarrow{\chi_{s||}}$ and $\overleftrightarrow{\chi_{s\perp}}$ can be expressed as in the Appendix C, with the elements of $\overleftrightarrow{\chi_u}$ and $\overleftrightarrow{\chi_{s||}}$ being fully described by bulk susceptibility investigations from Ref. [54]. The dipolar hyperfine tensors for the uniform and the staggered susceptibility, $\overleftrightarrow{A}_{dip,\uparrow\uparrow}$ and $\overleftrightarrow{A}_{dip,\uparrow\downarrow}$, are given in the Appendix B and have been obtained by dipole-field calculations as discussed above. In order to adequately describe the data one needs to take into account a finite moment transfer of 10% to the nitrogen atoms of the pyrimidine molecules in the calculation of $\overleftrightarrow{A}_{dip,\uparrow\uparrow}$. The moment transfer is consistent with preliminary electronic structure calculations (see section 6.1.3) and it is close to the value observed in a molecule-based magnet consisting of MnCu antiferromagnetic chains [150]. A finite moment transfer to the nitrogen atoms has also been considered in the calculations of $\overleftrightarrow{A}_{dip,\uparrow\downarrow}$. Here, a 100 % transverse moment on the Cu site yields the best description of the experimental data and is used further.

The chemical shift tensor $\overleftrightarrow{\sigma}$ was calculated from the extrapolated values σ_0 in the *Clogston-Jaccarino* plot in Fig. 55 for H || and ⊥ to the chain. Assuming the principal axes of the chemical shift tensor $\overleftrightarrow{\sigma}$ to be the C-H bond axis, the perpendicular axis lying in the plane of the pyrimidine molecule and the axis perpendicular to the pyrimidine ring [151], the two diagonal elements of $\overleftrightarrow{\sigma}$ for a rotation of a magnetic field H in the ac-plane can be obtained from the extrapolated values:

$$\sigma_0 = \sigma_{11} \cdot cos^2\beta + \sigma_{22} \cdot sin^2\beta. \qquad (118)$$

Here, σ_{11} and σ_{22} represent the diagonal elements in the principle axes system (PAS) of $\overleftrightarrow{\sigma}$ for C1 and C2, and β is the angle between the PAS and the applied external field H. Since in the experiment the resonance frequency has been chosen such that the two principal values

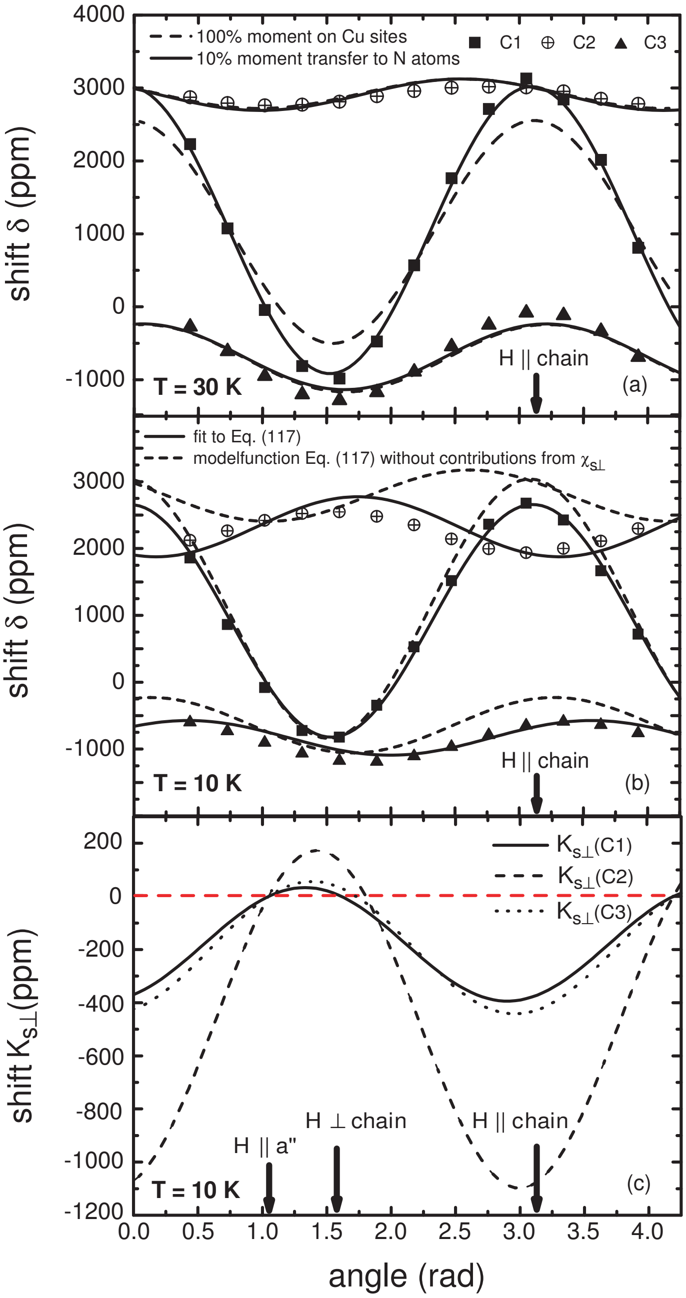

Figure 57: *The angular dependent NMR shift* δ *of CuPM at (a)* $T = 30$ *K and (b) 10 K, with the external field aligned in the ac-plane. The solid and dashed lines in (a) represent fits to Eq. 117, taking into account a finite moment transfer of 10% to the nitrogen atoms of the pyrimidine molecules in the calculation of* $\overleftrightarrow{A}_{dip,\uparrow\uparrow}$ *and considering solely moments on the Cu sites, respectively. The solid lines in (b) are fits to Eq. 117, while the transverse staggered component is omitted in the description represented by the dashed curves. (c) The angular dependent transverse staggered Knight shift* $K_{s\perp}$ *at* $T = 10$ *K, as obtained from the fits to Eq. 117.*

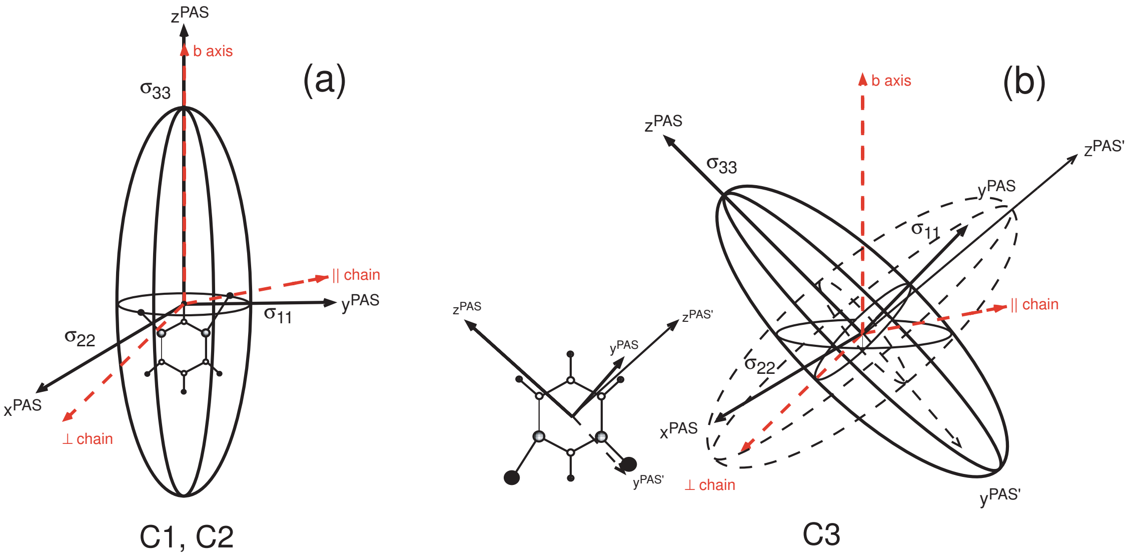

Figure 58: *The chemical shift tensor representation ellipsoid for the carbon sites (a) C1, C2 and (b) C3 on the pyrimidine molecule in CuPM. Note that the laboratory system is rotated around the crystallographic b direction by ≈ 6° with respect to the principal axes* σ_{11} *and* σ_{22} *of C1 and C2. In comparison to the principle axes system (PAS) of C1 and C2, the PAS of C3 is rotated around* x^{PAS} *by ≈ 65°.*

are positive, a connection can be made between Eq. 118 and the equation of an ellipse with semiaxes a and b, yielding

$$\frac{r^2 cos^2\beta}{a^2} + \frac{r^2 sin^2\beta}{b^2} = 1, \tag{119}$$

where $\mathbf{r}$ is the radius vector taken from the origin to a point on the surface of the ellipse. The semiaxes of the ellipse are given by $1/\sqrt{\sigma_{11}}$ and $1/\sqrt{\sigma_{22}}$, the representation of the ellipse thus allowing a geometrical interpretation of the chemical shift tensor. The full 3D-ellipsoid of $\overleftrightarrow{\sigma}$ for C1, C2 and C3 is depicted in Fig. 58. Since the two important sample directions, $||$ and $\perp$ to the Cu chains, follow from the principal axes of $\overleftrightarrow{\sigma}$ by a rotation about the b direction by $\approx 6°$ for C1 and C2, the experimental values already represent a good estimate for σ_{11} and σ_{22}. A comparison with chemical shift values for an isolated pyrimidine molecule, which have been calculated theoretically as well as determined from experimental shift data on a liquid crystal solution [151], is given in section 6.1.3.

The temperature independent isotropic hyperfine constant A_{iso} has been obtained from a fit of the data in Fig. 57(a) to Eq. 117. For 30 K the contributions from the staggered susceptibilities, $\overleftrightarrow{\chi}_{s||}$ and $\overleftrightarrow{\chi}_{s\perp}$, are nearly zero. Thus, to describe the experimental data at 30 K, A_{iso} is the only fit parameter and is determined to: $A_{iso,C1}$ = (0.05 ± 0.01)mole/emu, $A_{iso,C2}$ = (0.38 ± 0.01)mole/emu and $A_{iso,C3}$ = (-0.07 ± 0.02)mole/emu. An additional fit to the angular dependent data at 200 K (Fig. 53) confirmed the values within their error bars.

Then, using the isotropic constants A_{iso,C_i} determined at T = 30 K, the experimental chemical shift tensors $\overleftrightarrow{\sigma}_{C_i}$ and the experimental values for $\overleftrightarrow{\chi}_u$ and $\overleftrightarrow{\chi}_{s||}$ from Ref. [54], the remaining parameter to fit the angular dependent NMR shift data at 10 K is the transverse staggered susceptibility $\overleftrightarrow{\chi}_{s\perp}$. The solid lines in Fig. 57 (b) represent the fits to Eq. 117. Values of $m_{s\perp}$(C1) = (0.09±0.01)μ_B, $m_{s\perp}$(C2) = (0.20±0.02)μ_B and $m_{s\perp}$(C3) = (0.06±0.01)μ_B have been obtained for $\mu_0 H = 9.30$ T || chain. They are fully consistent with the results of the analysis of the temperature dependence of $K_{s\perp}$, as presented above. Fig. 57 (c) additionally depicts the angular dependent transverse staggered Knight shift component $K_{s\perp} = H^{-2}(\mathbf{H} \cdot \overleftrightarrow{A}_{dip,\uparrow\downarrow} \cdot \overleftrightarrow{\chi}_{s\perp} \cdot \mathbf{H})$. Obviously, $K_{s\perp}$ is equal to zero for H || a" and around $H \perp$ chain. If this transverse staggered component $K_{s\perp}$ is omitted in the description (see dashed curves in Fig. 57(b)), the NMR data cannot be reproduced.

The variance of the results of $m_{s\perp}$ for the three inequivalent carbon sites is attributed to the localized dipole approximation which has been used to calculate the dipolar hyperfine coupling tensors $\overleftrightarrow{A}_{dip}$. This indicates that in order to improve the description of the NMR data the effect of delocalization of spin density ought to be considered by means of extended electronic structure calculations.

6.1.3 Electronic Structure Calculations

In order to verify the results of the model used for the deduction of the transverse staggered magnetization and the hypothesis explaining the variance of the results of $m_{s\perp}$ for the three inequivalent carbon sites, electronic structure calculations have been carried out by K. Doll from the Institute of Mathematical Physics, TU Braunschweig. These calculations may further allow to verify the experimentally observed moment transfer of ≈ 10% to the N atoms on the PM molecules. Comparing to literature, an unexpectedly large value for the isotropic Fermi contact coupling at the carbon site C2 and comparatively large absolute values as well as anisotropy of the chemical shifts have been deduced from the NMR experiments, whose origin may also be elucidated by means of electronic structure calculations.

First, the ground state energies of the ferromagnetic and antiferromagnetic states were computed in the framework of density functional theory. The calculations were done with the electronic structure code CRYSTAL [152]. Spin polarized density functional calculations for the periodic system with the hybrid functional B3LYP (a mixture of Fock exchange, a modification of the Becke gradient corrected exchange functional, the Vosko-Wilk-Nusair local correlation functional, and the gradient corrected correlation potential by Lee, Yang and Parr) were performed. In order to test the stability of the results, the local density approximation (LDA) has additionally been employed, which is usually known as the most popular functional used for delocalized electrons in metallic compounds. The CRYSTAL code is based on local (Gaussian) orbitals, with the basis sets for copper chosen as [5s4p2d] [153], the oxygen basis set of the size [4s3p] [154], carbon and nitrogen sets of the size [3s2p1d] [155], and finally a [2s1p] hydrogen basis set was used [156].

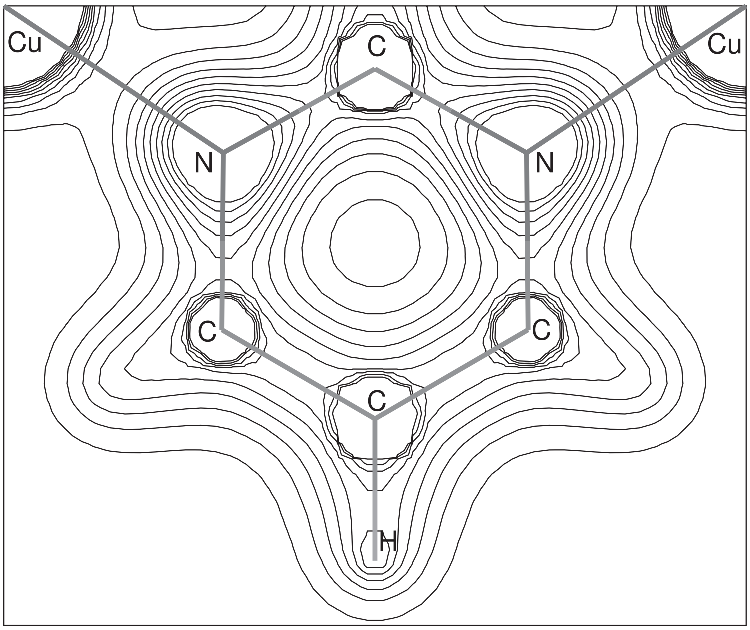

Figure 59: *The charge-density distribution in CuPM(NO$_3$)$_2$(H$_2$O)$_2$, plotted up to 0.5 $|e|/a.u.^3$ in steps of 0.05. The plane is chosen such that it contains the two Cu atoms and the carbon atom C2.*

From a comparison of the energy difference for the ferro- and antiferromagnet as obtained with the hybrid functional B3LYP, which is -0.000241 E_h (E_h = 1 hartree = 315773 K), the magnetic coupling strength J can be estimated assuming an Ising-like coupling H = -$\sum_{ij} JS_{iz}S_{jz}$. Then the energy difference between the ferromagnet and antiferromagnet ΔE would be J multiplied with the size of $S_z = 1/2$ squared, the number of couplings per cell (2, as the total energy is computed using a cell with 2 Cu atoms) and another factor 2 because of the difference between the ferromagnet, $S_{iz}S_{jz} = 1/4$, and antiferromagnet $S_{iz}S_{jz}$ = -1/4. A value of ΔE = -4J S_z^2 has been obtained, *i.e.*, $J \approx$ -0.000241E_h = -76 K, yielding a reasonable agreement between the theoretical and experimental (J_{exp} = -36 K) value, in particular considering that an overestimation by a factor 2 is not unusual with the B3LYP functional for exchange couplings [157, 158].

In the following, to elucidate the situation in the strong external field limit, as in our NMR experiment, the calculations for the ferromagnetic state will be presented. It has been found for CuPM that the Cu ion is in a d^9-state, with the d_{xy}-orbital being essentially single-occupied, if the geometry is chosen according to the crystallographic axes. Here, the tilting of the surrounding octahedra leads to a non-favorable orbital overlap between copper and axial nitrogen atoms and thus an essentially single-occupied d_{xy}-orbital.

From the calculations, the charges were determined to be +1.6 for Cu, between -0.1 and -0.3 for oxygen atoms from NO$_3$ groups, -0.6 for oxygen from H$_2$O molecules, -0.4 for N from NO$_3$ groups and -0.7 for N from pyrimidine molecules, while the carbon (+0.1 up to +0.7) and the hydrogen atoms (at most +0.2) were found to be slightly positive charged. This

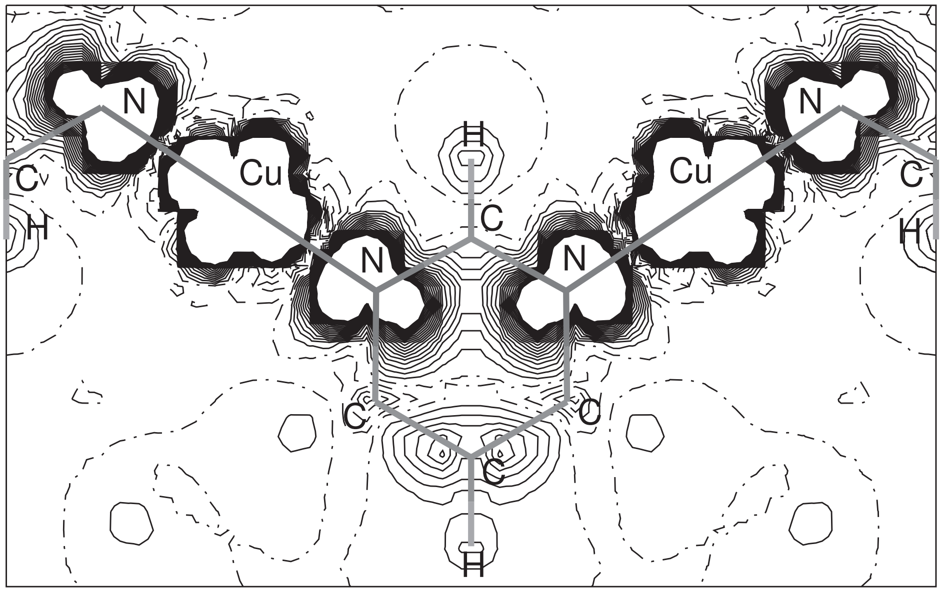

Figure 60: *The spin-density plot of $CuPM(NO_3)_2(H_2O)_2$ in the high-field limit. The spin density is plotted from - 0.005 to 0.005 $|e|/a.u.^3$ in steps of 0.0005. Positive spin density is indicated with full lines, negative spin density with dashed lines, and zero spin density with dash-dotted lines. The plane is chosen such that it contains the two Cu atoms and the carbon atom C2.*

is visualized in Fig. 59. The spin at the Cu site has been found to be $0.37|e|$ ($S = 1/2 \equiv 0.5|e|$), with a small spin transfer to the oxygen atoms from H_2O groups ($\approx 0.02|e|$ per site) and to the nitrogen atoms from pyrimidine molecules ($\approx 0.05|e|$ per site), confirming the results for the spin transfer from section 6.1.2. The magnitude of the spin at the other N, O, C and H sites is $\leq 0.01|e|$ and thus negligible. Fig. 60 illustrates these results, also clearly visualizing the magnetic exchange path via the pyrimidine molecule. The calculations are also in perfect agreement with the experimentally found discrepancy for the absolute values of the experimental and calculated hyperfine splittings for carbon sites C1, C2 and C3. Here, the discrepancy was large for sites C1 and C3 next to the nitrogen atoms, for which a large spin density has been found, while it was almost zero in the case of C2.

The dipole tensors $\overleftrightarrow{A}_{dip,\uparrow\uparrow}$ calculated by the LDA and B3LYP [159] functionals are given in the Appendix B for the three inequivalent carbon sites C1, C2 and C3. Qualitatively, the dipolar contributions for C1, C2 and C3 resemble the ones calculated within localized dipole approximation. On an absolute scale, however, the electronic structure calculations yield somewhat larger values, which may be attributed to *(i)* the distribution of spin density at the Cu site, yielding larger dipolar fields at the carbon sites, and *(ii)* the moment transfer to neighboring atoms such as oxygen in H_2O groups and carbon atoms themselves, the latter being small but non-negligible in the case of ^{13}C-NMR. The results for the isotropic Fermi contact hyperfine couplings for the B3LYP as well as for the LDA method are summarized

	exp.	B3LYP	LDA
A_{iso} (C1)	0.05±0.01	0.034	0.091
A_{iso} (C2)	0.38±0.01	0.077	0.087
A_{iso} (C3)	-0.07±0.02	-0.006	0.012

Table 2: *Isotropic Fermi contact hyperfine coupling constants A_{iso} (emu/mole) for the carbon sites C1, C2 and C3 in CuPM, as obtained from a fit to the experimental NMR shift data as well as calculated by electronic structure calculations using the B3LYP and LDA methods.*

	exp. on CuPM by ^{13}C-NMR	exp. in liquid crystal solutions from Ref. [151]	isolated PM B3LYP	PM/Cu complex B3LYP
$\sigma_{\|\|}/\sigma_{\perp}$ (C1)	467±40/117±30	-15±5/-134±2	-32/-131	22/-162
$\sigma_{\|\|}/\sigma_{\perp}$ (C2)	460±40/85±30	-53±6/-185±2	-74/-176	-54/-184
$\sigma_{\|\|}/\sigma_{\perp}$ (C3)	376±38/60±30	47±6/-158±2	28/-155	25/-175

Table 3: *The chemical shift values for a magnetic field $||$ and $\perp$ to the Cu chains in CuPM, $\sigma_{||}$ and $\sigma_{\perp}$ (ppm), for the carbon sites C1, C2 and C3 on the pyrimidine molecule, as obtained from NMR shift data of CuPM, of liquid crystal solutions of pyrimidine [151], as well as calculated results for the isolated PM molecule and a PM/Cu complex.*

in Table 2, together with the values obtained from a fit to the angular dependent NMR shift data of CuPM at $T = 30$ K and 200 K. A good qualitative and semi-quantitative agreement between the calculated values for the B3LYP method and the experimental values is observed. Only the too strong measured isotropic hyperfine coupling for carbon site C2 seems to require the consideration of additional processes. Presently, the origin of this large isotropic contribution is not clear.

The calculations for the shielding tensors $\overleftrightarrow{\sigma}^*$ for the carbon sites C1, C2 and C3 on the PM molecule were performed with the code Gaussian 03 [160]. Here, the gauge-independent atomic orbital method (GIAO) was employed, using the hybrid functional B3LYP and a 6-31G* Gaussian basis set for Cu, O, N, C and H atoms. Since both electronic structure codes, Gaussian 03 and CRYSTAL, can only calculate NMR shielding tensors on molecules, calculations on both an isolated pyrimidine molecule and an approximation to the real structure, *viz.*, a pyrimidine molecule situated between two Cu^{2+} ions, have been performed. In the latter case, in order to have an uncharged molecule four negative charges were put on the oxygen sites of the NO$_3$ group in CuPM, which are closest to the Cu ions. Before the NMR shielding tensors were obtained on an absolute scale, for the case of an isolated pyrimidine molecule a full geometry optimization with respect to all parameters had been performed.

The results for the calculated chemical shift for a magnetic field $||$ and $\perp$ to the Cu chains in CuPM, $\sigma_{||}$ and $\sigma_{\perp}$, for carbon sites C1, C2 and C3 on the pyrimidine molecule are summarized in Table 3 together with the values obtained from the *Clogston-Jaccarino* plot (sec. 6.1.2) and from Ref. [151]. The complete calculated shielding tensors, $\overleftrightarrow{\sigma}^* = -\overleftrightarrow{\sigma}$, for an absolute basis compared to a bare nucleus are given in the Appendix D. Note, that for an adequate comparison of the values from different sources both the experimental values, which were initially chosen with respect to ^{1}H in H_2O, and the values from Ref. [151], initially chosen with respect to ^{13}C in tetramethyl silane (TMS), have been transformed onto an absolute scale. Then, while the experimentally determined elements $\sigma_{||}$ and $\sigma_{\perp}$ of an isolated PM molecule from Ref. [151] are in good agreement with the calculations, the absolute values determined from the NMR investigations on CuPM as well as the anisotropy of $\overleftrightarrow{\sigma}$ are not reproduced well. Here, in contrast to the electronic structure calculations the experimental values are much higher and $\sigma_{||}>\sigma_{\perp}$ for all three sites.

In order to understand the difference, one needs to look at the various influences on the chemical shift. In general, the main contribution comes from the influence of low-lying electronic excited states. Heavier atoms tend to have more low-lying excited states than lighter atoms, leading to a larger chemical shift range for heavier isotopes. For example, the chemical shift range for ^{1}H is typically around 10 ppm, while for ^{13}C it is around 200 ppm. Heavy nuclei such as ^{209}Pb even have chemical shifts of many thousands of ppm. Further, the chemical shift correlates with the electronegativity of neighboring groups. Electronegative atoms like O, Cl, F, Se, etc. tend to reduce electron density, thus increasing the local field at the nuclei of neighboring atoms, which leads to increased σ_0-values (*e.g.*, an anisotropy of 506 ppm in a SeCSe molecule [161]). In the case of CuPM, the most important rule, however, which may explain the discrepancy, is that in rigid molecules with a well-defined three-dimensional crystallographic structure, the chemical shift is influenced by neighboring molecular units with a strong magnetic susceptibility, even if there is no chemical link. For example, a benzene ring readily supports induced electron currents and tends to decrease the local fields of nuclei situated close to the local symmetry axis (decreasing σ_0) and to increase the local fields of nuclei close to the plane of the ring (increasing σ_0). Hence, it may occur that the chemical shift in a solid is much different from the one of isolated molecules. In order to test this scenario, electronic structure calculations of the molecular complex consisting of pyrimidine and charged Cu ions have been performed as a first approximation to the real structure, which indicate that neighboring positive and negative charges change the chemical shift of C1, C2 and C3 on the PM ring by up to 54 ppm. For a direct verification, further calculations for CuPM in its crystal structure will be helpful, which, however, due to their complexity are very difficult to be carried out.

In Figs. 61(a) and (b) a comparison between the *experimental* angular dependent NMR shift data at T = 200 K and 30 K, respectively, with the sum of the *calculated* chemical, dipolar and isotropic hyperfine contributions is depicted. The plots clearly support the site association of C1, C2 and C3 to the corresponding NMR signal. While only a qualitative agreement could be achieved for site C2, a semi-quantitative agreement has been found between the experimental data and electronic structure calculations for the carbon sites C1 and C3. In these figures, the solid and dashed lines represent the calculations employing

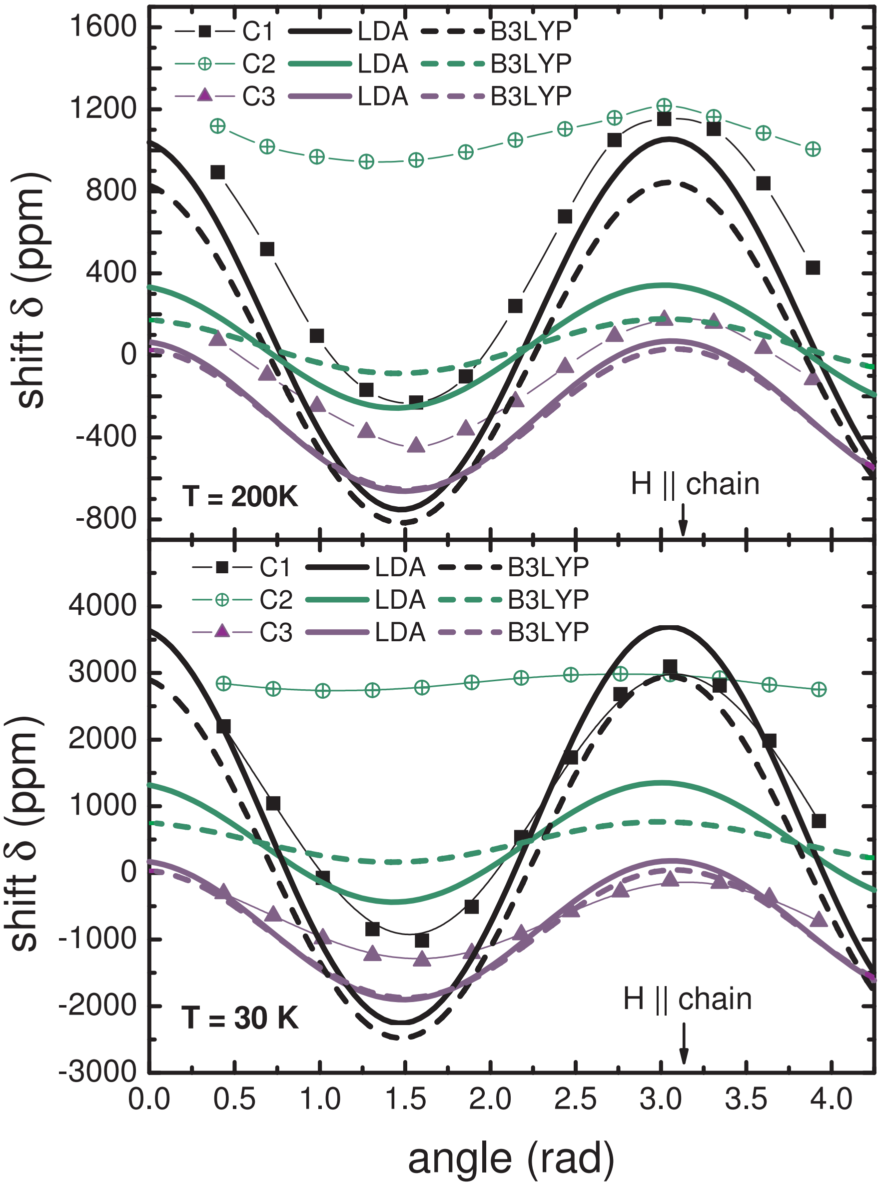

Figure 61: *A comparison of the angular dependent NMR shift* δ *with electronic structure calculations for* $T = 200\,\mathrm{K}$ *(a) and* $T = 30\,\mathrm{K}$ *(b), taking into account the sum of three different contributions, i.e., the chemical shift, the dipolar and the isotropic hyperfine coupling terms. The dashed lines display the calculations employing the hybrid functional B3LYP for all three contributions, while the thick solid lines have been obtained by electronic structure calculations using the LDA method for the dipolar and isotropic hyperfine coupling.*

the LDA method for the dipolar and isotropic hyperfine coupling and the hybrid functional B3LYP for all three contributions, respectively. The difference between both calculations yields an impression for the sensitivity regarding the choice of different functionals. As expected, the LDA method, which is known to describe only the homogeneous electron gas of metals very well, yields larger deviations between the experimental and calculated experimental case. The B3LYP yields better, but not full quantitative agreement with the data. Evidently, additional and improved electronic structure calculations will be needed for an accurate quantitative description of the experimental data.

6.1.4 Conclusions and Outlook

In conclusion, ^{13}C-NMR shift experiments have been performed on $CuPM(NO_3)_2(H_2O)_2$ as function of temperature and magnetic field orientation. The transverse staggered magnetization has been extracted as a low temperature deviation from the linear correlation between local and macroscopic susceptibility for 5 K $\leq T \leq$ 30 K, and from the orientation dependence of the NMR frequency shift at 10 K. The observed temperature dependence is in excellent agreement with theoretical results for the staggered $S = 1/2$ AFHC model. The observed giant spin canting at $T = 10$ K of 52°±4° with respect to the external field of 9.3 T $||$ to the Cu chains highlights the strong influence of only weak residual spin-orbit interactions in such systems. The NMR data also provide detailed information on the hyperfine coupling in $CuPM(NO_3)_2(H_2O)_2$ as well as on the absolute value of the staggered magnetization.

Up to now no further examples for the deduction of a giant spin canting in staggered $S = 1/2$ AFHCs have been found, while for two $S = 1$ Haldane-gap systems, $Ni(C_2H_8N_2)_2NO_2(ClO_4)$ (NENP) [162] and $Ni(C_5H_{14}N_2)_2N_3(PF_6)$ (NDMAP) [163], transverse staggered moments of $m_{s\perp} = 1.5\ \mu_B$ ($T = 4.2$ K, $\mu_0 H = 11.7$ T) and 1.1 μ_B ($T = 1.5$ K, $\mu_0 H = 10.9$ T) and similar giant spin cantings of $\sim 72°$ and $\sim 83°$, respectively, have been detected by means of proton NMR investigations. Whereas in Ref. [162] the transverse staggered moment has been extracted from a comparison of the observed and calculated spectral line shapes, Kobayashi et al. [163] estimated the staggered component in a similar manner as performed in this work, *i.e.*, from their angular dependent shift data by using isotropic and dipolar shift contributions. In a recent publication by Kodama et al. [164] a field-induced staggered magnetization has also been reported in a 2D frustrated dimer-singlet spin system $SrCu_2(BO_3)_2$ by ^{11}B-NMR. From these investigations the magnitudes of the intradimer DM interaction and the staggered g-tensor were determined, the DM interaction $D/J \approx$ 0.03-0.038 being a factor 4 smaller than the one in CuPM.

Electronic structure calculations for the paramagnetic regime of CuPM ($T > J/k_B$) verify both the moment transfer to the N atoms on the PM molecule by an amount of $\approx 10\%$, which has been found to be necessary for the analysis of the transverse staggered moment, and the isotropic Fermi contact coupling constants for carbon sites C1, C2 and C3 on a qualitative and semi-quantitative level. In the future, in order to clarify the origin of the observed large chemical shifts, it would be interesting to perform calculations of CuPM in its 3D crystal structure. Further, the variance of the results of $m_{s\perp}$ for the three inequivalent carbon sites, which has been attributed to the localized dipole approximation used to calculate the dipolar hyperfine coupling tensors $\overleftrightarrow{A}_{dip}$ in the analysis, calls for electronic structure calculations in the staggered regime.

6.2 Spin-Lattice Relaxation Experiments of Cu Pyrimidine Dinitrate

For $S = 1/2$ antiferromagnetic Heisenberg chains on low-symmetry crystallographic lattices, such as copper pyrimidine dinitrate CuPM$(NO_3)_2(H_2O)_2$, it has been demonstrated that the residual spin-orbit coupling fundamentally changes the magnetic properties. As a consequence an additional contribution to the susceptibility $\propto 1/T$, a giant spin canting, and an anisotropic magnetic field-induced spin gap $\Delta \propto H^{2/3}$ [54] can be observed. The gapped phase can be effectively described by the quantum sine-Gordon field theory and the excitation spectrum is represented by solitons, antisolitons and their bound states called breathers [40, 42]. In fact, recent ESR investigations on copper benzoate [43] represent the first direct proof of the particle-like excitations predicted for the staggered $S = 1/2$ AFHC by the quantum sine-Gordon model. Subsequently in 2004, in a detailed ESR study of the elementary excitation spectrum in CuPM signatures of three breather branches and a soliton, as well as several multi-particle excitation modes have been identified [52].

In this section, the spin-lattice relaxation rate $1/T_1$ of CuPM$(NO_3)_2(H_2O)_2$ is presented as a function of temperature at a constant external magnetic field of 9.30 T at the three inequivalent carbon sites in the pyrimidine molecule. Five distinct spin excitation modes are extracted from a fit of the data for $5\text{ K} \leq T \leq 120\text{ K}$ and $H \parallel$ chain, using a superposition of various activation laws. The results are discussed in context with recent ESR data from Ref. [52]. Concerning the five modes resolved in NMR a very good agreement between the two experimental techniques has been found. Angular dependent $1/T_1$ investigations as well as an unexpected low-temperature peak in the spin-lattice relaxation rate for the low-symmetry site, however, indicate the existence of additional relaxation processes beyond the quantum sine-Gordon field theory. A possible hypothesis for the origin of the low-temperature peak is discussed in the framework of the Bloembergen-Purcell-Pound (BPP) theory [165]. It is supported by field dependent studies of $1/T_1$ in the temperature interval $1.3\text{ K} \leq T \leq 40\text{ K}$ as well as by the observation of an additional line splitting for $T < 15$ K at the low-symmetry carbon site of the pyrimidine molecule.

6.2.1 Experimental Details

For the temperature and orientation dependent $1/T_1$ investigations at a constant external magnetic field of 9.30 T the same single crystal as for the NMR shift experiments has been used. The sample was oriented as described in section 6.1.1. Experiments have been carried out for the external field aligned along the chain direction and as function of angle in the crystallographic *ac*-plane. A second single crystal, grown by R. Feyerherm from the Hahn-Meitner-Institute in Berlin, has been employed for the study of the field dependence of the spin-lattice relaxation. Since this crystal has also been used for pressure dependent NMR studies, it had to be cut along the crystallographic c direction to $4 \times 3 \times 4$ mm^3 in order to fit into the clamped CuBe pressure cell. Since a maximal sample size, *viz.*, filling factor, is the prime requirement in the pressure experiments, with the given shape of the sample an alignment of the field along the crystallographic a'-axis was chosen.

^{13}C-NMR spin-lattice relaxation experiments have been performed using a home-built spectrometer in quadrature detection with either *(i)* a superconducting magnet operating at a constant field of 9.30 T and temperatures between 5 K and 200 K or *(ii)* a superconducting magnet operating at 3.44 T and 6.96 T and temperatures between 1.3 K and 40 K. The spin-lattice relaxation rates $1/T_1$ for carbon sites C1, C2 and C3 were obtained using a progressive saturation sequence with variable delay 0.3 ms $\leq \tau_{var} \leq$ 1.5 s and an echo subsequence at the end, $(\pi/2$ - *del.1* $)_n$ - τ_{var} - $\pi/2$ - *del.2* - π - *del.2* - *acq.*. Phase cycling with a special 8-phase sequence was used to cancel parasitic signals, either from multi-pulse experiments yielding phantom echoes, from transient responses of high-frequency pulses or imperfect hardware. Typical conditions of excitation were *(i)* $\pi/2 = 14\,\mu$s and $\pi = 28\,\mu$s in the case of the sample inside the polycarbonate tube and *(ii)* $\pi/2 = 4\,\mu$s and $\pi = 8\,\mu$s for the smaller sample inside the pressure cell. The variance of the pulse lengths mainly reflects the different filling factors and coils for the two experiments. Whereas the coil had to be wound around the polycarbonate tube for the orientation dependent experiments, an optimal filling factor could be achieved in the pressure cell, with the coil being directly wound around the sample. The delay *del.1* $= 250\mu$s was set to be much shorter than T$_1$ and *del.2* $= 10\,\mu$s to be shorter than T$_2$. Repetition rates were in the range 0.002 – 0.05 kHz. The additional spectra for the lines of the low-symmetry carbon site C3 were recorded piecewise by 50 kHz and 20 kHz sections, using Fourier transform NMR at 3.44, 6.96 and 9.30 T $||$ to the a' direction, and summation over the frequency range between 36.45 – 36.95 MHz, 74.10 – 74.80 MHz and 99.35 – 99.95 MHz, respectively.

6.2.2 Results and Discussion

The spin-lattice relaxation rate $1/T_1$ as function of temperature is shown in Figs. 62 and 63 for carbon sites C1, C2 and C3 with the external field $\mu_0 H$ = 9.30 T parallel to the Cu chains. As in the discussion of the static ^{13}C-NMR signal, the ^{1}H-split hyperfine doublets are represented by their average value for $1/T_1$.

In general, in magnetic systems such as CuPM temporal fluctuations of the local fields at ω_L originate from fluctuating electronic spins, leading to a contribution in the spin-lattice relaxation. According to Eq. 96 the spin-lattice relaxation rate $1/T_1$ can be expressed in terms of the imaginary part of the dynamic susceptibility as

$$\frac{1}{T_1} \approx \gamma_n^2 k_B T \sum_{\mathbf{q}} \frac{F_\perp(\mathbf{q})\chi_\perp{''}(\mathbf{q},\omega_L) + F_z(\mathbf{q})\chi_z{''}(\mathbf{q},\omega_L)}{\omega_L},$$

where γ_n is the nuclear gyromagnetic ratio of ^{13}C and ω_n is the nuclear Larmor frequency. $F_\perp(\mathbf{q}) = \sum_{\beta=x,y}(A_{x\beta}^2(\mathbf{q}) + A_{y\beta}^2(\mathbf{q}))$, $F_z(\mathbf{q}) = A_{xz}^2(\mathbf{q}) + A_{yz}^2(\mathbf{q})$ represent the so-called geometrical form factors, with $A_{ij}(\mathbf{q})$ ($i = x, y$, $j = x, y, z$) being the elements of the hyperfine coupling tensor in momentum space.

A schematic picture of the dispersion of single-particle excitations in staggered $S = 1/2$ AFHCs is given in Fig. 15. Direct spin excitation processes involving excitations from the ground state to the soliton and breather branches do not contribute to $1/T_1$, since the frequencies of such processes are much larger than the nuclear Larmor frequency ω_L. The only relevant relaxation channels in 1D spin-chain systems with a spin gap are those which are quasielastic and involve a scattering between two excited states. Since in the framework of the low-energy SG model the different excitation branches are well separated in energy compared to the nuclear Zeeman energy $\hbar\omega_L$, the spin-conserving two-magnon processes in the lowest breather branch (Fig. 17(a)) yield the only contributions to the spin-lattice relaxation for low temperatures $T \leq \Delta$. With increasing temperature, however, the higher branches, *i.e.*, the soliton (S) and higher breather branches (B2, B3), also become thermally excited, allowing further spin-conserving intrabranch processes. Finally, for high temperatures even spin-non-conserving three-magnon intrabranch (see Fig. 17(b) with activation energy $E_A = 2\Delta(H)$) and two-magnon interbranch processes (see Fig. 17(c) with $E_A = \Delta(H = 0)$) as well as multi-particle excitations of an extended continuum state may contribute to the spin-lattice relaxation rate.

Strictly speaking, the sine-Gordon model as used by Oshikawa and Affleck [39, 40] is limited to the low-field region. For higher external magnetic fields deviations from this model need to be considered [166]. For CuPM, a comparison of ESR data in magnetic fields up to $g\mu_B H \sim J$ with calculations on basis of the SG model by Zvyagin et al. [52] yield an excellent agreement for the entire field range, supporting the validity of the quantum field theory up to 24 T for this compound. Hence, with an external field of 9.30 T the NMR experiments of this work should be sufficiently described by the predictions of the quantum SG model.

Taking into account only the above described thermally activated processes [167, 168] and following the quantum sine-Gordon model, which predicts multiple spin excitation modes, the scattering process leads to a relaxation behavior

$$\frac{1}{T_1} \sim \sum_{\mathbf{q},i} |F_i(\mathbf{q})| exp(-\Delta_i(\mathbf{q})/T), \tag{120}$$

where $\Delta_i(\mathbf{q})$ denote the different gaps of each excitation mode.

The logarithmic plot of $1/T_1$ as function of $1/T$ (Fig. 62) indicates the existence of at least two different temperature domains, where the spin-lattice relaxation rate at the three

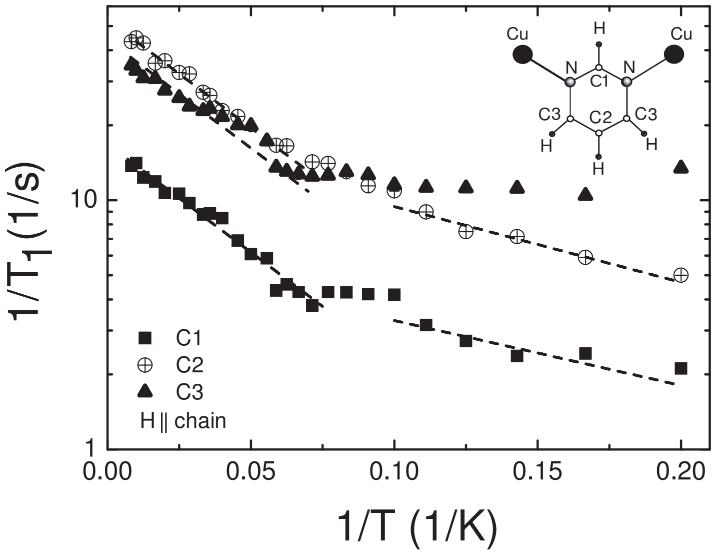

Figure 62: *Logarithmic plot of the spin-lattice relaxation rate* $1/T_1$ *against* $1/T$ *at the three inequivalent* ^{13}*C sites in CuPM in an external field* $\mu_0 H$ = *9.30 T || to the Cu chains. Each dashed line indicates a single activated behavior.*

inequivalent carbon sites follows an activated behavior with different activation energies, *viz.* excitation modes. However, the absolute values of the gaps can only be estimated from the slopes of the linear sections. Whereas C1 and C2 follow very similar activation laws, C3 shows a more complicated behavior. Especially at temperatures $T < 15$ K an increase of $1/T_1$ with decreasing temperature occurs for this low-symmetry site, which is tentatively attributed to an additional relaxation channel not incorporated in the sine-Gordon field theory. We have tried to reveal its origin by additional $1/T_1$ measurements for $T \leq 40$ K in external fields of $\mu_0 H = 3.44$ and 6.96 T. These data have been analyzed in the framework of the *BPP theory* [165], which will be discussed in detail below.

The experimental $1/T_1$ was fitted to Eq. 120, resulting in the solid lines in Fig. 63. For the fit the values of nine different excitation modes detected in ESR measurements [52] were used, *i.e.*, Δ_{B1}=7.2 K, Δ_S=8.8 K, Δ_{B2}=13.1 K, Δ_{B3}=16.4 K, Δ_{U2}=17.5 K, Δ_{U1}=18.6 K, Δ_{C1}=20.9 K, Δ_{C2}=25.8 K and Δ_{C3}=28.8 K (error bars ± 0.4 K), which had to be scaled by a factor $\cos^{2/3}(30°)$ due to a different field geometry (see sec. 4.1.2). The parameters $|F_i(\mathbf{q})|$ are independent fit parameters, describing the coupling strength of the excitations to the ^{13}C nucleus for each carbon site. Since neither the high-symmetry site C1 nor C2 are exactly situated between two Cu spins, the antiferromagnetic spin excitations at $q = \pi$ are not expected to be filtered out as in the case of ^{17}O spin-lattice relaxation experiments in the CuO$_2$ plane of high-T_c superconductors (see sec. 3.1.3). It is noted that the assignment of the different calculated excitations to the expected soliton and breather modes is still a matter of debate. Whereas Asano et al. [43] interpreted the lowest observed ESR resonance of copper benzoate as the soliton mode, Zvyagin et al. [52] associated the lowest excitation of CuPM as the first breather mode. Since in Ref. [52] seven different excitation modes have been identified, with the assigned soliton resonance being the only one crossing the frequency-field dependence of the other three breather and three multi-particle excitations, the assignment of Ref. [52] seems correct and will be taken as reference for this work.

In contrast to the breather excitations the soliton mass gap $\Delta_S = 8.8$ K, which was used for the fit of the data, is not identical with the experimentally determined ESR energy from Ref. [52], but is related to it by [52]

$$E_s \simeq \sqrt{\Delta_s^2 + (Jv_F k_0)^2}, \qquad (121)$$

with v_F as the Fermi velocity. This difference between E_s and Δ_S follows from a combination of the incommensurability of the soliton mode and the difference of the methods ESR and NMR. Whereas ESR usually probes the dynamic susceptibility at the momentum $q = 0$, NMR is sensitive to different q-components of spin dynamics. This opens up the possibility of a direct detection of spin excitation modes at incommensurate wave vectors by means of microscopic NMR experiments[12].

The results of the fits for $|F_i(\mathbf{q})|$ are shown in Fig. 64, where the hyperfine form factor of each spin excitation mode is plotted against the absolute value of its gap energy Δ_i for the inequivalent carbon sites C1, C2 and C3. It is found that the excitation modes denoted as B1 (breather1) and C3 (edge of soliton-breather continuum SB3) have maximal form factors for all three carbon sites here, while S (soliton) and C2 (edge of soliton-breather continuum SB2) are about a factor $\sim$ 2-5 weaker and B2 could only be detected at the carbon site C3. The latter is attributed to different form factors and thus different sensitivities at the inequivalent carbon sites. Signatures of another breather branch B3, multi-particle excitation mode C1 as well as the additional modes U1 and U2 known from ESR measurements could not be identified in these ^{13}C-NMR measurements. The absence of the remaining four modes probably originates from both *(i)* small intensities due to negligible form factors in NMR measurements and *(ii)* the proximity of various spin excitations, which in a temperature dependent experiment will cause an averaging over the different modes. Thus, an independent determination of each single mode is difficult here. To understand the differences between the excitation modes observed in ESR and NMR, theoretical calculations of the hyperfine form factors would be helpful.

The low temperature $1/T_1$ data for C1 and C2 can be analyzed in an alternative way. In the temperature regime $T \leq 10$ K only the lowest energy excitation mode(s) contributes sig-

---

[12] Strictly speaking, for the fit of the NMR data the gaps of the soliton excitation as well as those of the multi-particle excitations have to be extracted from the ESR resonance frequency following Eq. 121, projecting from $q = 0$ to the corresponding minima in $E(q)$. Due to the large experimental uncertainty in the ESR determination of the lower bound of the two-particle continuum as well as of the intensity distribution within this continuum [52], a conversion of the measured ESR frequency values into multi-particle gaps has been omitted in this work.

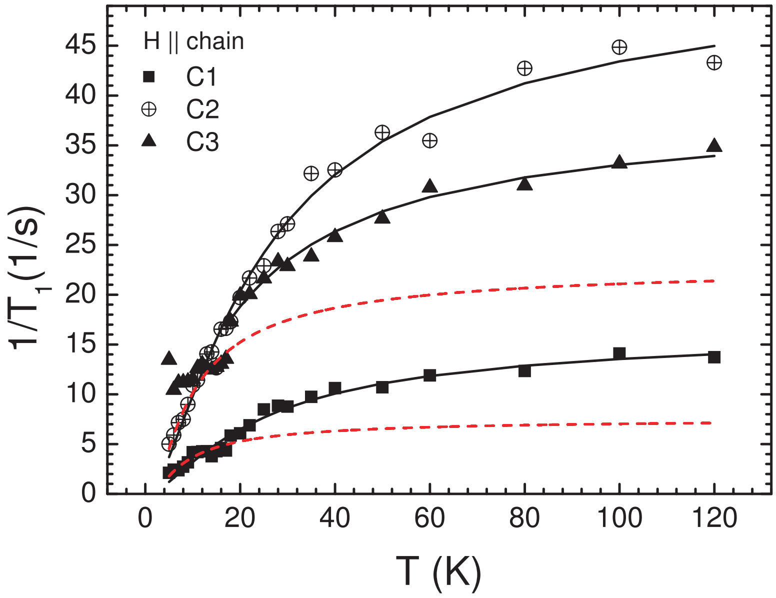

Figure 63: *The temperature dependent spin-lattice relaxation rate* $1/T_1$ *in* $CuPM(NO_3)_2(H_2O)_2$ *in an external field* $\mu_0 H$ *= 9.30 T || to the Cu chains. The solid lines are fits to Eq. 120 in (i) the whole temperature range 5 K≤T≤120 K for C1 and C2 and (ii) 18 K≤T≤120 K for site C3, respectively. The dashed lines for C1 and C2 represent fits to a single-exponential law for 5 K* $\leq T \leq$ *10 K.*

nificantly to the spin-lattice relaxation rate. Therefore, a single-exponential fit has been performed for carbon sites C1 and C2 in the temperature range 5 K $\leq T \leq$ 10 K. The results are shown in Fig. 63 as red dashed lines. While for temperatures $T \leq$ 15 K the experimental data are perfectly described by the fit, additional relaxation processes need to be accounted for in the higher temperature regime in order to describe the experimental spin-lattice relaxation rate, as expected. Absolute values of the lowest excitation mode, *i.e.*, Δ(C1) = (7±2) K and Δ(C2) = (8.1±1.0) K, have been obtained from the fit, which are in very good agreement with the first breather and soliton modes from Ref. [52] for CuPM in a field of $\mu_0 H$ = 9.3 T || to the Cu chains: Δ_{B1} = 7.2 K and Δ_S = 8.8 K.

In addition to the temperature dependent $1/T_1$ experiments, the orientation dependence of the spin-lattice relaxation has been investigated in the dominantly uniform and staggered regime at temperatures T = 30 K and 9 K, respectively[13]. This way, in principle the angular dependence of the hyperfine form factors $|F_i(\mathbf{q})|$ can be obtained for the inequivalent carbon sites.

---

[13] Due to the time consuming experimental procedure, the spin-lattice relaxation time has not been detected for carbon site C2 at T = 30 K.

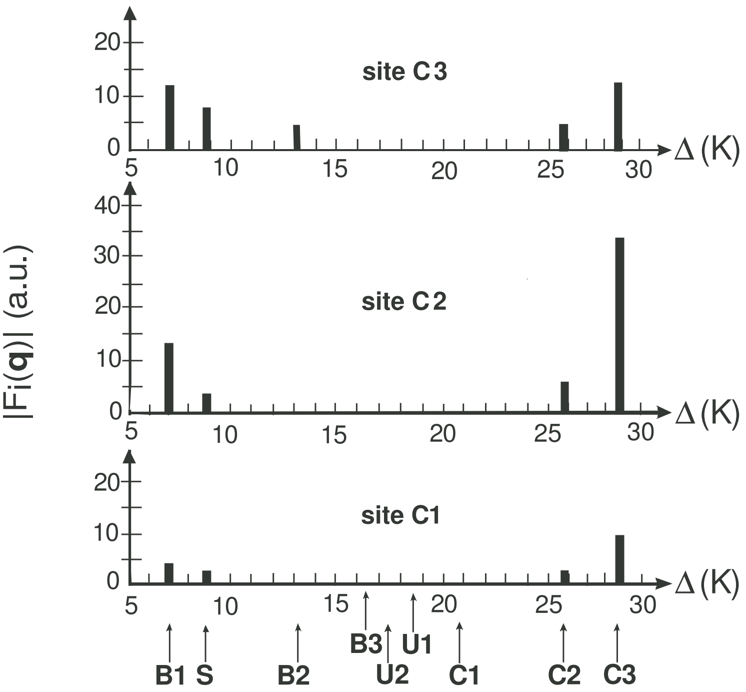

Figure 64: *The spin excitation spectrum of CuPM in an external field $\mu_0 H = 9.30$ T || to the Cu chains determined by ^{13}C-NMR. The nomenclature and absolute values of soliton, breather branches and multi-particle excitation modes are taken from Ref. [52], scaled by a factor $\cos^{2/3}(30°)$ due to a different field geometry.*

T_1 may be sensitive to both transverse and longitudinal spin fluctuations, and thus to different relaxation processes (Eq. 96). In T_1 experiments with the external field H applied along the dipolar principle axes for each carbon site the longitudinal contributions are expected to be absent, implying that relaxation occurs via transverse two-magnon interbranch ($E_A = \Delta(H = 0)$) and three-magnon intrabranch processes ($E_A = 2\Delta$) as the only contributions. Then, with the larger activation energies E_A for transverse spin fluctuations, an increase in the relaxation time T_1 should be visible for low temperatures at sites C1, C2 and C3. Further, with the anisotropy of the spin excitation gap, extremal spin-lattice relaxation times can be expected for the magnetically principal axes of CuPM, *i.e.*, a maximal spin-lattice relaxation time for $H \parallel c''$ and a minimal one for $H \parallel a''$.

The results for the orientation dependent spin-lattice relaxation investigations at $T =$ 30 K and 9 K are shown in Figs. 65(a) and (b), respectively. In the uniform regime at $T =$ 30 K the spin-lattice relaxation time T_1 exhibits two maxima near the dipolar principal axes, *i.e.*, H || and $\perp$ to the Cu chains. In these directions, completely diagonal dipolar hyperfine coupling tensors may lead to the absence of longitudinal spin fluctuations and increase the spin-lattice relaxation time, as discussed above. Whereas for the high-symmetry carbon site C1 the maximum || chain is much more pronounced as the one for $H \perp$ chain, the relative intensity of the maxima is reversed for the low-symmetry site C3.

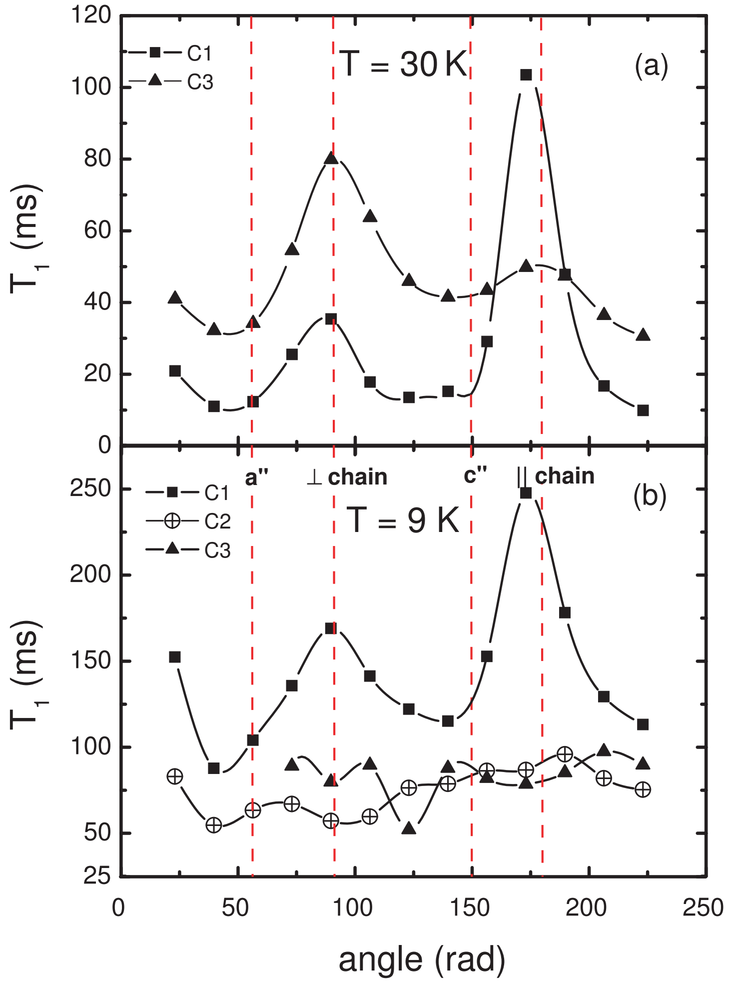

Figure 65: *The orientation dependent spin-lattice relaxation time* T_1 *at* $T = 30$ *K (a) and at* $T = 9$ *K (b) for carbon sites C1, C2 and C3 of* $CuPM(NO_3)_2(H_2O)_2$*, with the external field* $\mu_0 H = 9.30$ *T applied in the ac-plane. The solid lines are guides to the eye.*

In the dominantly staggered regime at $T = 9$ K, the spin-lattice relaxation time for C1 still exhibits two maxima for H || and ⊥ to the Cu chains. The situation changes drastically for carbon site C3. Here, in contrast to the results for the dominantly uniform regime, an approximately constant orientation dependence of T_1 is detected, showing a small minimum in T_1 for an arbitrary crystallographic direction somewhere between ⊥ chain and c''. Further, in Fig. 65(b) the orientation dependence of T_1 for the high-symmetry site C2 is included, which also shows hardly any orientation dependence of T_1 and resembles that of the low-symmetry carbon site C3. Apparently, the dipolar hyperfine coupling at the C2 and C3 site contains significant contributions from neighboring chains, washing out the strong anisotropy found for C1.

The observed anisotropy of T_1 cannot be understood assuming angular independent hyperfine form factors. In that case, a minimum of T_1 would be detected for $H \parallel a''$ and a maximum for $H \parallel c''$ due to the anisotropy of the spin excitation gap. This has neither been observed for the high- nor the low-symmetry carbon sites. Whereas the correlation of T_1 with the directions $\parallel$ and $\perp$ to the Cu chains indicates the dominance of the hyperfine form factor $|F_i(\mathbf{q})|$ for carbon site C1, together with the low-temperature peak in $1/T_1(T)$ it proves the existence of additional relaxation channels not incorporated in the sine-Gordon theory for site C3. Indications for such processes have also been described in Ref. [52], where three additional modes $U1-U3$ with large intensities have been reported, but for which the authors were not able to find an explanation on basis of the SG model.

To reveal the origin of the low-temperature peak, which has been observed for the low-symmetry carbon site C3 for $T < 15$ K in external fields $\mu_0 H = 9.30$ T $\parallel$ chain, additional $1/T_1$ measurements in the temperature interval 1.3 K $\leq T \leq$ 40 K in external fields of $\mu_0 H$ = 3.44 and 6.96 T $\parallel a'$ have been carried out, and which are depicted in Figs. 66(a) and (b), respectively. As can be seen, the spin-lattice relaxation rate $1/T_1$ for carbon site C3 exhibits a broad maximum, which shifts from $T_{max} \sim 2.6$ K for $\mu_0 H = 6.96$ T to $T_{max} \sim 1.5$ K for an external field $\mu_0 H = 3.44$ T, while it becomes smaller in width. This type of appearance of a relaxation mechanism resembles that of the model of Bloembergen, Purcell and Pound (BPP) [165].

In this approach, nuclear spin-lattice relaxation occurs through temporal fluctuations of the local magnetic field, which for instance result from reorientational motions of atoms or molecules. Here, the local field is of the form $< b_\alpha(t) b_\alpha(t+\tau) >_t = < b_\alpha^2 > exp(\frac{-|\tau|}{\tau_c})$, where τ_c is the correlation time. The standard expression for $1/T_1$ is given by Eq. 88 in section 3.1.3:

$$\frac{1}{T_1} = \gamma_n^2 (< b_x^2 > + < b_y^2 >) \frac{\tau_c}{1 + \omega_L^2 \tau_c^2}.$$

A slowing down of magnetic fluctuations means that the fluctuation rate $\nu_{fluc} = 1/\tau_c$ decreases on cooling, leading to an increase of $1/T_1$, which eventually reaches a maximum when $\nu_{fluc} = \omega_L$ (see Fig. 16).

For the analysis, the values $1/T_1$ had to be corrected for the background contributions from the sine-Gordon-like relaxation in the gapped regime, as discussed in the preceding section. Here, due to the absence of absolute values for the hyperfine form factors $|F_i(\mathbf{q})|$ for CuPM in literature, similar relative hyperfine form factors have been used as obtained for $\mu_0 H = 9.3$ T $\parallel$ chain (see Fig. 64). The absolute value of each excitation mode has been taken from Ref. [52] for $\mu_0 H = 3.44$ T and 6.96 T, scaled by a factor $\cos^{2/3}(56^\circ)$ due to a different field geometry. The background parametrization is included in Fig. 66 as black solid lines, with the resulting BPP peak, *i.e.*, the difference between the experimental $1/T_1$ data and the background parametrization, being depicted in Fig. 67(a) for external fields of 3.44 T and 6.96 T.

The fluctuation rate ν_{fluc} can be modelled as a thermally activated process, with activation energy E_A corresponding to the height of the potential barrier between two degenerate

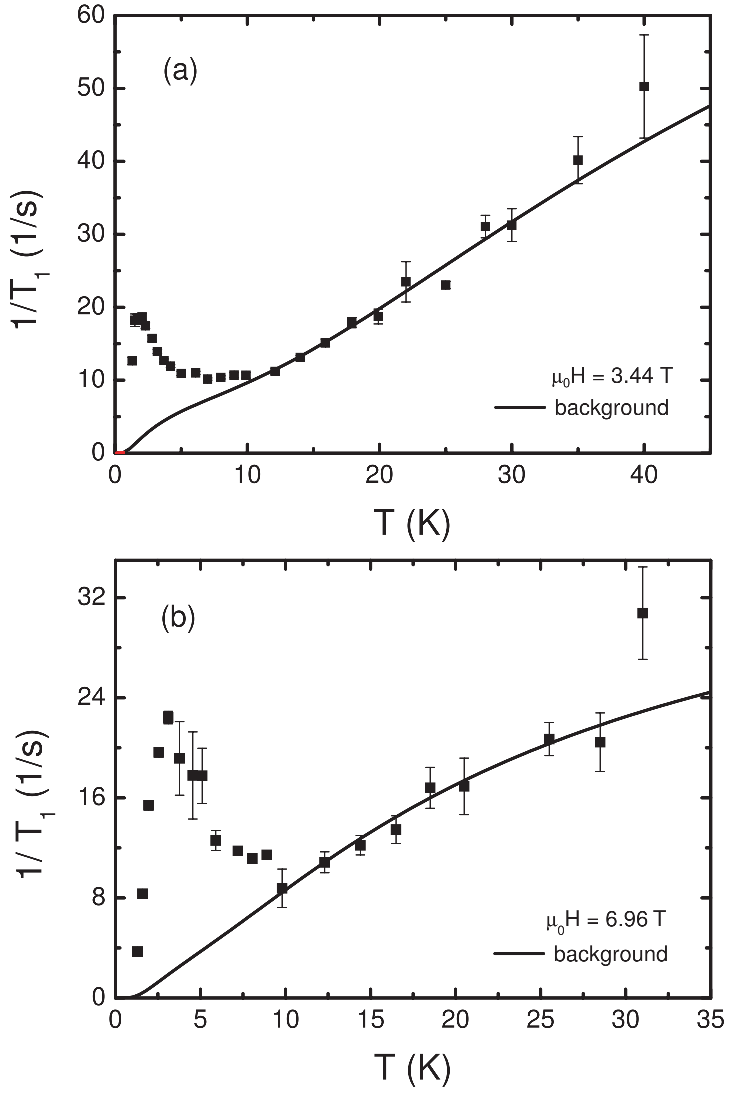

Figure 66: *The temperature dependent spin-lattice relaxation rate* $1/T_1$ *of* $CuPM(NO_3)_2(H_2O)_2$ *for carbon site C3 with the external field (a)* $\mu_0 H = 3.44$ *T and (b)* $\mu_0 H = 6.96$ *T* $\parallel a'$. *The solid black lines represent a parametrization for the background contributions of* $1/T_1$ *according to the excitations of the sine-Gordon model in Eq. 120; for details see text.*

ground state configurations [169, 170, 171]:

$$\nu_{fluc} = \nu_\infty \exp(\frac{-E_A}{k_B T}). \tag{122}$$

The combination of Eq. 122 with Eq. 88 yields

$$\frac{1}{T_1} = \gamma_n^2(< b_x^2 > + < b_y^2 >)\frac{\nu_\infty \exp(\frac{-E_A}{k_B T})}{\nu_\infty^2 \exp(\frac{-E_A}{k_B T})^2 + \omega_L^2}, \tag{123}$$

which has been used to fit the $1/T_1$ data in Fig. 67(a). Activation energies $E_A = (5.6\pm0.5)$ K and $E_A = (8\pm1)$ K have been obtained for fields of $\mu_0 H = 3.44$ T and 6.96 T, respectively, using $\gamma_n^2(< b_x^2 > + < b_y^2 >)$ and ν_∞ as adjustable parameters in the fit. Overall the matching between the experimental data and the fit is good.

According to the BPP theory the activation energy E_A is field independent. Therefore, in order to further test our model a fit combining the results for both fields has been performed. With Eq. 88 the factor $\gamma_n^2(< b_x^2 > + < b_y^2 >)$ can be calculated from the maximum in $1/T_1(T)$, where $\nu_{fluc} = \omega_L$ holds, and thus $1/T_1 = \gamma_n^2(< b_x^2 > + < b_y^2 >)/(2\omega_L)$. Having established[14] the prefactor $\gamma_n^2(< b_x^2 > + < b_y^2 >)$, subsequently the temperature dependence of the fluctuation rate $\nu_{fluc}(T) = 1/\tau_c(T)$ can be evaluated from $1/T_1(T)$, which is depicted in Fig. 67(b). From the combined fit to Eq. 122 an activation energy $E_A = (14\pm2)$ K has been obtained (dashed line).

The discrepancy between the values E_A obtained via the different procedures likely is caused by the complexity of the magnetic behavior of CuPM, in particular by the strong field and temperature dependence of the orientation of its magnetic moments. In this context it should also be noted, that in the framework of the original BPP theory a constant amplitude for the local fluctuating fields $< b_\alpha(t) b_\alpha(t+\tau) >_t$ results in a suppression of the peak with larger applied fields. In the case of CuPM, however, for low temperatures the dynamic susceptibility strongly depends on the external field and thus may change the factor $\gamma_n^2(< b_x^2 > + < b_y^2 >)$. In our analysis for $\nu_{fluc}(T)$, the value for the amplitude of the local fluctuating fields had to be increased by a factor of ~ 2.5 for the data obtained in an external field $\mu_0 H = 6.96$ T. Furthermore, for CuPM the factor $\gamma_n^2(< b_x^2 > + < b_y^2 >)$ becomes temperature dependent in contrast to the original BPP theory. This may result in small variances of E_A for the different fit procedures in this work, since the factor $\gamma_n^2(< b_x^2 > + < b_y^2 >)$ has been extracted either as a temperature average from the $1/T_1(T)$ data or from the $1/T_1(T)$ curve at T_{max}.

An estimate of the sensitivity of ν_{fluc} on the hyperfine form factors used for the background parametrization has been obtained by continuously increasing the relative weight of the multi-particle modes in contrast to the low-energy soliton and breather excitations. In

---

[14] The factor $\gamma_n^2(< b_x^2 > + < b_y^2 >)$ has been determined to (8620±440) $(10^{-3}s)^{-2}$ / (10260±950) $(10^{-3}s)^{-2}$ and 7773 $(10^{-3}s)^{-2}$ / 19233 $(10^{-3}s)^{-2}$ in external fields $\mu_0 H = 3.44$ T / 6.96 T for the independent $1/T_1(T)$ and combined ν_{fluc} analysis, respectively.

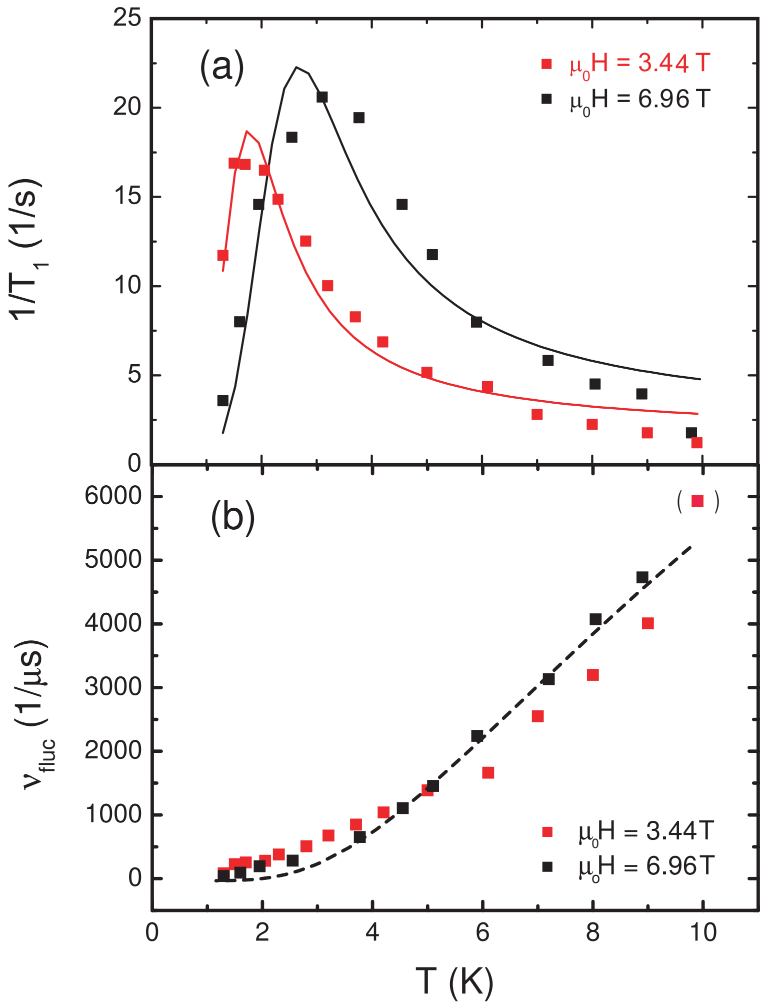

Figure 67: *(a) The temperature dependence of the BPP peak in* $1/T_1$ *for carbon site C3 and* $\mu_0 H$ *= 3.44 T and 6.96 T* $||$ a'*. The solid lines represent fits to Eq. 123. (b) Temperature dependence of the local field fluctuation rate* ν_{fluc}*. The solid line is a fit using a thermally activated behavior for the combined data for* $\mu_0 H$ *= 3.44 T and 6.96 T* $||$ a'*.*

fact, the deviations for ν_{fluc} remain $< 5\%$ for the different parametrizations at both fields $\mu_0 H = 3.44$ T and $\mu_0 H = 6.96$ T.

What is the microscopic mechanism leading to the peak in $1/T_1$ and to the observed activated behavior of $\nu_{fluc}(T)$? Clearly, these local field fluctuations cannot be explained on basis of the SG model. Remarkably, they change the local dipolar field at the low-symmetry carbon site C3 but not at the high-symmetry carbons C1 and C2. For CuPM, a hypothesis which would account for the occurrence of such an additional relaxation channel would be based on a picture of a strongly anharmonic potential, *i.e.*, a double-well potential (DWP) for site C3. From our data the depth of the DWP would be (14±2) K. Similar scenarios have also been proposed in Refs. [169, 170], where a peak in the spin-lattice relaxation rate has been interpreted in terms of a strongly anharmonic potential. In Ref. [170] the relevant molecular reorientation was identified as an intramolecular twisting around the central single bond of the diacethylene unit in disubstituted diacetylene 1,6-bis(2,4-dinitrophenoxy)-2,4-hexadiyne.

A real space realization of such a DWP in CuPM could possibly be a symmetry lowering at the C3 site, in that sense that the C3 atom is dynamically displaced out of its nominal position. A possible scenario is represented by a small dynamic twisting of the pyrimidine molecule along the local pyrimidine symmetry axis, which would correspond to a structural distortion of the system as illustrated in Fig. 68.

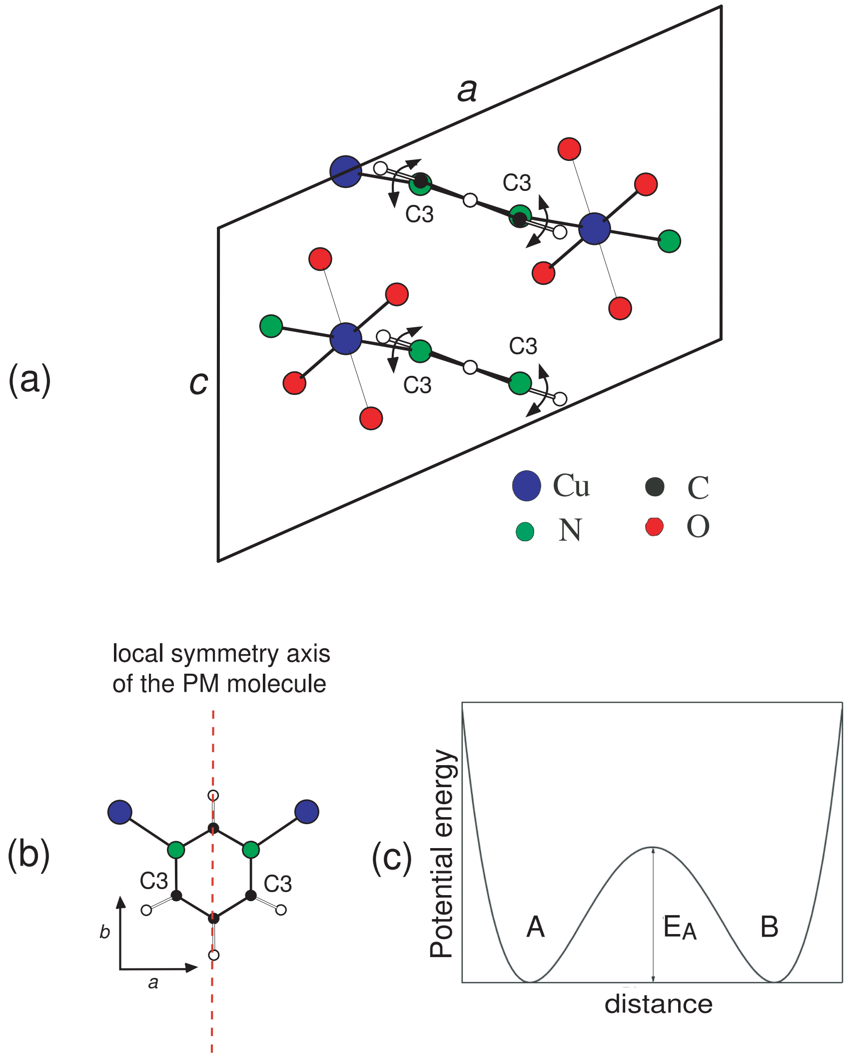

Figure 68: *(a) Schematic representation of a dynamic twisting at carbon site C3, which may possibly be present in CuPM. For clarity, not all atoms of the crystallographic structure are shown. The red dotted line in (b) represents the local symmetry axis of the twisting, i.e., the symmetry axis of the pyrimidine molecule. In (c) a schematic illustration of the strongly anharmonic local potential for carbon site C3 is shown.* E_A *denotes the activation energy.*

In this situation, due to the symmetry lowering an additional line splitting should occur for carbon site C3 for $T < 15$ K . It is recalled that this has been observed, as discussed in section 6.1.2, with Fig. 52 depicting the temperature dependence of the line splitting $\Delta\delta$ at site C3 in an external field $\mu_0 H = 9.30$ T $||$ chain. According to the BPP model, the splitting should strongly depend on the absolute value of the external magnetic field. Thus, in order to test our hypothesis, additional NMR shift investigations have been performed for $\mu_0 H = 3.44$ T, 6.96 T and 9.30 T $||$ a'. The temperature dependent results for site C3 are illustrated in Fig. 69, which qualitatively resemble the curve for the secular line broadening $1/T_2'(\tau_c)$ in Fig. 16, with both an increase of $1/T_2'$ for increasing correlation times and thus decreasing temperatures and a saturation for $T < T_{max}$. The onset of saturation of the splitting can only be recorded for the data in Fig. 69(b), since here the lowest experimental temperature $T = 1.3$ K is sufficiently smaller than $T_{max} \sim 2.6$ K. While the splitting can be observed for temperatures $T_{split} < 15$ K for an external magnetic field $\mu_0 H = 9.30$ T, the onset of splitting is shifted to lower temperatures for smaller field values: $T_{split} < 10$ K for $\mu_0 H = 6.96$ T and $T_{split} < 9$ K for $\mu_0 H = 3.44$ T. Hence, the field dependence of the splitting supports the hypothesis of a dynamic twisting of the pyrimidine molecule along the pyrimidine symmetry axis in CuPM. Surprisingly, the lower frequency line for carbon site C3 starts to split at lower temperatures as the higher frequency one for $\mu_0 H$ $||$ a'. This effect may be attributed to different sensitivities for the two lines due to the local gradient of the shifts as function of angle, as depicted in Fig. 53.

So far, structural investigations of the compound have not revealed evidence for such a distortion. In particular, one would expect either a line splitting or comparatively large values for the thermal displacement parameters, neither of which has been reported. However, these structural experiments have only been carried out for high temperatures [54, 172]. In order to test the proposed double-well potential for the C3 site, a much more detailed structural analysis would be necessary, in particular the temperature dependence of the structural parameters should be investigated.

In principle, a DWP might be observable in specific heat measurements, yielding additional specific heat contributions. Therefore, in order to test the consistency of our model, the specific heat data for $0.5\text{ K} \leq T \leq 15$ K, measured by R. Feyerherm et al. [54], has been reanalyzed. In a first step, to separate the different contributions, it is a common procedure to calculate the lattice parts via Debye and Einstein integrals. From this analysis dominant Debye contributions to the lattice specific heat have been found, with characteristic temperatures of the order of 150 K. Clearly, this is an energy scale distinct from the scale of the proposed DWP and cannot account for the observed relaxation phenomena. The analysis of the remaining specific heat contribution seems to indicate that it is dominated by magnetic fluctuations within the SG scenario. Hence, remaining contributions which might be attributed to a DWP scenario must be much smaller than the other specific heat terms. This would correspond to a small number of activated states for low temperatures $T \leq 15$ K. At present, it is unclear if this notion is consistent with the NMR observations.

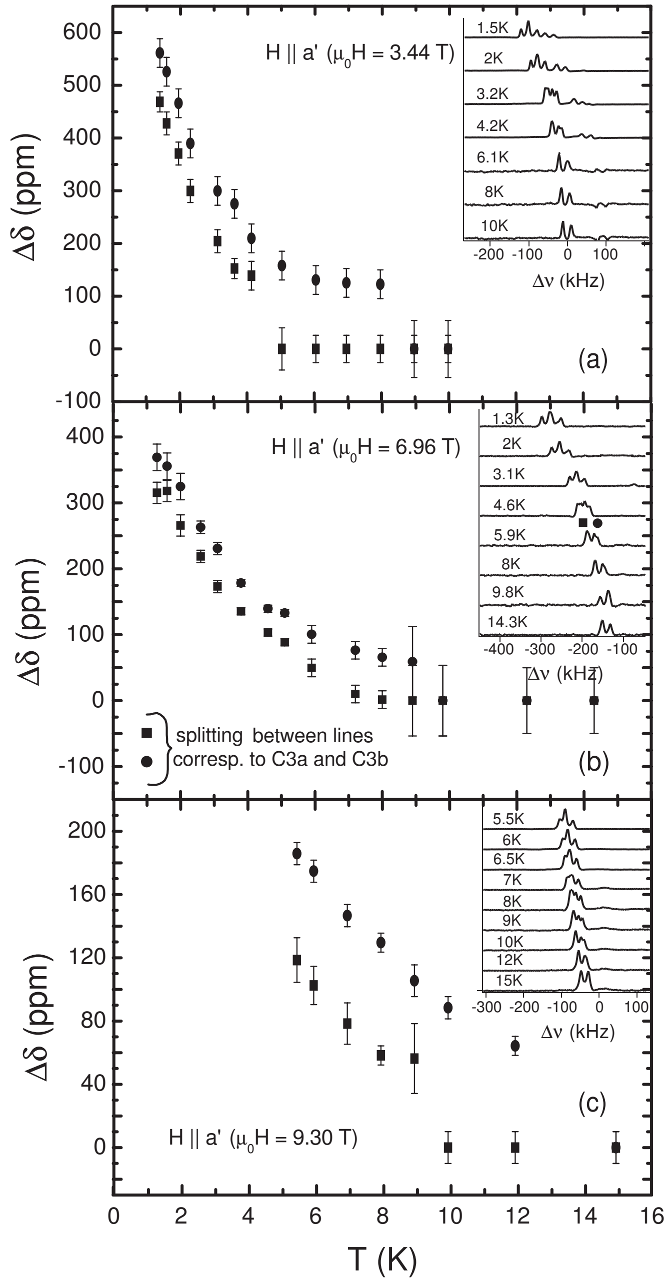

Figure 69: *The temperature dependence of the splitting $\Delta\delta$ between the NMR lines corresponding to carbon sites C3a and C3b for $\mu_0 H$ = 3.44 T (a), 6.96 T (b) and 9.30 T (c) applied along the a' direction. In the inset the NMR spectra of lines C3a and C3b are shown for various temperatures.*

6.2.3 Conclusions and Outlook

To conclude, ^{13}C-NMR experiments on CuPM$(NO_3)_2(H_2O)_2$ have been performed at a constant field of $\mu_0 H = 9.30$ T || chain and temperatures 5-120 K. In this study, the spin-lattice relaxation has been investigated on the three inequivalent carbon sites in CuPM. From a fit of the data to a superposition of various activation laws, using nine spin excitation modes recently found by ESR measurements on CuPM [52], five modes, namely S, B1, B2, C2 and C3, as well as the hyperfine form factors $|F_i(\mathbf{q})|$ have been determined for each carbon site. This way, for the first time a direct detection of bound spinons has been achieved via NMR measurements.

Surprisingly, orientation dependent spin-lattice relaxation investigations of CuPM for an external field $\mu_0 H = 9.30$ T as well as field dependent $1/T_1$ experiments for carbon site C3 in external magnetic fields $\mu_0 H = 3.44$ T and 6.96 T || a' reveal additional relaxation channels beyond the sine-Gordon model. A low-temperature peak in the spin-lattice relaxation rate for site C3 has been discussed on basis of the BPP theory and suggested to arise from a small dynamic twisting of the pyrimidine molecule along the pyrimidine symmetry axis.

For future studies of staggered $S = 1/2$ AFHCs, theoretical calculations of the form factors $|F_i(\mathbf{q})|$ and dynamic spin susceptibilities $\chi''(\mathbf{q}, \omega_L)$ would be helpful. Further, thorough temperature dependent structural investigations of the thermal displacement parameters for the atoms on the PM molecule as well as Raman scattering experiments will be useful in order to explain additional relaxation contributions, whose existence has already been revealed via ^{13}C-NMR and ESR [52] studies.

6.3 Pressure Studies on CuPM Dinitrate

Molecule-based magnets, with their structure consisting of magnetic units assembled within a supermolecular aggregate of organic components, tend to be soft materials. Therefore, they are fairly sensitive to the application of external pressure, as has been demonstrated for instance for purely organic magnets [173, 174, 175]. Unusual pressure dependencies have been observed, like periodic up/down variations of ferromagnetic transition temperatures or pressure induced ferro- to antiferromagnetic transitions. This reflects that applying pressure to a molecule-based magnet affects its properties by the variation of two structural entities: *(i)* the distance between the magnetic ions and *(ii)* the geometry of the exchange path.

In particular the latter, that is the ability to tune the properties of a magnet by modifying the geometric arrangement of nonmagnetic components, distinguishes molecular from conventional magnets. In consequence, to understand the interplay of structural and magnetic properties in molecule-based magnets it is necessary to determine the pressure dependence of both structural and magnetic parameters.

As has been demonstrated by a comparison of the staggered $S = 1/2$ AFHCs CuPM$(NO_3)_2$ and CuPM$(NO_3)_2(H_2O)_2$ [176], the characteristic parameters of such systems, *i.e.*, the magnetic coupling constant J/k_B and the spin excitation gap Δ, can be varied by applying chemical pressure. Correspondingly, a detailed structural and magnetic study of the staggered $S = 1/2$ antiferromagnetically coupled Heisenberg spin chain CuPM$(NO_3)_2(H_2O)_2$ as function of applied hydrostatic pressure will be useful, as it will yield more insight into the relationship of crystallographic structure/geometry and magnetic coupling. Therefore, in this chapter pressure dependent single-crystal ^{13}C-NMR shift and spin-lattice relaxation measurements of CuPM will be presented. From these studies the magnetic exchange parameter J/k_B and the size of the spin gap Δ have been determined as function of pressure. The observed response is discussed in comparison to related molecular materials.

6.3.1 Experimental Details

For the pressure dependent NMR shift and spin-lattice relaxation experiments the same single crystal as for the study of the field dependence of the spin-lattice relaxation has been used (size $\sim 4 \times 3 \times 4$ mm^3). The sample was prepared for the pressure experiments as discussed in sec. 3.1.5. Since a maximal sample size, *viz.*, filling factor, is the prime requirement in the pressure experiments, with the shape of the sample an alignment of the field along the crystallographic a'-axis was chosen. The NMR measurements were carried out as described in sections 6.1.1 and 6.2.1, using a home-built spectrometer in quadrature detection with a superconducting magnet operating at a constant field of 9.30 T and temperatures between 5 and 120 K.

6.3.2 Results and Discussion

The NMR shift at ambient pressure and at 10 kbar is presented in Fig. 70. As before, three sets of double pairs of lines from the hydrogen-split inequivalent carbon sites are detected (see section 6.1.2). The solid and dashed lines in Fig. 70 represent a fit to the staggered S = 1/2 AFHC model, $\delta = \sigma_0 + A_{dip,\uparrow\uparrow}(\chi_u(T) + \chi_{s||}(T)) + A_{dip,\uparrow\downarrow}\chi_{s\perp}(T)$, which combines the chemical shift (σ_0) with the longitudinal ($\chi_u(T) + \chi_{s||}(T)$), and the transverse susceptibility contributions ($\chi_{s\perp}(T) = C_s^*/T$) of a staggered S = 1/2 AFHC. In the uniform regime for T > 30 K, the staggered contributions, *i.e.*, $\chi_{s||}$ and $\chi_{s\perp}$, are negligible.

Whereas for sites C1 and C2 positive hyperfine coupling constants $A_{dip,\uparrow\uparrow}$ and negative values for $A_{dip,\uparrow\downarrow}$ are used, both coupling constants are negative for site C3. Using the Bonner-Fisher behavior of the uniform S = 1/2 AFHC for $\chi_u(T)$ given in Eq. 17 and Curie-like contributions for $\chi_{s\perp} = C_s^*/T$ and $\chi_{s||} = C_s/T$, the exchange parameter J/k_B is determined to J/k_B = (36.5 ± 0.3) K for C1, C2 and J/k_B = (36.7± 2) K for C3 for ambient pressure as well as for 10 kbar. At ambient pressure, this is in perfect agreement with J/k_B = 36 K from susceptibility investigations in Ref. [54] and J/k_B = 36.3(5) K from high-field magnetization experiments. Analogously, the sum of the staggered contributions to the NMR shift have been obtained from the fit for T < 30 K at ambient and applied pressure. Within the error bars of the fit (< 7%), the staggered part of the NMR shift seems also not to be affected by the application of 10 kbar.

Furthermore, in order to investigate the response of the spin excitation gap under hydrostatic pressure spin-lattice relaxation measurements of CuPM have been performed at ambient pressure and 10 kbar. The results are depicted in Fig. 71. From this figure a temperature dependence of $1/T_1$ following an Arrhenius law as described in Eq. 120, $1/T_1 \sim \sum_{\mathbf{q},i} |F_i(\mathbf{q})| exp(-\Delta_i(\mathbf{q})/T)$, is found for carbon sites C1, C2 and C3[15].

Whereas the qualitative and quantitative behavior of $1/T_1(T)$ for carbon sites C2 and C3 for both ambient and applied pressure resembles that presented in section 6.2.2 for $H \parallel$ chain, the absolute values of $1/T_1$ for carbon site C1 are increased, which would correspond to much larger values for Δ_i as in the case of sites C2 and C3. The origin of the increase in the spin-lattice relaxation is presently not clear. According to the orientation dependent $1/T_1$ data from Fig. 65, an enhanced spin-lattice relaxation rate for $H \parallel a'$ indicates either the dominance of the hyperfine form factor $|F_i(\mathbf{q})|$ compared to the anisotropy of the spin excitation gap for carbon site C1, or the existence of additional relaxation channels beyond the sine-Gordon theory. Thus, a fit to the temperature dependent spin-lattice relaxation rate for ambient pressure and 10 kbar, following Eq. 120 and using the nine different excitation modes from Ref. [52], fails to work in this case.

From a single-exponential fit for carbon sites C1 and C2 in the range 5 K $\leq T \leq$ 10 K, a quantitative estimate for the pressure dependence of the lowest observable excitation mode can be derived. Absolute values of Δ(C1) = (7±1.5) K, Δ(C2) = (8±1) K and Δ(C1) = (6.6±1) K, Δ(C2) = (9.8±1.4) K have been obtained at ambient pressure and 10 kbar, respectively. They are in good agreement with the soliton and second breather modes from Ref. [52] for CuPM in a field of $\mu_0 H = 9.30$ T $\parallel a'$, *i.e.*, $\Delta_S = 6.6$ K and $\Delta_{B2} = 9.8$ K. Thus, within the experimental error the size of the gap Δ seems also not to be affected by the application of 10 kbar.

In a recent study on a related compound, FePM$_2$Cl$_2$, a combined structural and magnetic study has been performed via neutron powder diffraction and susceptibility experiments under externally applied hydrostatic pressure. FePM$_2$Cl$_2$ belongs to a series of magnetically ordered transition metal complexes of the general formula TX$_2$(PM)$_2$, T = Fe, Co, Ni and X = Cl or Br [134, 135]. The transition metal ions are connected via pyrimidine rings, thus forming a three-dimensional network of transition metal-pyrimidine complexes. In consequence, a pyrimidine ring mediated superexchange yields magnetic coupling between the metal ions, causing transitions into long-range magnetically ordered states at low temperatures [177]. Pressure dependent susceptibility measurements indicated a persistence of the canted antiferromagnetic state of FePM$_2$Cl$_2$, demonstrating that applying pressure does not change the overall magnetic behavior. The pressure response of the antiferromagnetic transition temperature T_N, however, increases by more than 20 % in about 7 kbar (see Fig. 72). This large response reflects the softness of the lattice and is a consequence of the reduction of the superexchange pathway. It leads to an increase of the orbital overlap between Fe and

---

[15] For carbon site C3 additional contributions to the spin-lattice relaxation have to be considered for temperatures $T < 15$ K, as described in section 6.2.2.

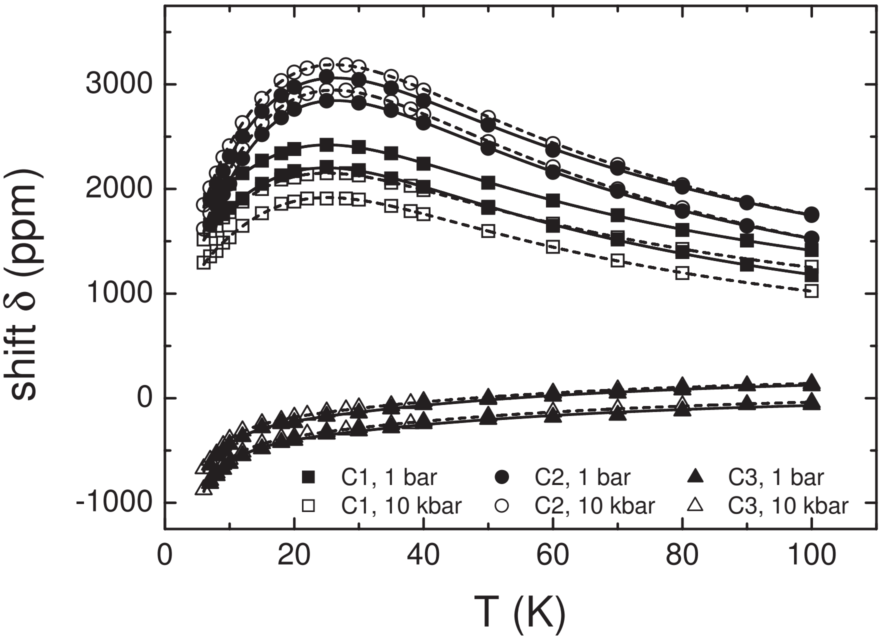

Figure 70: *The temperature dependence of the NMR shift for the three inequivalent carbon sites of CuPM at ambient pressure and 10 kbar for* $\mu_0 H = 9.30$ *T* $\|$ a'*. The solid and dashed lines represent fits to the staggered* $S = 1/2$ *AFHC model,* $\delta = \sigma_0 + A_{dip,\uparrow\uparrow}(\chi_u(T) + \chi_{s||}(T)) + A_{dip,\uparrow\downarrow}\chi_{s\perp}(T)$*; for details see text.*

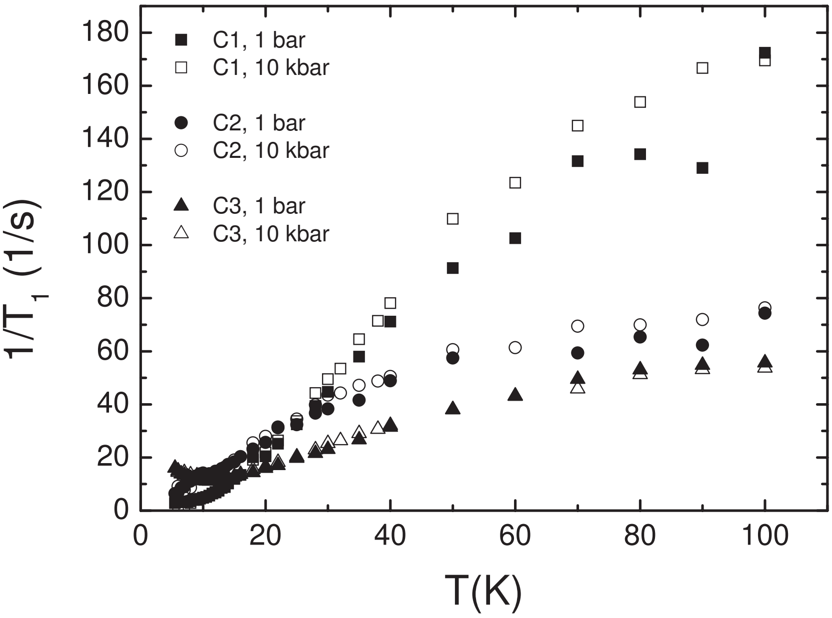

Figure 71: *The temperature dependence of* $1/T_1$ *at ambient pressure and 10 kbar for the three inequivalent carbon sites C1, C2 and C3 of CuPM and* $\mu_0 H = 9.30$ *T* $\|$ a'*.*

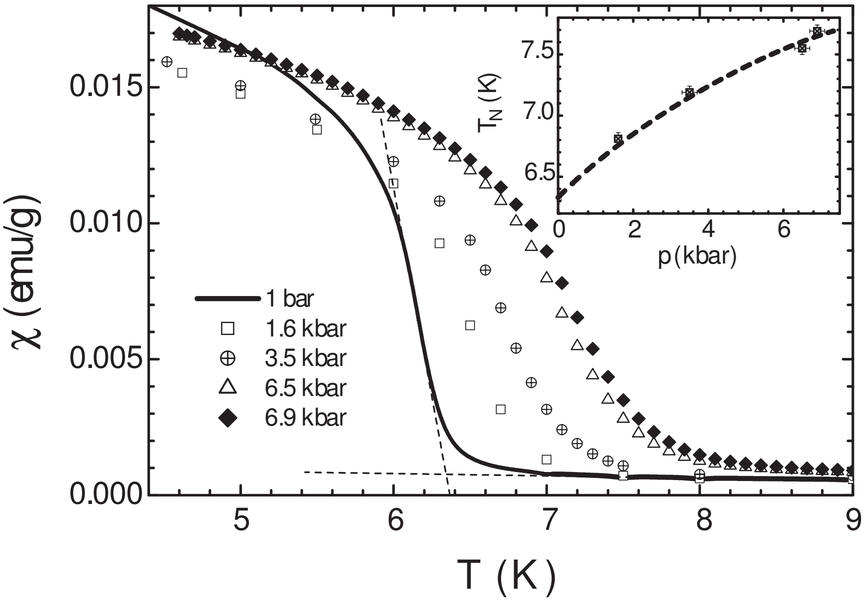

Figure 72: *The temperature dependence of the susceptibility of* $FePM_2Cl_2$ *in a field of 0.1 T for ambient and externally applied pressure. In the inset the pressure dependence of the antiferromagnetic transition temperature of* $FePM_2Cl_2$ *is shown.*

the PM molecule, which controls the interaction strength. Because the same magnetic exchange path is present in CuPM, a significant increase of J/k_B would be expected by applying hydrostatic pressures of ~ 10 kbar. As this has not been detected, it indicates that other structural parameters also control the magnetic coupling in CuPM.

This hypothesis is supported by a study of $CuPM(NO_3)_2$, the dehydrated analogue of $CuPM(NO_3)_2(H_2O)_2$ [176]. In this material, the general structural motif, namely the formation of infinite Cu-PM chains, is retained. The intrachain Cu-Cu distances are increased from 5.71 Å in $CuPM(NO_3)_2(H_2O)_2$ to 5.80 Å in $CuPM(NO_3)_2$, while the interchain distance is very significantly reduced (6.84 Å vs. 5.98 Å). In contrast to the hydrated compound, where the Cu ions are sixfold coordinated, dehydration leads to a fourfold coordination of the Cu ions in $CuPM(NO_3)_2$. The temperature dependence of the magnetic susceptibility exhibits the characteristic features of a staggered $S = 1/2$ AFHC, but with an increased magnetic coupling constant $J/k_B = 46$ K and a reduced staggered susceptibility compared to the parent compound $CuPM(NO_3)_2(H_2O)_2$. Here, the stronger coupling was related to the change of the Cu-N-C bond angle from 116.9° in $CuPM(NO_3)_2(H_2O)_2$ to 115.4° in $CuPM(NO_3)_2$ upon increasing the Cu-Cu distance [176]. The reduction of the staggered field on the contrary has been associated with the smaller staggering angle between the g-tensors of neighboring Cu ions (± 16.2° in $CuPM(NO_3)_2$ vs. ± 30.8° in $CuPM(NO_3)_2(H_2O)_2$).

In view of these results on $FePM_2Cl_2$ and $CuPM(NO_3)_2$, it appears that in CuPM two competing effects control the magnetic exchange, *i.e.*, *(i)* increasing the orbital overlap enhances J/k_B, while *(ii)* increasing the Cu-N-C bond angle reduces it. As a result, a negligible change of J/k_B is observed in pressurized CuPM. To verify this hypothesis high pressure structural investigations to determine the compressibility and pressure induced structural modifications of CuPM should be carried out.

6.3.3 Conclusions and Outlook

Summarizing, NMR shift and spin-lattice relaxation experiments on the staggered $S = 1/2$ antiferromagnetic Heisenberg chain CuPM$(NO_3)_2(H_2O)_2$ have been carried out at ambient pressure and an applied pressure of 10 kbar. Unlike other molecule-based magnets, the magnetic properties of CuPM, *i.e.*, the magnetic coupling constant along the Cu chain J/k_B, the staggered susceptibility χ_s and the spin excitation gap Δ, are not affected by the application of 10 kbar. Comparing these results to previous studies on FePM$_2$Cl$_2$ and on the dehydrated analogue of CuPM [176], it appears that in CuPM two competing effects control the magnetic exchange. While an increase of the orbital overlap seems to enhance J/k_B, an increase of the Cu-N-C bond angle seems to reduce it.

An alternative way to tune the magnetic properties of a material is the application of chemical instead of hydrostatic pressure. Aside from dehydration [176], it can also be achieved by doping on the metallic ion and/or organic ligand site. In this context, impurity effects in quantum spin chains have attracted recent interest [178, 179, 180, 181, 182, 183], since even a nonmagnetic defect may disturb the correlated ground state of the bulk quite substantially and locally restore magnetic behavior. For Cu^{2+} with periodic boundary conditions, each $S = 1/2$ forms a singlet with its nearest neighbor. Introducing a nonmagnetic impurity through doping is equivalent to removing one $S = 1/2$. This is expected to give rise to two free $S = 1/2$ at each end of the chain. The general case of half-integer-spin Heisenberg chains has been considered by Eggert and Affleck [178, 179], who found that the local susceptibility near an open end of a semi-infinite chain has a large alternating component. This means that a uniform magnetic field will induce local staggered magnetization near the chain end, which approximatively increases as $1/T$ with decreasing temperature.

Hence, for the staggered $S = 1/2$ AFHCs considered in this work, by doping with nonmagnetic impurities we expect to see an increase of the Curie-like contributions at low temperatures. Here, as a first approximation for $T > 0.15J/k_B$, the two different Curie contributions, which either stem from the intrinsic or from the impurity-induced staggered field, should simply add to each other.

In a first step towards a controlled doping of nonmagnetic impurities in staggered $S = 1/2$ AFHCs, single crystals of $\sim$ 10% Mg or Zn doped $Cu_{0.9}X_{0.1}(C_6H_5COO)_2{\cdot}3H_2O$, Z = (Mg, Zn), have been synthesized following the recipe in section 5.2.1. Isovalent Mg and Zn ions have been used for these experiments with their ionic radius in octahedral coordination being similar to Cu^{2+}. Note, that the value of $\sim$ 10% only represents the nominal composition as estimated from the molar ratio between $CuSO_4{\cdot}5H_2O$ and $MgSO_4{\cdot}7H_2O/ZnSO_4{\cdot}7H_2O$. For a detailed study of the magnetic properties as function of doping, a complete structural

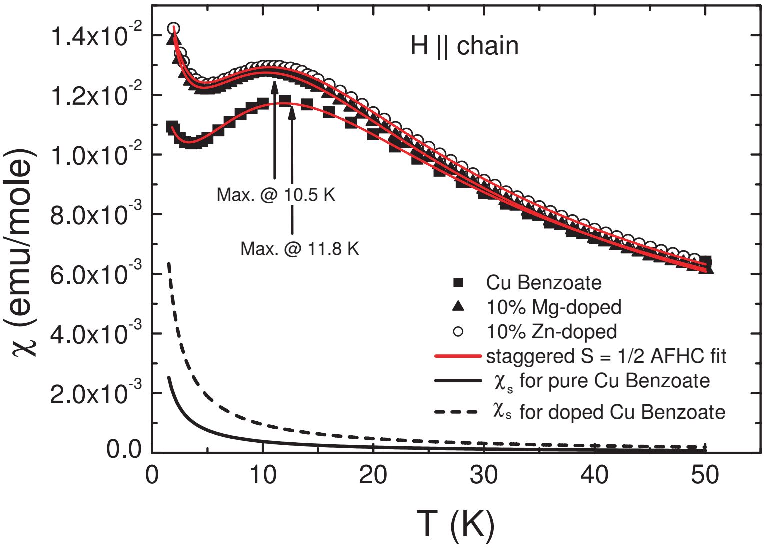

Figure 73: *The temperature dependence of the magnetic susceptibility of $Cu_{0.9}X_{0.1}(C_6H_5COO)_2 \cdot 3H_2O$, X = Mg, Zn. The red solid lines represent fits to the staggered S = 1/2 AFHC model, $\chi(T) = \chi_u(T) + \chi_{s||}(T)$, which combines the uniform susceptibility, $\chi_u(T)$, with the staggered one, $\chi_{s||}(T) = C_s/T$. The staggered part, as obtained from the fit, is shown as solid and dashed black lines for pure and doped copper benzoate, respectively.*

analysis of the doped samples will be necessary.

Fig. 73 depicts the temperature dependence of the magnetic susceptibility of $\mathrm{Cu_{0.9}X_{0.1}}$ $(\mathrm{C_6H_5COO})_2 \cdot 3\mathrm{H_2O}$, X = Mg/Zn. The red solid lines represent fits to the staggered S = 1/2 AFHC model, $\chi(T) = \chi_u(T) + \chi_{s||}(T)$, which combines the uniform susceptibility, $\chi_u(T)$, with a staggered one, $\chi_{s||}(T)$. Using the Bonner-Fisher behavior of the uniform S = 1/2 AFHC for $\chi_u(T)$ (Eq. 17) and a Curie-like contribution for $\chi_{s||}$, the exchange parameter J/k_B can be determined. A slight decrease of the magnetic coupling constant has been derived, with J/k_B = 19.1(2) K for the parent compound $\mathrm{Cu(C_6H_5COO)_2{\cdot}3H_2O}$, J/k_B = 17.9(1) K for $\mathrm{Cu_{0.9}Mg_{0.1}(C_6H_5COO)_2 \cdot 3H_2O}$ and J/k_B = 18.5(1) K for $\mathrm{Cu_{0.9}Zn_{0.1}(C_6H_5COO)_2 \cdot 3H_2O}$. The Curie contribution as obtained from the fit, which contains both intrinsic and impurity contributions, is shown in Fig. 73 as solid and dashed black lines for pure and doped copper benzoate, respectively. As expected, an increase of $\chi_s(T)$ is observed, which for the doped compounds is more than twice as large as for the pure material. Following these results, for future activities in this field it will be interesting to perform a combined experimental and theoretical study of controlled doping with nonmagnetic impurities in S = 1/2 AFHCs. This way, according to recent experiments [180, 184, 185, 186] the magnetic correlation of low-dimensional AFHCs can be investigated as function of doping in a sophisticated way.

7 Summary

In this thesis the magnetization and the dynamic spin excitations of two $S = 1/2$ antiferromagnetically coupled Heisenberg chains ($S = 1/2$ AFHC) with alternating local symmetry, *i.e.*, copper pyrimidine dinitrate, $CuPM(NO_3)_2(H_2O)_2$ (PM = pyrimidine = $C_4N_2H_4$), and copper benzoate, $Cu(C_6H_5COO)_2 \cdot 3H_2O$, have been investigated and discussed. Due to the exotic character of the spin polarization on the copper ions, a combined macroscopic and microscopic study via high-field magnetization and ^{13}C-NMR experiments has been chosen to study this class of materials.

The case of an alternating local environment of the magnetic ion can be treated theoretically including the Dzyaloshinskii-Moriya interaction and/or a staggered g-tensor, both as consequence of a residual spin-orbit coupling [39, 40]. Whereas the Heisenberg exchange $J\mathbf{S}_i \cdot \mathbf{S}_{i+1}$ prefers collinear spin arrangements, the DM interaction $\mathbf{D} \cdot (\mathbf{S}_i \times \mathbf{S}_{i+1})$ prefers canted ones. The combination gives rise to an effective staggered field h_s perpendicular to the applied magnetic field H. Resulting from this extension of the uniform $S = 1/2$ antiferromagnetic Heisenberg chain are additional magnetization components parallel and perpendicular to the external field, the opening of an anisotropic field-induced spin excitation gap and new, particle-like excitations such as solitons, antisolitons and their bound state, the "breather" [41, 43]. Whereas these effects are most pronounced for the magnetically main axis c'', they vanish for one direction perpendicular to c'' in the ac-plane, which is referred to as a''. These features demonstrate that the ground state magnetic properties of the ideal $S = 1/2$ AFHC are highly sensitive to even small modifications. Hence, these materials open the unique possibility to directly study and compare the critical behavior of an ideal $S = 1/2$ AFHC chain with the one of a spin chain that has been exposed to small perturbations.

Via high-field magnetization investigations in the directions of maximum and zero spin excitation gap the qualitatively different behavior of the different longitudinal magnetization components has been established. The data have been analyzed via exact diagonalization of a linear spin chain with up to 20 sites, on basis of the thermodynamic Bethe ansatz equations or via the transfer matrix renormalization group (TMRG) method. For both directions a very good agreement between experimental data and theoretical calculations is found. The magnetic coupling strength J/k_B along the chain direction has been extracted to 36.3(5) K and 18.9(1) K for copper pyrimidine dinitrate and copper benzoate, respectively, and the field dependence of the staggered magnetization component m_s has successfully been determined. The anisotropy parameter $c = 0.11$ and $c = 0.043$, which relates the staggered field h_s to the external uniform field H, $c = h_s/(gH)$, has been obtained for copper pyrimidine dinitrate and copper benzoate, respectively.

Further, in this work for the first time the existence of the transverse staggered magnetization for $CuPM(NO_3)_2(H_2O)_2$, together with a determination of its magnitude and temperature dependence has been directly proven by means of a microscopic technique, *viz.*, NMR. From the local susceptibility measured by ^{13}C-NMR at the three inequivalent carbon sites on the pyrimidine molecule a giant spin canting has been deduced. The averaged magnitude of the transverse magnetization for the three inequivalent carbon sites, the spin canting of (52±4)° at 10 K and 9.3 T external field || to the Cu chains, and its temperature dependence are in excellent agreement with exact diagonalization calculations on basis of the staggered $S = 1/2$ AFHC model.

Moreover, temperature dependent spin-lattice relaxation investigations on copper pyrimidine dinitrate have been performed to study the proposed particle-like spin excitations. From these studies the magnetic excitation spectrum of copper pyrimidine dinitrate has been deduced at a constant applied magnetic field of 9.3 T. The experimental data have been discussed in context with recent ESR investigations, which have been interpreted in terms of breather, soliton and multi-particle excitations based on the quantum sine-Gordon field theory. In addition, for low temperatures $T < 10$ K an enhanced spin-lattice relaxation rate and a line splitting for the low-symmetry carbon site proves the existence of additional relaxation channels beyond the sine-Gordon theory. It has tentatively been attributed to local field fluctuations, possibly stemming from a small dynamic twisting of the pyrimidine molecule along the local pyrimidine symmetry axis [170].

Projects, which are in progress or envisaged for the near future, include an investigation of *(i)* a predicted low-field/high-field crossover in the staggered magnetization of copper benzoate [123] and of *(ii)* a pronounced variance in the susceptibility data for different samples of copper benzoate. The sample dependencies may be related to dehydration, leading to micro cracks in the sample. This scenario in principle can be tested via synchrotron X-ray diffraction studies, in order to probe the width and diffusive background of the Bragg peaks.

Concerning CuPM, electronic structure calculations for the staggered regime will be informative to clarify the origin of a variance in the transverse staggered magnetization for the three inequivalent carbon sites. At this point, it has been attributed to the localized dipole approximation used to calculate the dipolar hyperfine coupling tensors. Last but not least, a direct experimental proof for the theoretically proposed finite-size effects of finite $S = 1/2$ antiferromagnetic Heisenberg chains should be useful. Finite chains can be realized by doping nonmagnetic defects, allowing a direct test of exact diagonalization results on finite spin chains through experiment.

A Dipole Programme

The FORTRAN programme, which has been used for the calculation of the dipolar hyperfine tensors $\overleftrightarrow{A}_{dip,\uparrow\uparrow}$ and $\overleftrightarrow{A}_{dip,\uparrow\downarrow}$ for the carbon sites C1, C2 and C3, has initially been written by H.-H. Klauss from the Institute of Condensed Matter Physics, TU Braunschweig, Germany. It has been adapted to the specific crystallographic structure of copper pyrimidine dinitrate and to the specific conditions of this thesis, with the changes being summarized in the following:

- The factor 9.271 in the formula for the calculation of the tensor elements $A_{dip,ij}$ has been substituted by the factor 1.66 in order to obtain the tensor in units $mole/emu$ instead of kG/μ_B.

- Since the tensor is given in cartesian coordinates, a transformation of the initial atomic coordinates into cartesian coordinates a, b and c_{cart} had to be performed (see formula for XX, YY, ZZ in the programme). This way, a correct consideration of the monoclinic crystallographic structure of CuPM has been achieved.

- The calculation of off-diagonal elements $A_{dip,ij}$ $(i \neq j)$ had to be implemented into the programme due to the anisotropic g-tensor of CuPM, which results in an anisotropic susceptibility tensor.

- A subroutine for a calculation combining different magnetic moments on different magnetic sublattices, *i.e.*, the Cu and two N sublattices, has been added in the programme. Hereby, a magnetic moment transfer of the Cu moments to the N atoms of the pyrimidine molecule could be achieved. Via the new variables `FAKTOR` and `VORZEICH`, the magnitude of this transfer and the relative orientation of the magnetic moments in one sublattice as well as in different sublattices could be adjusted.

The programme and an example for the .start file, which contains specific parameters such as the positions of the probing nuclei, the amount of a possible moment transfer to neighboring atoms, and the size of the sphere surrounding the off-atom, are given in the following:

```
cupm: Tensorberechnung Axx, Ayy, Azz, und Nicht-Diagonalelemente

 1                           #GITTERTYP
 12.17   11.46   7.47        #GITTERKONSTANTEN
 0.5  0.52711   0.25         #SONDENPLATZ
 0                           #SPINTRANSFER
 0.5                         #MAGNETISCHES MOMENT
 12.0                        #EINFLUSSRADIUS
```

```
      PROGRAMM ATENSOR

************************************************************************
*                                                                      *
*     Dieses Programm berechnet Hyperfeinwechselwirkungstensoren in    *
*     CuPM Nitrat mit magnetischen Untergittern.                       *
*     EINHEIT des TENSORS : mol/emu   !!!!!!!                          *
*     Datum 16.4.02    H.-H. Klauss, modifiziert von A.U.B. Wolter     *
*                                                                      *
*     Belegung der I/O-Kan{le:                                         *
*     Kanal 1     Parameterinput                                       *
*     Kanal 2     Ergebnisausgabe f}r Protokollfile                    *
*                                                                      *
************************************************************************

      IMPLICIT REAL*8 (A-H,O-Z)

      INTEGER   NMAX,KMAXZEL
      PARAMETER (NMAX = 50000)

      INTEGER NSPIN(2,NMAX),GITTYP,MAXZEL,KANAL
      INTEGER TNSPIN(6),TTSPIN,NSHELL(6)

      REAL*8 RMAX,RAD,SHRAD(2,NMAX),BMY(2,NMAX,9),BMYUG(2,9)
      REAL*8 BMYG(9),SPDVAL,SPBETR,MYSITE(3)
      REAL*8 MAXGIT,KREALMAX
      REAL*8 WINVEK(100)
      REAL*8 Mysite0(3),VORZEICH,FAKTOR

      CHARACTER TITLE*60

      LOGICAL INSERT

      COMMON / LCELL /  A,B,C,SITE,UGANZ,SPANZ
      INTEGER  UGANZ,SPANZ(6),FILELAENGE
      REAL*8 A,B,C,SITE(6,16,3)
      CHARACTER*20 FILENAME

C*******************************************************
```

```
C*Oeffnen der files
C*******************************************************
C
         WRITE(6,*) 'FILENAME BITTE: '
         READ(5,'(A)')  FILENAME
         FILELAENGE = INDEX (FILENAME, ' ')
         FILELAENGE = FILELAENGE -1
         OPEN (UNIT=1, FILE=FILENAME(1:FILELAENGE)//'.'//'start',
     &   ERR =258, STATUS='UNKNOWN')
         OPEN (UNIT=2, FILE=FILENAME(1:FILELAENGE)//'.'//'proto',
     &   ERR =258,
     &   STATUS='UNKNOWN')
C
         GOTO 259
 258     WRITE(6,*) 'ERROR IM LESEN VON DATEI'
 259     CONTINUE

C***********************************************************************
C     Einlesen der Parameter:
C***********************************************************************

      READ(1,'(A60)') TITLE
      READ(1,*)   GITTYP
      READ(1,*)   A,B,C
      READ(1,*)   (MYSITE0(I),I=1,3)
      write(*,*) (mysite0(i),i=1,3)
      READ(1,*)   SPDVAL
      READ(1,*)   SPBETR
      READ(1,*)   MAXGIT

C***********************************************************************
C     Ausgabe des Titels :
C***********************************************************************

      WRITE(2,*)
      WRITE(2,*)  ' ---------------------------------------------------
     &------------ '
      WRITE(2,*)  ' ---------------------------------------------------
     &------------ '
      WRITE(2,*)' D I P O L F E L D   A M   S O N D E N O R T '
      WRITE(2,*)  ' ---------------------------------------------------
     &------------ '
```

```
      WRITE(2,*)' Programm DIPOL Version Dipoltensor'
      WRITE(2,*)  ' ----------------------------------------------------
     &------------ '
      WRITE(2,*)  ' ----------------------------------------------------
     &------------ '

      WRITE(6,*)
      WRITE(6,*)  ' ----------------------------------------------------
     &------------ '
      WRITE(6,*)  ' ----------------------------------------------------
     &------------ '
      WRITE(6,*)' D I P O L F E L D   A M   S O N D E N O R T '
      WRITE(6,*)  ' ----------------------------------------------------
     &------------ '
      WRITE(6,*)' Programm DIPOL Version DIPOLTENSOR'
      WRITE(6,*)  ' ----------------------------------------------------
     &------------ '
      WRITE(6,*)  ' ----------------------------------------------------
     &------------ '

C**********************************************************************
C     Einheitszelle und Spinrichtungen festlegen :
C**********************************************************************

      IF (GITTYP .EQ. 1) CALL cupm

C**********************************************************************
C     Summationsradius berechnen :
C**********************************************************************

      RMAX = MAXGIT * A
      MAXZEL = DINT(MAXGIT) + 2
      KREALMAX= MAXZEL * 6
      KMAXZEL= DINT(KREALMAX) +  5

C**********************************************************************
C     Ausgabe der Parameter :
C**********************************************************************

      WRITE(6,*)' Eingabeparameter       : '
      WRITE(6,*)' ------------------------ '
      WRITE(6,'(2X,A60)') TITLE
```

```
      WRITE(6,13) ' primaerer  Sondenplatz : ', MYSITE0(1),MYSITE0(2),
     &                     MYSITE0(3)
      WRITE(6,13) ' Gitterkonstanten (A) : ',A,B,C
      WRITE(6,14) ' Spintransfer       : ',SPDVAL
      WRITE(6,14) ' Spinbetrag (MYB)     : ', SPBETR
      WRITE(6,*)' ---------------------------------------------------'
      WRITE(6,17)  ' Einflussradius ',MAXGIT,' Gitterkonstante(n)'

      WRITE(2,*)' ---------------------------------------------------'
      WRITE(2,*)' Eingabeparameter       : '
      WRITE(2,*)' ----------------------- '
      WRITE(2,'(2X,A60)') TITLE
      WRITE(2,13) ' primaerer  Sondenplatz : ', MYSITE0(1),MYSITE0(2),
     &                      MYSITE0(3)
      WRITE(2,13) ' Gitterkonstanten (A) : ',A,B,C
      WRITE(2,14) ' Spintransfer       : ',SPDVAL
      WRITE(2,14) ' Spinbetrag (MYB)     : ', SPBETR
      WRITE(2,*)' ---------------------------------------------------'
      WRITE(2,17)  ' Einflussradius ',MAXGIT,' Gitterkonstante(n)'
      WRITE(2,*)' ---------------------------------------------------'

C***********************************************************************
C     Sondenplatz festlegen:
C***********************************************************************

         MYSITE(1) = MYSITE0(1)
         MYSITE(2) = MYSITE0(2)
         MYSITE(3) = MYSITE0(3)

C***********************************************************************
C     Einheitszelle und Spinrichtungen festlegen :
C***********************************************************************

       IF (GITTYP .EQ. 1) CALL cupm

         BMYG(1)=0.0
         BMYG(2)=0.0
         BMYG(3)=0.0
         BMYG(4)=0.0
         BMYG(5)=0.0
         BMYG(6)=0.0
         BMYG(7)=0.0
```

```
         BMYG(8)=0.0
         BMYG(9)=0.0
         TTSPIN=0

C**********************************************************************
C     Schleife }ber alle Untergitter :
C**********************************************************************

         DO 20 NGIT=1,UGANZ
         FAKTOR=(1.0-2.0*SPDVAL)
         IF ( NGIT .GT. 1 ) FAKTOR=SPDVAL

            BMYUG(NGIT,1)=0.0
            BMYUG(NGIT,2)=0.0
            BMYUG(NGIT,3)=0.0
            BMYUG(NGIT,4)=0.0
            BMYUG(NGIT,5)=0.0
            BMYUG(NGIT,6)=0.0
            BMYUG(NGIT,7)=0.0
            BMYUG(NGIT,8)=0.0
            BMYUG(NGIT,9)=0.0
            TNSPIN(NGIT)=0

            DO 21 ISHELL=1,NMAX
               NSPIN(NGIT,ISHELL)=0
               BMY(NGIT,ISHELL,1)=0.0
               BMY(NGIT,ISHELL,2)=0.0
               BMY(NGIT,ISHELL,3)=0.0
               BMY(NGIT,ISHELL,4)=0.0
               BMY(NGIT,ISHELL,5)=0.0
               BMY(NGIT,ISHELL,6)=0.0
               BMY(NGIT,ISHELL,7)=0.0
               BMY(NGIT,ISHELL,8)=0.0
               BMY(NGIT,ISHELL,9)=0.0
  21        CONTINUE

            NSHELL(NGIT)=1
            SHRAD(NGIT,1)=0.0

C**********************************************************************
C     SCHLEIFE }BER EINE ANZAHL EINHEITSZELLEN
C**********************************************************************
```

```
            DO 25 I=-MAXZEL-1,MAXZEL+1
               DO 30 J=-MAXZEL-1,MAXZEL+1
                  DO 40 K=-KMAXZEL-1,KMAXZEL+1

C        SCHLEIFE UEBER ALLE SPINS DES UNTERGITTERS

                     DO 50 L=1,SPANZ(NGIT)
         VORZEICH=1.0
         IF ( L .gt. 2 ) VORZEICH=1.0
         write(*,*) l, vorzeich*faktor

         IF (SPDVAL .EQ. 0.0 ) THEN
            GOTO 33
         END IF

  33     AX=(DFLOAT(I)+SITE(NGIT,L,1)-MYSITE(1))
         AY=(DFLOAT(J)+SITE(NGIT,L,2)-MYSITE(2))
         AZ=(DFLOAT(K)+SITE(NGIT,L,3)-MYSITE(3))
         XX=AX*A-AZ*C*0.403545296
         YY=AY*B
         ZZ=AZ*C*0.914959667
         RAD=DSQRT(XX*XX+YY*YY+ZZ*ZZ)
         SRAD=DNINT(RAD*1000000000.)/1000000000.

C**********************************************************************
C        RADIUS GROESSER ALS RMAX, VERGISS DEN SPIN:
C**********************************************************************

         IF (SRAD.GT.RMAX) GOTO 50

C**********************************************************************
C        SPIN WIRD BER}CKSICHTIGT UND MUSS EINGEORDNET WERDEN:
C**********************************************************************

C        BIS JETZT HABEN WIR DEN SPIN NOCH NIRGENDWO UNTERGEBRACHT:
         INSERT=.FALSE.

C        ANZAHL SCHALEN:
         H=1

C****************** WHILE H <= NSHELL(NGIT) DO BEGIN *****************
```

```
C       GIBT ES SCHON EINE SCHALE MIT DEM RADIUS SRAD?

   60   CONTINUE
           IF (H.LE.NSHELL(NGIT)) THEN

              IF (SRAD.EQ.SHRAD(NGIT,H)) THEN

C                 RICHTIGE SCHALE GEFUNDEN
C                 SPIN DA REINPACKEN

                 NSPIN(NGIT,H)=NSPIN(NGIT,H)+1

**************************************************************************
**************************************************************************
             IF (NGIT.eq.1)  THEN

C    Formeln fuer Dipol-Tensorberechnung

C          1.Komponente ist Axx:
                 BMY(NGIT,H,1)=BMY(NGIT,H,1)-FAKTOR*VORZEICH*1.66*(1.
     &           -3.*XX*XX/RAD/RAD)/RAD/RAD/RAD

C          2. Komponente ist Ayy:

                 BMY(NGIT,H,2)=BMY(NGIT,H,2)-FAKTOR*VORZEICH*1.66*(1.
     &           -3.*YY*YY/RAD/RAD)/RAD/RAD/RAD

C          3. Komponente ist Azz:

                 BMY(NGIT,H,3)=BMY(NGIT,H,3)-FAKTOR*VORZEICH*1.66*(1.
     &           -3.*ZZ*ZZ/RAD/RAD)/RAD/RAD/RAD

C          4. Komponente ist Axy:

                 BMY(NGIT,H,4)=BMY(NGIT,H,4)+FAKTOR*VORZEICH*(1.66*
     &           3.*XX*YY/RAD/RAD)/RAD/RAD/RAD

C          5. Komponente ist Axz:

                 BMY(NGIT,H,5)=BMY(NGIT,H,5)+FAKTOR*VORZEICH*(1.66*
     &           3.*XX*ZZ/RAD/RAD)/RAD/RAD/RAD
```

```
C          6. Komponente ist Ayx:

                BMY(NGIT,H,6)=BMY(NGIT,H,6)+FAKTOR*VORZEICH*(1.66*
     &          3.*YY*XX/RAD/RAD)/RAD/RAD/RAD

C          7. Komponente ist Ayz:

                BMY(NGIT,H,7)=BMY(NGIT,H,7)+FAKTOR*VORZEICH*(1.66*
     &          3.*YY*ZZ/RAD/RAD)/RAD/RAD/RAD

C          8. Komponente ist Azx:

                BMY(NGIT,H,8)=BMY(NGIT,H,8)+FAKTOR*VORZEICH*(1.66*
     &          3.*ZZ*XX/RAD/RAD)/RAD/RAD/RAD

C          9. Komponente ist Azy:

                BMY(NGIT,H,9)=BMY(NGIT,H,9)+FAKTOR*VORZEICH*(1.66*
     &          3.*ZZ*YY/RAD/RAD)/RAD/RAD/RAD

          ELSE

C    Formeln fuer Dipol-Tensorberechnung

C          1. Komponente ist Axx:

                BMY(NGIT,H,1)=BMY(NGIT,H,1)-FAKTOR*VORZEICH*1.66*(1.
     &          -3.*XX*XX/RAD/RAD)/RAD/RAD/RAD

C          2. Komponente ist Ayy:

                BMY(NGIT,H,2)=BMY(NGIT,H,2)-FAKTOR*VORZEICH*1.66*(1.
     &          -3.*YY*YY/RAD/RAD)/RAD/RAD/RAD

C          3. Komponente ist Azz:

                BMY(NGIT,H,3)=BMY(NGIT,H,3)-FAKTOR*VORZEICH*1.66*(1.
     &          -3.*ZZ*ZZ/RAD/RAD)/RAD/RAD/RAD

C          4. Komponente ist Axy:

                BMY(NGIT,H,4)=BMY(NGIT,H,4)+FAKTOR*VORZEICH*(1.66*
```

```
     &          3.*XX*YY/RAD/RAD)/RAD/RAD/RAD

C          5. Komponente ist Axz:

                BMY(NGIT,H,5)=BMY(NGIT,H,5)+FAKTOR*VORZEICH*(1.66*
     &          3.*XX*ZZ/RAD/RAD)/RAD/RAD/RAD

C          6. Komponente ist Ayx:

                BMY(NGIT,H,6)=BMY(NGIT,H,6)+FAKTOR*VORZEICH*(1.66*
     &          3.*YY*XX/RAD/RAD)/RAD/RAD/RAD

C          7. Komponente ist Ayz:

                BMY(NGIT,H,7)=BMY(NGIT,H,7)+FAKTOR*VORZEICH*(1.66*
     &          3.*YY*ZZ/RAD/RAD)/RAD/RAD/RAD

C          8. Komponente ist Azx:

                BMY(NGIT,H,8)=BMY(NGIT,H,8)+FAKTOR*VORZEICH*(1.66*
     &          3.*ZZ*XX/RAD/RAD)/RAD/RAD/RAD

C          9. Komponente ist Azy:

                BMY(NGIT,H,9)=BMY(NGIT,H,9)+FAKTOR*VORZEICH*(1.66*
     &          3.*ZZ*YY/RAD/RAD)/RAD/RAD/RAD

           END IF

*********************************************************************************

                 H=NSHELL(NGIT)+1

C               SPIN UNTERGEBRACHT:
                INSERT=.TRUE.

             ELSE IF (SRAD.LT.SHRAD(NGIT,H)) THEN

C               ES MUSS EINE SCHALE EINGEFUEGT WERDEN
C               AB DIESER SCHALE ALLE SCHALEN EINEN HOEHER STUFEN:

                NSHELL(NGIT)=NSHELL(NGIT)+1
```

```
                  DO 70 M=NSHELL(NGIT),H+1,-1
                     NSPIN(NGIT,M)=NSPIN(NGIT,M-1)
                     SHRAD(NGIT,M)=SHRAD(NGIT,M-1)
                     BMY(NGIT,M,1)=BMY(NGIT,M-1,1)
                     BMY(NGIT,M,2)=BMY(NGIT,M-1,2)
                     BMY(NGIT,M,3)=BMY(NGIT,M-1,3)
                     BMY(NGIT,M,4)=BMY(NGIT,M-1,4)
                     BMY(NGIT,M,5)=BMY(NGIT,M-1,5)
                     BMY(NGIT,M,6)=BMY(NGIT,M-1,6)
                     BMY(NGIT,M,7)=BMY(NGIT,M-1,7)
                     BMY(NGIT,M,8)=BMY(NGIT,M-1,8)
                     BMY(NGIT,M,9)=BMY(NGIT,M-1,9)

   70             CONTINUE

C                 JETZT DEN SPIN IN DIE SCHALE H REINPACKEN:

                  SHRAD(NGIT,H)=SRAD
                  NSPIN(NGIT,H)=1

********************************************************************************
********************************************************************************

           IF (NGIT.eq.1) THEN

C    Formeln fuer Dipol-Tensorberechnung

C           1. Komponente ist Axx:

                  BMY(NGIT,H,1)=-FAKTOR*VORZEICH*1.66*(1.
     &            -3.*XX*XX/RAD/RAD)/RAD/RAD/RAD

C           2. Komponente ist Ayy:

                  BMY(NGIT,H,2)=-FAKTOR*VORZEICH*1.66*(1.
     &            -3.*YY*YY/RAD/RAD)/RAD/RAD/RAD

C           3. Komponente ist Azz:

                  BMY(NGIT,H,3)=-FAKTOR*VORZEICH*1.66*(1.
     &            -3.*ZZ*ZZ/RAD/RAD)/RAD/RAD/RAD
```

```
C           4. Komponente ist Axy:

                  BMY(NGIT,H,4)=FAKTOR*VORZEICH*(1.66*
     &            3.*XX*YY/RAD/RAD)/RAD/RAD/RAD

C           5. Komponente ist Axz:

                  BMY(NGIT,H,5)=FAKTOR*VORZEICH*(1.66*
     &            3.*XX*ZZ/RAD/RAD)/RAD/RAD/RAD

C           6. Komponente ist Ayx:

                  BMY(NGIT,H,6)=FAKTOR*VORZEICH*(1.66*
     &            3.*YY*XX/RAD/RAD)/RAD/RAD/RAD

C           7. Komponente ist Ayz:

                  BMY(NGIT,H,7)=FAKTOR*VORZEICH*(1.66*
     &            3.*YY*ZZ/RAD/RAD)/RAD/RAD/RAD

C           8. Komponente ist Azx:

                  BMY(NGIT,H,8)=FAKTOR*VORZEICH*(1.66*
     &            3.*ZZ*XX/RAD/RAD)/RAD/RAD/RAD

C           9. Komponente ist Azy:

                  BMY(NGIT,H,9)=FAKTOR*VORZEICH*(1.66*
     &            3.*ZZ*YY/RAD/RAD)/RAD/RAD/RAD

            ELSE

C    Formeln fuer Dipol-Tensorberechnung

C           1. Komponente ist Axx:

                  BMY(NGIT,H,1)=-FAKTOR*VORZEICH*1.66*(1.
     &            -3.*XX*XX/RAD/RAD)/RAD/RAD/RAD

C           2. Komponente ist Ayy:

                  BMY(NGIT,H,2)=-FAKTOR*VORZEICH*1.66*(1.
```

```
     &           -3.*YY*YY/RAD/RAD)/RAD/RAD/RAD

C          3. Komponente ist Azz:

                BMY(NGIT,H,3)=-FAKTOR*VORZEICH*1.66*(1.
     &           -3.*ZZ*ZZ/RAD/RAD)/RAD/RAD/RAD

C          4. Komponente ist Axy:

                BMY(NGIT,H,4)=FAKTOR*VORZEICH*(1.66*
     &           3.*XX*YY/RAD/RAD)/RAD/RAD/RAD

C          5. Komponente ist Axz:

                BMY(NGIT,H,5)=FAKTOR*VORZEICH*(1.66*
     &           3.*XX*ZZ/RAD/RAD)/RAD/RAD/RAD

C          6. Komponente ist Ayx:

                BMY(NGIT,H,6)=FAKTOR*VORZEICH*(1.66*
     &           3.*YY*XX/RAD/RAD)/RAD/RAD/RAD

C          7. Komponente ist Ayz:

                BMY(NGIT,H,7)=FAKTOR*VORZEICH*(1.66*
     &           3.*YY*ZZ/RAD/RAD)/RAD/RAD/RAD

C          8. Komponente ist Azx:

                BMY(NGIT,H,8)=FAKTOR*VORZEICH*(1.66*
     &           3.*ZZ*XX/RAD/RAD)/RAD/RAD/RAD

C          9. Komponente ist Azy:

                BMY(NGIT,H,9)=FAKTOR*VORZEICH*(1.66*
     &           3.*ZZ*YY/RAD/RAD)/RAD/RAD/RAD

           END IF

************************************************************************

                H=NSHELL(NGIT)+1
```

```
C                 SPIN UNTERGEBRACHT:
                  INSERT=.TRUE.

               ELSE IF (SRAD.GT.SHRAD(NGIT,H)) THEN
                  H=H+1
               END IF
               GOTO 60
            END IF
C********************** END OF WHILE ***********************************

            IF (.NOT.INSERT) THEN

C              SPIN NOCH NICHT UNTERGEBRACHT:
C              SPIN IN NEUE SCHALE MIT GROESSTEM RADIUS

               NSHELL(NGIT)=NSHELL(NGIT)+1
               SHRAD(NGIT,NSHELL(NGIT))=SRAD
               NSPIN(NGIT,NSHELL(NGIT))=1
************************************************************************
************************************************************************
          IF (NGIT.eq.1)  THEN

C    Formeln fuer Dipol-Tensorberechnung

C           1. Komponente ist Axx:

                  BMY(NGIT,NSHELL(NGIT),1)=-FAKTOR*VORZEICH*1.66*(1.
     &            -3.*XX*XX/RAD/RAD)/RAD/RAD/RAD

C           2. Komponente ist Ayy:

                  BMY(NGIT,NSHELL(NGIT),2)=-FAKTOR*VORZEICH*1.66*(1.
     &            -3.*YY*YY/RAD/RAD)/RAD/RAD/RAD

C           3. Komponente ist Azz:

                  BMY(NGIT,NSHELL(NGIT),3)=-FAKTOR*VORZEICH*1.66*(1.
     &            -3.*ZZ*ZZ/RAD/RAD)/RAD/RAD/RAD

C           4. Komponente ist Axy:
```

```
            BMY(NGIT,NSHELL(NGIT),4)=FAKTOR*VORZEICH*(1.66*
     &      3.*XX*YY/RAD/RAD)/RAD/RAD/RAD

C      5. Komponente ist Axz:

            BMY(NGIT,NSHELL(NGIT),5)=FAKTOR*VORZEICH*(1.66*
     &      3.*XX*ZZ/RAD/RAD)/RAD/RAD/RAD

C      6. Komponente ist Ayx:

            BMY(NGIT,NSHELL(NGIT),6)=FAKTOR*VORZEICH*(1.66*
     &      3.*YY*XX/RAD/RAD)/RAD/RAD/RAD
C      7. Komponente ist Ayz:

            BMY(NGIT,NSHELL(NGIT),7)=FAKTOR*VORZEICH*(1.66*
     &      3.*YY*ZZ/RAD/RAD)/RAD/RAD/RAD

C      8. Komponente ist Azx:

            BMY(NGIT,NSHELL(NGIT),8)=FAKTOR*VORZEICH*(1.66*
     &      3.*ZZ*XX/RAD/RAD)/RAD/RAD/RAD

C      9. Komponente ist Azy:

            BMY(NGIT,NSHELL(NGIT),9)=FAKTOR*VORZEICH*(1.66*
     &      3.*ZZ*YY/RAD/RAD)/RAD/RAD/RAD

       ELSE

C    Formeln fuer Dipol-Tensorberechnung

C      1. Komponente ist Axx:

            BMY(NGIT,NSHELL(NGIT),1)=-FAKTOR*VORZEICH*1.66*(1.
     &      -3.*XX*XX/RAD/RAD)/RAD/RAD/RAD

C      2. Komponente ist Ayy:

            BMY(NGIT,NSHELL(NGIT),2)=-FAKTOR*VORZEICH*1.66*(1.
     &      -3.*YY*YY/RAD/RAD)/RAD/RAD/RAD

C      3. Komponente ist Azz:
```

```
                  BMY(NGIT,NSHELL(NGIT),3)=-FAKTOR*VORZEICH*1.66*(1.
     &            -3.*ZZ*ZZ/RAD/RAD)/RAD/RAD/RAD

C           4. Komponente ist Axy:

                  BMY(NGIT,NSHELL(NGIT),4)=FAKTOR*VORZEICH*(1.66*
     &            3.*XX*YY/RAD/RAD)/RAD/RAD/RAD

C           5. Komponente ist Axz:

                  BMY(NGIT,NSHELL(NGIT),5)=FAKTOR*VORZEICH*(1.66*
     &            3.*XX*ZZ/RAD/RAD)/RAD/RAD/RAD

C           6. Komponente ist Ayx:

                  BMY(NGIT,NSHELL(NGIT),6)=FAKTOR*VORZEICH*(1.66*
     &            3.*YY*XX/RAD/RAD)/RAD/RAD/RAD
C           7. Komponente ist Ayz:

                  BMY(NGIT,NSHELL(NGIT),7)=FAKTOR*VORZEICH*(1.66*
     &            3.*YY*ZZ/RAD/RAD)/RAD/RAD/RAD

C           8. Komponente ist Azx:

                  BMY(NGIT,NSHELL(NGIT),8)=FAKTOR*VORZEICH*(1.66*
     &            3.*ZZ*XX/RAD/RAD)/RAD/RAD/RAD

C           9. Komponente ist Azy:

                  BMY(NGIT,NSHELL(NGIT),9)=FAKTOR*VORZEICH*(1.66*
     &            3.*ZZ*YY/RAD/RAD)/RAD/RAD/RAD
            END IF

**********************************************************************

            END IF
   50                  CONTINUE
   40               CONTINUE
   30            CONTINUE
   25       CONTINUE
```

```
C*********************************************************************
C     Berechne Dipolfeld des Untergitters und
C     Anzahl der Spins des
C  Untergitters
C*********************************************************************

            DO 90 I=1,NSHELL(NGIT)
               BMYUG(NGIT,1)=BMYUG(NGIT,1)+BMY(NGIT,I,1)
               BMYUG(NGIT,2)=BMYUG(NGIT,2)+BMY(NGIT,I,2)
               BMYUG(NGIT,3)=BMYUG(NGIT,3)+BMY(NGIT,I,3)
               BMYUG(NGIT,4)=BMYUG(NGIT,4)+BMY(NGIT,I,4)
               BMYUG(NGIT,5)=BMYUG(NGIT,5)+BMY(NGIT,I,5)
               BMYUG(NGIT,6)=BMYUG(NGIT,6)+BMY(NGIT,I,6)
               BMYUG(NGIT,7)=BMYUG(NGIT,7)+BMY(NGIT,I,7)
               BMYUG(NGIT,8)=BMYUG(NGIT,8)+BMY(NGIT,I,8)
               BMYUG(NGIT,9)=BMYUG(NGIT,9)+BMY(NGIT,I,9)
               TNSPIN(NGIT)=TNSPIN(NGIT)+NSPIN(NGIT,I)
   90       CONTINUE

C*********************************************************************
C     Berechne Gesamtdipolfeld und Gesamtanzahl der Spins :
C*********************************************************************

            BMYG(1)=BMYG(1)+BMYUG(NGIT,1)
            BMYG(2)=BMYG(2)+BMYUG(NGIT,2)
            BMYG(3)=BMYG(3)+BMYUG(NGIT,3)
            BMYG(4)=BMYG(4)+BMYUG(NGIT,4)
            BMYG(5)=BMYG(5)+BMYUG(NGIT,5)
            BMYG(6)=BMYG(6)+BMYUG(NGIT,6)
            BMYG(7)=BMYG(7)+BMYUG(NGIT,7)
            BMYG(8)=BMYG(8)+BMYUG(NGIT,8)
            BMYG(9)=BMYG(9)+BMYUG(NGIT,9)
             TTSPIN=TTSPIN+TNSPIN(NGIT)

   20    CONTINUE

C*********************************************************************
C     Ausgabe des Dipoltensors :
C*********************************************************************

      WRITE(6,*)  ' ----------------------------------------------------
     &------------ '
```

```
      WRITE(6,*)  ' Ausgabe des Dipoltensors :'
      WRITE(6,*)  ' ----------------------------------------------------
     &------------ '
      WRITE(6,*)  ' Axx (mol/emu)     Ayy  (mol/emu)    Azz  (mol/emu)
     &              Axy (mol/emu)     Axz  (mol/emu)    Ayx  (mol/emu)
     &              Ayz (mol/emu)     Azx  (mol/emu)    Azy  (mol/emu)'
      WRITE(6,'(2X,E20.12,2X,E20.12,2X,E20.12,
     &          2X,E20.12,2X,E20.12,2X,E20.12,
     &          2X,E20.12,2X,E20.12,2X,E20.12)')
     &         BMYG(1),BMYG(2),BMYG(3),
     &         BMYG(4),BMYG(5),BMYG(6),
     &         BMYG(7),BMYG(8),BMYG(9)
      WRITE(6,*)  ' ----------------------------------------------------
     &------------ '

      WRITE(6,*)  ' Anzahl der ber}cksichtigten Spins : ',TTSPIN
      WRITE(6,*)  ' Anzahl der Untergitter            : ',UGANZ
      WRITE(6,*)' ---------------------------------------------------'

      DO 700 NGIT=1,UGANZ
         WRITE(6,18)  ' Beitrag von Untergitter ',NGIT,' mit ',
     &                TNSPIN(NGIT),' Spins '
         WRITE(6,'(2X,E20.12,2X,E20.12,2X,E20.12,
     &             2X,E20.12,2X,E20.12,2X,E20.12,
     &             2X,E20.12,2X,E20.12,2X,E20.12)')
     &               BMYUG(NGIT,1),BMYUG(NGIT,2),BMYUG(NGIT,3),
     &               BMYUG(NGIT,4),BMYUG(NGIT,5),BMYUG(NGIT,6),
     &               BMYUG(NGIT,7),BMYUG(NGIT,8),BMYUG(NGIT,9)
         WRITE(6,*)  ' -------------------------------------------------
     &--------------- '
700   CONTINUE

      DO 705 NGIT=1,UGANZ
         WRITE(6,19)  ' Beitr{ge der ersten 4 Schalen von Untergitter '
     &              ,NGIT
         WRITE(6,*)  ' Schale  Spinanz   Radius (A)          X
     &  Y           Z '
         WRITE(6,*)  ' -------------------------------------------------
     &--------------- '
         DO 710 I=1,4
            WRITE(6,'(5X,I3,6X,I3,6X,F7.3,
     &           E12.4,E12.4,E12.4,
```

```
     &          E12.4,E12.4,E12.4,
     &          E12.4,E12.4,E12.4)')
     &                 I,NSPIN(NGIT,I),SHRAD(NGIT,I),
     &                 BMY(NGIT,I,1),BMY(NGIT,I,2),BMY(NGIT,I,3),
     &                 BMY(NGIT,I,4),BMY(NGIT,I,5),BMY(NGIT,I,6),
     &                 BMY(NGIT,I,7),BMY(NGIT,I,8),BMY(NGIT,I,9)
710      CONTINUE
         WRITE(6,*)  ' -------------------------------------------------
     &--------------- '
705   CONTINUE
      WRITE(6,*)  ' ----------------------------------------------------
     &------------ '



      WRITE(2,*)  ' ----------------------------------------------------
     &------------ '
      WRITE(2,*)  ' Ausgabe des Dipoltensors :'
      WRITE(2,*)  ' ----------------------------------------------------
     &------------ '
      WRITE(2,*)  ' Axx (mol/emu)     Ayy  (mol/emu)    Azz  (mol/emu)
     &              Axy (mol/emu)     Axz  (mol/emu)    Ayx  (mol/emu)
     &              Ayz (mol/emu)     Azx  (mol/emu)    Azy  (mol/emu)'
      WRITE(2,'(2X,E20.12,2X,E20.12,2X,E20.12,
     &         2X,E20.12,2X,E20.12,2X,E20.12,
     &         2X,E20.12,2X,E20.12,2X,E20.12)')
     &          BMYG(1),BMYG(2),BMYG(3),
     &          BMYG(4),BMYG(5),BMYG(6),
     &          BMYG(7),BMYG(8),BMYG(9)
      WRITE(2,*)  ' Anzahl der ber}cksichtigten Spins : ',TTSPIN
      WRITE(2,*)  ' Anzahl der Untergitter            : ',UGANZ
      WRITE(2,*)' ---------------------------------------------------'

      DO 600 NGIT=1,UGANZ
         WRITE(2,18)  ' Beitrag von Untergitter ',NGIT,' mit ',
     &                TNSPIN(NGIT),' Spins '
         WRITE(2,'(2X,E20.12,2X,E20.12,2X,E20.12,
     &             2X,E20.12,2X,E20.12,2X,E20.12,
     &             2X,E20.12,2X,E20.12,2X,E20.12)')
     &               BMYUG(NGIT,1),BMYUG(NGIT,2),BMYUG(NGIT,3),
     &               BMYUG(NGIT,4),BMYUG(NGIT,5),BMYUG(NGIT,6),
     &               BMYUG(NGIT,7),BMYUG(NGIT,8),BMYUG(NGIT,9)
```

```
         WRITE(2,*)  ' -------------------------------------------------
     &--------------- '
600   CONTINUE

      DO 605 NGIT=1,UGANZ
         WRITE(2,19)  ' Beitr{ge der ersten 10 Schalen von Untergitter '
     &              ,NGIT
         WRITE(2,*)  ' Schale  Spinanz   Radius (A)        XX   YY
     &  ZZ    XY    XZ    YX    YZ    ZX    ZY      '
         WRITE(2,*)  ' -------------------------------------------------
     &--------------- '
         DO 610 I=1,10
       WRITE(2,'(5X,I3,6X,I3,6X,F7.3,
     &           E12.4,E12.4,E12.4,
     &           E12.4,E12.4,E12.4,
     &           E12.4,E12.4,E12.4)')
     &                  I,NSPIN(NGIT,I),SHRAD(NGIT,I),
     &                  BMY(NGIT,I,1),BMY(NGIT,I,2),BMY(NGIT,I,3),
     &                  BMY(NGIT,I,4),BMY(NGIT,I,5),BMY(NGIT,I,6),
     &                  BMY(NGIT,I,7),BMY(NGIT,I,8),BMY(NGIT,I,9)
610      CONTINUE
         WRITE(2,*)  ' -------------------------------------------------
     &--------------- '
605   CONTINUE
      WRITE(2,*)  ' ----------------------------------------------------
     &------------ '



 11   FORMAT(5X,I3,6X,I3,6X,F7.3,E12.4,E12.4,E12.4)
 12   FORMAT(1X,A32)
 13   FORMAT(1X,A24,F7.3,2X,F7.3,2X,F7.3)
 14   FORMAT(1X,A24,F7.3)
 16   FORMAT(3X,E10.2,2X,E10.2,2X,E10.2)
 17   FORMAT(1X,A16,F6.2,A19)
 18   FORMAT(1X,A25,I3,A5,I6,A6)
 19   FORMAT(1X,A48,I3)

         close(1)
         close(2)

      END
```

```
************************************************************************

      SUBROUTINE cupm

************************************************************************
*                                                                      *
*     Unterroutine des Programms DIPOL zur Definition der Spin-        *
*     positionen und -richtungen.                                      *
*                                                                      *
************************************************************************

      IMPLICIT REAL*8 (A-H,O-Z)

      COMMON / LCELL /  A,B,C,SITE,UGANZ,SPANZ
      INTEGER  UGANZ,SPANZ(6)
      REAL*8 A,B,C,SITE(6,16,3)

C***********************************************************************
C     Anzahl der Untergitter, Spinpositionen und -richtungen festlegen
C***********************************************************************

      UGANZ = 3
C      write(2,*) 'BIN IN spinkette'
C      write(2,*) 'UGANZ IN SUBR=',UGANZ
      DO 10 I=1, UGANZ
         SPANZ(I) = 4
  10  CONTINUE

      SITE(1,1,1) = 0.25
      SITE(1,1,2) = 0.25
      SITE(1,1,3) = 0

      SITE(1,2,1) = 0.75
      SITE(1,2,2) = 0.75
      SITE(1,2,3) = 0

      SITE(1,3,1) = 0.75
      SITE(1,3,2) = 0.25
      SITE(1,3,3) = 0.5

      SITE(1,4,1) = 0.25
      SITE(1,4,2) = 0.75
```

```
      SITE(1,4,3) = 0.5



      SITE(2,1,1) = 0.39981
      SITE(2,1,2) = 0.34852
      SITE(2,1,3) = 0.13612

      SITE(2,2,1) = 0.89981
      SITE(2,2,2) = 0.84852
      SITE(2,2,3) = 0.13612

      SITE(2,3,1) = 0.60019
      SITE(2,3,2) = 0.34852
      SITE(2,3,3) = 0.36388

      SITE(2,4,1) = 0.10019
      SITE(2,4,2) = 0.84852
      SITE(2,4,3) = 0.36388



      SITE(3,1,1) = 0.60019
      SITE(3,1,2) = 0.65148
      SITE(3,1,3) = 0.86388

      SITE(3,2,1) = 0.10019
      SITE(3,2,2) = 0.15148
      SITE(3,2,3) = 0.86388

      SITE(3,3,1) = 0.39981
      SITE(3,3,2) = 0.65148
      SITE(3,3,3) = 0.63612

      SITE(3,4,1) = 0.89981
      SITE(3,4,2) = 0.15148
      SITE(3,4,3) = 0.63612


      RETURN
      END
```

B Dipolar Hyperfine Tensors

The dipolar hyperfine tensors in the uniform ($\overleftrightarrow{A}_{dip,\uparrow\uparrow}$) and in the staggered regime ($\overleftrightarrow{A}_{dip,\uparrow\downarrow}$), which have been calculated in localized dipole approximation, are listed below for the inequivalent carbon sites C1, C2 and C3 on the pyrimidine molecule in CuPM. Note, that $\overleftrightarrow{A}_{dip,\uparrow\uparrow}$ and $\overleftrightarrow{A}_{dip,\uparrow\downarrow}$ are given in cartesian coordinates a, b, c_{cart} in units mole/emu.

- 100% magnetic moment on the Cu sites

$$\overleftrightarrow{A}_{dip,\uparrow\uparrow} = \begin{pmatrix} 0.114198 & 0 & 0.182643 \\ 0 & -0.117936 & 0 \\ 0.182643 & 0 & 0.003738 \end{pmatrix} (C1) \tag{124}$$

$$\overleftrightarrow{A}_{dip,\uparrow\uparrow} = \begin{pmatrix} 0.003413 & 0 & 0.008511 \\ 0 & 0.015737 & 0 \\ 0.008511 & 0 & -0.019149 \end{pmatrix} (C2) \tag{125}$$

$$\overleftrightarrow{A}_{dip,\uparrow\uparrow} = \begin{pmatrix} -0.016704 & \pm 0.055706 & 0.027660 \\ \pm 0.055706 & 0.061270 & \pm 0.031532 \\ 0.027660 & \pm 0.031532 & -0.044566 \end{pmatrix} (C3) \tag{126}$$

$$\overleftrightarrow{A}_{dip,\uparrow\downarrow} = \begin{pmatrix} 0 & -0.059000 & 0 \\ -0.059000 & 0 & -0.040592 \\ 0 & -0.040592 & 0 \end{pmatrix} (C1) \tag{127}$$

$$\overleftrightarrow{A}_{dip,\uparrow\downarrow} = \begin{pmatrix} 0 & -0.080723 & 0 \\ -0.080723 & 0 & -0.035437 \\ 0 & -0.035437 & 0 \end{pmatrix} (C2) \tag{128}$$

$$\overleftrightarrow{A}_{dip,\uparrow\downarrow} = \begin{pmatrix} 0.011514 & \mp 0.108047 & -0.017683 \\ \mp 0.108047 & -0.061479 & \mp 0.056967 \\ -0.017683 & \mp 0.056967 & 0.049965 \end{pmatrix} (C3) \tag{129}$$

- total moment transfer of 10 % to the N atoms on the pyrimidine molecule

$$\overleftrightarrow{A}_{dip,\uparrow\uparrow} = \begin{pmatrix} 0.122958 & 0 & 0.244930 \\ 0 & -0.127481 & 0 \\ 0.244930 & 0 & 0.004523 \end{pmatrix} (C1) \tag{130}$$

$$\overleftrightarrow{A}_{dip,\uparrow\uparrow} = \begin{pmatrix} -0.005168 & 0 & 0.008205 \\ 0 & 0.027264 & 0 \\ 0.008205 & 0 & -0.02210 \end{pmatrix} (C2) \tag{131}$$

$$\overleftrightarrow{A}_{dip,\uparrow\uparrow} = \begin{pmatrix} -0.047845 & \pm 0.050380 & 0.027128 \\ \pm 0.050380 & 0.118867 & \pm 0.020178 \\ 0.027128 & \pm 0.020178 & -0.071022 \end{pmatrix} (C3) \tag{132}$$

In the following, the dipole tensors as calculated by means of electronic structure calculations are listed for the inequivalent carbon sites C1, C2 and C3. Note, that the tensors are given in cartesian coordinates a, b, c_{cart} in units mole/emu.

- B3LYP method

$$\overleftrightarrow{A}_{dip,\uparrow\uparrow} = \begin{pmatrix} 0.063373 & 0 & 0.364683 \\ 0 & -0.052895 & 0 \\ 0.364683 & 0 & -0.010478 \end{pmatrix} (C1) \tag{133}$$

$$\overleftrightarrow{A}_{dip,\uparrow\uparrow} = \begin{pmatrix} 0.009908 & 0 & 0.038765 \\ 0 & -0.009273 & 0 \\ 0.038765 & 0 & -0.000634 \end{pmatrix} (C2) \tag{134}$$

$$\overleftrightarrow{A}_{dip,\uparrow\uparrow} = \begin{pmatrix} -0.096355 & \pm 0.055003 & 0.11202 \\ \pm 0.055003 & 0.208981 & \pm 0.046694 \\ 0.11202 & \pm 0.046694 & -0.112626 \end{pmatrix} (C3) \tag{135}$$

- LDA method

$$\overleftrightarrow{A}_{dip,\uparrow\uparrow} = \begin{pmatrix} 0.083444 & 0 & 0.406814 \\ 0 & -0.076409 & 0 \\ 0.406814 & 0 & -0.007035 \end{pmatrix} (C1) \tag{136}$$

$$\overleftrightarrow{A}_{dip,\uparrow\uparrow} = \begin{pmatrix} 0.005045 & 0 & 0.119342 \\ 0 & 0.002706 & 0 \\ 0.119342 & 0 & -0.007751 \end{pmatrix} (C2) \tag{137}$$

$$\overleftrightarrow{A}_{dip,\uparrow\uparrow} = \begin{pmatrix} -0.111328 & \pm 0.072967 & 0.126751 \\ \pm 0.072967 & 0.233827 & \pm 0.070222 \\ 0.126751 & \pm 0.070222 & -0.122163 \end{pmatrix} (C3) \tag{138}$$

C Susceptibility Tensors

In the coordinate system referred to the principal axes of the g-tensor, *i.e.*, the $a'bc'$ system, the uniform susceptibility tensor can be expressed in the general form

$$\overleftrightarrow{\chi}_{u} = \begin{pmatrix} \chi^{u}_{a'a'} & 0 & 0 \\ 0 & \chi^{u}_{bb} & 0 \\ 0 & 0 & \chi^{u}_{c'c'} \end{pmatrix} . \tag{139}$$

In its principal axes system $a''bc''$, the tensor of the longitudinal part of the staggered susceptibility is written as

$$\overleftrightarrow{\chi}_{s||} = \begin{pmatrix} 0 & 0 & 0 \\ 0 & \chi^{s}_{bb} & 0 \\ 0 & 0 & \chi^{s}_{c''c''} \end{pmatrix} , \tag{140}$$

while the transverse staggered susceptibility tensor yields the form

$$\overleftrightarrow{\chi}_{s\perp} = \begin{pmatrix} 0 & 0 & 0 \\ 0 & 0 & \pm\chi^{s}_{bc''} \\ 0 & \pm\chi^{s}_{c''b} & 0 \end{pmatrix} . \tag{141}$$

Note, that in the calculation for the angular dependent shift (Eq. 117) the susceptibility tensors have been transformed from their principal axes systems (PAS) into the laboratory system abc_{cart} by a rotation around the b-axis.

D Chemical Shift Tensors

The experimentally determined chemical shift tensors in the *ac*-plane result in

$$\overleftrightarrow{\sigma} = \begin{pmatrix} 503 \pm 40 & 0 \\ 0 & 146 \pm 30 \end{pmatrix} (C1), \tag{142}$$

$$\overleftrightarrow{\sigma} = \begin{pmatrix} 496 \pm 40 & 0 \\ 0 & 113 \pm 30 \end{pmatrix} (C2), \tag{143}$$

$$\overleftrightarrow{\sigma} = \begin{pmatrix} 412 \pm 38 & 0 \\ 0 & 88 \pm 30 \end{pmatrix} (C3) \tag{144}$$

for carbon sites C1, C2 and C3, respectively. The elements σ_{11} and σ_{22} are in units ppm. Note, that the tensors are given in the PAS of C1 and C2, *i.e.*, the axis perpendicular to the C-H bond lying in the plane of the pyrimidine molecule, approximately corresponding to the Cu chain direction, and the axis perpendicular to the pyrimidine ring, approximately corresponding to the axis perpendicular to the Cu chains in the *ac*-plane. A schematic picture of the PAS of C1 and C2 is presented in Fig. 58(a) in section 6.1.2.

The shielding tensors $\overleftrightarrow{\sigma^*}$ = -$\overleftrightarrow{\sigma}$ obtained by electronic structure calculations for the isolated PM molecule are given by

$$\overleftrightarrow{\sigma^*} = \begin{pmatrix} 31 & 0 & 0 \\ 0 & 132 & 0 \\ 0 & 0 & -57 \end{pmatrix} (C1), \tag{145}$$

$$\overleftrightarrow{\sigma^*} = \begin{pmatrix} 73 & 0 & 0 \\ 0 & 179 & 0 \\ 0 & 0 & -28 \end{pmatrix} (C2), \tag{146}$$

$$\overleftrightarrow{\sigma^*} = \begin{pmatrix} 29 & 0 & 0 \\ 0 & 157 & 0 \\ 0 & 0 & -64 \end{pmatrix} (C3) \tag{147}$$

for carbon sites C1, C2 and C3, respectively. The elements are in units ppm. Note, that the tensors are given in the PAS of C1,C2 and C3, *i.e.*, the axis perpendicular to the C-H bond lying in the plane of the pyrimidine molecule, and the axis perpendicular to the pyrimidine ring and the axis of the C-H bond itself. The principal axes system of the carbon sites C1, C2 and C3 are given in Figs. 58(a) and (b), respectively, in section 6.1.2.

The calculations for the corresponding shielding tensors for a PM/Cu complex yield

$$\overleftrightarrow{\sigma}^{*} = \begin{pmatrix} -24 & 0 & 0 \\ 0 & 164 & 0 \\ 0 & 0 & -44 \end{pmatrix} (C1), \tag{148}$$

$$\overleftrightarrow{\sigma}^{*} = \begin{pmatrix} 52 & 0 & 0 \\ 0 & 186 & 0 \\ 0 & 0 & -26 \end{pmatrix} (C2), \tag{149}$$

$$\overleftrightarrow{\sigma}^{*} = \begin{pmatrix} 0 & 0 & 0 \\ 0 & 177 & 0 \\ 0 & 0 & -74 \end{pmatrix} (C3). \tag{150}$$

References

[1] M. N. Baibich, J. M. Broto, A. Fert, F. Nguyen Van Dau, F. Petroff, P. Etienne, G. Creuzet, A. Friederich, J. Chazelas, Phys. Rev. Lett. **61** (1988) 2472.

[2] J. G. Bednorz, K. A. Müller, Z. Phys. B **64** (1986) 189.

[3] M. K. Wu, J. R. Ashburn, C. J. Torng, P. H. Hor, R. L. Meng, L. Gao, Z. J. Huang, Y. Q. Wang, C. W. Chu, Phys. Rev. Lett. **58** (1987) 908.

[4] M. Uehara, T. Nagata, J. Akimitsu, H. Takahashi, N. Môri, K. Kinoshita, J. Phys. Soc. Jpn. **65** (1996) 2764.

[5] N. Fujiwara, N. Môri, Y. Uwatoko, T. Matsumoto, N. Motoyama, S. Uchida, Phys. Rev. Lett. **90** (2003) 137001.

[6] D. Jérome, A. Mazaud, M. Ribault, K. Bechgaard, J. Phys. Lett. **41** (Paris) (1980) L95.

[7] D. Jérome, Nature **387** (1997) 235.

[8] D. Jaccard, H. Wilhelm, D. Jérome, J. Moser, C. Carcel, J. M. Fabre, J. Phys.: Condens. Matter **13** (2001) L89.

[9] S. Tomonaga, Prog. Theor. Phys. **5** (1950) 544.

[10] J. M. Luttinger, J. Math. Phys. **4** (1963) 1154.

[11] I. S. Jacobs, J. W. Bray, H. R. Hart, Jr., L. V. Interrante, J. S. Kasper, G. D. Watkins, D. E. Prober, J. C. Bonner, Phys. Rev. B **14** (1976) 3036.

[12] M. Hase, I. Terasaki, K. Uchinokura, Phys. Rev. Lett. **70** (1993) 3651.

[13] M. Azuma, Z. Hiroi, M. Takano, K. Ishida, Y. Kitaoka, Phys. Rev. Lett. **73** (1994) 3463.

[14] E. Dagotto, T. M. Rice, Science **271** (1996) 618.

[15] O. Kahn, *Molecular Magnetism* (John Wiley & Sons, INC., New York, 1993).

[16] M. Verdaguer, Polyhedron **20** (2001) 1115.

[17] J. S. Miller, A. J. Epstein, Angew. Chem. Int. Ed. (Engl.) **33** (1994) 385.

[18] D. Gatteschi, Adv. Mater. **6** (1994) 635.

[19] E. Coronado, J. R. Galán-Mascarós, C. J. Gómez-Garcia, V. Laukhin, Nature **408** (2000) 447.

[20] S. Bénard, P. Yu, J. P. Audière, E. Rivière, R. Clément, J. Guilhem, L. Tchertanov, K. Nakatani, J. Am. Chem. Soc. **122** (2000) 9444.

[21] P. Gütlich, Struct. Bonding (Berlin) **44** (1981) 83.

[22] E. König, Struct. Bonding (Berlin) **76** (1991) 51.

[23] O. Kahn, Cur. Op. Solid State & Materials Science **1** (1996) 547.

[24] A. Desaix, O. Roubeau, J. Jeftic, J. G. Haasnoot, K. Boukheddaden, E. Codjovi, J. Linarès, M. Noguès, F. Varret, Eur. Phys. J. B **6** (1998) 183.

[25] J. Zarembowitch, O. Kahn, New J. Chem. **15** (1991) 181.

[26] O. Kahn, J. Kröber, C. Jay, Adv. Mat. **4** (1992) 718.

[27] O. Kahn, C. Jay Martinez, Science **279** (1998) 44.

[28] N. Motoyama, N. Eisaki, S. Uchida, Phys. Rev. Lett. **76** (1996) 3212.

[29] I. A. Zaliznyak, C. Broholm, M. Kibune, M. Nohara, H. Takagi, Phys. Rev. Lett. **83** (1999) 5370.

[30] M. Takigawa, N. Motoyama, H. Eisaki, S. Uchida, Phys. Rev. Lett. **76** (1996) 4612.

[31] S. E. Nagler, D. A. Tennant, R. A. Cowley, T. G. Perring, S. K. Satija, Phys. Rev. B **44** (1991) 12361.

[32] D. A. Tennant, R. A. Cowley, S. E. Nagler, A. M. Tsvelik, Phys. Rev. B **52** (1995) 13368.

[33] B. Lake, D. A. Tennant, S. E. Nagler, Phys. Rev. Lett. **85** (2000) 832.

[34] R. Coldea, D. A. Tennant, R. A. Cowley, D. F. McMorrow, B. Dorner, Z. Tylczynski, Phys. Rev. Lett. **79** (1997) 151.

[35] P. R. Hammar, M. B. Stone, D. H. Reich, C. Broholm, P. J. Gibson, M. M. Turnball, C. P. Landee, M. Oshikawa, Phys. Rev. B **59** (1999) 1008.

[36] D. C. Dender, D. Davidovic, D. H. Reich, C. Broholm, K. Lefmann, G. Aeppli, Phys. Rev. B **53** (1996) 2583.

[37] M. B. Stone, D. H. Reich, C. Broholm, K. Lefmann, C. Rischel, C. P. Landee, M. M. Turnbull, Phys. Rev. Lett. **91** (2003) 037205.

[38] G. Müller, H. Thomas, H. Beck, J. C. Bonner, Phys. Rev. B **24** (1981) 1429.

[39] M. Oshikawa, I. Affleck, Phys. Rev. Lett. **79** (1997) 2883.

[40] I. Affleck, M. Oshikawa, Phys. Rev. B **60** (1999) 1038.

[41] F. H. L. Essler, A. M. Tsvelik, Phys. Rev. B **57** (1998) 10592.

[42] F. H. L. Essler, Phys. Rev. B **59** (1999) 14376.

[43] T. Asano, H. Nojiri, Y. Inagaki, J. P. Boucher, T. Sakon, Y. Ajiro, M. Motokawa, Phys. Rev. Lett. **84** (2000) 5880.

[44] J. S. Russell, *Report of the Fourteenth Meeting of the British Association for the Advancement of Sciene* (Murray, London, 1844), pp. 311-390.

[45] J. Denschlag, J. E. Simsarian, D. L. Feder, C. W. Clark, L. A. Collins, J. Cubizolles, L. Deng, E. W. Hagley, K. Helmerson, W. P. Reinhardt, S. L. Rolston, B. I. Schneider, W. D. Phillips, Science **287** (2000) 97.

[46] K. E. Strecker, G. B. Partridge, A. G. Truscott, R. G. Hulet, Nature **417** (2002) 150.

[47] S. E. Nagler, W. J. L. Buyers, R. L. Armstrong, B. Briat, Phys. Rev. B **27** (1983) 1784.

[48] D. C. Dender, P. R. Hammar, D. H. Reich, C. Broholm, G. Aeppli, Phys. Rev. Lett. **79** (1997) 1750.

[49] R. B. Laughlin, Rev. Mod. Phys. **71** (1999) 863.

[50] L. F. Mollenauer, R. H. Stolen, J. P. Gordon, Phys. Rev. Lett. **45** (1980) 1095.

[51] M. Tinkham, *Introduction to Superconductivity* (McGraw-Hill, New York, 1996).

[52] S. A. Zvyagin, A. K. Kolezhuk, J. Krzystek, R. Feyerherm, Phys. Rev. Lett. **93** (2004) 027201.

[53] M. Kenzelmann, Y. Chen, C. Broholm, D. H. Reich, Y. Qiu, Phys. Rev. Lett. **93** (2004) 017204.

[54] R. Feyerherm, S. Abens, D. Günther, T. Ishida, M. Meißner, M. Meschke, T. Nogami, M. Steiner, J. Phys.: Condens. Matter **12** (2000) 8495.

[55] R. Helfrich, M. Köppen, M. Lang, F. Steglich, A. Ochiai, J. Magn. Magn. Mater. **177-181** (1998) 309.

[56] M. Oshikawa, K. Ueda, H. Aoki, A. Ochiai, M. Kohgi, J. Phys. Soc. Jpn. **68** (1999) 3181.

[57] M. Köppen, M. Lang, R. Helfrich, F. Steglich, P. Thalmeier, B. Schmidt, B. Wand, D. Pankert, H. Benner, H. Aoki, A. Ochiai, Phys. Rev. Lett. **82** (1999) 4548.

[58] W. Lenz, Z. Physik **21** (1920) 613.

[59] E. Ising, Z. Physik **31** (1925) 253.

[60] H.-J. Mikeska, A. K. Kolezhuk, *One-Dimensional Magnetism*, Lect. Notes Phys. **645** (2004) 1.

[61] L. J. de Jongh, A. R. Miedema, Adv. Phys. **23** (1974) 1.

[62] L. D. Faddeev, L. A. Takhtajan, Phys. Lett. **85A** (1981) 375.

[63] F. D. M. Haldane, Phys. Rev. Lett. **50** (1983) 1153.

[64] I. U. Heilmann, G. Shirane, Y. Endoh, R. J. Birgeneau, S. L. Holt, Phys. Rev. B **18** (1978) 3530.

[65] W. Heisenberg, Z. Physik **49** (1928) 619.

[66] H. A. Bethe, Z. Phys. **71** (1931) 205.

[67] N. D. Mermin, H. Wagner, Phys. Rev. Lett. **17** (1966) 1133.

[68] H. A. Kramers, Physica **1** (1934) 182.

[69] P. W. Anderson, Phys. Rev. **79** (1950) 350.

[70] J. B. Goodenough, Phys. Rev. **100** (1955) 564.

[71] J. B. Goodenough, J. Phys. Chem. Solids **6** (1958) 287.

[72] P. W. Anderson in "*Magnetism*", G. T. Rado and H. Suhl Eds. (Academic Press, New York, 1963).

[73] D. Coffey, K. S. Bedell, S. A. Trugman, Phys. Rev. B **42** (1990) 6509.

[74] D. Coffey, T.M. Rice, F. C. Zhang, Phys. Rev. B **44** (1991) 10112.

[75] N. E. Bonesteel, T. M. Rice, F. C. Zhang, Phys. Rev. Lett. **68** (1992) 2684.

[76] L. Shekhtman, A. Aharony, O. Entin-Wohlman, Phys. Rev. B **47** (1993) 174.

[77] N. E. Bonesteel, Phys. Rev. B **47** (1993) 11302.

[78] T. Moriya, Phys. Rev. **120** (1960) 91.

[79] J. des Cloizeaux, J. J. Pearson, Phys. Rev. **128** (1962) 2131.

[80] J. C. Bonner, M. E. Fisher, Phys. Rev. **135** (1964) A640.

[81] R. B. Griffiths, Phys. Rev. **133** (1964) A768.

[82] S. Eggert, I. Affleck, M. Takahashi, Phys. Rev. Lett. **73** (1994) 332.

[83] A. Fledderjohann, C. Gerhardt, K. H. Mütter, A. Schmitt, M. Karbach, Phys. Rev. B **54** (1996) 7168.

[84] M. Karbach, G. Müller, A. H. Bougourzi, A. Fledderjohann, K.-H. Mütter, Phys. Rev. B **55** (1997) 12510.

[85] A. Klümper, Eur. Phys. J. B **5** (1998) 677.

[86] A. Klümper, D. C. Johnston, Phys. Rev. Lett. **84** (2000) 4701.

[87] D. C. Johnston, R. K. Kremer, M. Troyer, X. Wang, A. Klümper, S. L. Bud'ko, A. F. Panchula, P. C. Canfield, Phys. Rev. B **61** (2000) 9558.

[88] M. Takahashi, *Thermodynamics of One-Dimensional Solvable Models* (Cambridge University Press, Cambridge, 1999).

[89] S. Lukyanov, Nucl. Phys. B **522** (1998) 533.

[90] L. Hulthén, Arkiv Mat. Astron. Fysik **26A**, No. 11 (1938).

[91] J. C. Bonner, B. Sutherland, P. M. Richards, in *Magnetism and Magnetic Materials - 1974 (San Francisco)*, Proceedings of the 20th Annual Conference on Magnetism and Magnetic Materials, AIP Conf. Proc. No. **24**, edited by C. D. Graham, G. H. Lander, J. J. Rhyne, (AIP, New York, 1975) 335.

[92] T. Yamada, Prog. Theor. Phys. Jpn. **41** (1969) 880.

[93] G. Müller, H. Thomas, H. Beck, in *Ordering in Strongly Fluctuating Condensed Matter Systems*, edited by T. Riste (Plenum, New York, 1980) p. 151 (Proceedings of the NATO AS1 Conference, Geilo, Norway, 1979).

[94] N. Shibata, K. Ueda, J. Phys. Soc. Jpn. **70** (2001) 3690.

[95] J. Lou, S. Qin, C. Chen, Z. Su, and L. Yu, Phys. Rev. B **65** (2002) 064420.

[96] A. M. Tsvelik, *Quantum Field Theory in Condensed Matter Physics* (Cambridge University Press, Cambridge, 1995).

[97] R. F. Dashen, B. Hasslacher, A. Neveu, Phys. Rev. D **11** (1975) 3424.

[98] see *http://www.pha.jhu.edu/~broholm/homepage/talks/*.

[99] Al. B. Zamolodchikov, Int. J. Mod. Phys. A **10** (1995) 1125.

[100] F. H. L. Essler, A. Furusaki, T. Hikihara, Phys. Rev. B **68** (2003) 064410.

[101] C. P. Slichter, *Principles of Magnetic Resonance* (Harper & Row Publishers, New York, 1963).

[102] A. Abragam, *The Principles of Nuclear Magnetism* (Clarendon Press, Oxford, 1961).

[103] A. P. Guimarães, *Magnetism and Magnetic Resonance in Solids* (John Wiley & Sons, INC., New York, 1998).

[104] E. Fukushima and S. B. W. Roeder, *Experimental Pulse NMR* (Addison-Wesley, Massachusetts, 1981).

[105] W. D. Knight, Phys. Rev. **76** (1949) 1259.

[106] E. Fermi, Z. Phys. **60** (1930) 320.

[107] J. A. Weil, J. R. Bolton and J. E. Wertz, *Electron Paramagnetic Resonance, Elementary Theory and Practical Applications* (John Wiley & Sons, INC, New York, 1994).

[108] M. H. Levitt, *Spin Dynamics, Basics of Nuclear Magnetic Resonance* (John Wiley & Sons, LTD, Chichester, 2001).

[109] P. C. Hammel, M. Takigawa, R. H. Heffner, Z. Fisk, K. C. Ott, Phys. Rev. Lett. **63** (1989) 1992.

[110] A. J. Millis, H. Monien, D. Pines, Phys. Rev. B **42** (1990) 167.

[111] A. J. Millis, H. Monien, Phys. Rev. B **45** (1992) 3059.

[112] M. Horvatic, C. Berthier, Y. Berthier, P. Ségransan, P. Butaud, W. G. Clark, J. A. Gillet, J. Y. Henry, Phys. Rev. B **48** (1993) 13848.

[113] J. Sagi, I. Affleck, Phys. Rev. B **53** (1996) 9188.

[114] G. Chaboussant, M.-H. Julien, Y. Fagot-Revurat, M. Hanson, L. P. Lévy, C. Berthier, M. Horvatic, O. Piovesana, Eur. Phys. J. B **6** (1998) 167.

[115] M. Horvatić and C. Berthier, *NMR Studies of Low-Dimensional Quantum Antiferromagnets*, Lect. Notes Phys. **595**, C. Berthier, L. P. Lévy, and G. Martinez (Eds.) (Springer Verlag, Berlin, 2002).

[116] M. Takigawa, Phys. Rev. B **49** (1994) 4158.

[117] A. J. Millis, H. Monien, Phys. Rev. B **54** (1996) 16172.

[118] A. Goto, T. Shimizu, Phys. Rev. B **57** (1998) 7977.

[119] P. Auban-Senzier and D. Jérome, *Présentation des techniques haute pression utilisées et développées à Orsay dans le but de mesures physiques spécifiques*, in "2eme forum de la Technologie des Hautes Pressions, Méthodes d´analyses physico-chimiques", edited by the Réseau Hautes Pressions de CNRS, Autrans, France, 07.-11.06.1999.

[120] O. Portugall, F. Lecouturier, J. Marquez, D. Givord, S. Askénazy, Physica B **294-295** (2001) 579.

[121] F. Dupouy, Ph.D. Thesis, INSA Toulouse, France (1995).

[122] Webpage of the LNCMP, *www.lncmp.org*.

[123] J. Z. Zhao, X. Q. Wang, T. Xiang, Z. B. Su, L. Yu, Phys. Rev. Lett. **90** (2003) 207204.

[124] M. Kohgi, K. Iwasa, J.-M. Mignot, B. Fåk, P. Gegenwart, M. Lang, A. Ochiai, H. Aoki, T. Suzuki, Phys. Rev. Lett. **86** (2001) 2439.

[125] P. Gegenwart, H. Aoki, T. Cichorek, J. Custers, N. Harrison, M. Jaime, M. Lang, A. Ochiai, F. Steglich, Physica B **312-313** (2002) 315.

[126] K. Iwasa, M. Kohgi, A. Gukasov, J.-M. Mignot, N. Shibata, A. Ochiai, H. Aoki, T. Suzuki, Phys. Rev. B **65** (2002) 052408.

[127] C. P. Landee, A. C. Lamas, R. E. Greeney, K. G. Bücher, Phys. Rev. B **35** (1987) 228.

[128] A. Ochiai, T. Suzuki, T. Kasuya, J. Phys. Soc. Jpn. **59** (1990) 4129.

[129] P. Fulde, B. Schmidt, P. Thalmeier, Europhys. Lett. **31** (1995) 323.

[130] H. Shiba, K. Ueda, O. Sakai, J. Phys. Soc. Jpn. **69** (2000) 1493.

[131] D. B. Losee, H. W. Richardson, W. E. Hatfield, J. Chem. Phys. **59** (1973) 3600.

[132] H. W. Richardson, W. E. Hatfield, J. Am. Chem. Soc. **98** (1976) 835.

[133] H. W. Richardson, J. R. Wasson, W. E. Hatfield, Inorg. Chem. **16** (1977) 484.

[134] T. Ishida, T. Nogami, Recent Res. Dev. Pure Appl. Chem. **1** (1997) 1.

[135] T. Ishida, K. Nakayama, M. Nakagawa, W. Sato, Y. Ishikawa, M. Yasui, F. Iwasaki, T. Nogami, Synth. Met. **85** (1997) 1655.

[136] R. Feyerherm, T. Ishida, T. Nogami, and M. Steiner, Mol. Cryst. Liq. Cryst. **335** (1999) 947.

[137] H. J. Schulz, Phys. Rev. Lett. **77** (1996) 2790.

[138] H. Koizumi, K. Osaki, T. Watanabé, J. Phys. Soc. Japan **18** (1963) 117.

[139] K. Oshima, K. Okuda, M. Date, J. Phys. Soc. Jpn. **44** (1978) 757.

[140] M. Date, H. Yamazaki, M. Motokawa, S. Tazawa, Suppl. Progr. Theor. Phys. **46** (1970) 194.

[141] H. Mollymoto, E. Fujiwara, M. Motokawa, M. Date, J. Phys. Soc. Jpn. **48** (1980) 1771.

[142] S. Inawashiro, S. Katsura, Phys. Rev. **140** (1965) A892.

[143] F. Capraro, C. Gros, Eur. Phys. J. **B 29** (2002) 35.

[144] T. Asano, D. Nomura, Y. Inagaki, Y. Ajiro, H. Nojiri, Y. Narumi, K. Kindo, T. Ishida, T. Nogami, Physica B **329-333** (2003) 1006.

[145] B. Wolf, S. Zherlitsyn, B. Lüthi, N. Harrison, U. Löw, V. Pashchenko, M. Lang, G. Margraf, H.-W. Lerner, E. Dahlmann, F. Ritter, W. Assmus, M. Wagner, Phys. Rev. B **69** (2004) 092403.

[146] R. Feyerherm, unpublished.

[147] A. M. Clogston, V. Jaccarino, Y. Yafet, Phys. Rev. **134** (1964) A650.

[148] Y. Ajiro, K. Enomoto, N. Terata, M. Matsuura, Solid State Comm. **20** (1976) 1151.

[149] M. Matsuura, Y. Ajiro, J. Phys. Soc. Jpn. **41** (1976) 44.

[150] B. Gillon, Mol. Cryst. Liq. Cryst. **335** (1999) 53.

[151] P. Parhami, B. M. Fung, J. Am. Chem. Soc. **107** (1985) 7304.

[152] V. R. Saunders, R. Dovesi, C. Roetti, R. Orlando, C. M. Zicovich-Wilson, N. M. Harrison, K. Doll, B. Civalleri, I. J. Bush, Ph. D'Arco, M. Llunell, CRYSTAL2003 Users Manual (University of Torino, Torino, Italy, 2004).

[153] M. D. Towler, R. Dovesi, V. R. Saunders, Phys. Rev. B **52** (1995) 10150.

[154] R. Dovesi, C. Roetti, C. Freyria-Fava, M. Precipe, V. R. Saunders, J. Chem. Phys. **156** (1991) 11.

[155] R. Dovesi, M. Causá, R. Orlando, C. Roetti, V. R. Saunders, J. Chem. Phys. **92** (1990) 7402.

[156] R. Ditchfield, W. J. Hehre, J. A. Pople, J. Chem. Phys. **54** (1971) 724.

[157] I. de P. R. Moreira, F. Illas, R. L. Martin, Phys. Rev. B **65** (2002) 155102.

[158] H. Nieber, K. Doll, G. Zwicknagel, Eur. Phys. J. B **44** (2005) 209.

[159] K. Raghavachari, Theor. Chem. Acc. **103** (2000) 361.

[160] M. J. Frisch, G. W. Trucks, H. B. Schlegel, G. E. Scuseria, M. A. Robb, J. R. Cheeseman, J. A. Montgomery, Jr., T. Vreven, K. N. Kudin, J. C. Burant, J. M. Millam, S. S. Iyengar, J. Tomasi, V. Barone, B. Mennucci, M. Cossi, G. Scalmani, N. Rega, G. A. Petersson, H. Nakatsuji, M. Hada, M. Ehara, K. Toyota, R. Fukuda, J. Hasegawa, M. Ishida, T. Nakajima, Y. Honda, O. Kitao, H. Nakai, M. Klene, X. Li, J. E. Knox, H. P. Hratchian, J. B. Cross, V. Bakken, C. Adamo, J. Jaramillo, R. Gomperts, R. E. Stratmann, O. Yazyev, A. J. Austin, R. Cammi, C. Pomelli, J. W. Ochterski, P. Y. Ayala, K. Morokuma, G. A. Voth, P. Salvador, J. J. Dannenberg, V. G. Zakrzewski, S. Dapprich, A. D. Daniels, M. C. Strain, O. Farkas, D. K. Malick, A. D. Rabuck, K. Raghavachari, J. B. Foresman, J. V. Ortiz, Q. Cui, A. G. Baboul, S. Clifford, J. Cioslowski, B. B. Stefanov, G. Liu, A. Liashenko, P. Piskorz, I. Komaromi, R. L. Martin, D. J. Fox, T. Keith, M. A. Al-Laham, C. Y. Peng, A. Nanayakkara, M. Challacombe, P. M. W. Gill, B. Johnson, W. Chen, M. W. Wong, C. Gonzalez, and J. A. Pople, Gaussian 03, Revision C.02 (Gaussian, Inc., Wallingford CT, 2004).

[161] C. J. Jameson in "*Encyclopedia of Nuclear Magnetic Resonance*", D. M. Grant and R. K. Harris Eds. (John-Wiley & Sons, Chichester, 1996), Vol. 2, pp. 1273-1281.

[162] M. Chiba, Y. Ajiro, H. Kikuchi, T. Kubo, T. Morimoto, Phys. Rev. B **44** (1991) 2838(R).

[163] T. C. Kobayashi, K. Tanaka, K. Fujiwara, K. Amaya, N. Aizawa, T. Ishii, M. Yamashita, J. Magn. Magn. Matter **226-230** (2001) 423.

[164] K. Kodama, S. Miyahara, M. Takigawa, M. Horvatic, C. Berthier, F. Mila, H. Kageyama, Y. Ueda, J. Phys.: Condens. Matter **17** (2005) L61.

[165] N. Bloembergen, E. M. Purcell, R. V. Pound, Phys. Rev. **73** (1948) 679.

[166] M. Kenzelmann, C. D. Batista, Y. Chen, C. Broholm, D. H. Reich, S. Park, Y. Qiu, Phys. Rev. B **71** (2005) 094411.

[167] K. Magishi, S. Matsumoto, Y. Kitaoka, K. Ishida, K. Asayama, M. Uehara, T. Nagata, J. Akimitsu, Phys. Rev. B **57** (1998) 11533.

[168] Y. Piskunov, D. Jérome, P. Auban-Senzier, P. Wzietek, A. Yakubovsky, Phys. Rev. B **69** (2004) 014510.

[169] S. Torre, A. Rigamonti, Phys. Rev. B **36** (1987) 8274.

[170] H. Winter, E. Dormann, M. Bertault, L. Toupet, Phys. Rev. B **46** (1992) 8057.

[171] G. Zimmer, M. Mehring, C. Goze, F. Rachdi, Phys. Rev. B **52** (1995) 13300.

[172] M. Yasui, Y. Ishikawa, N. Akiyama, T. Ishida, T. Nogami, F. Iwasaki, Acta Cryst. B **57** (2001) 288.

[173] M. Mito, T. Kawae, M. Takumi, K. Nagata, M. Tamura, M. Kinoshita, K. Takeda, Phys. Rev. B **56** (1997) R14255.

[174] M. Mito, T. Kawae, A. Ikegami, M. Hitaka, K. Takeda, S. Nakatsuji, H. Morimoto, H. Anzai, Physica B **284-288** (2000) 1493.

[175] M. Mito, T. Kawae, M. Hitaka, K. Takeda, T. Ishida, T. Nogami, Chem. Phys. Lett. **333** (2001) 69.

[176] R. Feyerherm, J. Magn. Magn. Matter **256** (2003) 328.

[177] K. Zusai, T. Kusaka, T. Ishida, R. Feyerherm, M. Steiner, T. Nogami, Mol. Cryst. Liq. Cryst. **343** (2000) 127.

[178] S. Eggert, I. Affleck, Phys. Rev. B **46** (1992) 10866.

[179] S. Eggert, I. Affleck, Phys. Rev. Lett. **75** (1995) 934.

[180] M. Takigawa, N. Motoyama, H. Eisaki, S. Uchida, Phys. Rev. B **55** (1997) 14129.

[181] F. Tedoldi, R. Santachiara, M. Horvatic, Phys. Rev. Lett. **83** (1999) 412.

[182] S. Botti, A. Rosso, R. Santachiara, F. Tedoldi, Phys. Rev. B **63** (2000) 012409.

[183] J. Das, A. V. Mahajan, J. Bobroff, H. Alloul, F. Alet, E. S. Sørensen, Phys. Rev. B **69** (2004) 144404.

[184] D. V. Lang, J. B. Boyce, D. C. Lo, C. P. Slichter, Phys. Rev. Lett. **29** (1972) 776.

[185] J. Bobroff, H. Alloul, Y. Yoshinari, A. Keren, P. Mendels, N. Blanchard, G. Collin, J.-F. Marucco, Phys. Rev. Lett. **79** (1997) 2117.

[186] M. I. Larkin, Y. Fudamoto, I. M. Gat, A. Kinkhabwala, K. M. Kojima, G. M. Luke, J. Merrin, B. Nachumi, Y. J. Uemura, M. Azuma, T. Saito, M. Takano, Phys. Rev. Lett. **85** (2000) 1982.

Acknowledgements

I sincerely wish to express my gratitude to everybody who contributed to the completion of this thesis.

First of all, I would like to thank my supervisors Dr. Hans-Henning Klauss and Prof. Dr. Stefan Süllow for giving me the opportunity to work on a fascinating branch of solid state physics in the inspiring scientific environment of Braunschweig, Paris and Toulouse. I truly appreciate their enthusiasm for physics and I particularly enjoyed their cheerful mood. Especially, I am deeply indebted to Prof. Dr. Stefan Süllow for countless discussions and for always having a sympathetic ear when I had a problem. I was given an excellent scientific training through him, which has always motivated me. Furthermore, I would like to thank him for never being filled with despair each time I felt discouraged. I am very grateful to Dr. Hans-Henning Klauss for introducing me to the NMR technique during my diploma thesis, for his advice and for many fruitful discussions. I am also thankful to Prof. Dr. Jochen Litterst who, in spite of the great amount of work involved in his presidency of the Technical University of Braunschweig, always had time for fruitful discussions. In this context I should also not forget to mention Dr. Ralf Feyerherm, who started with the project on copper pyrimidine dinitrate, and whose precious advice, ideas and permanent will to discuss helped me settling in the world of staggered $S = 1/2$ AHFCs. Further, I am particularly happy that Prof. Dr. Michael Lang agreed to referee this thesis, for which I would really like to thank him.

My special thanks goes to my office mate Anna Otop for tirelessly withstanding my questions, my constant excited and passionate ”private talks” and for becoming more than just a colleague during the five years. Thanks for the good time we had together! I would also like to thank all the other present and former members of our ”merged” μSR, NMR and transport group, namely Dr. Dirk Baabe, Matthias Bleckmann, Dr. Michael Birke, Anika Bosse, Marc Broekelmann, Fathi Gouider, Hannes Kühne, Jan Kreitlow, Dr. Igor Maksimov, Christopher Mennerich, Dirk Mienert, and Sascha Populoh for the good work climate and for the jokes and great laughter each day. I am indebted to the people from the machine shop in Braunschweig, Arno Ellermann and Robert Hofmann for their technical support. I also feel grateful to Heiko Ahlers and Joachim Lüdke from the PTB, as well as to Dr. Dirk Menzel, who gave me support for the SQUID measurements. Thanks for the delicious tea, Joachim!

I am particularly happy about the collaboration with Dr. Klaus Doll and Dr. Andreas Honecker, whom I would like to thank for the pleasant and fruitful discussions and who never seemed to be annoyed about my ”silly” questions about theory. As you know Klaus, ”saving my life” will always be rewarded with a bottle of champagne! I also wish to express my gratitude to Prof. Dr. Wolfram Brenig, Stefan Glocke, Prof. Dr. Andreas Klümper, Dr. Alexei Kolezhuk, and Dr. Sergei Zvyagin for fruitful discussions and successful team work between theoretical and experimental physicists.

I owe a special debt of gratitude to Dr. Pawel Wzietek, who has become a true friend and whose profound NMR experience and cooperativeness made my stay in Orsay become a successful and pleasant chapter in my life. Not only have I greatly benefitted from our encouraging discussions, but I also enjoyed his unfailing cheerful mood. I am also deeply grateful to Prof. Dr. Denis Jérome and his group from the Laboratoire de Physique des Solides for many discussions, experimental support, and for hospitality, namely Dr. Pascale Auban-Senzier, Nada Joo, Dr. Patrice Limelette, Dr. Claude Pasquier, and Dr. Pawel Wzietek. Without their excellent knowledge and help, my investigations would never have been possible. Further, I would like to thank my friends from the LPS, Martin Bauer, Nada Joo, and Sondes Trabelsi, for giving me support and for making me feel at home in Paris.

I would also like to thank Prof. Dr. Jean-Marc Broto, Dr. Mathilde Costes and Dr. Harison Rakoto from the Laboratoire National des Champs Magnétique Pulsés for the assistance with the high-field magnetization experiments. Thank you for forcing me to speak french during my second stay. It helped me a lot improving my vocabulary! The pleasant atmosphere in Toulouse really made a mark on my "francophil" personality.

Dr. Hans-Henning Klauss, Dr. Pawel Wzietek, and in particular Prof. Dr. Stefan Süllow have shared the tedious task of proofreading this thesis, for which I am deeply indebted to them.

Finally, I am very grateful to my friends Imke Baumgärtel, Stephanie Buss, and Monika Dudda for our friendship and for all their support and inspiration, while I was writing this thesis. I am sure that our discussions beyond physics have prevented me from losing my fantasy and humanity especially during the last few months!

It is with particular pleasure that I express my affectionate and deeply-felt gratitude to my family for their continual encouragement, confidence and kind moral support in any situation beyond the realm of physics. Without their support and warmth I would have never been able to finish my thesis! Thank you for being by my side.

Curriculum Vitae

Personal Data

Name	Anja Ursula Brigitte Wolter
Date of birth	13.02.1975
Place of birth	Braunschweig, Germany
Nationality	German

Education and Academic Degrees

1981–1987	Primary School Lehndorf, Braunschweig
1987–1994	Hoffmann-von-Fallersleben Gymnasium Braunschweig (High School) School leaving certificate (*Abitur*, 1994)
1994–2000	Technical University of Braunschweig Degree in physics (*Diplom*, 2000) Subject of diploma thesis: *NMR Untersuchungen an der Heusler Verbindung* Co_2NbSn

Current Position

2001–2005	Research assistant at the Institute for Condensed Matter Physics, Technical University of Braunschweig Preparation of the Ph.D. thesis Thesis subject: *Longitudinal and Transverse Magnetization in* *Low-Dimensional Molecule-Based Quantum Magnets* Supervisor: Jun.-Prof. Dr. Stefan Süllow, TU Braunschweig
2001–2002	Research stay (10 month) at the Laboratoire de Physique des Solides, University Paris-Sud, in the research group of Prof. Dr. D. Jérome
since July 2005	at the Berliner Elektronenspeicherring-Gesellschaft für Synchrotron Strahlung (BESSY), Berlin, working on "Structural Analysis of Organic Superconductors"

Further Publications

- A. U. B. Wolter, H.-H. Klauß, F. J. Litterst, C. Geibel, S. Süllow, *Magnetic history effects in the Heusler compound* Co_2NbSn, J. Magn. Magn. Mater. **242-245** (2002) 888.

- A. U. B. Wolter, A. Bosse, D. Baabe, I. Maksimov, D. Mienert, H. H. Klauß, F. J. Litterst, D. Niemeier, R. Michalak, C. Geibel, R. Feyerherm, R. Hendrikx, J. A. Mydosh, S. Süllow, *Structure and magnetic order of the Heusler compound* Co_2NbSn, Phys. Rev. B **66** (2002) 174428.

- J. Kreitlow, D. Baabe, A. U. B. Wolter, S. Süllow, F. J. Litterst, D. J. Price, H.-H. Klauss, *Mössbauer studies on the Fe(II) oxalate spin ladder* $Na_2Fe_2(C_2O_4)_3(H_2O)_2$, J. Magn. Magn. Mater. **272-276** (2004) 152.

Conference Contributions

- A. Wolter, A. Bosse, D. Mienert, S. Suellow, H. H. Klauß, F. J. Litterst, C. Geibel, *NMR Studies on the Heusler Compound* Co_2NbSn (poster), DPG Frühjahrstagung 2000, Regensburg, Germany, 27.-31.03.2000.

- A. Wolter, A. Bosse, D. Mienert, S. Süllow, H.-H. Klauß, F. J. Litterst, C. Geibel, *Magnetische Ordnung in der Heuslerverbindung* Co_2NbSn (poster), DPG Frühjahrstagung 2001, Hamburg, Germany, 26.-30.03.2001.

- A. Wolter, A. Bosse, H. H. Klauß, F. J. Litterst, R. Feyerherm, C. Geibel, S. Süllow, *Magnetic ordering in the Heusler compound* Co_2NbSn (poster), Joint European Magnetic Symposia, Grenoble, France, 28.08.-01.09.2001.

- Anja Wolter, Jan Kreitlow, Dirk Baabe, Hans-Henning Klauss, Stefan Süllow, Dirk Mienert, Jochen Litterst, Daniel J. Price, A. Amato, *Magnetic Correlations in Co and Fe Oxalate Spin Ladders* (poster), VIIIth International Conference on Molecule-based Magnets, ICMM´2002, Valencia, Spain, 05.10.-10.10.2002.